Assembly and Regulation of the Inflammasome Governed by a Unified Polymerization Mechanism

A dissertation presented

by

Alvin Ziying Lu

to

The Committee on Higher Degrees in Chemical Biology

in partial fulfillment of the requirements

for the degree of

Doctor of Philosophy

in the subject of

Chemical Biology

Harvard University

Cambridge, Massachusetts

April 2016

Dissertation Advisor:
Professor Hao Wu

Author:
Alvin Ziying Lu

Assembly and Regulation of the Inflammasome

Governed by a Unified Polymerization Mechanism

Abstract

The innate immune system employs a diverse set of pattern recognition receptors to detect intrinsic and extrinsic danger signals for host protection. Inflammasomes represent an important class of receptors that elicit inflammatory response through the maturation of pro-inflammatory cytokines and the induction of a form of cell death known as pyroptosis. Assembly of a functional inflammasome typically involves an upstream sensor component, an adaptor component, and an effector caspase. The upstream sensor oligomerizes upon detection of pro-inflammatory triggers to recruit the adaptor, which in turn drives caspase activation. The assembled inflammasome proteolytically cleaves interleukin-1β (IL-1β) and interleukin-18, which are the cytokines responsible for downstream signaling events. Previously, our understanding of this assembly process had been limited by the lack of biochemical data and high-resolution structures.

In this dissertation, I present key findings that provide novel perspectives on the assembly and regulation of inflammasomes using structural and biochemical approaches. More specifically, a two-step nucleated polymerization mechanism governs the assembly and activation of inflammasomes that require the filamentous scaffold of an adaptor known as Apoptosis-associated Speck-like protein containing a CARD (ASC). Upstream sensors oligomerize to nucleate the formation of ASC filaments, which in turn nucleate the effector caspase-1 to form another set of filaments. These signaling filaments coalesce into a micron-sized perinuclear puncta, which could be observed under light microscopes. Moreover, I also present evidence to support a capping mechanism for inflammasome regulation. Inhibitor of

CARD (INCA) terminates caspase-1 filaments by binding to their ends, which effectively blocks proximity-driven activation of pro-caspase-1 and dampens IL-1β maturation. Both activation and regulation of the inflammasome rely on the special properties of homotypic interaction domains that belong to the death domain superfamily.

Collectively, these studies support a novel paradigm in which the innate immune system exploits signaling filaments for the desired functional outcomes. By understanding the structural and biophysical properties of these supramolecular complexes, we may begin to identify novel targets for therapeutic intervention. In the last chapter, I will also discuss some remaining questions of the inflammasome field, particularly the ones that could be addressed by structural and biochemical methods.

Table of Contents

Acknowledgements

I would like to take this opportunity to express the greatest appreciation to my advisor, Professor Hao Wu, who has guided me through the long but hasty journey of graduate school and provided the utmost support that she could offer. The transition from Weill Cornell Medical School to Harvard University was somewhat intimidating and took some getting used to (both personally and academically). Thankfully, it went much smoother than I expected with her help. I am always amazed by her cheerful personality and scientific curiosity, which have been very inspiring in many occasions. I will never forget the persistence and passion she has embarking on her scientific endeavors, and her incredible energy level always amazes me.

I also want to thank my lab members and collaborators who have helped me on various aspects of my projects over the years. Instead of thanking them individually, I will mention their contributions at the beginning of each chapter. In particular, I would like to thank Dr. Qian Yin and Dr. Tian-min Fu, who have also provided intellectual support and valuable discussions in the lab. I also want to thank Professor Edward Egelman and Dr. Florian Schmidt, who are the major collaborators on my projects. Professor Egelman has worked closely with us on helical reconstructions. Florian from the Ploegh lab has given tremendous help on cellular experiments.

In addition, I would like to acknowledge our past and present lab managers / technicians to whom we may have not given enough credits. Ermelinda Damko was our lab manager at Weill Cornell who helped me on cloning and expression problems when I first joined the lab. Qiubai Li is our current lab manager and technician who generated small-scale insect cell expression test-preps during my initial construct screening. Claire Richards was our lab manager and gave help on everyone's projects until she moved on to start her studies in medical school. Unfortunately, Claire passed away after fighting a hard battle with melanoma. It is such a shame because she always had a cheerful and optimistic personality, which would have made her a great physician.

I am fortunate to be supported by members of my dissertation advisory committee – Professor Tim Mitchison, Professor Steve Harrison, and Professor Jim Hogle – who are making sure that I stay on track for graduation. As experts in their own fields, they have also provided fresh perspectives and valuable ideas on my projects. My program coordinators in Chemical Biology, Jason Millberg and Samantha Reed, have navigated me through these four years, for which I feel very grateful.

I also want to give special thanks to Dr. Yuying Gosser, who was my undergraduate research advisor and insisted that I should pursue a doctorate degree in science. The decision to embark on such a long journey was not easy, but I am glad that she geared me toward such direction when I had little clue of what I wanted to do after finishing college. I have now begun to appreciate science and enjoy doing research, and I owe her many thanks for that.

My family has also given me unconditional supports and encouragement. My parents, who speak little English and understand only popular science, had once been against my decision to apply for PhD programs. However, they still supported me and cheered for me during these six years. I also want to thank my wife for her continuous emotional support and for accepting me into her life, even though she knows that pursuing a career in science may entail minimalistic personal life. Lastly, I would like to thank all my friends, both in New York and in Boston, who have cheered for me during all these years.

Chapter One

Introduction

In the human innate immune system, there is a diverse set of sensors that recognize the stimuli derived from infection or cell damage. In myeloid cells, multiple cytosolic sensors and adaptors come together spatially to coordinate an inflammatory response through the assembly of macromolecular protein complexes known as the inflammasomes. The sensor component of an inflammasome is responsible for detection of one or more specific ligands and/or inflammatory perturbations in the cell. It may then activate to recruit an adaptor component, which relays the signal to the effector component. Upon assembly and activation, inflammasomes can then drive the maturation of pro-inflammatory cytokines and also lead to a form of cell death known as pyroptosis, which is characterized by cell swelling, pore formation, and cell lysis.

Inflammasome Components

Canonical inflammasomes assemble upon activation of two classes of sensor molecules – NOD-like receptors (NLRs) and AIM2-like receptors (ALRs). The human genome encodes 22 NLRs [1], but only NLRP1 [2], NLRP3 [3, 4], NLRP6 [5], NLRP7 [6], NLRP12 [7], and the NAIP/NLRC4 complex [8-11] have been reported to assemble into their respective inflammasomes. These essential sensor proteins contain an effector domain such as caspase recruitment domain (CARD), Pyrin domain (PYD), or baculoviral IAP repeat (BIR) domain for downstream interactions, a nucleotide-binding and oligomerization domain NBD or NACHT, and a leucine-rich repeats (LRR) domain (**Figure 1.1**). Structural evidence concludes that both NACHT and LRR are important for auto-inhibition of the sensor proteins in the absence of stimulation [12]. ALRs comprise a PYD domain and a dsDNA-binding domain HIN200, and are simpler than NLRs.

The assembly of inflammasomes relies on homotypic interactions between component proteins. For a subset of them, the upstream sensor proteins, such as NLRP3 and AIM2, recruit the Apoptosis-associated Speck-like protein containing a CARD (ASC), via interactions between

their PYDs. ASC then interacts with caspase-1, the principal cysteine protease, via their CARD/CARD interactions. Consequently, the bipartite nature of ASC represents the core structure of these "ASC-dependent" inflammasomes. The NAIP/NLRC4/caspase-1 complex is a representative ASC-independent inflammasome, in which NAIP is the sensor and NLRC4 is the adaptor, although both NAIP and NLRC4 belong to NLRs by domain definition (**Figure 1.1**). NLRC4 contains a CARD and can directly recruit and activate caspase-1.

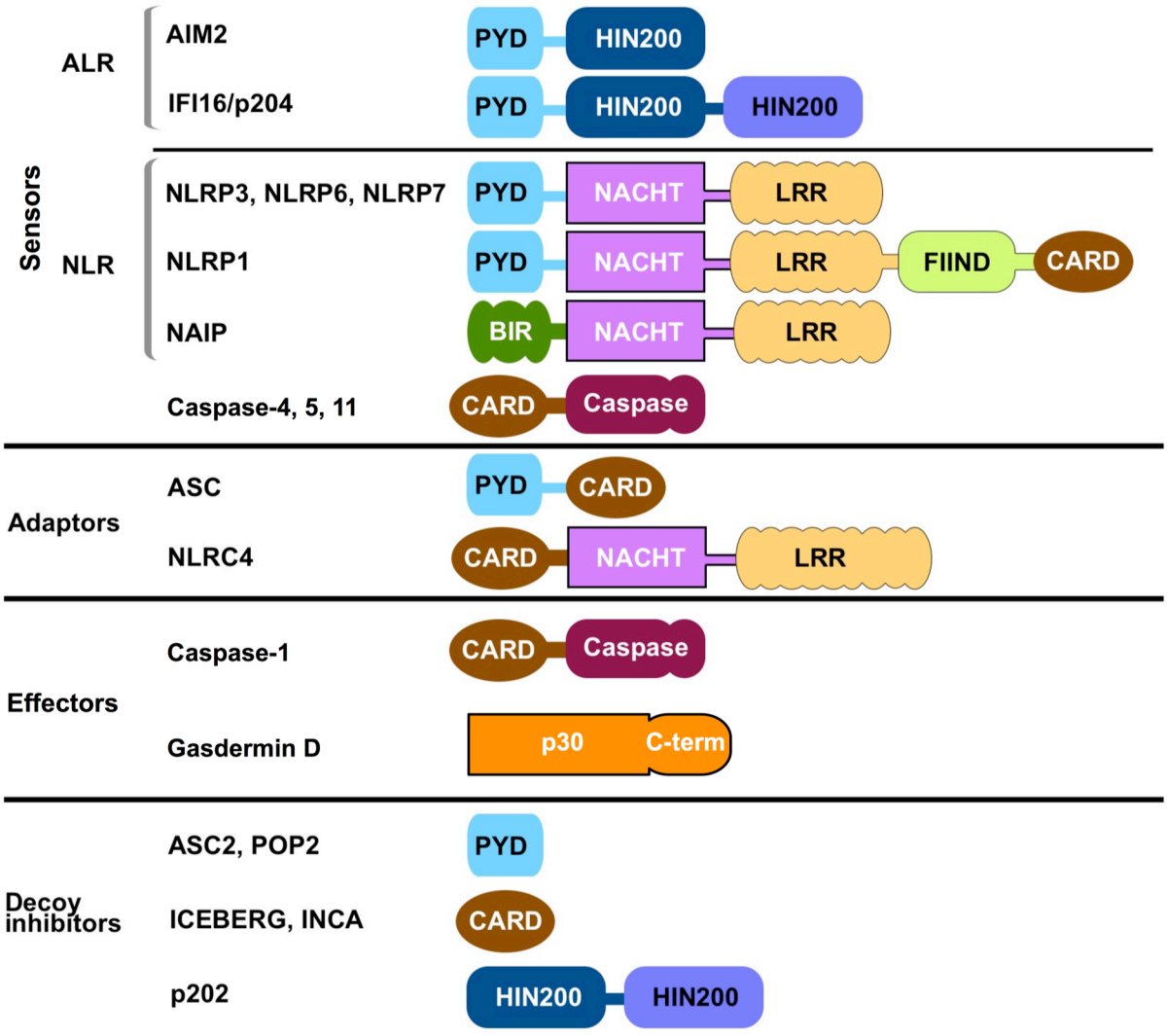

Figure 1.1. Domain Architecture of Inflammasome Components. Modified from a figure of our review article published in the *FEBS Journal* [13].

More recently, the role of caspase-4, 5 and 11 during Gram-negative bacterial infections defines non-canonical inflammasomes. Caspae-4 and caspase-5 are human homologs of capase-11 in mouse. Caspase-11 has long been thought to directly activate caspase-1, because of their close resemblance in domain architecture and enzymatic activity [4, 14, 15]. However, recent discoveries have re-defined caspase-11 as a sensor (rather then just an effector) component for the detection of intracellular lipopolysaccharides (LPS), which are a signature of bacterial infection [16, 17]. Binding of cytosolic LPS to the CARD of caspase-11 leads to oligomerization and proximity-driven activation [16]. The downstream component to the caspase-11 inflammasome has recently been confirmed to be gasdermin D [17, 18]. It belongs to the gasdermin gene family whose members have been implicated in apoptosis of epithelial cells and autosomal recessive deafness, although this particular member, gasdermin D, had not been well characterized [19] (**Figure 1.1**). Cleavage of gasdermin D between Asp276 and Gly277 by caspase-11 releases the function N-terminal domain that facilitates the release of matured IL-1β and pyroptotic cell death [17, 18], presumably through rupturing the cell membrane. The exact molecular action requires future structural studies because gasdermin D has no predicted transmembrane feature.

Inflammasome Activation Requires Priming of the Component Proteins

Prior to inflammasome activation, component proteins are suppressed in many levels. For example, NLRP3 expression is kept at a basal level until LPS-dependent activation of the Toll-Like Receptor 4 (TLR4) pathway results in the activation of the transcription factor NF-κB and induction of NLRP3 expression [20]. This transcriptional priming step is required to provide a sufficient level of, not only sensor proteins such as NLRP3, but also pro-inflammatory cytokines [21, 22]. Moreover, deubiquitination of NLRP3 by a transcriptional-independent priming step also potentiates inflammasome activation. Brief stimulation of the TLR4 pathway without inducing NLRP3 expression was sufficient to sensitize the system for NLRP3 triggers

[23]. The adaptor molecule MyD88 and IRAK family kinases are responsible for this alternative priming mechanism [23, 24].

Caspase-8, a proapoptotic initiator caspase, also plays a role in the transcriptional priming of inflammasome. Traditionally, it mediates the extrinsic apoptosis pathway in response to external stimuli and protects against an inflammatory form of cell death known as necroptosis [25]. Surprisingly, caspase-8 deficiency in macrophages impaired LPS-induced expression of NLRP3 and pro-IL-1β expression [26, 27]. This piece of evidence suggests that caspase-8 may at least have a role in priming the inflammasome, which indicates a crosstalk between the inflammatory and apoptotic pathways.

ASC-dependent Inflammasomes

The NLR and ALR families of ASC-dependent inflammasomes respond to distinct sets of intrinsic and extrinsic damage-associated or pathogen-associated molecular patterns (DAMPs and PAMPs). The AIM2-like receptors have the most defined ligand – they detect double-stranded DNA with their HIN200 domain. Double stranded DNA in the cytosol is a strong indicator of bacterial or viral infection. In addition, intrinsic cellular insults such as mitochondrial damage, lysosomal rupture, and leakage of nuclear DNA also contribute to the pool of cytosolic DNA [28, 29]. Binding of cytosolic dsDNA to the C-terminal HIN200 domain of AIM2 releases the N-terminal PYD domain from autoinhibition, which thereby assembles the AIM2 inflammasome [30, 31]. The nucleoplasm-localized IFI16 has also been proposed to assemble a functional ALR inflammasome [32, 33], although it is not very well characterized [22].

Among the NLR inflammasome members, NLRP3 responds to the broadest spectrum of stimuli and is the most disease-relevant inflammasome. Ion flux across plasma and mitochondrial membranes activates the NLRP3 inflammasome. Potassium efflux to the extracellular space due to destabilization of the plasma membrane by pore-forming toxins and particulate matter is a common NLRP3 trigger [34]. In addition, calcium influx to the cytosol in

response to some of the NLRP3 agonists, such as mitochondrial damage, also contributes to inflammasome activation [35]. Translocation of the ER-resident NLRP3 and the nucleus-resident adaptor ASC co-localizes them with mitochondria at the perinuclear space, and the release of reactive oxygen species (ROS) from the mitochondria may thereby facilitate NLRP3 inflammasome activation [36]. The release of mitochondrial DNA, the association of the inner mitochondrial membrane-specific lipid cardiolipin with NLRP3, and the release of lysosomal cathepsins into the cytosol are also associated with NLRP3 inflammasome activation [37, 38]. However, the structural mechanism by which NLRP3 is activated has yet to be elucidated, whether it is through an unidentified ligand or an intermediate signaling event.

The activation mechanism of NLRP1 inflammasome is complicated by its genetic variation. There are three paralogs of mouse NLRP1 (NLRP1a, b, and c) but only the single paralog in human [39]. For NLRP1b alone, at least five allelic variants exist in different inbred mouse strains. This genetic complexity may indicate that NLRP1 is under positive (diversifying) selection pressure, which is consistent with its role as an important pathogen-recognition receptor [39]. NLRP1 has been shown to sense anthrax lethal toxin (LeTx), which is a virulence factor deployed by the Gram-positive, rod-shaped bacteria *Bacillus anthracis* that causes anthrax disease. LeTx is a bipartite toxin containing protective antigen (PA) and lethal factor (LF). The proteolytic activity of LF is critical for activating NLRP1b inflammasome by an incompletely understood mechanism. LF may directly proteolyze NLRP1b to release the N-terminal fragment that autoinhibits the NBD. Alternatively, it may cleave an unknown negative regulator of NLRP1b which leads to proteasome-dependent degradation of this regulator to NLRP1b inflammasome activation [39]. Muramyl dipeptide (MDP), a bacterial peptidoglycan, has been proposed to induce the binding of ATP to NLRP1 to promote its oligomerization and caspase-1 activation [39]. However, there is no clear evidence of direct binding between MDP and NLRP1, or any sign of FIIND domain (**Figure 1.1**) auto-processing, which is considered to be critical for NLRP1 inflammasome activation [2, 39].

The existence of other NLR inflammasomes composed of NLRP2, NLRP6, NLRP7, or NLRP12 remains debatable [22, 40]. These sensors may form *bona fide* inflammasomes or act as negative regulators of inflammasome pathways. NLRP2 has been shown to inhibit NF-κB activation, although it was also reported to enhance caspase-1 activation [41, 42]. NLRP6 was shown to suppress NF-κB activation during *Listeria monocytogenes* and *Salmonella typhimurium* infection [43], while a more recent study found that expression of NLRP6 in intestinal globlet cells played a protective role against *Citrobacter rodentium* infection through induction of autophagy [44, 45]. NLRP7 was found to assemble a caspase-1-activating inflammasome in response to microbial diacylated lipopeptides in human macrophages [6]. However, the absence of NLRP7 in the mouse genome makes it challenging to confirm its role *in vivo* [40]. NLRP12 is thought to play an inhibitory role in colon inflammation through the suppression noncanonical NF-κB signaling [46]. Meanwhile, NLRP12 knockout mice were shown to have increased susceptibility to *Yersinia pestis* infection, suggesting the existence of the NLRP12 inflammasome [7].

ASC-independent Inflammasomes

NLRs containing a CARD, such as NLRC4, may directly interact with caspase-1 to elicit pro-inflammatory responses in the absence of ASC. NAIP family sensor proteins directly bind to bacterial components and recruit NLRC4 as the adaptor (**Figure 1.1**). Human NAIP binds the bacterial type III secretory system (T3SS) needle protein to form a NAIP/NLRC4 inflammasome [47]. In mice, NAIP1 also detects T3SS needle protein, while T3SS rod protein is recognized by NAIP2, and bacterial flagellin by both NAIP5 and NAIP6 [9, 47, 48]. In addition, phosphorylation of Ser533 on NLRC4 also contributes to NAIP/NLRC4 inflammasome activation [8].

Although the NAIP/NLRC4 inflammasomes are generally considered ASC-independent, the presence of ASC contributes to the maximal pro-inflammatory response during inflammasome activation [22]. The absence of ASC had no effect on macrophage pyroptosis

upon NAIP/NLRC4 inflammasome activation but impaired secretion of IL-1β, suggesting that ASC could enhance inflammasome activation [49]. In addition, ASC^{CARD} has been shown to physically interact with $NLRC4^{CARD}$ on a yeast two-hybrid system [50]. This interaction is critical for foci formation during NAIP/NLRC4 inflammasome activation [51]. ASC may therefore mediate signal convergence of the NAIP/NLRC4 inflammasome and other ASC-dependent inflammasomes for improved pro-inflammatory response or autophagosomal clearance.

Molecular Details on the Activation of AIM2 and NAIP/NLRC4 Inflammasomes

While a direct ligand or a common co-activator of NLRP3 is yet to be confirmed, AIM2 and NAIP have been shown to directly bind double-stranded DNA (dsDNA) and bacterial components respectively. The structures of $AIM2^{HIN}$/dsDNA and $IFI16^{HINb}$/dsDNA complexes have been determined previously [33]. A typical HIN200 of the HIN domain superfamily contains ~200 residues that encompasses two oligonucleotide/oligosaccharide-binding (OB) folds. The structures of the complexes reveal that the tandem OB folds are positioned almost orthogonal to each other with a connecting α-helix. Both AIM2 and IFI16 HINs have a similar binding mode in which a highly charged surface on the HIN domain contacts the dsDNA sugar-phosphate backbone. This interaction is sensitive to salt concentration and can be disrupted by high ionic strength in the buffer. In addition, this binding is non-sequence specific and targets both strands of the dsDNA, across both major and minor grooves [33]. Cellular dsDNA-transfection experiment found that ~80-bp dsDNA was optimal for AIM2 inflammasome activation as determined by IL-1β secretion [33]. Recent *in vitro* experiments measured the footprint of $AIM2^{FL}$ to be ~12bp per AIM2 protomer [52]. Those data also nicely demonstrated the cooperativity of the HIN/dsDNA binding – a stretch of dsDNA corresponding to ~6 AIM2 protomers would set the threshold for efficient binding. DNA sizes above this threshold oligomerized AIM2 in a cooperative manner, presumably to provide a “digitized” response [52, 53].

The PYD domain of AIM2 was thought to inhibit the HIN domain in the resting state. However, without a full-length structure in the autoinhibited state, the relationship between PYD and HIN remains controversial. Biochemical data showed that DNA competed with PYD for HIN binding [33]. On the other hand, recent evidence suggested that PYD played a positive role in dsDNA mediated AIM2 inflammasome assembly, by formation of Brussels sprout-like filaments [52]. This filamentous assembly of PYD domains was found to be critical for inflammasome activation [54].

The NAIP/NLRC4 inflammasome is another inflammasome that has a well-characterized activation mechanism. Crystal structure of the ΔCARD of mouse NLRC4 clearly illustrates its monomeric, autoinhibted state [12]. The central NACHT domain is composed of the nucleotide-binding domain (NBD), the helical domain HD1, and the winged-helix domain (WHD). The C-terminal LRR domain is connected to the NACHT via the helical domain HD2. The C-terminal LRR domain prevents NLRC4 oligomerization by occluding a critical interface, which is better demonstrated by comparing the crystal structure of the autoinhibited NLRC4 and the recent cryo-EM reconstructions of the NAIP/NLRC4 complex [10, 12]. In the autoinhibted state, NLRC4ΔCARD is bound by endogenous adenosine diphosphate (ADP), which mediates hydrogen-bond interactions with WHD that lock NLRC4 in the closed inactive conformation [12]. The exchange of ADP for adenosine triphosphate (ATP) has been shown to activate NLRC4 [55], as well as other NBD-containing proteins [56, 57]. Recent cryo-EM studies of NAIP/NLRC4 complexes have revealed molecular details of the disk-like assembly [10, 11]. The number of subunits in the NAIP/NLRC4 disk could vary from 10 to 12 protomers [10]. Each disk contains only one copy of NAIP, as shown by nanogold labeling experiments [10, 11]. To transition from the inactive conformation to the active conformation, the WHD-HD2-LRR module has to rotate ~87.5° with respect to NBD-HD1, in order to expose an additional surface to interact with the adjacent subunit [10]. This additional surface may provide a “nucleation interface” to recruit and activate another NLRC4 molecule that propagates to form the disk-like structure [10]. At the

current resolution achieved by these two cryo-EM studies, the bacterial T3SS rod protein PrgJ could not be resolved, and the exact molecular details of NAIP activation remain to be seen [58]. In addition, the structures do not provide definitive evidence of the ADP-ATP exchange requirement during NLRC4 activation [58]. The current hypothesis predicts that the release of ADP may be sufficient for the conformational change to occur [10].

Structural Mechanisms of ASC-dependent Inflammasomes

I present in the main body of this dissertation several structural studies to elucidate the mechanisms of ASC-dependent inflammasome assembly and regulation. Prior to our work and the contemporary work of other groups, previously proposed models have inaccurately described the assembly mechanism of inflammasomes. Apoptosome sensor proteins including the human Apaf-1, the *D. melanogaster* Dark, and the *C. elegans* CED-4 share similar domain architecture to NLRs [55, 59, 60]. CED-4 protomers form a disk-like octameric assembly as determined by X-ray crystallography [61]. The heptameric and octameric structures of the human Apaf-1 and *Drosophila* Dark have also been visualized by cryo-EM to reveal NACHT domain oligomerization, which is characteristic of the AAA+ ATPases [62-64]. It has been observed that the inflammasomes share the same disk-like appearance for the NLRP1 and NAIP/NLRC4 inflammasomes [2, 55]. However, the formation of ASC-dependent inflammasomes had raised questions because of several observations. Firstly, it had been shown that ASC-dependent inflammasomes such as the NLRP3 and AIM2 inflammasomes formed large perinuclear punctate structures upon activation [65]. In addition, both the PYD and the CARD domains of the bipartite ASC adaptor had been shown to aggregate strongly, and the NMR structure of the monomeric form of full-length ASC could only be determined at acidic pH when oligomerization was disrupted [66]. Therefore, the aggregation propensity of ASC at physiological conditions seemed to play a functional role in inflammasome formation.

With these observations in mind, I set out to investigate the biophysical properties of ASC and attempted to purify a soluble complex of ASC with fragments of inflammasome sensor proteins suitable for X-ray crystallographic studies. This strategy was successful for determining the IRAK family kinase activating Myddosome complex and the caspase-2 activating PIDDosome complexes [67]. Although this effort failed to yield crystalizable complexes in my case, it led to the observation that PYD of ASC might form functional filaments to provide a platform for AIM2 and NLRP3 inflammasome activation. In collaboration with the Egelman lab, we obtained the cryo-EM structure of ASC^{PYD} filament. In addition, I studied the monomeric mutant of $AIM2^{PYD}$ by X-ray crystallography and the filamentous form of the wild-type AIM^{PYD} by cryo-EM that further supported a nucleated polymerization-based model of ASC-dependent inflammasome activation. I will present these studies in Chapters Two, Three, and Four of this dissertation, which will be summarized in the following section. Moreover, I also expanded the scope of my work to study the regulation of inflammasome assembly with two additional projects. Chapter Five presents a collaborative project that involved the generation of a novel ASC^{CARD}-binding heavy-chain antibody, which defined the role of ASC^{CARD} in crosslinking PYD filaments. Chapter Six presents a study on the caspase-1^{CARD} filament structure by cryo-EM and the regulatory role of a CARD-only protein in preventing filament formation via a novel capping mechanism. These two studies will also be summarized in the following section. Collectively, the work presented in this dissertation provides structural and biochemical insights into mechanisms of inflammasome activation and regulation.

Chapter Summary

Nucleated Polymerization Mechanism Governing the Inflammasome Assembly

Chapter Two of this dissertation presents a study on the assembly of ASC-dependent inflammasomes that involve a two-step nucleated polymerization mechanism. Using *in vitro* reconstitution, electron microscopy, and polymerization assays, I characterized the AIM2 and NLRP3 inflammasomes. Contrary to the assumption that the different domain architectures of AIM2 and NLRP3 may give rise to distinct inflammasome morphology, the adapter ASC unifies the assemblies by forming filamentous assemblies, which coalesce into a large perinuclear punctum. AIM2, upon activation by dsDNA, and NLRP3, upon oligomerization through the NACHT domain, interact with ASC through homotypic PYD-PYD interaction which leads to the formation of ASC^{PYD} filaments. These ASC^{PYD} filaments serve as a platform for caspase-1^{CARD} filament formation, resulting in proximity-induced caspase dimerization and activation (**Figure 1.2**). Cryo-EM structure of the ASC^{PYD} filament reveals critical interactions that mediate the formation of this scaffold. Reconstitution of the ternary inflammasome complex yields star-shaped branched filamentous structures composed of component proteins with unequal stoichiometry. Structure-based mutagenesis *in vitro* and in cells confirms the importance of homotypic PYD-PYD interactions within ASC filaments and between sensor protein and ASC. Collectively, these data support a universal model for the assembly of ASC-dependent inflammasomes, regardless of their activation mechanism.

Chapters Three and Four present structural studies on $AIM2^{PYD}$ in the monomeric and oligomeric states. In Chapter Three, I describe the crystal structure of a monomeric mutant of $AIM2^{PYD}$ and present mutagenesis data to compare the oligomerization interface of this inflammasome sensor PYD to the death effector domain of caspase-8. The crystal structure bears an F27A mutation at the predicted type Ib surface, and the type Ia surface includes a L10/L11 motif, which forms a hydrophobic interaction with F27. This interaction is conserved

between AIM2^{PYD} and caspase-8^{DED}, suggesting that DED and PYD share a common ancestor during the divergence of death domains [68]. Chapter Four presents more evidence of the conserved interactions for AIM2^{PYD} and ASC^{PYD}. Based on sequence and structural alignments

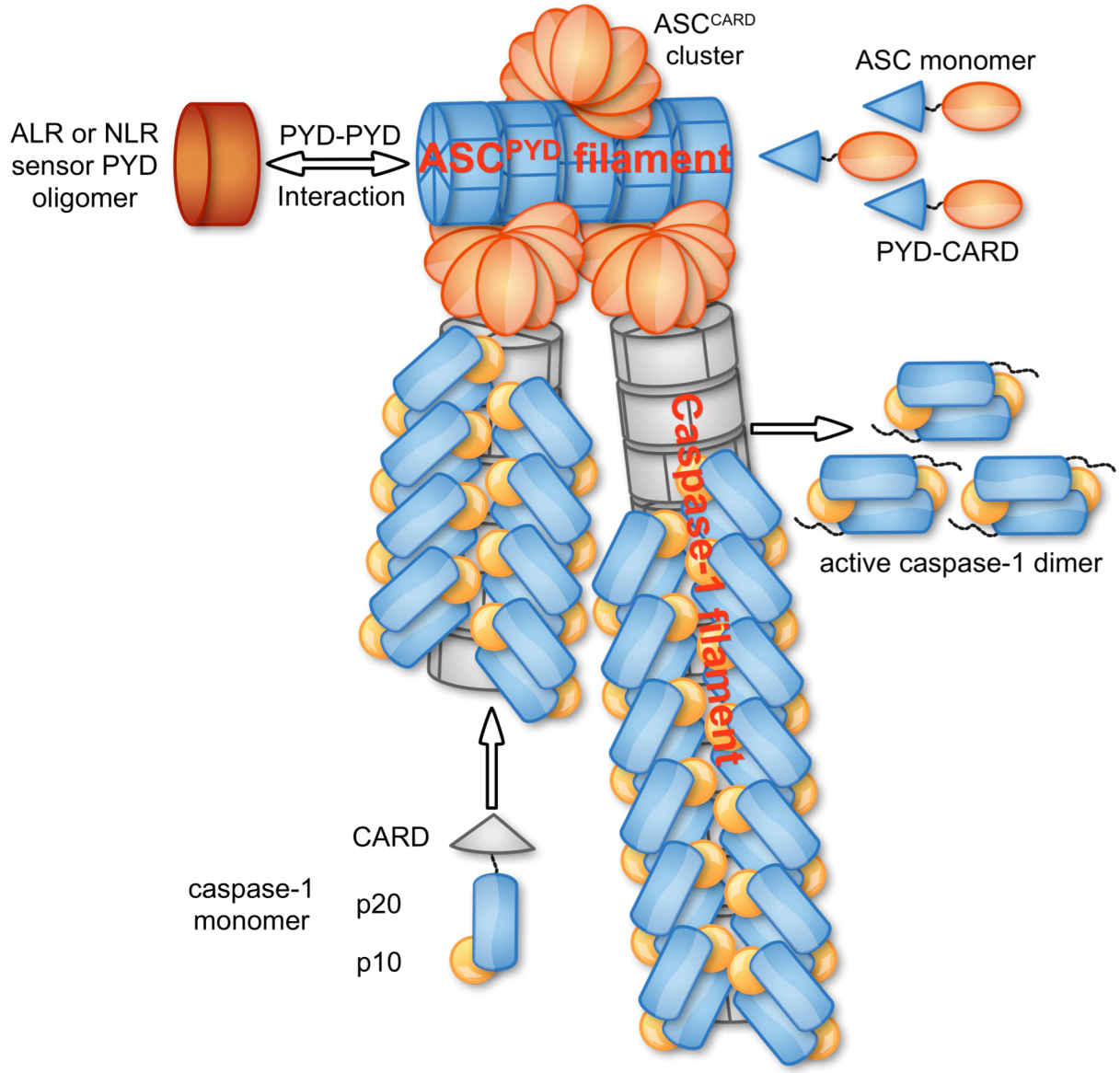

Figure 1.2. Assembly Mechanism of the ASC-dependent Inflammasomes.

Upon activation of the ALR or NLR family sensor proteins, a layer of PYD oligomers is formed, which nucleates the formation of ASC^{PYD} filaments by recruiting ASC monomers for polymerization. Clusters of ASC^{CARD} further nucleate the formation of caspase-1 filaments via CARD-CARD interaction. Proximity-driven dimerization of the caspase domains results in caspase-1 activation and the release of active caspase-1 dimers.

and previous knowledge in death domain interaction, it had been hypothesized that AIM2^{PYD} must nucleate ASC^{PYD} filaments with the same interaction observed in the ASC^{PYD} filaments. The filamentous assembly of GFP-tagged AIM2^{PYD} forms a 1-start helix with helical parameters distinct from those of the 3-start ASC^{PYD} filament. However, detailed comparison shows that orientations of the interaction interfaces have minimal local differences. Directions of the three types of interactions are also conversed between AIM2^{PYD} and ASC^{PYD} filaments. The plasticity of PYD assembly that allows for twist variability and spatial compatibility may be important for ASC to serve as a universal adaptor.

ASC-binding Nanobody Defines the Role of ASC^{CARD}

I present in Chapter Five a collaborative project that exploits an alpaca single domain antibody (nanobody) for structural and functional characterization of the adaptor ASC. The VHH$_{ASC}$ nanobody binds to the CARD domain of human ASC and blocks CARD/CARD interactions *in vitro* and inflammasome activation in cells. In addition, the crystal structures of VHH$_{ASC}$ alone and in complex with ASC^{CARD} reveal critical interfaces for ASC^{CARD} oligomerization. *In vitro* and cellular assays using this nanobody conclude that ASC CARD domains play a functional role in crosslinking ASC^{PYD} filaments to form ASC foci (**Figure 1.3**). In effect, this approach allows modulation of the inflammasome system at the molecular level.

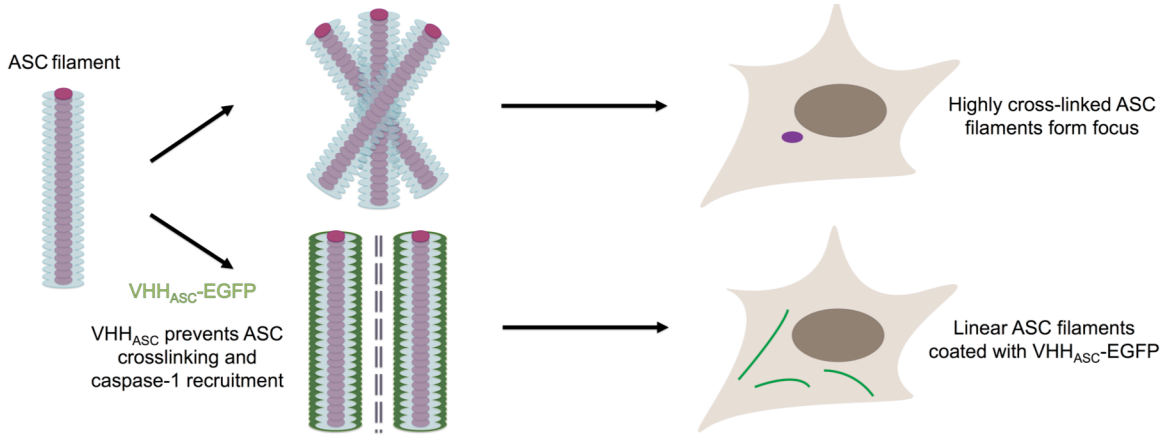

Figure 1.3. VHH$_{ASC}$ defines the role of ASC^{CARD} in crosslinking ASC^{PYD} filaments.

A Novel Capping Mechanism for the Regulation of Inflammasome

To further understand the CARD/CARD interaction of the inflammasome assembly that had not been fully characterized in previous studies, I investigated how CARD-only proteins negatively regulate caspase-1^{CARD} filament formation. Many negative regulators of the inflammasome pathways have been identified, such as an NLR protein lacking the LRR domain NLRP10 [69], a HIN-only ALR protein p202 [70], PYD-only proteins [71, 72], and CARD-only proteins [73-75] (**Figure 1.1 and Figure 1.4**). These proteins interfere with inflammasome activation at different steps of the assembly process (**Figure 1.4**).

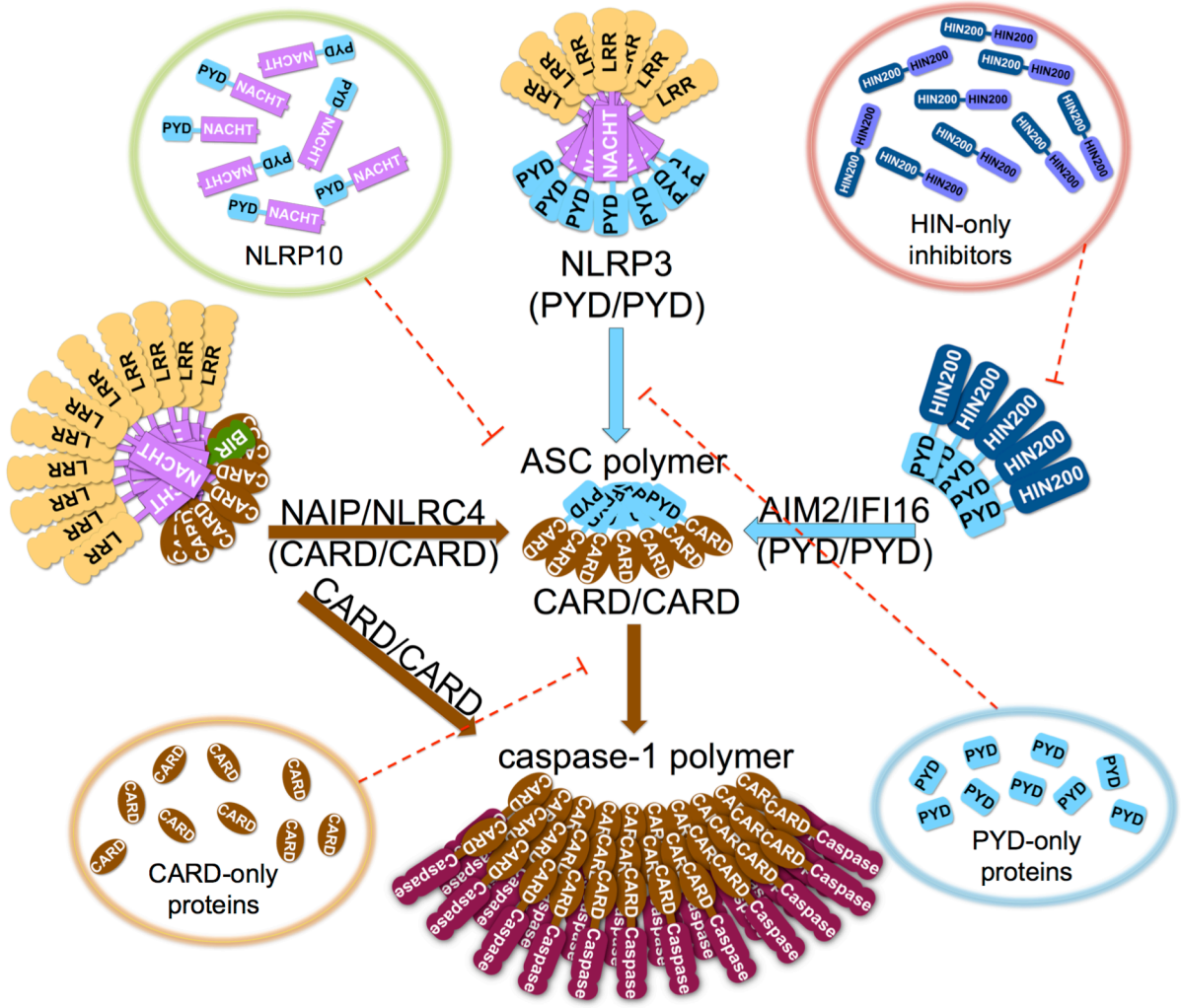

Figure 1.4. Regulation of the Inflammasomes at Different Assembly Steps. Modified from a figure of our review article published in the *FEBS Journal* [13]. This simplified figure illustrates additional components that play regulatory roles during the inflammasome assembly.

In Chapter Six, I first present the cryo-EM structure of the caspase-1^{CARD} filament and then describe biochemical evidence to support a capping mechanism for inflammasome inhibition by a CARD-only protein, INCA. Results from gold labeling experiments, polymerization assays, and a homology modeling exercise conclude that INCA is able to cap growing caspase-1^{CARD} oligomers to prevent their polymerization, and hence robustly inhibits inflammasome assembly *in vitro* at low nM concentrations. This study puts inflammasomes in the new perspective of signaling filaments and further supports our original model of the nucleated polymerization mechanism.

Cryo-electron Microscopy and Helical Reconstruction

This dissertation presents studies of the filamentous structures in the inflammasome assembly. Cryo-electron microscopy and helical reconstruction constitute a large portion of these studies by providing the necessary means for obtaining near-atomic resolution structural information and visualizing intermolecular interactions. The recent advances with direct detection cameras made it possible to obtain high quality EM images primarily by increasing the signal-to-noise ratio. And with the use of rigorous computational algorisms, we were able to obtain near-atomic resolution cryo-EM maps of the ASC^{PYD}, AIM2^{PYD}, and caspase-1^{CARD} filaments.

The program – Iterative Helical Real Space Reconstruction (IHRSR) – developed by our collaborator, Professor Edward Egelman, is at the core of our reconstruction procedure [76]. This program took advantage of the helical symmetry of biological polymers to overcome some of the obstacles that prevent resolving structures to higher resolution, such as filament heterogeneity and helical disorder. Computational algorithms of helical reconstructions have existed since the 1980s [77]. One common feature is that the helical symmetry of the filament – also known as helical indexing – needs to be identified by examining the averaged power

spectrum of boxed filaments or filament segments, which is essentially the Fourier transform of the real space images [76, 77].

Similar to three-dimensional crystals, helical assemblies are two-dimensional lattices. Ordered protein filaments give rise to “diffraction” patterns on power spectra analogous to the diffraction patterns in X-ray crystallography [77]. These patterns of helical assembly consist of horizontal layer lines, which are pairs of spots situated symmetrically about the meridian (**Figure 1.5A**). Each layer line has a corresponding order (n), which is defined by the number of times a family of helical lattice lines cut across the equatorial plane. The distance from the equator to the first meridional reflection (n = 0, aka the layer line with a maximum on the meridian) is reciprocally related to the axial rise per subunit (**Figure 1.5A**). The height of each layer line corresponds to the inverse of its pitch, p, which arises from the repeating features of a helical lattice (**Figure 1.5A**). The number of continuous helices that connect all subunits of this filament defines the “start” of a filament (1-start, 2-start, 3-start…). For instance, the subunits of a 1-start filament can all be connected by drawing a single helix, while a 2-start filament can be represented by two intertwined helices [77]. Helical assemblies may also have rotational symmetry. In such cases, the subunits on the same equatorial plane are related by a rotation about the helical axis.

For indexing an experimental power spectrum, the order of a layer line is equal to the circumference (2πr) of the helix divided by the distance between lattice lines (d). The radius r can be measured from the electron micrographs in real space, while d is approximated by the x coordinate of the layer line on the power spectrum (d ≈ 1/R). Taking into account Fourier transformation, the formula becomes the following, $n + 2 \approx \frac{2\pi r R}{\text{pixel size} \times \text{image dimention}}$, where R is the x coordinate in pixel [77]. To obtain a possible set of indexes, both nearest integer numbers of the approximated order need to be considered for each layer lines [77].

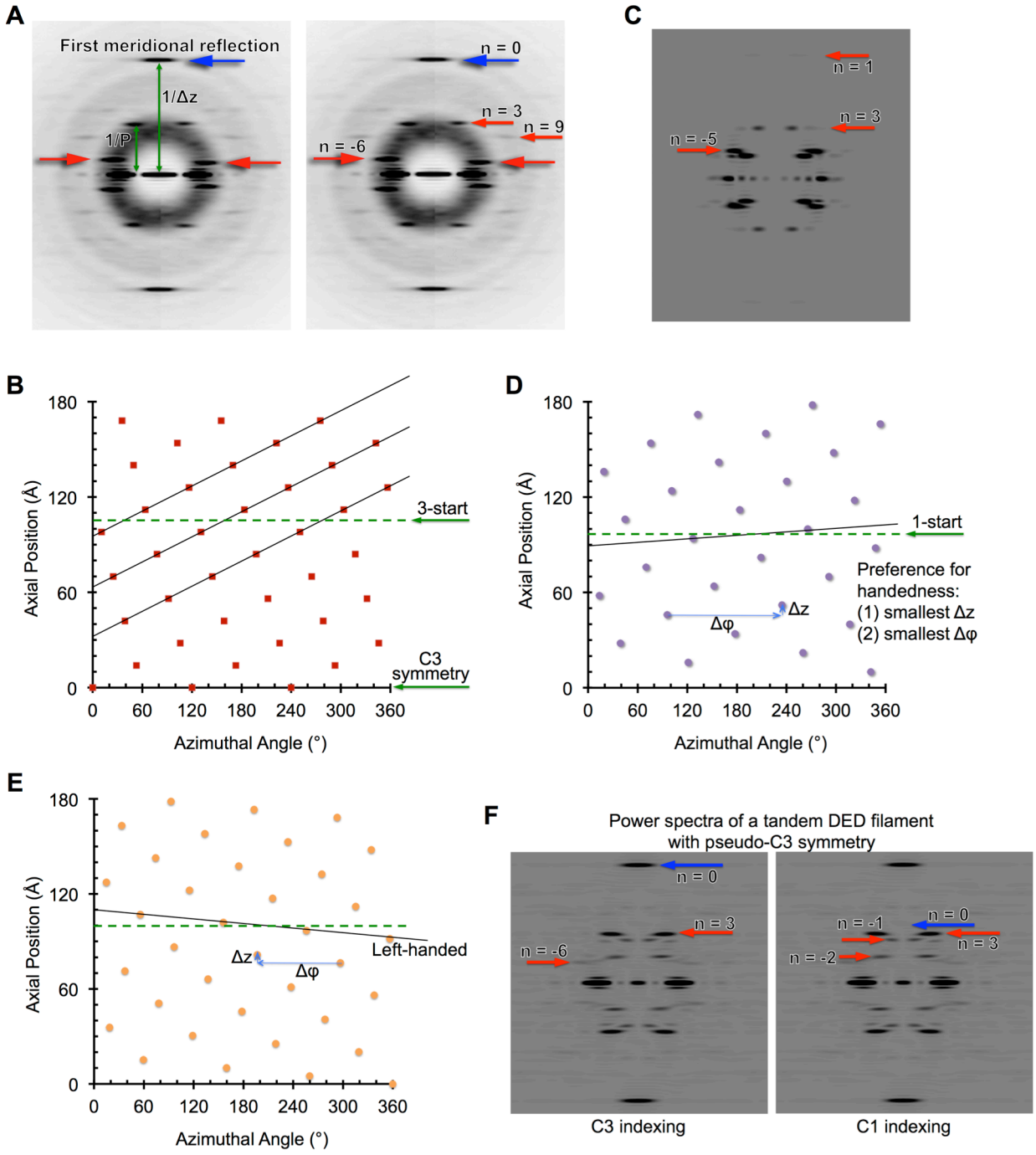

Figure 1.5. Comparison of different DD-fold filaments.

A. Power spectrum of ASC^{PYD} filament (modified from **Figure 2.3B**).

B. Helical net plot of ASC^{PYD} filament (modified from **Figure 4.2B**).

C. Power spectrum of $AIM2^{PYD}$ filament (modified from **Figure 4.1D**).

D. Helical net plot of $AIM2^{PYD}$ filament (modified from **Figure 4.2B**).

E. Helical net plot of caspase-1^{CARD} filament.

In order to perform IHRSR, two fundamental parameters are extracted from indexing the initial averaged power spectrum – axial rise (Δz) and rotation about the helical axis (Δφ) per subunit, which will be iteratively refined during the alignment stages. The axial rise per subunit can be experimentally determined from the height of the first meridional reflection (**Figure 1.5A**), or deduced from three independent layer lines whose orders add to n = 0. The helical axis is calculated from the pitch (P) of the lowest order layer line, which is the axial distance of one complete turn (360°). For the simplest 1-start helices, axial rise per subunit is equal to, $\Delta\varphi = \frac{360° \times \Delta z}{P}$, where P is the inverse of the height of the n = 1 layer line from the equator.

The ASC^{PYD} structure presented in Chapter Two is a right-handed 3-start filament with C3 symmetry (**Figure 1.5A**). By definition of a 3-start filament, three intertwined helices cross the equatorial plane three times (**Figure 1.5B**). It also has a C3 symmetry as shown by the three subunits with 120° rotation on the equatorial plane – the Bessel orders of the layer lines are therefore multiples of 3 (**Figure 1.5B**). The $AIM2^{PYD}$ structure presented in Chapter Four has a very similar architecture but with a distinct set of helical parameters (such similarity will be discussed later). It is a right-handed 1-start filament with no rotational symmetry (**Figure 1C and D**). In addition, the caspase-1^{CARD} structure presented in Chapter Six is a left-handed 1-start filament (**Figure 1.5E**). When indexing these filaments, the convention for handedness assignment prioritizes the smallest axial rise per subunit (Δφ), and additionally, if there is rotational symmetry, the nearest subunit with a smaller rotation angle is preferred (Δz) (**Figure 1D and E**). Interestingly, the filament formed by a tandem DED domain has a more complex power spectrum, which may complicate the indexing process (manuscript in preparation). Subunits of this filament are twice the size of a PYD, and the power spectrum shows a striking resemblance to that of the ASC^{PYD} filament (**Figure 1F**), with the meridional reflection and n = 3 layer line at similar locations. However, the n = -6 layer line is not obvious. Because of the increase in subunit size, this filament could not assume a true C3 symmetry and could only be

indexed with no rotational symmetry (**Figure 1F**). In summary, helical reconstruction has been essential to our structural studies of the inflammasome assemblies.

Scope of Dissertation

This dissertation deals primarily with the assembly and regulation mechanisms of inflammasomes. I present structural and biochemical evidence of critical interactions during inflammasome activation to address many previously unanswered questions and to support a two-step nucleated polymerization assembly model.

Questions addressed in Chapter Two:

1. How do the upstream sensor proteins interaction with the adaptor ASC?
2. How does ASC integrate different inflammasome signals to caspase-1 activation?
3. What are the molecular details of homotypic PYD-PYD interaction in ASC^{PYD} filaments?
4. How does such interaction confer inflammasome activation?

Questions addressed in Chapter Three:

1. What are the similarities and differences between ASC-ASC interaction and AIM2-ASC interaction?
2. How is the $AIM2^{PYD}$ oligomerization similar to caspase-8^{DED} oligomerization?

Questions addressed in Chapter Four:

1. What are the differences between the AIM2 filament and the ASC filament?
2. How does the AIM2-ASC interaction tolerate the apparent helical difference?
3. How may dsDNA stimulate AIM2 oligomerization?

Questions addressed in Chapter Five:

1. What are the structural roles of ASC CARD domain during ASC oligomerization?
2. How does an ASC-binding nanobody prevent inflammasome activation?
3. What is the role of ASC during NAIP/NLRC4 inflammasome activation?

Questions addressed in Chapter Six:

1. How does caspase-1 oligomerize during inflammasome activation?
2. What are the biophysical properties of two CARD-only proteins that regulate inflammasome activation?
3. How does a monomeric CARD-only protein, INCA, interact with caspase-1 and negatively regulate inflammasome activation?
4. What are the critical interactions during caspase-1 oligomerization disrupted by INCA?

References

1. Ting, J. P., Lovering, R. C., Alnemri, E. S., Bertin, J., Boss, J. M., Davis, B. K., Flavell, R. A., Girardin, S. E., Godzik, A., Harton, J. A., Hoffman, H. M., Hugot, J. P., Inohara, N., Mackenzie, A., Maltais, L. J., Nunez, G., Ogura, Y., Otten, L. A., Philpott, D., Reed, J. C., Reith, W., Schreiber, S., Steimle, V. & Ward, P. A. (2008) The NLR gene family: a standard nomenclature, *Immunity.* **28**, 285-7.

2. Faustin, B., Lartigue, L., Bruey, J. M., Luciano, F., Sergienko, E., Bailly-Maitre, B., Volkmann, N., Hanein, D., Rouiller, I. & Reed, J. C. (2007) Reconstituted NALP1 inflammasome reveals two-step mechanism of caspase-1 activation, *Molecular cell.* **25**, 713-24.

3. Shenoy, A. R., Wellington, D. A., Kumar, P., Kassa, H., Booth, C. J., Cresswell, P. & MacMicking, J. D. (2012) GBP5 promotes NLRP3 inflammasome assembly and immunity in mammals, *Science.* **336**, 481-5.

4. Rathinam, V. A., Vanaja, S. K., Waggoner, L., Sokolovska, A., Becker, C., Stuart, L. M., Leong, J. M. & Fitzgerald, K. A. (2012) TRIF licenses caspase-11-dependent NLRP3 inflammasome activation by gram-negative bacteria, *Cell.* **150**, 606-19.

5. Elinav, E., Strowig, T., Kau, A. L., Henao-Mejia, J., Thaiss, C. A., Booth, C. J., Peaper, D. R., Bertin, J., Eisenbarth, S. C., Gordon, J. I. & Flavell, R. A. (2011) NLRP6 inflammasome regulates colonic microbial ecology and risk for colitis, *Cell.* **145**, 745-57.

6. Khare, S., Dorfleutner, A., Bryan, N. B., Yun, C., Radian, A. D., de Almeida, L., Rojanasakul, Y. & Stehlik, C. (2012) An NLRP7-containing inflammasome mediates recognition of microbial lipopeptides in human macrophages, *Immunity.* **36**, 464-76.

7. Vladimer, G. I., Weng, D., Paquette, S. W., Vanaja, S. K., Rathinam, V. A., Aune, M. H., Conlon, J. E., Burbage, J. J., Proulx, M. K., Liu, Q., Reed, G., Mecsas, J. C., Iwakura, Y., Bertin, J., Goguen, J. D., Fitzgerald, K. A. & Lien, E. (2012) The NLRP12 inflammasome recognizes Yersinia pestis, *Immunity.* **37**, 96-107.

8. Qu, Y., Misaghi, S., Izrael-Tomasevic, A., Newton, K., Gilmour, L. L., Lamkanfi, M., Louie, S., Kayagaki, N., Liu, J., Komuves, L., Cupp, J. E., Arnott, D., Monack, D. & Dixit, V. M. (2012) Phosphorylation of NLRC4 is critical for inflammasome activation, *Nature.* **490**, 539-42.

9. Kofoed, E. M. & Vance, R. E. (2011) Innate immune recognition of bacterial ligands by NAIPs determines inflammasome specificity, *Nature.* **477**, 592-5.

10. Zhang, L., Chen, S., Ruan, J., Wu, J., Tong, A. B., Yin, Q., Li, Y., David, L., Lu, A., Wang, W. L., Marks, C., Ouyang, Q., Zhang, X., Mao, Y. & Wu, H. (2015) Cryo-EM structure of the activated NAIP2-NLRC4 inflammasome reveals nucleated polymerization, *Science*.

11. Hu, Z., Zhou, Q., Zhang, C., Fan, S., Cheng, W., Zhao, Y., Shao, F., Wang, H. W., Sui, S. F. & Chai, J. (2015) Structural and biochemical basis for induced self-propagation of NLRC4, *Science*.

12. Hu, Z., Yan, C., Liu, P., Huang, Z., Ma, R., Zhang, C., Wang, R., Zhang, Y., Martinon, F., Miao, D., Deng, H., Wang, J., Chang, J. & Chai, J. (2013) Crystal structure of NLRC4 reveals its autoinhibition mechanism, *Science.* **341**, 172-5.

13. Lu, A. & Wu, H. (2014) Structural mechanisms of inflammasome assembly, *FEBS J.* **282**, 435-44.

14. Wang, S., Miura, M., Jung, Y., Zhu, H., Li, E. & Yuan, J. (1998) Murine caspase-11, an ICE-interacting protease, is essential for the activation of ICE, *Cell.* **92**, 501-509.

15. Kayagaki, N., Warming, S., Lamkanfi, M., Vande Walle, L., Louie, S., Dong, J., Newton, K., Qu, Y., Liu, J., Heldens, S., Zhang, J., Lee, W. P., Roose-Girma, M. & Dixit, V. M. (2011) Non-canonical inflammasome activation targets caspase-11, *Nature.* **479**, 117-21.

16. Shi, J., Zhao, Y., Wang, Y., Gao, W., Ding, J., Li, P., Hu, L. & Shao, F. (2014) Inflammatory caspases are innate immune receptors for intracellular LPS, *Nature.* **514**, 187-92.

17. Kayagaki, N., Stowe, I. B., Lee, B. L., O'Rourke, K., Anderson, K., Warming, S., Cuellar, T., Haley, B., Roose-Girma, M., Phung, Q. T., Liu, P. S., Lill, J. R., Li, H., Wu, J., Kummerfeld, S., Zhang, J., Lee, W. P., Snipas, S. J., Salvesen, G. S., Morris, L. X., Fitzgerald, L., Zhang, Y., Bertram, E. M., Goodnow, C. C. & Dixit, V. M. (2015) Caspase-11 cleaves gasdermin D for non-canonical inflammasome signalling, *Nature.* **526**, 666-71.

18. Shi, J., Zhao, Y., Wang, K., Shi, X., Wang, Y., Huang, H., Zhuang, Y., Cai, T., Wang, F. & Shao, F. (2015) Cleavage of GSDMD by inflammatory caspases determines pyroptotic cell death, *Nature.* **526**, 660-5.

19. Tamura, M., Tanaka, S., Fujii, T., Aoki, A., Komiyama, H., Ezawa, K., Sumiyama, K., Sagai, T. & Shiroishi, T. (2007) Members of a novel gene family, Gsdm, are expressed exclusively in the epithelium of the skin and gastrointestinal tract in a highly tissue-specific manner, *Genomics.* **89**, 618-29.

20. Bauernfeind, F. G., Horvath, G., Stutz, A., Alnemri, E. S., MacDonald, K., Speert, D., Fernandes-Alnemri, T., Wu, J., Monks, B. G., Fitzgerald, K. A., Hornung, V. & Latz, E. (2009) Cutting edge: NF-kappaB activating pattern recognition and cytokine receptors license NLRP3 inflammasome activation by regulating NLRP3 expression, *J Immunol.* **183**, 787-91.

21. Guo, H., Callaway, J. B. & Ting, J. P. (2015) Inflammasomes: mechanism of action, role in disease, and therapeutics, *Nature medicine.* **21**, 677-87.

22. Lamkanfi, M. & Dixit, V. M. (2014) Mechanisms and functions of inflammasomes, *Cell.* **157**, 1013-22.

23. Juliana, C., Fernandes-Alnemri, T., Kang, S., Farias, A., Qin, F. & Alnemri, E. S. (2012) Non-transcriptional priming and deubiquitination regulate NLRP3 inflammasome activation, *The Journal of biological chemistry.* **287**, 36617-22.

24. Fernandes-Alnemri, T., Kang, S., Anderson, C., Sagara, J., Fitzgerald, K. A. & Alnemri, E. S. (2013) Cutting edge: TLR signaling licenses IRAK1 for rapid activation of the NLRP3 inflammasome, *J Immunol.* **191**, 3995-9.

25. Salvesen, G. S. & Walsh, C. M. (2014) Functions of caspase 8: the identified and the mysterious, *Seminars in immunology.* **26**, 246-52.

26. Gurung, P., Anand, P. K., Malireddi, R. K., Vande Walle, L., Van Opdenbosch, N., Dillon, C. P., Weinlich, R., Green, D. R., Lamkanfi, M. & Kanneganti, T. D. (2014) FADD and caspase-8 mediate priming and activation of the canonical and noncanonical Nlrp3 inflammasomes, *J Immunol.* **192**, 1835-46.

27. Allam, R., Lawlor, K. E., Yu, E. C., Mildenhall, A. L., Moujalled, D. M., Lewis, R. S., Ke, F., Mason, K. D., White, M. J., Stacey, K. J., Strasser, A., O'Reilly, L. A., Alexander, W., Kile, B. T., Vaux, D. L. & Vince, J. E. (2014) Mitochondrial apoptosis is dispensable for NLRP3 inflammasome activation but non-apoptotic caspase-8 is required for inflammasome priming, *EMBO reports.* **15**, 982-90.

28. West, A. P., Shadel, G. S. & Ghosh, S. (2011) Mitochondria in innate immune responses, *Nature reviews Immunology.* **11**, 389-402.

29. Paludan, S. R. & Bowie, A. G. (2013) Immune sensing of DNA, *Immunity.* **38**, 870-80.

30. Hornung, V., Ablasser, A., Charrel-Dennis, M., Bauernfeind, F., Horvath, G., Caffrey, D. R., Latz, E. & Fitzgerald, K. A. (2009) AIM2 recognizes cytosolic dsDNA and forms a caspase-1-activating inflammasome with ASC, *Nature.* **458**, 514-8.

31. Fernandes-Alnemri, T., Yu, J. W., Datta, P., Wu, J. & Alnemri, E. S. (2009) AIM2 activates the inflammasome and cell death in response to cytoplasmic DNA, *Nature.* **458**, 509-13.

32. Unterholzner, L., Keating, S. E., Baran, M., Horan, K. A., Jensen, S. B., Sharma, S., Sirois, C. M., Jin, T., Latz, E., Xiao, T. S., Fitzgerald, K. A., Paludan, S. R. & Bowie, A. G. (2010) IFI16 is an innate immune sensor for intracellular DNA, *Nature immunology.* **11**, 997-1004.

33. Jin, T., Perry, A., Jiang, J., Smith, P., Curry, J. A., Unterholzner, L., Jiang, Z., Horvath, G., Rathinam, V. A., Johnstone, R. W., Hornung, V., Latz, E., Bowie, A. G., Fitzgerald, K. A. & Xiao, T. S. (2012) Structures of the HIN domain:DNA complexes reveal ligand binding and activation mechanisms of the AIM2 inflammasome and IFI16 receptor, *Immunity.* **36**, 561-71.

34. Munoz-Planillo, R., Kuffa, P., Martinez-Colon, G., Smith, B. L., Rajendiran, T. M. & Nunez, G. (2013) K(+) Efflux Is the Common Trigger of NLRP3 Inflammasome Activation by Bacterial Toxins and Particulate Matter, *Immunity.* **38**, 1142-53.

35. Murakami, T., Ockinger, J., Yu, J., Byles, V., McColl, A., Hofer, A. M. & Horng, T. (2012) Critical role for calcium mobilization in activation of the NLRP3 inflammasome, *Proceedings of the National Academy of Sciences of the United States of America.* **109**, 11282-7.

36. Zhou, R., Yazdi, A. S., Menu, P. & Tschopp, J. (2011) A role for mitochondria in NLRP3 inflammasome activation, *Nature.* **469**, 221-5.

37. Hornung, V., Bauernfeind, F., Halle, A., Samstad, E. O., Kono, H., Rock, K. L., Fitzgerald, K. A. & Latz, E. (2008) Silica crystals and aluminum salts activate the NALP3 inflammasome through phagosomal destabilization, *Nature immunology.* **9**, 847-56.

38. Sutterwala, F. S., Haasken, S. & Cassel, S. L. (2014) Mechanism of NLRP3 inflammasome activation, *Annals of the New York Academy of Sciences.* **1319**, 82-95.

39. Chavarria-Smith, J. & Vance, R. E. (2015) The NLRP1 inflammasomes, *Immunological reviews.* **265**, 22-34.

40. Lupfer, C. & Kanneganti, T. D. (2013) Unsolved Mysteries in NLR Biology, *Frontiers in immunology.* **4**, 285.

41. Bruey, J. M., Bruey-Sedano, N., Newman, R., Chandler, S., Stehlik, C. & Reed, J. C. (2004) PAN1/NALP2/PYPAF2, an inducible inflammatory mediator that regulates NF-kappaB and caspase-1 activation in macrophages, *The Journal of biological chemistry.* **279**, 51897-907.

42. Fontalba, A., Gutierrez, O. & Fernandez-Luna, J. L. (2007) NLRP2, an inhibitor of the NF-kappaB pathway, is transcriptionally activated by NF-kappaB and exhibits a nonfunctional allelic variant, *J Immunol.* **179**, 8519-24.

43. Anand, P. K., Malireddi, R. K., Lukens, J. R., Vogel, P., Bertin, J., Lamkanfi, M. & Kanneganti, T. D. (2012) NLRP6 negatively regulates innate immunity and host defence against bacterial pathogens, *Nature.* **488**, 389-93.

44. Wlodarska, M., Thaiss, C. A., Nowarski, R., Henao-Mejia, J., Zhang, J. P., Brown, E. M., Frankel, G., Levy, M., Katz, M. N., Philbrick, W. M., Elinav, E., Finlay, B. B. & Flavell, R. A. (2014) NLRP6 inflammasome orchestrates the colonic host-microbial interface by regulating goblet cell mucus secretion, *Cell.* **156**, 1045-59.

45. Atianand, M. K., Rathinam, V. A. & Fitzgerald, K. A. (2013) SnapShot: inflammasomes, *Cell.* **153**, 272-272 e1.

46. Allen, I. C., Wilson, J. E., Schneider, M., Lich, J. D., Roberts, R. A., Arthur, J. C., Woodford, R. M., Davis, B. K., Uronis, J. M., Herfarth, H. H., Jobin, C., Rogers, A. B. & Ting, J. P. (2012) NLRP12 suppresses colon inflammation and tumorigenesis through the negative regulation of noncanonical NF-kappaB signaling, *Immunity.* **36**, 742-54.

47. Yang, J., Zhao, Y., Shi, J. & Shao, F. (2013) Human NAIP and mouse NAIP1 recognize bacterial type III secretion needle protein for inflammasome activation, *Proceedings of the National Academy of Sciences of the United States of America.* **110**, 14408-13.

48. Zhao, Y., Yang, J., Shi, J., Gong, Y. N., Lu, Q., Xu, H., Liu, L. & Shao, F. (2011) The NLRC4 inflammasome receptors for bacterial flagellin and type III secretion apparatus, *Nature.* **477**, 596-600.

49. Miao, E. A., Leaf, I. A., Treuting, P. M., Mao, D. P., Dors, M., Sarkar, A., Warren, S. E., Wewers, M. D. & Aderem, A. (2010) Caspase-1-induced pyroptosis is an innate immune effector mechanism against intracellular bacteria, *Nature immunology.* **11**, 1136-42.

50. Geddes, B. J., Wang, L., Huang, W. J., Lavellee, M., Manji, G. A., Brown, M., Jurman, M., Cao, J., Morgenstern, J., Merriam, S., Glucksmann, M. A., DiStefano, P. S. & Bertin, J. (2001) Human CARD12 is a novel CED4/Apaf-1 family member that induces apoptosis, *Biochemical and biophysical research communications.* **284**, 77-82.

51. Proell, M., Gerlic, M., Mace, P. D., Reed, J. C. & Riedl, S. J. (2013) The CARD plays a critical role in ASC foci formation and inflammasome signalling, *The Biochemical journal.* **449**, 613-21.

52. Morrone, S. R., Matyszewski, M., Yu, X., Delannoy, M., Egelman, E. H. & Sohn, J. (2015) Assembly-driven activation of the AIM2 foreign-dsDNA sensor provides a polymerization template for downstream ASC, *Nature communications.* **6**, 7827.

53. Wu, H. (2013) Higher-order assemblies in a new paradigm of signal transduction, *Cell.* **153**, 287-92.

54. Lu, A., Magupalli, V. G., Ruan, J., Yin, Q., Atianand, M. K., Vos, M. R., Schroder, G. F., Fitzgerald, K. A., Wu, H. & Egelman, E. H. (2014) Unified polymerization mechanism for the assembly of ASC-dependent inflammasomes, *Cell.* **156**, 1193-206.

55. Halff, E. F., Diebolder, C. A., Versteeg, M., Schouten, A., Brondijk, T. H. & Huizinga, E. G. (2012) Formation and structure of a NAIP5-NLRC4 inflammasome induced by direct interactions with conserved N- and C-terminal regions of flagellin, *The Journal of biological chemistry.* **287**, 38460-72.

56. Martinon, F., Burns, K. & Tschopp, J. (2002) The inflammasome: a molecular platform triggering activation of inflammatory caspases and processing of proIL-beta, *Molecular cell.* **10**, 417-26.

57. Duncan, J. A., Bergstralh, D. T., Wang, Y., Willingham, S. B., Ye, Z., Zimmermann, A. G. & Ting, J. P. (2007) Cryopyrin/NALP3 binds ATP/dATP, is an ATPase, and requires ATP binding to mediate inflammatory signaling, *Proceedings of the National Academy of Sciences of the United States of America.* **104**, 8041-6.

58. Liu, Z. & Xiao, T. S. (2015) STRUCTURAL BIOLOGY. Assembling the wheel of death, *Science.* **350**, 376-7.

59. Martinon, F., Mayor, A. & Tschopp, J. (2009) The inflammasomes: guardians of the body, *Annual review of immunology.* **27**, 229-65.

60. Zou, H., Li, Y., Liu, X. & Wang, X. (1999) An APAF-1.cytochrome c multimeric complex is a functional apoptosome that activates procaspase-9, *The Journal of biological chemistry.* **274**, 11549-56.

61. Qiao, Q., Yang, C., Zheng, C., Fontan, L., David, L., Yu, X., Bracken, C., Rosen, M., Melnick, A., Egelman, E. H. & Wu, H. (2013) Structural Architecture of the CARMA1/Bcl10/MALT1 Signalosome: Nucleation-Induced Filamentous Assembly, *Molecular cell.* **51**, 766-79.

62. Yuan, S., Yu, X., Topf, M., Ludtke, S. J., Wang, X. & Akey, C. W. (2010) Structure of an apoptosome-procaspase-9 CARD complex, *Structure.* **18**, 571-83.

63. Yuan, S., Yu, X., Asara, J. M., Heuser, J. E., Ludtke, S. J. & Akey, C. W. (2011) The holo-apoptosome: activation of procaspase-9 and interactions with caspase-3, *Structure.* **19**, 1084-96.

64. Yuan, S., Yu, X., Topf, M., Dorstyn, L., Kumar, S., Ludtke, S. J. & Akey, C. W. (2011) Structure of the Drosophila apoptosome at 6.9 a resolution, *Structure.* **19**, 128-40.

65. Bryant, C. & Fitzgerald, K. A. (2009) Molecular mechanisms involved in inflammasome activation, *Trends in cell biology.* **19**, 455-64.

66. de Alba, E. (2009) Structure and interdomain dynamics of apoptosis-associated speck-like protein containing a CARD (ASC), *The Journal of biological chemistry.* **284**, 32932-41.

67. Ferrao, R. & Wu, H. (2012) Helical assembly in the death domain (DD) superfamily, *Current opinion in structural biology.* **22**, 241-7.

68. Kersse, K., Verspurten, J., Vanden Berghe, T. & Vandenabeele, P. (2011) The death-fold superfamily of homotypic interaction motifs, *Trends Biochem Sci.* **36**, 541-52.

69. Imamura, R., Wang, Y., Kinoshita, T., Suzuki, M., Noda, T., Sagara, J., Taniguchi, S., Okamoto, H. & Suda, T. (2010) Anti-inflammatory activity of PYNOD and its mechanism in humans and mice, *J Immunol.* **184**, 5874-84.

70. Yin, Q., Sester, D. P., Tian, Y., Hsiao, Y. S., Lu, A., Cridland, J. A., Sagulenko, V., Thygesen, S. J., Choubey, D., Hornung, V., Walz, T., Stacey, K. J. & Wu, H. (2013) Molecular mechanism for p202-mediated specific inhibition of AIM2 inflammasome activation, *Cell Rep.* **4**, 327-39.

71. Stehlik, C., Krajewska, M., Welsh, K., Krajewski, S., Godzik, A. & Reed, J. C. (2003) The PAAD/PYRIN-only protein POP1/ASC2 is a modulator of ASC-mediated nuclear-factor-kappa B and pro-caspase-1 regulation, *The Biochemical journal.* **373**, 101-13.

72. Bedoya, F., Sandler, L. L. & Harton, J. A. (2007) Pyrin-only protein 2 modulates NF-kappaB and disrupts ASC:CLR interactions, *J Immunol.* **178**, 3837-45.

73. Druilhe, A., Srinivasula, S. M., Razmara, M., Ahmad, M. & Alnemri, E. S. (2001) Regulation of IL-1beta generation by Pseudo-ICE and ICEBERG, two dominant negative caspase recruitment domain proteins, *Cell death and differentiation.* **8**, 649-57.

74. Humke, E. W., Shriver, S. K., Starovasnik, M. A., Fairbrother, W. J. & Dixit, V. M. (2000) ICEBERG: a novel inhibitor of interleukin-1beta generation, *Cell.* **103**, 99-111.

75. Lamkanfi, M., Denecker, G., Kalai, M., D'Hondt, K., Meeus, A., Declercq, W., Saelens, X. & Vandenabeele, P. (2004) INCA, a novel human caspase recruitment domain protein that inhibits interleukin-1beta generation, *The Journal of biological chemistry.* **279**, 51729-38.

76. Egelman, E. H. (2007) The iterative helical real space reconstruction method: surmounting the problems posed by real polymers, *Journal of structural biology.* **157**, 83-94.

77. Steward, M. (1988) Computer Image Processing of Electron Micrographs of Biological Structures with Helical Symmetry, *Journal of Electron Microscopy Technique.* **9**, 325-358.

Chapter Two

A Structural and Mechanistic Study of the ASC^{PYD} Filament

Citation. This chapter has been assembled with minor modifications from the final version of the following published manuscript:

Cell **156**, 1193-206 (2014)

Unified Polymerization Mechanism for the Assembly of ASC-dependent inflammasomes

Alvin Lu[1,2,†], Venkat Giri Magupalli[1,2,†], Jianbin Ruan[1,2,†], Qian Yin[1,2], Maninjay K. Atianand[3], Matthijn Vos[4], Gunnar F. Schröder[5], Katherine A. Fitzgerald[3], Hao Wu[1,2,*] and Edward H. Egelman[6]

[1]Department of Biological Chemistry and Molecular Pharmacology, Harvard Medical School, Boston, MA 02115

[2]Program in Cellular and Molecular Medicine, Boston Children's Hospital, Boston, MA 02115

[3]Division of Infectious Diseases and Immunology, Department of Medicine, University of Massachusetts Medical School, Worcester, MA 01655

[4]FEI NanoPort, 5651 Eindhoven, Netherlands

[5]Institute of Complex Systems, Forschungszentrum Jülich, 52425 Jülich, Germany

[6]Department of Biochemistry and Molecular Genetics, University of Virginia, Charlottesville, VA 22908

[†]Co-first authors

*Corresponding author

Contributions. This study was a highly collaborative project amongst several members of the Wu lab, as well as between the Wu lab and the Egelman lab. I am very grateful for their contribution to this study, which would be impossible without everyone's tremendous support and great enthusiasm.

I initiated the project and performed *in vitro* reconstitution, electron microscopy on reconstituted samples, polymerization assays, and initial cryo-EM characterization of filament quality. Professor Wu, Professor Egelman, Dr. Magupalli, Dr. Ruan, and I conceived this study and together wrote and revised the manuscript. I prepared Figures 2.1, 2.2, 2.5D-F, 2.6C-F, 2.6H, S2.1, S2.2, S2.4I, S2.6A, S2.6C, and S2.7B. Dr. Magupalli performed confocal microscopy, cellular electron microscopy, immunoprecipitation, and western blotting, as shown in Figures 2.5B, 2.5C, 2.6G, 2.7A-D, S2.5, S2.6B, S2.7A, and S2.7C-E. Dr. Ruan performed structural analysis, refinement, and structure-based mutagenesis *in vitro*, and prepared Figures 2.3D, 2.3E, 2.4, 2.5A, 2.6A, 2.6B, part of S2.3B, S2.3D, and S2.4A-H. Professor Egelman, with the help of Dr. Vos and Dr. Schröder, collected the final cryo-electron micrographs and reconstructed the electron density model. Professor Fitzgerald and Dr. Atianand performed the cellular reconstitution assays.

I would also like to thank Natacha Opalka, Seth Darst, Leona Cohen-Gould, Maria Ericsson, William Rice, and Mariena Silvestry Ramos for help with EM imaging, Harry Leung for help with confocal microscopy, and Gabriel Nuñez for providing cDNAs.

Supplemental materials. Seven Supplemental Figures (Figures S2.1-2.7), four Supplemental Tables (Tables S2.1-2.4), a Supplemental Movie (Movie S2.1), Materials and Methods, and Supplemental References can be found in Appendix I.

Abstract

Inflammasomes elicit host defense inside cells by activating caspase-1 for cytokine maturation and cell death. AIM2 and NLRP3 are representative sensor proteins in two major families of inflammasomes. The adaptor protein ASC bridges the sensor proteins and caspase-1 to form ternary inflammasome complexes, achieved through pyrin domain (PYD) interactions between sensors and ASC, and caspase activation and recruitment domain (CARD) interactions between ASC and caspase-1. We found that PYD and CARD both form filaments. Activated AIM2 and NLRP3 nucleate PYD filaments of ASC, which in turn cluster the CARD of ASC to nucleate CARD filaments of caspase-1 to induce proximity-induced activation. Endogenous NLRP3 inflammasome is also filamentous. The cryo-EM structure of ASC^{PYD} filament at near-atomic resolution provides a template for homo- and hetero-PYD/PYD associations, as confirmed by structure-guided mutagenesis. We propose that ASC-dependent inflammasomes in both families share a unified assembly mechanism that involves two successive steps of nucleation-induced polymerization.

Introduction

The immune system provides protection from the environment and is critically important for multiple aspects of mammalian biology. It consists of an adaptive component that generates specific antibodies and cells through clonal selection, and an innate component that utilizes preformed receptors. Innate immunity offers the first line of defense against infections and hazards by directly recognizing conserved pathogen- and danger-associated molecular patterns (PAMPs and DAMPs) to alert the immune system [1]. Inflammasomes are key components of innate immunity inside the cell. They are formed in response to PAMPs and DAMPs, and activate inflammatory caspases such as caspase-1 and -11 [2-4]. Caspase activation can lead to proteolytic maturation of cytokines IL-1β and IL-18, and elicit the inflammatory form of cell death pyroptosis, as ways to control exogenous and endogenous invasions.

Inflammasomes are supramolecular assemblies composed of at least a sensor protein and a caspase, and often the adapter protein ASC. Based on the domain architecture of the sensor protein, inflammasomes may be divided into two families. The first family is known as ALR [Absent in Melanoma 2 (AIM2)-like receptor], named after the first identified member (**Figure 2.1A**). ALRs are composed of an N-terminal PYD and one or two HIN domains [2]. AIM2 directly senses the cytosolic PAMPs dsDNAs, such as those associated with viruses, using its HIN domain [2, 5]. The second class of inflammasomes contains receptors in the NLR [nucleotide-binding domain (NBD) and leucine rich repeat (LRR)–containing receptors] family (**Figure 2.1A**). NBD belongs to the AAA+ superfamily of ATPase domains. Most NLRs contain an N-terminal PYD and are known as NLRPs. The best-studied NLRP3 inflammasome is activated following a wide range of pathogen and danger signals including extracellular ATP and uric acid crystals [2-4]. Upon activation, both AIM2 and NLRP3 recruit the PYD- and CARD-containing bipartite adapter ASC (apoptosis-associated speck-like protein containing a CARD) through PYD/PYD interactions [6]. ASC in turn recruits caspase-1 through CARD/CARD interactions (**Figure 2.1A**). PYD and CARD both belong to the death domain (DD) fold superfamily [7], for which structures of two defined DD helical assemblies are known [8, 9].

Malfunctioning of inflammasomes is associated with serious human diseases [10]. Mutations in inflammasome proteins NLRP3, NLRP12 and MEFV (also known as Pyrin) are linked to autoinflammatory and fever syndromes [2]. Aberrations in NLR inflammasome activation have been connected to psoriasis, type II diabetes, inflammatory bowel diseases and Alzheimer's disease [2-4, 10]. The PYD-less ALR member, mouse p202, interacts with the HIN domain of AIM2 to inhibit inflammasome and potentiate lupus [11].

Immunofluorescence microscopy showed that transfected full-length ASC (ASC^{FL}) and endogenous ASC upon stimulation both form speck-like aggregates [6]. Because transfected PYD and CARD-only ASC fragments are filamentous [12], the specks are most likely dense, crosslinked composites of PYD and CARD filaments. Because of the strong tendency of ASC to

aggregate, the structures of ASC PYD (ASC^{PYD}) and ASC^{FL} were solved in monomeric states using nuclear magnetic resonance (NMR) at acidic conditions [13, 14]. Although additional monomeric PYD structures have been reported, including those of NLRP3 [15] and AIM2 [16], the mode of homo- and hetero-PYD associations is entirely unknown.

Here, we used *in vitro* reconstitution, electron microscopy (EM) and polymerization assays to address assembly mechanisms for ASC-dependent AIM2 and NLRP3 inflammasomes. In contrast to the presumption that the different domain structures of AIM2 and NLRP3 may lead to considerable differences in the inflammasome architectures, we showed that both AIM2 upon dsDNA interaction and NLRP3 oligomerized through its NBD nucleate ASC^{PYD} filaments. This is particularly surprising for NLRP3; due to the domain similarity of NLRs to Apaf-1-like molecules that form ring-like platforms [17], the overarching paradigm had presumed that NLR inflammasomes are also ring-like structures. The flexibly linked ASC CARD (ASC^{CARD}) then clusters along the ASC^{PYD} filament to act as the platform for caspase-1^{CARD} filament formation, leading to proximity-induced caspase dimerization and activation. The ternary inflammasome complex showed star-shaped branched filamentous morphology, and exhibited unequal stoichiometries among the component proteins. We determined the cryo-EM structure of the ASC^{PYD} filament at near atomic resolution through helical reconstruction. The structure revealed molecular details of ASC^{PYD}/ASC^{PYD} interactions and allowed modeling of $AIM2^{PYD}$/ASC^{PYD} and $NLRP3^{PYD}$/ASC^{PYD} interactions. Structure-based mutagenesis confirmed the importance of ASC^{PYD}/ASC^{PYD}, $AIM2^{PYD}$/ASC^{PYD} and $NLRP3^{PYD}$/ASC^{PYD} interactions *in vitro* and in cells. EM of immunoprecipitated endogenous NLRP3 inflammasome showed similar filamentous morphology as *in vitro* reconstituted inflammasomes and quantitative Western blotting confirmed the over-stoichiometry of caspase-1 to ASC. Our studies collectively revealed a universal assembly process for ASC-dependent inflammasomes in both ALR and NLR families that involves nucleation-induced polymerization.

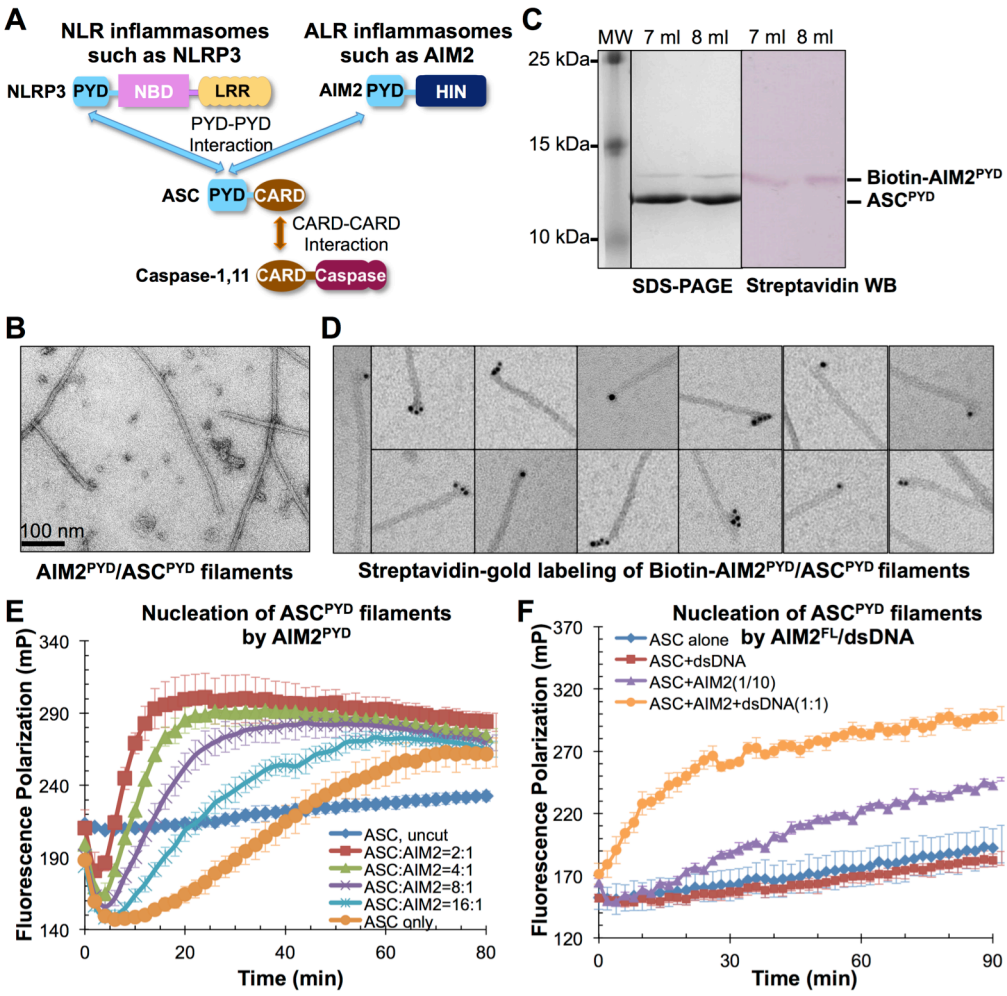

Figure 2.1. AIM2 Promotes Formation of ASC^{PYD} Filaments

A. Domain composition and interaction hierarchy of NLRP3 and AIM2 inflammasomes.

B. An electron micrograph of the AIM2^{PYD}/ASC^{PYD} binary complex.

C. Gel filtration fractions of biotinylated AIM2^{PYD}/ASC^{PYD} complex as visualized by Coomassie Blue-stained SDS-PAGE (left) and streptavidin-alkaline phosphatase Western blot (right).

D. Labeling of biotinylated AIM2^{PYD}/ASC^{PYD} binary complex by streptavidin-gold conjugate (6 nm).

E. Fluorescence polarization (FP) assay of AIM2^{PYD}-nucleated ASC^{PYD} filament formation. mP: unit for FP. Data are represented as mean±SD (N=3).

F. Effect of dsDNA on AIM2^{FL}-nucleated ASC^{PYD} filament formation. 2 μM of AIM2^{FL} monomer from gel filtration was incubated with or without equimolar 300-bp dsDNA (assuming a 10-bp footprint of AIM2 for molar calculation) for 30 minutes before diluting to a working concentration 0.1 μM (ASC^{PYD}: AIM2^{FL}=10:1) for the FP assay. Data are represented as mean±SD (N=3).

See also **Figure S2.1**

Results

The AIM2^{PYD}/ASC^{PYD} Complex is Filamentous with End Location of AIM2^{PYD}

To elucidate the assembly mechanisms for ASC-containing inflammasomes, we first reconstituted the interaction between AIM2 and ASC. Co-expression of AIM2^{PYD} with ASC^{PYD} showed that the complex eluted at the void position of a Superdex 200 gel filtration column (**Figure S2.1A**), suggesting formation of large "aggregates". We used EM to visualize the negatively stained AIM2^{PYD}/ASC^{PYD} complex, which revealed filaments with uniform diameters of ~9 nm (**Figure 2.1B**).

AIM2^{PYD} exists in sub-stoichiometric molar ratio in the AIM2^{PYD}/ASC^{PYD} complex (**Figure S2.1A, 2.1C**). To understand this observation, we generated a construct of AIM2^{PYD} capable of enzymatic biotinylation during expression. Co-expression of the AIM2^{PYD} construct with ASC^{PYD} generated a complex with specific biotinylation of AIM2^{PYD}, shown by streptavidin Western blotting (**Figure 2.1C**). Labeling biotinylated AIM2^{PYD} by 6 nm streptavidin-gold particles showed that AIM2^{PYD} is localized at one end of the filaments (**Figure 2.1D**). The number of bound gold particles varies between one and several, consistent with the ability of AIM2^{PYD} to form filaments when expressed alone (**Figure S2.1B**). In the presence of ASC^{PYD}, AIM2^{PYD} preferentially associated with ASC^{PYD} to generate short heterogeneous AIM2^{PYD} filaments in complex with much longer ASC^{PYD} filaments. In contrast, Ni-NTA-gold labeling of His-tagged ASC^{PYD} in the biotinylated AIM2^{PYD}/ASC^{PYD} complex showed uniform distribution along the filaments (**Figure S2.1C**), confirming that ASC^{PYD} forms the main filament body.

AIM2^{PYD} and the Full-length AIM2/dsDNA Complex Nucleate ASC^{PYD} Filaments

End labeling of AIM2^{PYD} suggested its role as the nucleator for directional polymerization of ASC^{PYD}. To quantitatively assess ASC^{PYD} filament formation, we set up a fluorescence polarization (FP) assay *in vitro* using a His-MBP-ASC^{PYD} fusion construct with an added C-

terminal Cys for conjugating with Alexa488 fluorophore. The large fusion tag MBP inhibited ASC^{PYD} polymerization to enable His-MBP-ASC^{PYD} to be expressed in the monomeric form (**Figure S2.1D**). Polymerization of Alexa488-labeled monomeric ASC^{PYD} was initiated by addition of the TEV protease to remove His-MBP from the fusion protein. The increase in FP, which indicates ASC^{PYD} polymerization, was monitored as a function of time (**Figure 2.1E**). Although ASC^{PYD} did polymerize on its own upon His-MBP removal, the rates of polymerization were dramatically enhanced in the presence of increasing amounts of sub-stoichiometric $AIM2^{PYD}$ (1/16 – 1/2 molar ratios) (**Figure 2.1E**). The initial drop in FP corresponded with His-MBP removal by TEV and the decrease in size of ASC^{PYD}. At 5 min after TEV addition, about 75% His-MBP was removed from the fusion protein (**Figure S2.1E**). The $AIM2^{PYD}$/ASC^{PYD} filaments generated from the polymerization assay (**Figure S2.1F**) showed similar morphology to the co-expressed complex (**Figure 2.1B**).

Full-length AIM2 ($AIM2^{FL}$) is a cytosolic dsDNA sensor in which the interaction of its C-terminal HIN domain with dsDNA induces ASC recruitment and inflammasome formation. The PYD in AIM2 has been shown to interact with its HIN domain to provide autoinhibition in the absence of dsDNA binding [16]. To reconstitute AIM2 inflammasome activation *in vitro*, we expressed $AIM2^{FL}$ as a His-MBP fusion. Purified His-MBP-$AIM2^{FL}$ was first incubated with equimolar 300-bp dsDNA (molar ratio calculated based on 10-bp footprint of AIM2 on dsDNA), followed by mixing with Alexa488-labeled His-MBP-ASC^{PYD}. TEV was added to remove His-MBP to initiate ASC^{PYD} polymerization as monitored by FP (**Figure 2.1F**). A dramatic increase in FP was observed upon activation of $AIM2^{FL}$ by dsDNA, recapitulating the cellular event of inflammasome activation. These data suggest that overcome of autoinhibition and oligomerization of AIM2 by dsDNAs are crucial for inducing ASC^{PYD} polymerization.

$NLRP3^{PYD\text{-}NBD}$ Nucleates and End-labels ASC^{PYD} Filaments

NLRs share similar domain architectures and are recognized to be autoinhibited in the

absence of suitable ligands. In NLRC4, an NLR with a CARD, its LRR domain plays an important role in inhibiting NLR oligomerization [18]. Due to their domain similarity to Apaf-1-like molecules that form ring-like platforms through the NBDs to induce caspase activation and apoptosis [17], the overarching paradigm appears to presume that NLRP inflammasomes are also ring-like structures organized by the NBD. Formation of filamentous structures in the $AIM2^{PYD}$/ASC^{PYD} interaction prompted us to examine ASC-dependent NLRP inflammasomes using the prototypical member NLRP3.

We expressed and purified $NLRP3^{PYD}$, $NLRP3^{PYD\text{-}NBD}$ and $NLRP3^{FL}$. While $AIM2^{PYD}$ exists as filamentous oligomers and was sufficient in promoting ASC^{PYD} polymerization, $NLRP3^{PYD}$ is a monomer and did not cause significant enhancement in ASC^{PYD} polymerization (**Figure 2.2A**). Both insect cell and *E. coli* expressed $NLRP3^{PYD\text{-}NBD}$ with inclusion of the NBD eluted from the void position of a Superdex 200 gel filtration column, and induced greatly increased ASC^{PYD} polymerization (**Figure 2.2B**). In comparison, $NLRP3^{PYD\text{-}NBD}$ is a much stronger promoter of ASC^{PYD} polymerization than $AIM2^{PYD}$; it caused significant enhancement of ASC^{PYD} polymerization at a low 1:1,600 molar ratio (**Figure 2.2B**). Notably, under the physiological intracellular condition of 140 mM KCl and 10 mM NaCl at pH 7.4 and a lower ASC concentration, ASC^{PYD} did not significantly polymerize unless increasing amounts of $NLRP3^{PYD\text{-}NBD}$ were added (**Figure S2.2A**), suggesting that ASC does not polymerize under steady physiological state without stimulation. The PYD of NLRP3 is required for ASC^{PYD} polymerization because $NLRP3^{PYD\text{-}NBD}$ proteins with mutations on PYD are compromised in this function (see below), suggesting that NBD-oligomerized $NLRP3^{PYD}$ forms the platform for ASC^{PYD} polymerization.

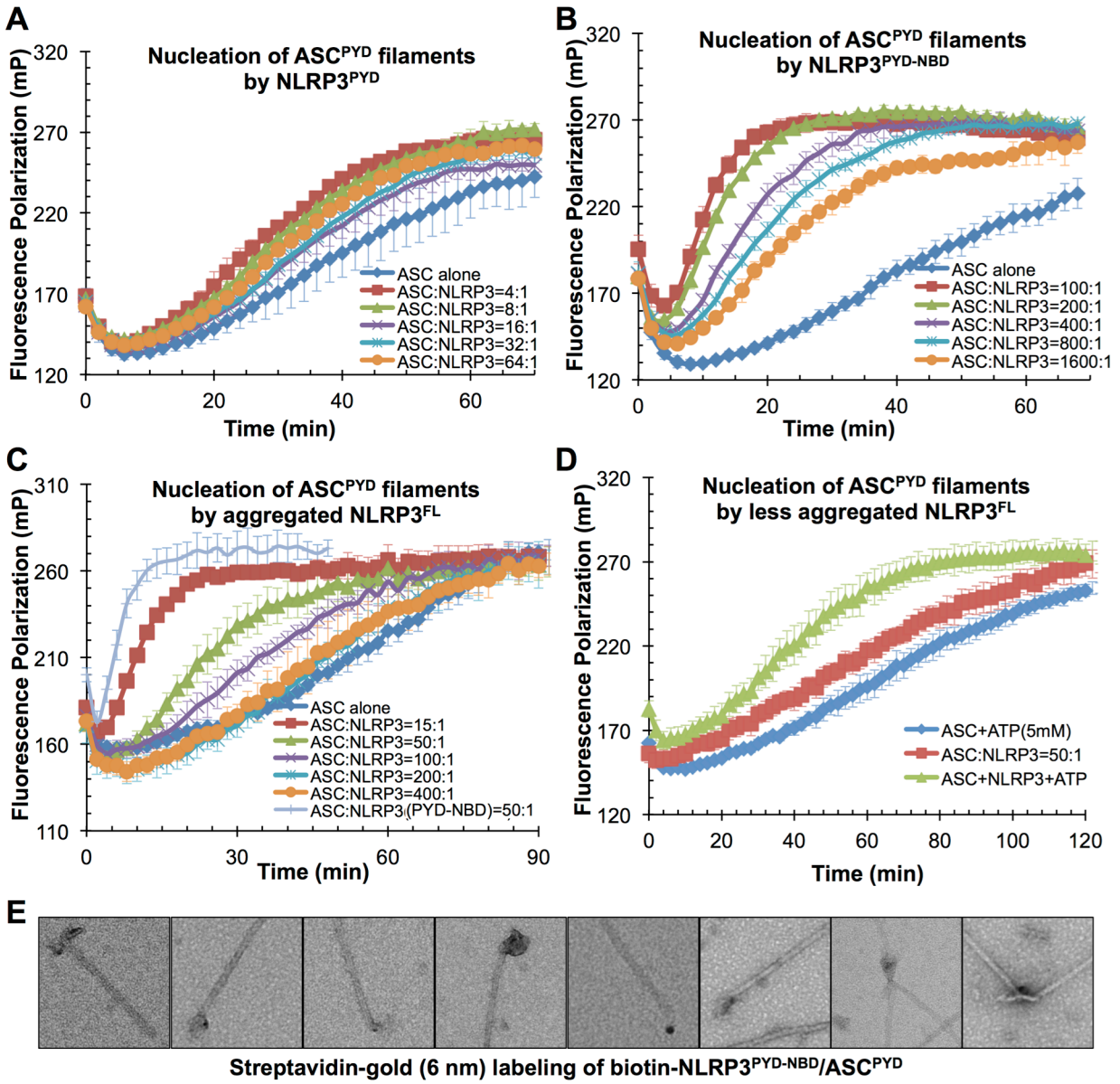

Figure 2.2. NLPR3^{FL} and NLRP3$^{PYD-NBD}$ but not NLRP3^{PYD} Promote ASC^{PYD} Filament Formation

A, B, C. Nucleation of ASC^{PYD} filaments by titrating increasing amounts of NLRP3^{PYD} (A), NLRP3$^{PYD-NBD}$ (B), NLRP3^{FL} (C) as monitored by fluorescence polarization. Data are represented as mean±SD (N=3).

D. A less aggregated gel filtration fraction of NLRP3 was subjected to ASC^{PYD} polymerization assay with or without 5 mM ATP. Data are represented as mean±SD (N=3).

E. Streptavidin-gold (6 nm) labeling of biotinylated NLRP3$^{PYD-NBD}$/ASC^{PYD} binary complex.

See also **Figure S2.2**.

Insect cell expressed NLRP3^{FL} showed a wide distribution on a Superdex 200 gel filtration column (**Figure S2.2B**). In keeping with autoinhibition in NLRP3^{FL} as in NLRC4 [18], we found that even the highly aggregated NLRP3^{FL} showed less activity than NLRP3$^{PYD-NBD}$ in promoting ASC^{PYD} polymerization because more molar quantities of NLRP3^{FL} were required to achieve similar degrees of FP enhancement (**Figure 2.2B, 2.2C**). Despite being activated by an extensive list of stimuli, it is uncertain what constitutes the direct activator of NLRP3 [2]. We found that addition of ATP enhanced the less aggregated fractions of recombinant NLRP3^{FL} in activating ASC^{PYD} polymerization (**Figure 2.2D**); however this activation is minimal in comparison. It is likely that ATP binding by the NBD is associated with, but not sufficient for, NLRP3 activation.

Induction of ASC^{PYD} polymerization by NLRP3 suggests that NLRP3 may reside at the end of ASC^{PYD} filaments. We generated a His-MBP-NLRP3$^{PYD-NBD}$ construct capable of enzymatic biotinylation during expression. We mixed purified His-MBP-NLRP3$^{PYD-NBD}$-Biotin with His-MBP-ASC^{PYD} and added the TEV protease to cleave off His-MBP to allow ASC^{PYD} polymerization. The purified NLRP3-Biotin/ASC complex was subjected to negative stain EM and 6 nm streptavidin-gold labeling, which confirmed localization of NLRP3 to the end of ASC^{PYD} filaments (**Figure 2.2E**). Using negative stain EM, we showed that purified NLRP3$^{PYD-NBD}$ is heterogeneous with a mixture of disk-like structures and filaments (**Figure S2.2C**). The latter may represent the spiral, lock washer-like mode of oligomerization of the NBD.

Cryo-Electron Microscopy Structure of ASC^{PYD} at Near Atomic Resolution

To generate a homogeneous population of ASC^{PYD} filaments without the AIM2 or NLRP3 nucleators, we used *in vitro* ASC^{PYD} polymerization starting from purified monomeric His-MBP-ASC^{PYD} (**Figure S2.1D**). Upon TEV treatment to cleave off His-MBP, ASC^{PYD} filaments spontaneously formed as shown by cryo-EM (**Figure 2.3A**). Cryo-EM images were collected using automated data acquisition on a Titan Krios with a backthinned CMOS direct electron

detector. Averaged power spectra of segments from cryo-EM images of the helical filaments showed a strong meridional reflection at 1/13.9 $Å^{-1}$, which corresponds to the reciprocal of the axial rise, but exhibited variable twist (**Figure 2.3B, 2.3C**), like many other helical polymers [19]. The magnitude of this variation can be seen in **Movie S2.1**.

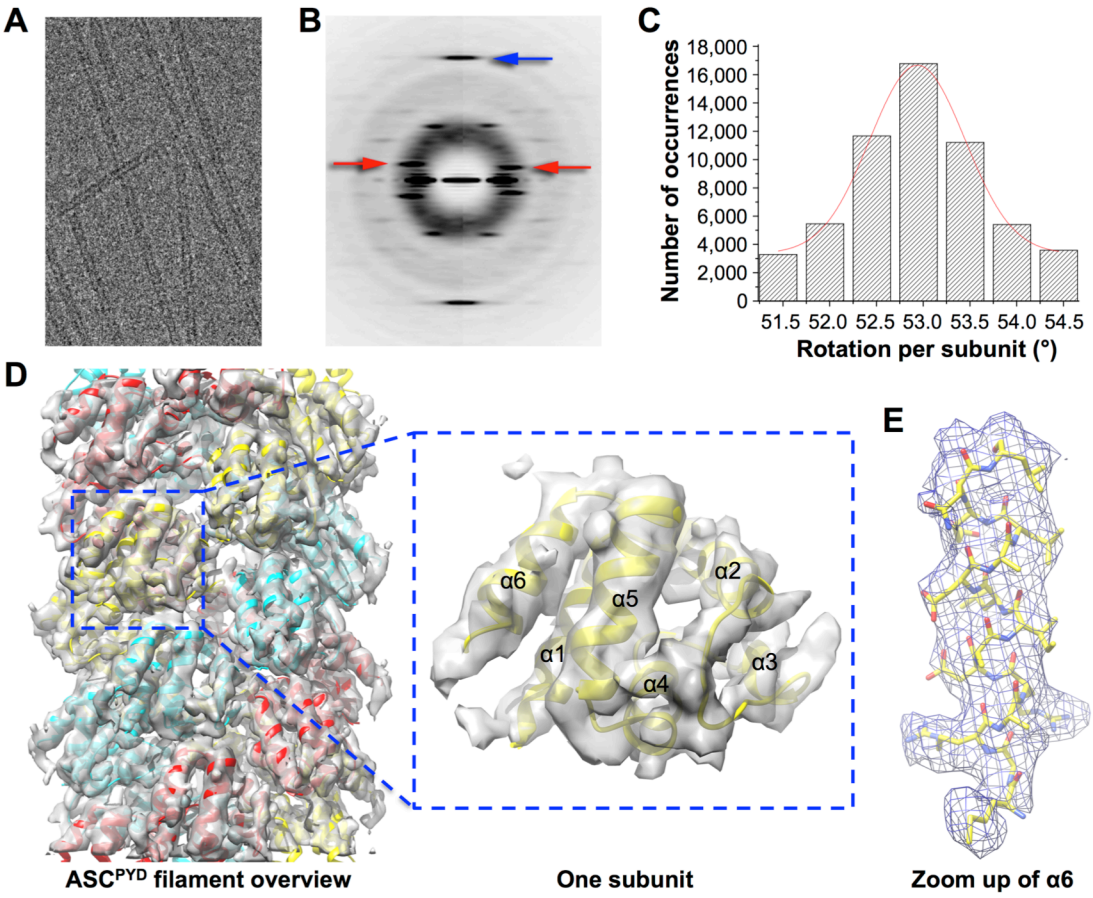

Figure 2.3. Cryo-EM Structure of the ASC^{PYD} Filament at Near Atomic Resolution

A. A cryo-EM image of ASC^{PYD} filaments.

B. Average power spectra of ASC^{PYD} filaments in two twist bins (left and right halves) showing constant axial rise per subunit (blue arrow) and variable long-range twist features (red arrows).

C. Filament segments can be divided into separate twist bins according to azimuth angle, or rotation per subunit.

D. Cryo-EM reconstruction of the ASC^{PYD} filament, superimposed with the final atomic model shown in three colors each for one start of the three-start helical assembly.

E. A zoom up view of helix α6 shown in stick model and superimposed with the EM density.

See also **Figure S2.3** and **Movie S2.1**.

Images were processed using the Iterative Helical Real Space Reconstruction (IHRSR) method with a solid cylinder as the initial reference [20]. The helical heterogeneity was dealt with by sorting images by twist to generate a subset with similar helical parameters, resulting in a map at ~6Å resolution. Correction of out of plane tilt was applied to further improve the map to a conservatively estimated resolution of ~3.8 Å as determined by both Fourier shell correlation (FSC) [21] (**Figure S2.3A**), and comparison with the final atomic model (**Figure S2.3B, S2.3C**).

Rigid body fitting of the NMR structure of ASC^{PYD} [13] into the cryo-EM map generated a pseudo atomic model of the ASC^{PYD} filament. The fit of the NMR structure resolved the enantiomorphic ambiguity in EM reconstructions, but even without the NMR structure the hand of the α-helices in the reconstruction was clear eliminating such ambiguities. The rigid-body fit was followed by real-space refinement [22] to generate a final atomic model with clearly defined side chain densities (**Figure 2.3D, 2.3E, S2.3D**). The ASC^{PYD} filament is hollow with inner and outer diameters of ~20 Å and ~90 Å, respectively (**Figure 2.4A**). The polar filament has a C3 point group symmetry with 53° right-handed rotation and 14.0 Å axial rise per subunit, after correcting for a mean out-of-plane tilt of ~6°.

The structure of ASC^{PYD} in the filament exhibits conformational differences with that of ASC^{PYD} alone (**Figure 2.4B**). This is apparent in the highly variable α2-α3 loop and the short α3 helix, with clear cryo-EM density (**Figure S2.4A**). PYDs share a unique feature: the α3 helix is shortened or missing, and follows the long and flexible α2-α3 loop (**Figure S2.4B**). The conformational changes are likely due to participation of this region in all three types of interactions in the filament (see below and **Figure S2.3D**). Although the ASC^{PYD} alone structure was determined at a pH below 4.0 [13], lack of significant conformational differences elsewhere and absence of acidic residues in α3 helix support the structural changes as due to filament formation. Among known PYD structures, $NLRP3^{PYD}$ and $ASC2^{PYD}$ possess a conformation similar to the filament conformation of ASC^{PYD} (**Figure 2.4C**), suggesting that $NLRP3^{PYD}$ and $ASC2^{PYD}$ may be better interactors with ASC^{PYD}. The former similarity may account for the high

Figure 2.4. Detailed Cryo-EM Model of the ASC^{PYD} Filament

A. The ASC^{PYD} filament is a three-start helical assembly with C3 symmetry as shown in a surface representation. The three-start helical strands are denoted by red, cyan, and yellow, respectively, with alternating darker and lighter shades to show subunit boundaries.

B. Comparison of the initial ASC^{PYD} subunit model (gray, PDB: 1UCP) and the subunit structure after refinement against the cryo-EM density (cyan).

C. Structures of ASC2^{PYD} (magenta) and NLRP3^{PYD} (orange) are similar to the ASC^{PYD} subunit structure in the filament (cyan).

D. Electrostatic surface representations of approximate cross sections of the filament.

E. A schematic diagram of the ASC^{PYD} filament and the three types of asymmetric interactions, defined in accordance with the previously observed DD/DD interactions.

F. Comparison of the Type III interactions in the ASC^{PYD} filament (cyan) and in the MyD88/IRAK4/IRAK2 DD complex (orange).

G, H, I. Detailed interactions in Type I, II, and III interfaces, respectively. Side chains of interfacial residues are shown as stick models and labeled.

See also **Figure S2.4**.

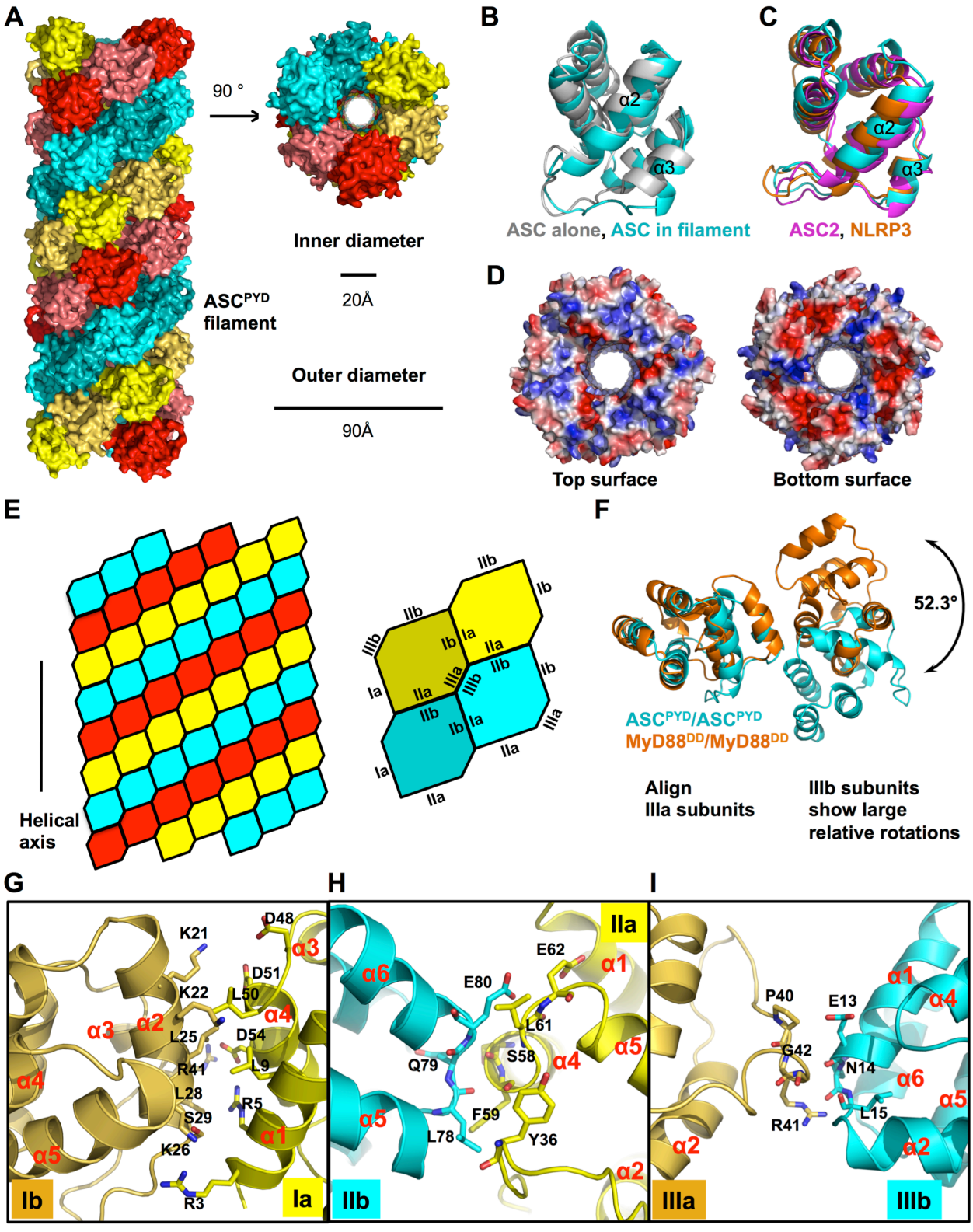

Figure 2.4 (Continued)

efficiency of NLRP3$^{PYD-NBD}$ in promoting ASC^{PYD} polymerization (**Figure 2.2B**). ASC2 is a PYD only protein that is highly homologous to ASC^{PYD} and has been shown to associate with ASC to modulate caspase-1 activation [23]. If ASC2 can be incorporated into ASC^{PYD} filaments but lacks the effector CARD, it could inhibit caspase-1 recruitment and activation. One face of a cross section of the filament is largely negatively charged while the opposite face is largely positively charged (**Figure 2.4D**), suggesting the role of charge complementarity in filament assembly.

Detailed Interactions in the ASC^{PYD} Filament

There are three major asymmetric interfaces (types I, II, III) in the filament, one within each of the three-start helical strands (type I), and two between the strands (type II and III) (**Figure 2.4E**). Remarkably, despite being within the DD superfamily, the PYD/PYD interactions show remarkable differences to the DD complex structures (**Figure 2.4F and S2.4C-E, Table S2.1**). If one of the subunits is aligned, the corresponding partner subunit would need to rotate by 15-26°, 21-35° and 18-52° for the type I, II and III interfaces respectively, relative to the corresponding interfaces in the MyD88/IRAK4/IRAK2 DD complex and the PIDD/RAIDD DD complex [7-9] (**Figure S2.4C-E, Table S2.1**). Relatively, the structural superposition indicates that the type I interaction is the most conserved, which is also the most dominant, burying about 880 Å^2 of surface area. Type II and III interactions are highly variable and bury 540 Å^2 and 360 Å^2 of surface area, respectively. Structural differences between PYD and other members of the DD fold superfamily, and formation of a substantial central cavity may have shifted the relative orientations of the subunits in the type I, II and III interactions.

In the previously observed DD/DD interactions, type I is mediated by residues at α1 and α4 (type Ia) and residues at α2 and α3 (type Ib) [7-9]. Despite being the most conserved, the relative shift in orientation and the structural differences between DDs and PYDs minimized the involvement of α3 in the intra-strand type I PYD/PYD interaction (**Figure 2.4G, S2.3D**). In the

inter-strand type II PYD/PYD interaction, residues at the α4-α5 corner of one ASC^{PYD} (type IIa) and residues at the α5-α6 corner of the second ASC^{PYD} (type IIb) mediate this interaction (**Figure 2.4H, Fig. S2.3D**). In the inter-strand type III PYD/PYD interaction, α2-α3 corner of one ASC^{PYD} (type IIIa) interacts with the α1-α2 corner (type IIIb) of the other subunit (**Figure 2.4I, S2.3D**). Prominently, the PYD-unique and highly variable α2-α3 loop participates in all three types of PYD/PYD interactions (**Figure S2.3D**), which may explain the conformational changes in this region upon filament formation (**Figure 2.4B**). Overall the interactions contain charged, hydrophilic and hydrophobic components, with charge interactions playing an important role (**Figure S2.4F-H**). Consistently, ASC^{PYD} polymerization exhibits salt dependence (**Figure S2.4I**).

Structure-based Mutagenesis *in Vitro* and in Cells

Structure-guided mutagenesis *in vitro* confirmed the role of type I, II and III interactions in ASC^{PYD} filament formation, as shown by elution in more monomeric fractions (**Figure 2.5A**). In particular, K21Q, K21E/K22E, K26E, R41E, D48R, D48N and D51R of the type I interface, F59E of the type II interface, and E13R and R41E of the type III interface, abolished filament formation (**Figure 2.5A, Table S2.2**). Additional mutations, R3E and L50A of the type I interface, and Y36A and E80R of the type II interface, weakened filament formation as shown by increased presence in the monomeric fractions in comparison with the wildtype (WT) (**Figure 2.5A, Table S2.2**). Mutations that disrupted filament formation *in vitro* also abrogated the ability of eGFP-ASC^{PYD} to form filaments in cells as shown by confocal and fluorescence microscopy (**Figure 2.5B, S2.5A-B**) and by EM of immunopurified samples (**Figure S2.5C-D**). A previous extensive mutagenesis study on surface exposed charged residues confirmed the importance of additional observed interfacial residues in ASC^{PYD} filament formation in cells [24] (**Table S2.2**).

In contrast to disruptive phenotypes of mutations on interfacial residues, the charge reversal mutation E67R outside the interface did not affect eGFP-ASC^{PYD} filament formation

Figure 2.5. Structure-based Mutations Disrupts ASC^{PYD} Filament Formation, $AIM2^{PYD}/ASC^{PYD}$ Interaction and $NLRP3^{PYD}/ASC^{PYD}$ Interaction *in Vitro* and in Cells

A. Size-exclusion chromatography of WT and mutant ASC^{PYD} showing both filamentous (void) and monomeric fractions from a Superdex 200 column. Hyphen denotes ASC^{PYD} and asterisk denotes a contaminant.

B. Morphology of transfected WT and mutant eGFP-tagged ASC^{PYD} constructs visualized by confocal laser scanning microscopy. The arrowhead depicts filaments. n: nucleus; scale bars = 10 μm.

C. Morphology of transfected eGFP-tagged ASC^{PYD} visualized by confocal laser scanning microscopy. Top: ASC^{PYD} with charge reversal mutation on a residue outside the filament interface. Bottom: ASC^{PYD} with triple charge reversal mutation that rescued the defectiveness of the single mutants. Arrowheads depict filaments.

D. A schematic model of $AIM2^{PYD}/ASC^{PYD}$ or $NLRP3^{PYD}/ASC^{PYD}$ filaments composed of a top $AIM2^{PYD}$ or $NLRP3^{PYD}$ layer extended by ASC^{PYD} filament body.

E, F. Mutations of conserved interfacial residues on $AIM2^{PYD}$ (E) and $NLRP3^{PYD\text{-}NBD}$ (F) reduced or abolished their ability to nucleate ASC^{PYD} filaments.

See also **Figure S2.5**.

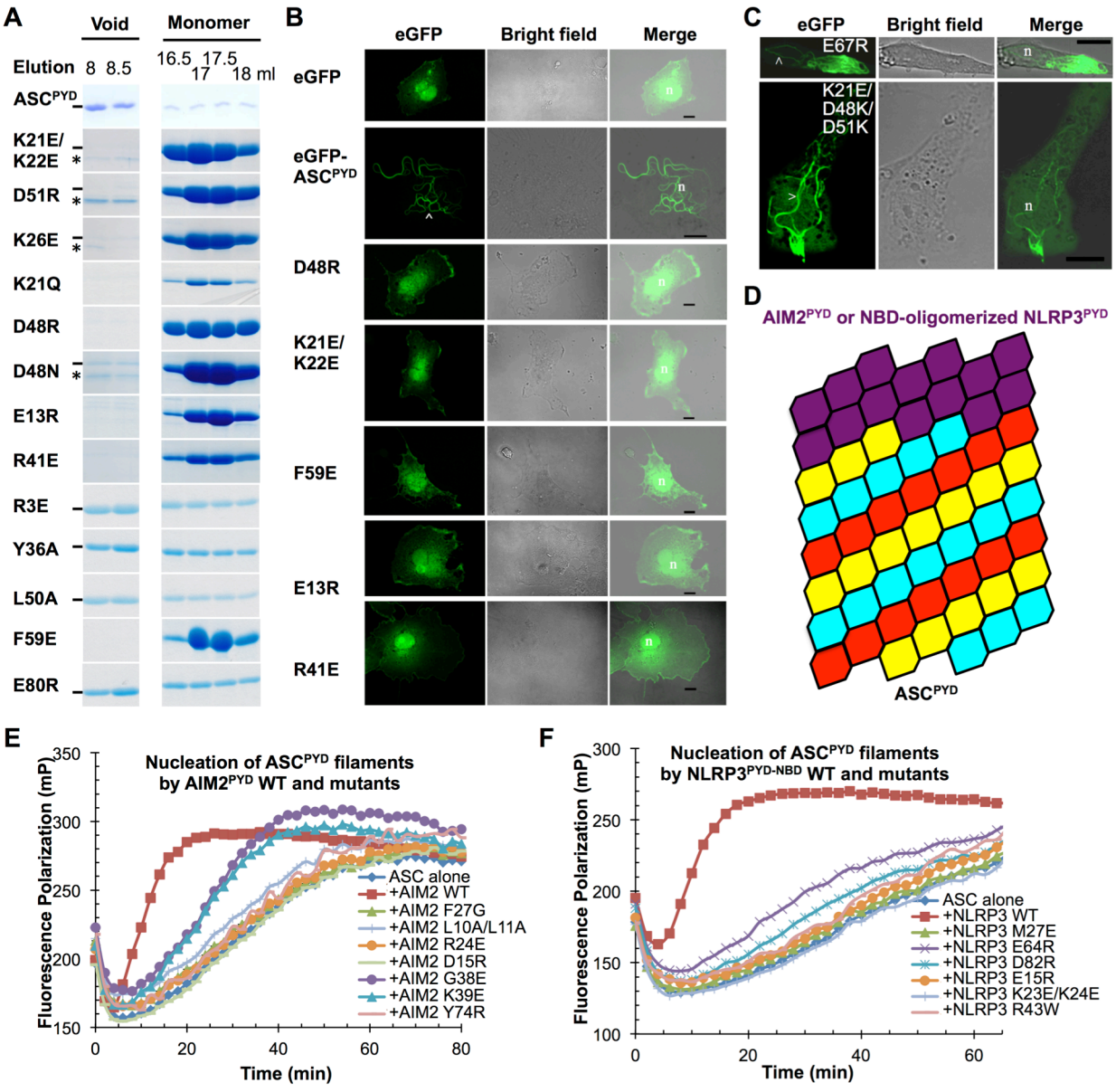

Figure 2.5 (Continued)

(**Figure 2.5C**). At the type I interface, K21, D48 and D51 interact with each other (**Figure 2.4G**) and mutations on each of the residues disrupt filament formation (**Figure 2.5A, 2.5B**). Remarkably, the triple charge reversal mutant K21E/D48K/D51K rescued eGFP-ASC^{PYD} filament formation in cells (**Figure 2.5C**), supporting the validity of the structurally observed interactions.

Modeled AIM2^{PYD}/ASC^{PYD} and NLRP3$^{PYD-NBD}$/ASC^{PYD} Interactions

The ASC^{PYD} filament structure provides a template for modeling the AIM2^{PYD}/ASC^{PYD} and NLRP3^{PYD}/ASC^{PYD} hetero-PYD/PYD interactions using the published crystal structures of AIM2^{PYD} [16] and NLRP3^{PYD} [15]. End locations of AIM2^{PYD} and NLRP3^{PYD} in their complexes with ASC^{PYD} filaments suggest that the PYDs in AIM2 and NLRP3 continue the helical arrangement seen in the ASC^{PYD} filament using a combination of the same type I, II and III interactions (**Figure 2.5D**). Given the observed conformational changes at the α2-α3 corner, which points down in the helical diagram (**Figure 2.4D**), we reasoned that AIM2 and NLRP3 PYDs should reside above the ASC^{PYD} filament (**Figure 2.5D**).

We selected residues in AIM2^{PYD} and NLRP3^{PYD} structures corresponding to those in ASC^{PYD} that caused impairment in filament formation when mutated (**Figure 2.5A, 2.5B**). Assaying the ability of AIM2^{PYD} and NLRP3$^{PYD-NBD}$ mutants in promoting ASC^{PYD} polymerization showed that mutations on each of the predicted interfaces in AIM2^{PYD}, including L10A/L11A, R24E and F27G of the type I interface, Y74R of the type II interface, and G38E, K39E and D15R of the type III interface, either abolished or showed greatly reduced promotion of ASC^{PYD} polymerization (**Figure 2.5E, Table S2.3**). Additionally, in a recently published study on AIM2^{PYD}, the D19A/E20A/E21A/D23A mutation, which harbors mostly type I interface residues, abolished the interaction with ASC^{PYD} [16]. Similarly, mutations at each of the predicted type I, II and III interfacial residues on NLRP3^{PYD}, including K23E/K24E and M27E of the type I interface, E64R and D82R of the type II interface, and R43W and E15R of the type III interface, caused

almost complete impairment in promoting ASC^{PYD} polymerization by the $NLRP3^{PYD-NBD}$ construct (**Figure 2.5F, Table S2.3**). It should be noted because $AIM2^{PYD}$ also aggregates into similar filaments (**Figure S2.1B**), the same mutations would likely affect both AIM2/ASC interaction and AIM2 self-association. For NLRP3, the PYD does not self-associate while the NBD mediates self-association; therefore the PYD mutations in NLRP3 would directly affect ASC interaction. Collectively, these data support that the interactions in the ASC^{PYD} filament also define the mode of hetero-oligomerization in the $AIM2^{PYD}$/ASC^{PYD} and $NLRP3^{PYD}$/ASC^{PYD} interaction pairs.

Reconstitution of the Ternary AIM2 Inflammasome

The C-termini of ASC^{PYD} subunits extend prominently outward from the filament (**Figure 2.6A**), providing a connection to the CARD in ASC after a 23-residue linker. Superposition of the NMR structure of ASC^{FL} [14] with ASC^{PYD} in the filament displayed the flexibly linked, peripheral ASC^{CARD} (**Figure 2.6B**). To reveal the structural architecture of full ternary inflammasomes, we expressed and purified His-GFP-caspase-1^{CARD}, His-MBP-ASC^{FL} and His-MBP-$AIM2^{PYD}$. We mixed the three proteins with the TEV protease to allow His-MBP removal and formation of a ternary complex. His-tag pulldown showed that His-GFP-caspase-1^{CARD} interacted with ASC^{FL} and $AIM2^{PYD}$ (**Figure 2.6C**). The stoichiometry between ASC^{FL} and $AIM2^{PYD}$ in the ternary complex is consistent with that in the $AIM2^{PYD}$/ASC^{PYD} binary complex with $AIM2^{PYD}$ under-stoichiometric (**Figure 2.1C**). ASC in turn appeared under-stoichiometric to caspase-1. EM showed that the ternary complex is star-shaped (**Figure 2.6D**). Anti-ASC immunogold-labeling (15 nm) showed that ASC resides in the center of the stars (**Figure 2.6D**). In contrast, Ni-NTA conjugated with 6 nm gold particles labeled His-GFP-caspase-1^{CARD} along the arms of the stars (**Figure 2.6E**). These data suggest that $AIM2^{PYD}$ nucleates short filaments of ASC^{FL} through PYD/PYD interactions and ASC^{CARD} further initiates caspase-1^{CARD} filaments to promote caspase-1 activation. Because the linker between ASC PYD and CARD is flexible, the outer

CARDs should be able to cluster together and act as the platform for caspase-1 polymerization (**Figure 2.6B**).

We tested the role of ASC^{CARD} in inflammasome assembly using a caspase-1^{CARD} polymerization assay. We used "sandwich"-tagged His-MBP-caspase-1^{CARD}-Sumo construct because N-terminally tagged His-MBP-caspase-1^{CARD} construct still formed filaments. A sortase motif was added for fluorophore labeling [25]. Polymerization of caspase-1^{CARD} was initiated by addition of TEV to cleave off His-MBP and monitored by fluorescence polarization. In the presence ASC^{FL} or ASC^{CARD} at sub-stoichiometric ratios, caspase-1^{CARD} polymerization was greatly enhanced (**Figure 2.6F**), consistent with nucleation of caspase-1 polymerization by ASC.

It is intriguing that the ASC^{FL} component in the ternary complex does not display as long filaments as in the binary $AIM2^{PYD}$/ASC^{PYD} or $NLRP3^{PYD\text{-}NBD}$/ASC^{PYD} complexes. We reasoned that since His-MBP-ASC^{FL} forms bundled clusters minutes after removal of the His-MBP tag (**Figure S2.6A**) and precipitates, likely due to the CARD and its potential to crosslink filaments, ASC^{FL} might only exist as short filaments such that almost all ASC^{CARD} molecules are in complex with caspase-1^{CARD}. To determine if the same ASC^{PYD} interactions in the observed filament govern those in the context of ASC^{FL}, we co-transfected Myc-His-tagged ASC^{FL} with WT and mutant ASC^{PYD}-eGFP in 293T cells. Immunoprecipitated with anti-His antibody followed by anti-eGFP Western showed that Myc-His-ASC^{FL} pulled down WT ASC^{PYD}-eGFP, but was severely impaired in interacting with ASC^{PYD}-eGFP that harbors mutations on residues important for the ASC^{PYD} filament formation (**Figure 2.6G, S2.6B**). We further tested the effects of PYD mutations in ASC^{FL} using the *in vitro* inflammasome reconstitution assay. His-GFP-caspase-1^{CARD} pulled down $AIM2^{PYD}$ in the presence of WT ASC^{FL}, but not mutant ASC^{FL} defective in formation of PYD filaments (**Figure S2.6C**), demonstrating that the same interactions in the PYD filaments govern the interaction in the ternary inflammasome complex.

Figure 2.6. Reconstitution of the Full Ternary AIM2 Inflammasome

A. The ASC^{PYD} filament structure in a ribbon representation. The protruding C-termini for connecting to ASC^{CARD} are labeled for the subunits at the right.

B. ASC^{FL} NMR structure (PDB: 2KN6) is superimposed on the ASC^{PYD} model to show the outward located ASC^{CARD}.

C. Pull-down of the core AIM2 inflammasome *in vitro* as visualized on Coomassie-Blue stained SDS-PAGE.

D, E. Electron micrographs of His-GFP-caspase-1^{CARD}/ASC^{FL}/$AIM2^{PYD}$ ternary complex labeled with anti-ASC gold (**D**) and Ni-NTA gold (**E**).

F. Promotion of His-MBP-caspase-1^{CARD}-Sumo (3 μM) polymerization by ASC^{FL} or ASC^{CARD} at substoichiometric ratios of 1:20 and 1:10 upon removal of His-MBP by TEV. ASC^{PYD} did not enhance caspase-1^{CARD} polymerization.

G. Mutations in ASC^{PYD} reduced its binding to ASC^{FL}. ASC^{FL}-Myc-His was co-transfected with WT and mutant ASC^{PYD}-eGFP. Immunoprecipitation and Western blotting was carried out using anti-His and anti-eGFP antibodies respectively.

H. Model of inflammasome assembly. Upstream sensing proteins such as AIM2 and NLRP3 oligomerize upon activation to form a platform of PYDs that induces ASC filament assembly through PYD/PYD interactions. Multiple ASC^{CARD} molecules cluster to promote caspase-1 filament formation through CARD/CARD interactions. Proximity induced dimerization of the caspase domain activates the enzyme followed by auto-cleavage.

See also **Figure S2.6**.

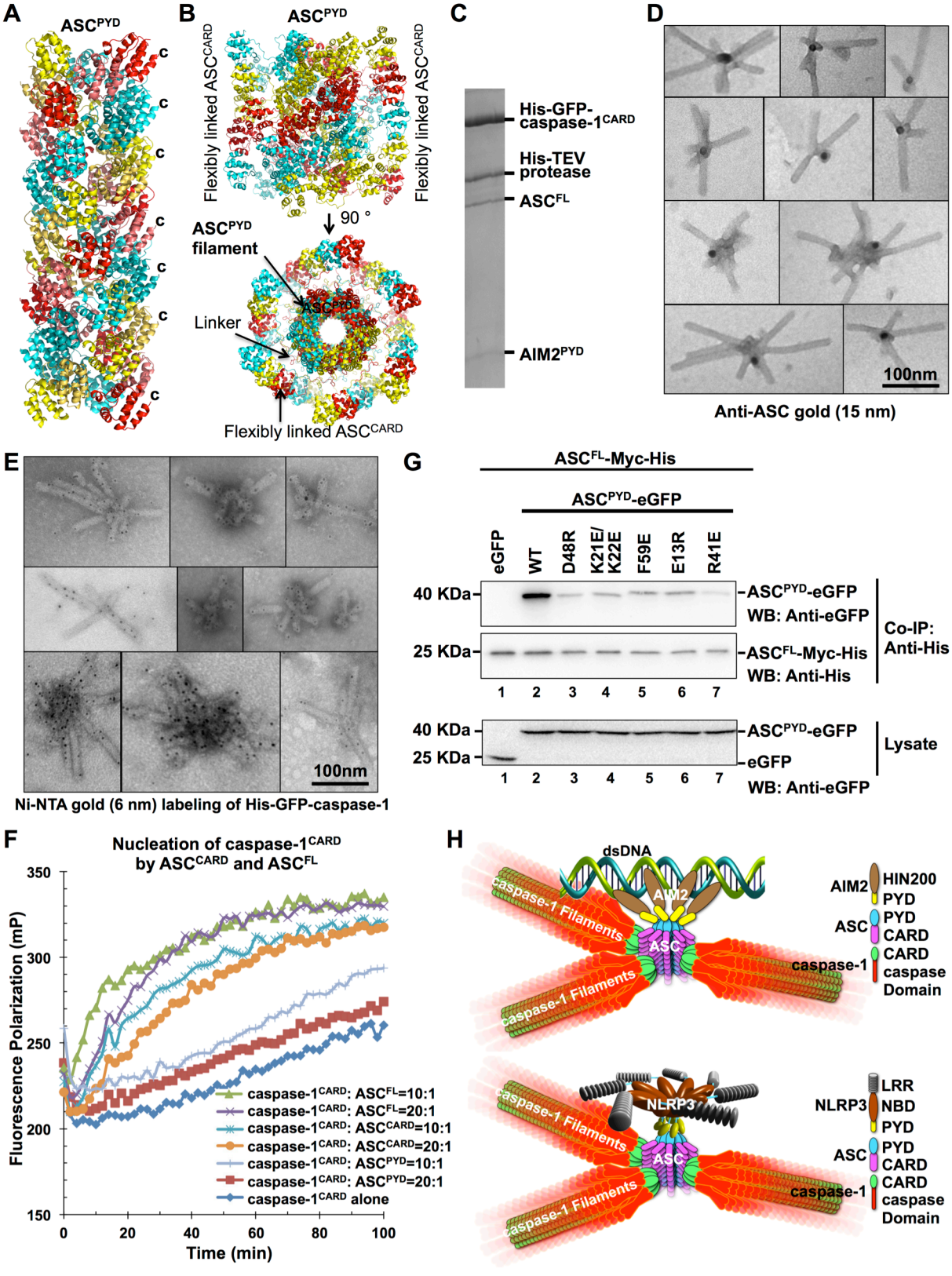

Figure 2.6 (Continued)

Morphology and Stoichiometry of Endogenous NLRP3 Inflammasome

Our data suggest a unified model of inflammasome assembly in which AIM2 upon dsDNA interaction or NLRP3 upon activation nucleates ASC helical clusters through PYD/PYD interactions (**Figure 2.6H**). The oligomerized ASC CARDs then form the platform for caspase-1^{CARD} to nucleate into filaments, which in turn bring caspase domains into proximity for dimerization, trans-auto-cleavage and activation (**Figure 2.6H**). To elucidate the morphology of endogenous inflammasomes, we stimulated THP-1 cells with uric acid crystals, immunoprecipitated the activated NLRP3 inflammasome using anti-ASC antibody, and subjected the immunoprecipitated sample to negative stain EM. The images contained both single filaments (**Figure 2.7A**) and intertwined filaments (**Figure S2.7A**); the former resemble subcomplexes of *in vitro* reconstituted inflammasomes and the latter resemble clustered, ball of yarn-like reconstituted inflammasomes that form upon overnight incubation (**Figure S2.7B**).

It has been shown previously that upon stimulation, each cell forms one gigantic NLRP3 punctum adjacent to the nucleus [26]. To visualize the structure of such a punctum *in situ*, we expressed ASC-eGFP in COS-1 cells and performed immunogold EM on ultrathin cryosections that preserve native structures. Control cells transfected with eGFP alone showed neither punctum nor anti-ASC gold labeling, and ASC-eGFP transfected cells did not exhibit gold labeling in the absence of the anti-ASC primary antibody (**Figure S2.7C**). Specific gold labeling was shown in ASC-eGFP transfected cells in the presence of anti-ASC primary antibody and protein A-gold (10 nm) treatment (**Figure 2.7B**). The labeling revealed a densely packed perinuclear punctum of about 2 μm in size, in contrast to the hollow structure implicated previously [6]. The dense structures are consistent with the ball of yarn-like architectures of *in vitro* reconstituted and in cell immunoprecipitated inflammasomes.

In vitro reconstitution of the ternary inflammasome suggests an over-stoichiometry of caspase-1 to ASC (**Figure 2.6C**). To determine if endogenous ASC-dependent inflammasomes from cells also possess the similar property, we stimulated THP-1 cells with uric acid crystals,

Figure 2.7. Morphology, Stoichiometry and ProIL-1β Processing in Inflammasomes

A. Morphology of anti-ASC immunoprecipitated NLRP3 inflammasomes from uric acid crystal activated THP-1 cells analyzed by negative stain EM. Arrows denote filaments.

B. Immunogold EM on ultrathin cryosections from ASC^{FL}-eGFP transfected COS-1 cells. The ASC-containing compact structure is densely decorated by gold particles (10 nm). N, nucleus; NM, nuclear membrane.

C, D. Quantification of immunoprecipitated ASC-containing complex (IP) from uric acid crystal activated THP-1 cells using quantitative anti-ASC (C) and anti-caspase-1 p12 (D) Western blotting. Known amounts of recombinant His-MBP-ASC and His-GFP-caspase-1 were Western blotted to generate standard curves. The full-length caspase-1 and the cleaved p12 bands were both included in the quantification.

E. AIM2 inflammasome reconstitution in HEK293T cells to define the functional consequence of structure-based mutations in AIM2. Cells were co-transfected with plasmids encoding proIL-1□ and caspase-1 (lane 1), plus ASC alone (lane 2), or WT AIM2 alone (lane 11), or ASC together with WT or indicated AIM2 mutants (lanes 3 to 10). Maturation of proIL-1□ into biologically active IL-1□ was detected by Western blotting using anti-IL-1□ antibody (top panel). The expression levels of HA-ASC and Flag-AIM2 were detected by Western blotting using anti-HA and anti-Flag antibodies (lower panels).

See also **Figure S2.7**.

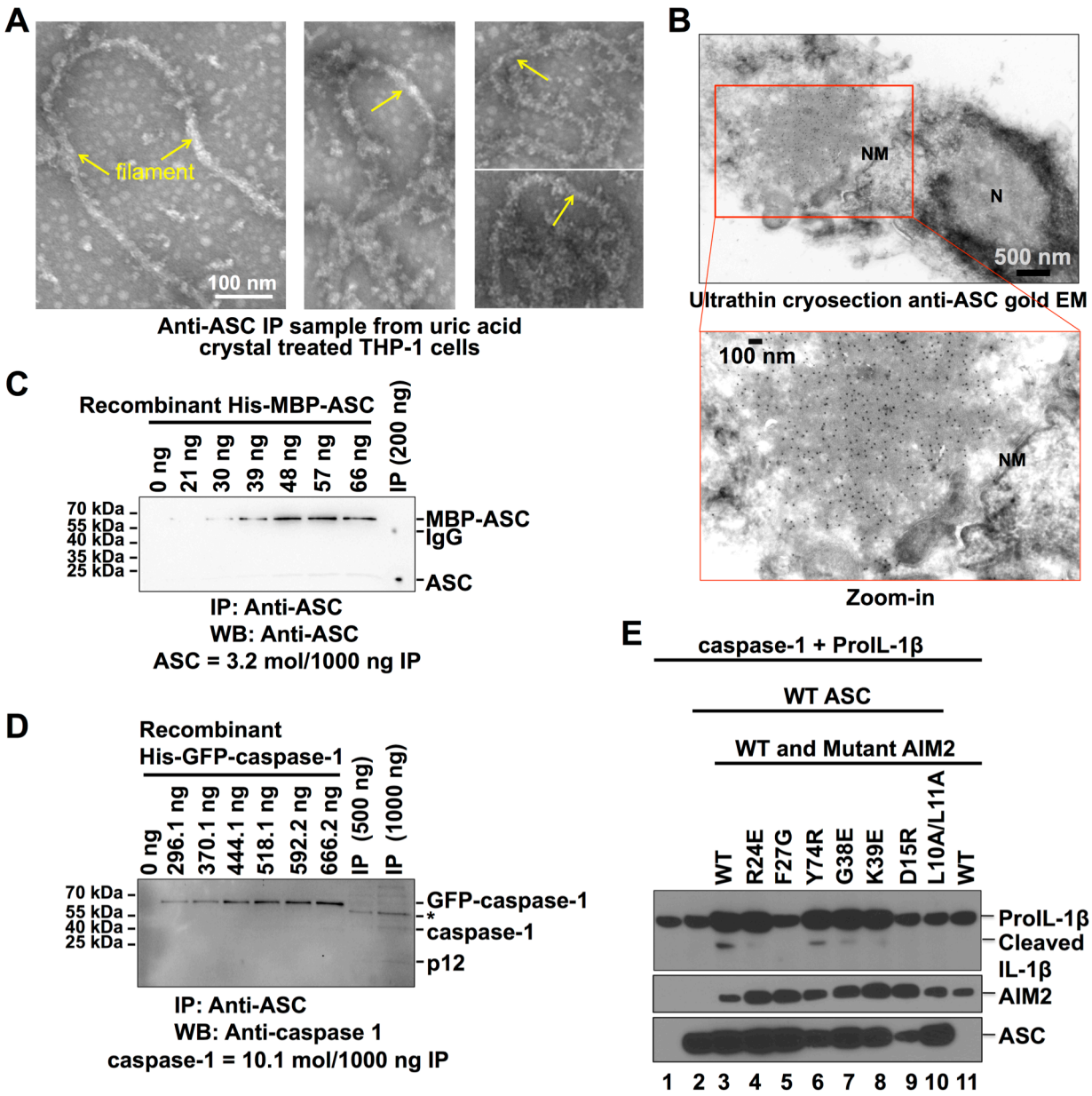

Figure 2.7 (Continued)

immunoprecipitated the activated NLRP3 inflammasome using anti-ASC antibody, and performed quantitative Western blotting using recombinant caspase-1 and ASC as standards. These experiments showed that caspase-1 is over-stoichiometric to ASC, by ~3.5-fold in the current experiment (**Figure 2.7C, 2.7D, S2.7D, S2.7E**). It should be noted that an anti-ASC antibody would have precipitated both ASC alone and its complex with caspase-1 and therefore the measured 3.5-fold over-stoichiometry should be an underestimation.

Structure-guided PYD Mutations Compromise IL-1β Processing

One main biological consequence of inflammasome activation is the processing of proIL-1β by caspase-1 to IL-1β. To address the consequence of structure-based mutations in biological function, we used a co-transfection strategy to assay IL-1β processing [5]. Co-transfection of caspase-1, proIL-1β and ASC did not cause significant cleavage of proIL-1β into mature IL-1β (**Figure 2.7E**). While addition of WT AIM2 activated the inflammasome and led to IL-1β production, co-transfection of PYD-interaction defective AIM2 mutants compromised IL-1β conversion (**Figure 2.7E**), demonstrating the functional consequence of observed PYD/PYD interactions.

Discussions

A Near Atomic Resolution Structure by Cryo-EM

Our reconstruction of a small, structurally variable biological sample represents a significant advance in high-resolution structure determination by cryo-EM made possible by automated microscopy [27], a state-of-the-art electron microscope (the Titan Krios), and a new generation of direct electron detectors [28-31], combined with existing computational approaches for variable twist polymers [19, 20]. Most of the structures that have been currently solved by cryo-EM to near-atomic resolution are icosahedral viruses that are highly ordered and with a high degree of internal symmetry [32]. In the absence of any mechanism to maintain long-range order all biological polymers will display cumulative disorder [33]. We think that the new hardware and software advances in cryo-EM will have an enormous impact in allowing many biological polymers, including those whose helical symmetry could not even be determined with confidence, to now be reconstructed at near-atomic resolution.

PYD/PYD Interactions

The ASC^{PYD} filament structure presented here provides insights into molecular mechanisms of homo- and hetero-PYD associations in inflammasomes. Among the PYDs with known structures, NLRP3, NLRP12, AIM2 and ASC2 have been shown to interact with ASC [2, 23]. Consistently, they exhibit the highest sequence conservation at the ASC-interaction surfaces with 61%, 54%, 50%, and 89% homology, respectively (**Table S2.4**). The ASC^{PYD} structure may also provide a template for other PYDs with no structures such as the $IFI16^{PYD}$ filament cooperatively assembled on dsDNA [34].

A number of mutations in NLRP3, NLRP12 and MEFV have been shown to associate with hereditary periodic fever syndromes. For NLRP3, all mutations are dominant and likely cause activation by overcoming autoinhibition [35]. For NLRP12, a nonsense mutation and a

splicing defect generate truncated proteins at residues 284 and 646, respectively, and cause spontaneous inflammation [36], suggesting that the PYD and part of the NBD are sufficient for inflammasome formation and activation. For MEFV, hundreds of variants, most of which are associated with Familial Mediterranean Fever (FMF), have been identified [35]. Gene insertion "knockin" (KI) mouse models with three frequent FMF-associated mutations (M680I, M694V, and V726A) showed that they caused severe spontaneous inflammatory phenotypes [37]. Most relevant to the PYD interactions, six mutants, T12I, Y19C, K25R, R39G, E84K and A89T, have been mapped to the PYD of MEFV [35]. None of these residues directly map to the PYD/PYD interaction surfaces (**Figure S2.3D**), and may therefore act by overcoming autoinhibition.

A Unified Assembly Mechanism for Inflammasomes

Our data here present a mechanism for the assembly of ASC-dependent inflammasomes, in which AIM2 and NLRP3 both nucleate helical ASC clusters through PYD/PYD interactions, and ASC in turn nucleates caspase-1 filaments through CARD/CARD interactions (**Figure 2.6H**). These minimal structures coalesce to form the micron-sized, dense structures we observed *in situ*. We propose that CARD-containing NLRs (NLRCs), which are independent of ASC, may also form filamentous structures by directly promoting caspase-1 polymerization through CARD/CARD interactions. Therefore, the mechanism of nucleation-induced filament formation may extend beyond ASC-dependent inflammasomes. It has been shown that uncleaved caspase-1 catalytic domain forms dimers in crystals [38]; the dimerization may occur within caspase-1 filaments in inflammasomes, resulting in intradimer cleavage, stabilization of dimerization, and enhancement of enzymatic activity.

Recent studies have revealed that in many innate immune pathways, multiple intracellular signaling proteins assemble into higher-order signaling machines for transmission of receptor activation information to cellular responses, with implicated new molecular mechanisms for threshold behavior, time delay of activation, and temporal and spatial control of

signal transduction [39]. Here we show that inflammasomes also assemble into higher-order signalosomes that likely impart similar properties to its activation and kinetics. In this scenario, upon reaching the NLRP3 or AIM2 activation threshold, caspase-1 may polymerize until its concentrations falls below the dissociation constant. Given that caspase-1 is over-stoichiometric to ASC by just a few fold, the average lengths of individual ASC-nucleated caspase-1 filaments in cells may be shorter than those reconstituted *in vitro*, leading to punctate, rather than filamentous morphology of intact inflammasomes. Once formed, inflammasomes may require active processes such as autophagy for their degradation [40]. This scenario is reminiscent of the case for the filamentous CARMA1/Bcl10/MALT1 signalosome [41], and may represent a general mechanism of disassembly of higher-order signalosomes in innate immunity to terminate signaling.

References

1. Medzhitov, R. & Janeway, C., Jr. (2000) Innate immune recognition: mechanisms and pathways, *Immunol Rev.* **173**, 89-97.

2. Rathinam, V. A., Vanaja, S. K. & Fitzgerald, K. A. (2012) Regulation of inflammasome signaling, *Nat Immunol.* **13**, 333-2.

3. Lamkanfi, M. & Dixit, V. M. (2012) Inflammasomes and their roles in health and disease, *Annu Rev Cell Dev Biol.* **28**, 137-61.

4. Franchi, L., Munoz-Planillo, R. & Nunez, G. (2012) Sensing and reacting to microbes through the inflammasomes, *Nat Immunol.* **13**, 325-32.

5. Jin, T., Perry, A., Jiang, J., Smith, P., Curry, J. A., Unterholzner, L., Jiang, Z., Horvath, G., Rathinam, V. A., Johnstone, R. W., Hornung, V., Latz, E., Bowie, A. G., Fitzgerald, K. A. & Xiao, T. S. (2012) Structures of the HIN domain:DNA complexes reveal ligand binding and activation mechanisms of the AIM2 inflammasome and IFI16 receptor, *Immunity.* **36**, 561-71.

6. Masumoto, J., Taniguchi, S., Ayukawa, K., Sarvotham, H., Kishino, T., Niikawa, N., Hidaka, E., Katsuyama, T., Higuchi, T. & Sagara, J. (1999) ASC, a novel 22-kDa protein, aggregates during apoptosis of human promyelocytic leukemia HL-60 cells, *The Journal of biological chemistry.* **274**, 33835-8.

7. Ferrao, R. & Wu, H. (2012) Helical assembly in the death domain (DD) superfamily, *Current opinion in structural biology.* **22**, 241-7.

8. Park, H. H., Logette, E., Rauser, S., Cuenin, S., Walz, T., Tschopp, J. & Wu, H. (2007) Death domain assembly mechanism revealed by crystal structure of the oligomeric PIDDosome core complex, *Cell.* **128**, 533–546.

9. Lin, S. C., Lo, Y. C. & Wu, H. (2010) Helical assembly in the MyD88-IRAK4-IRAK2 complex in TLR/IL-1R signalling, *Nature.* **465**, 885-890.

10. Strowig, T., Henao-Mejia, J., Elinav, E. & Flavell, R. (2012) Inflammasomes in health and disease, *Nature.* **481**, 278-86.

11. Yin, Q., Sester, D. P., Tian, Y., Hsiao, Y. S., Lu, A., Cridland, J. A., Sagulenko, V., Thygesen, S. J., Choubey, D., Hornung, V., Walz, T., Stacey, K. J. & Wu, H. (2013) Molecular mechanism for p202-mediated specific inhibition of AIM2 inflammasome activation, *Cell reports.* **4**, 327-39.

12. Masumoto, J., Taniguchi, S. & Sagara, J. (2001) Pyrin N-terminal homology domain- and caspase recruitment domain-dependent oligomerization of ASC, *Biochem Biophys Res Commun.* **280**, 652-5.

13. Liepinsh, E., Barbals, R., Dahl, E., Sharipo, A., Staub, E. & Otting, G. (2003) The death-domain fold of the ASC PYRIN domain, presenting a basis for PYRIN/PYRIN recognition, *Journal of molecular biology.* **332**, 1155-63.

14. de Alba, E. (2009) Structure and interdomain dynamics of apoptosis-associated speck-like protein containing a CARD (ASC), *The Journal of biological chemistry.* **284**, 32932-41.

15. Bae, J. Y. & Park, H. H. (2011) Crystal structure of NALP3 protein pyrin domain (PYD) and its implications in inflammasome assembly, *The Journal of biological chemistry.* **286**, 39528-36.

16. Jin, T., Perry, A., Smith, P. T., Jiang, J. & Xiao, T. S. (2013) Structure of the AIM2 pyrin domain provides insights into the mechanisms of AIM2 autoinhibition and inflammasome assembly, *The Journal of biological chemistry*.

17. Yuan, S. & Akey, C. W. (2013) Apoptosome structure, assembly, and procaspase activation, *Structure.* **21**, 501-15.

18. Hu, Z., Yan, C., Liu, P., Huang, Z., Ma, R., Zhang, C., Wang, R., Zhang, Y., Martinon, F., Miao, D., Deng, H., Wang, J., Chang, J. & Chai, J. (2013) Crystal structure of NLRC4 reveals its autoinhibition mechanism, *Science.* **341**, 172-5.

19. Egelman, E. H., Francis, N. & DeRosier, D. J. (1982) F-actin is a helix with a random variable twist, *Nature.* **298**, 131-5.

20. Egelman, E. H. (2000) A robust algorithm for the reconstruction of helical filaments using single-particle methods, *Ultramicroscopy.* **85**, 225-34.

21. Rosenthal, P. B. & Henderson, R. (2003) Optimal determination of particle orientation, absolute hand, and contrast loss in single-particle electron cryomicroscopy, *Journal of molecular biology.* **333**, 721-45.

22. Schröder, G. F., Brunger, A. T. & Levitt, M. (2007) Combining efficient conformational sampling with a deformable elastic network model facilitates structure refinement at low resolution, *Structure.* **15**, 1630-41.

23. Stehlik, C., Krajewska, M., Welsh, K., Krajewski, S., Godzik, A. & Reed, J. C. (2003) The PAAD/PYRIN-only protein POP1/ASC2 is a modulator of ASC-mediated nuclear-factor-kappa B and pro-caspase-1 regulation, *Biochem J.* **373**, 101-13.

24. Moriya, M., Taniguchi, S., Wu, P., Liepinsh, E., Otting, G. & Sagara, J. (2005) Role of charged and hydrophobic residues in the oligomerization of the PYRIN domain of ASC, *Biochemistry.* **44**, 575-83.

25. Theile, C. S., Witte, M. D., Blom, A. E., Kundrat, L., Ploegh, H. L. & Guimaraes, C. P. (2013) Site-specific N-terminal labeling of proteins using sortase-mediated reactions, *Nature protocols.* **8**, 1800-7.

26. Fernandes-Alnemri, T., Wu, J., Yu, J. W., Datta, P., Miller, B., Jankowski, W., Rosenberg, S., Zhang, J. & Alnemri, E. S. (2007) The pyroptosome: a supramolecular assembly of ASC dimers mediating inflammatory cell death via caspase-1 activation, *Cell Death Differ.* **14**, 1590-604.

27. Potter, C. S., Chu, H., Frey, B., Green, C., Kisseberth, N., Madden, T. J., Miller, K. L., Nahrstedt, K., Pulokas, J., Reilein, A., Tcheng, D., Weber, D. & Carragher, B. (1999) Leginon: a system for fully automated acquisition of 1000 electron micrographs a day, *Ultramicroscopy.* **77**, 153-161.

28. Li, X., Mooney, P., Zheng, S., Booth, C. R., Braunfeld, M. B., Gubbens, S., Agard, D. A. & Cheng, Y. (2013) Electron counting and beam-induced motion correction enable near-atomic-resolution single-particle cryo-EM, *Nat Methods.* **10**, 584-590.

29. Bammes, B. E., Rochat, R. H., Jakana, J., Chen, D. H. & Chiu, W. (2012) Direct electron detection yields cryo-EM reconstructions at resolutions beyond 3/4 Nyquist frequency, *JStructBiol.* **177**, 589-601.

30. Bai, X. C., Fernandez, I. S., McMullan, G. & Scheres, S. H. (2013) Ribosome structures to near-atomic resolution from thirty thousand cryo-EM particles, *Elife.* **2**, e00461.

31. Liao, M., Cao, E., Julius, D. & Cheng, Y. (2013) Structure of the TRPV1 ion channel determined by electron cryo-microscopy, *Nature.* **504**, 107-12.

32. Zhou, Z. H. (2011) Atomic resolution cryo electron microscopy of macromolecular complexes, *AdvProtein ChemStructBiol.* **82**, 1-35.

33. Egelman, E. H. & DeRosier, D. J. (1982) The Fourier transform of actin and other helical systems with cumulative random angular disorder, *Acta Cryst* **A38**, 796-9.

34. Morrone, S. R., Wang, T., Constantoulakis, L. M., Hooy, R. M., Delannoy, M. J. & Sohn, J. (2013) Cooperative assembly of IFI16 filaments on dsDNA provides insights into host defense strategy, *Proceedings of the National Academy of Sciences of the United States of America*.

35. Touitou, I., Lesage, S., McDermott, M., Cuisset, L., Hoffman, H., Dode, C., Shoham, N., Aganna, E., Hugot, J. P., Wise, C., Waterham, H., Pugnere, D., Demaille, J. & Sarrauste de Menthiere, C. (2004) Infevers: an evolving mutation database for auto-inflammatory syndromes, *Hum Mutat.* **24**, 194-8.

36. Jeru, I., Duquesnoy, P., Fernandes-Alnemri, T., Cochet, E., Yu, J. W., Lackmy-Port-Lis, M., Grimprel, E., Landman-Parker, J., Hentgen, V., Marlin, S., McElreavey, K., Sarkisian, T., Grateau, G., Alnemri, E. S. & Amselem, S. (2008) Mutations in NALP12 cause hereditary periodic fever syndromes, *Proceedings of the National Academy of Sciences of the United States of America.* **105**, 1614-9.

37. Chae, J. J., Cho, Y. H., Lee, G. S., Cheng, J., Liu, P. P., Feigenbaum, L., Katz, S. I. & Kastner, D. L. (2011) Gain-of-function Pyrin mutations induce NLRP3 protein-independent interleukin-1beta activation and severe autoinflammation in mice, *Immunity.* **34**, 755-68.

38. Elliott, J. M., Rouge, L., Wiesmann, C. & Scheer, J. M. (2009) Crystal structure of procaspase-1 zymogen domain reveals insight into inflammatory caspase autoactivation, *The Journal of biological chemistry.* **284**, 6546-53.

39. Wu, H. (2013) Higher-order assemblies in a new paradigm of signal transduction, *Cell.* **153**, 287-92.

40. Saitoh, T., Fujita, N., Jang, M. H., Uematsu, S., Yang, B. G., Satoh, T., Omori, H., Noda, T., Yamamoto, N., Komatsu, M., Tanaka, K., Kawai, T., Tsujimura, T., Takeuchi, O., Yoshimori, T. & Akira, S. (2008) Loss of the autophagy protein Atg16L1 enhances endotoxin-induced IL-1beta production, *Nature.* **456**, 264-8.

41. Qiao, Q., Yang, C., Zheng, C., Fontan, L., David, L., Yu, X., Bracken, C., Rosen, M., Melnick, A., Egelman, E. H. & Wu, H. (2013) Structural Architecture of the CARMA1/Bcl10/MALT1 Signalosome: Nucleation-Induced Filamentous Assembly, *Mol Cell.* **51**, 766-79.

Chapter Three

Monomeric Mutant of AIM2 PYD

Reveals Critical Interactions for Self-Association

Citation. This chapter has been assembled with minor modifications from the final version of the following published manuscript:

Journal of Molecular Biology **426**, 1420-7 (2014)

Crystal Structure of the F27G AIM2 PYD Mutant and Similarities of its Self-association to DED/DED Interactions

Alvin Lu, Venkataraman Kabaleeswaran, Tian-Min Fu, Venkat Giri Magupalli and Hao Wu*

Department of Biological Chemistry and Molecular Pharmacology, Harvard Medical School, Program in Cellular and Molecular Medicine, Boston Children's Hospital, Boston, MA 02115

*Corresponding author

Contributions. This study was made possible with the generous help of several members of the Wu lab. I am very grateful for everyone's contribution, including help with experimental design, data collection and processing, as well as manuscript drafting.

I am responsible for cloning, expression, and purification of the mutant protein, as well as the crystallization experiments. Crystal diffraction experiment was assisted by Dr. Ryan Ferrao, a former graduate student at our laboratory. I performed the size-exclusion experiments (Figure 3.1B), the multi-angle light scattering (MALS) experiment (Figure 3.1C), and the negative-stain EM experiment (Figure 3.2A). Data processing, including phasing and structure refinement, was done by Dr. Kabaleeswaran. The transfection and confocal experiments on

AIM2^{PYD} mutants, as shown in Figure 3.2C, was assisted by Dr. Fu. The confocal experiment on full-length and truncation mutants of AIM2, as shown in Figure 3.2B, was contributed by Dr. Magupalli. Professor Wu and I together analyzed the crystal structure, generated the figures, and wrote the manuscript.

I would also like to acknowledge the staff scientists at beamlines X25 and X29 of National Synchrotron Light Source (NSLS) for assistance with data collection.

Supplemental materials. Two Supplemental Tables and Supplemental References can be found in Appendix II.

Abstract

Absent in melanoma 2 (AIM2) is a cytoplasmic dsDNA sensor involved in innate immunity. It uses its C-terminal HIN domain for recognizing dsDNA and its N-terminal Pyrin domain (PYD) for eliciting downstream effects through recruitment and activation of Apoptosis-associated Speck-like protein containing CARD (ASC). ASC in turn recruits caspase-1 and/or caspase-11 to form the AIM2 inflammasome. The activated caspases process proinflammatory cytokines IL-1β and IL-18, and induce the inflammatory form of cell death pyroptosis. Here we show that AIM PYD ($AIM2^{PYD}$) self-oligomerizes. We notice significant sequence homology of $AIM2^{PYD}$ with the hydrophobic patches of death effector domain (DED)-containing proteins, and confirm that mutations on these residues disrupt $AIM2^{PYD}$ self-association. The crystal structure at 1.82 Å resolution of such a mutant, F27G of $AIM2^{PYD}$, shows the canonical six-helix (H1-H6) bundle fold in the death domain (DD) superfamily. In contrast to the wild-type (WT) $AIM2^{PYD}$ structure crystallized in fusion with the large maltose-binding protein tag, the H2-H3 region of the $AIM2^{PYD}$ F27G is well defined with low B-factors. Structural analysis shows that the conserved hydrophobic patches engage in a type I interaction that has been observed in DED/DED and other DD superfamily interactions. While previous mutagenesis studies of PYDs point to the involvement of charged interactions, our results reveal the importance of hydrophobic interactions in the same interfaces. These centrally localized hydrophobic residues within fairly charged patches may form the hot spots in $AIM2^{PYD}$ self-association, and may represent a common mode of PYD/PYD interactions in general.

Introduction

Inflammasomes are large supramolecular complexes responsible for sensing cytosolic danger signals associated with microbial infection or endogenous perturbations in the cell. The assembly of the inflammasomes is important for eliciting innate immune responses through the maturation and secretion of two inflammatory cytokines, IL-1β and IL-18, and may lead to an

inflammatory form of cell death known as pyroptosis [4-6]. Inflammasomes are typically composed of an upstream sensor molecule, an adaptor protein known as Apoptosis-associated Speck-like protein containing CARD (ASC), and an effector molecule caspase-1 (and/or caspase-11). Upon recruitment into a full inflammasome, caspase-1 activates through dimerization and auto-proteolysis in order to process pro-inflammatory cytokines.

The sensor molecules, after which the inflammasomes are named, can be grouped into two families – NOD-like receptors (NLRs) and AIM2-like receptors (ALRs), based on their distinct domain architecture. There are a total of 23 NLRs in the human genome [5]. Most NLRs contain an N-terminal interaction domain (PYD, CARD, or BIR), followed by a nucleotide binding and oligomeriziation domain (NACHT or NBD), along with a C-terminal leucine-rich repeat (LRR) responsible for auto-inhibition [7]. Only a handful of these NLRs are found to assemble into functional inflammasomes, including NLRP1, 6, 7, 12, and NLRC4, while the functions of the other NLRs remain to be elucidated. ALRs, which include absent in melanoma 2 (AIM2) and interferon inducible protein 16, also assemble functional inflammasomes [8-12]. They lack the NACHT domain found in NLRs and directly bind to dsDNA, a trigger associated with microbial invasion, though a C-terminal HIN domain [13].

The NLRP3, 6, 7, and 12 inflammasomes and the AIM2 and IFI16 inflammasomes require the bipartite adaptor molecule, ASC, which contains an N-terminal pyrin domain (PYD) followed by a C-terminal caspase recruitment and activation domain (CARD). ASC is recruited by homotypic PYD/PYD interaction with the activated upstream sensor. Oligomerization of the sensor molecules, either through oligomerization of the NACHT domain in NLRs [5, 14] or the release of an auto-inhibition mechanism in ALRs [13, 15], initiates inflammasome assembly. To date, several PYD monomeric structures have been solved using crystallography and NMR. These include the solution structure of ASC^{PYD} [16], full-length (ASC^{FL}) [17], $NALP1^{PYD}$ [18], ASC2 [19], $NLRP10^{PYD}$ [20], $NLRP7^{PYD}$ [21], $NLRP12^{PYD}$ [22], $NALP3^{PYD}$ [23], and $MNDA^{PYD}$.

While our paper was in preparation, the crystal structure of WT AIM2^{PYD} as a fusion protein to maltose binding protein (MBP) was also reported [15].

PYD belongs to the death domain (DD) superfamily, which also includes two other subfamilies – CARD and death-effector domain (DED) [24]. Many PYDs also oligomerize, in addition to interactions with other PYD-containing proteins. This property is observed in DD signalosomes such as the MyDDosome and PIDDosome complexes [25, 26]. In other cases, these homotypic complexes can form extensive cytosolic signaling filaments, such as the DED filaments of caspase-8 [27, 28] and the CBM filamentous complex in NF-κB activation [29]. Therefore, the oligomerization property of AIM2^{PYD} may represent a suitable activation mechanism of the AIM2 inflammasome and warrants more careful studies. Here we used biochemical and structural studies to deduce the mode of AIM2 oligomerization.

Results and Discussions

Sequence similarity with DED and mutagenesis of AIM2^{PYD}

As a first step in the elucidation of AIM2 inflammasome formation, we decided to pursue the structure determination of the PYD of AIM2 (AIM2^{PYD}). However, AIM2^{PYD} (residues 1-100) was insoluble when expressed alone. Even when fused with the solubility tag Sumo, AIM2 still formed large aggregates. Upon searching for suitable mutation sites to solubilize and de-aggregate AIM2 ^{PYD}, we noticed a short, but significant, sequence homology between AIM2^{PYD} and the DEDs of FADD, v-FLIP and caspase-8 centered at the known conserved hydrophobic patches of DEDs (**Figure 3.1A**). In particular, the sequence homology placed F27 of AIM2 as the homologous residue for the surface exposed F25 of FADD, which has been shown to be important for apoptosis induction [1]. While F25W and F25Y essentially maintained the activity of WT FADD, F25G and F25V are almost completely compromised in the cell death induction function. The mutations on F25 disrupted FADD self-association [2] and rendered the proteins

monomeric [1]. They also compromised the ability of FADD to interact with the FLICE-inhibitory protein c-FLIP, a caspase-8-like protein [3]. In the tandem DED structure of a viral caspase-8-like protein known as the v-FLIP MC159 from the poxvirus Molluscum contagiosum virus, the F25-analagous residue in the similar hydrophobic patch of the first DED (DED1, F30) interacts

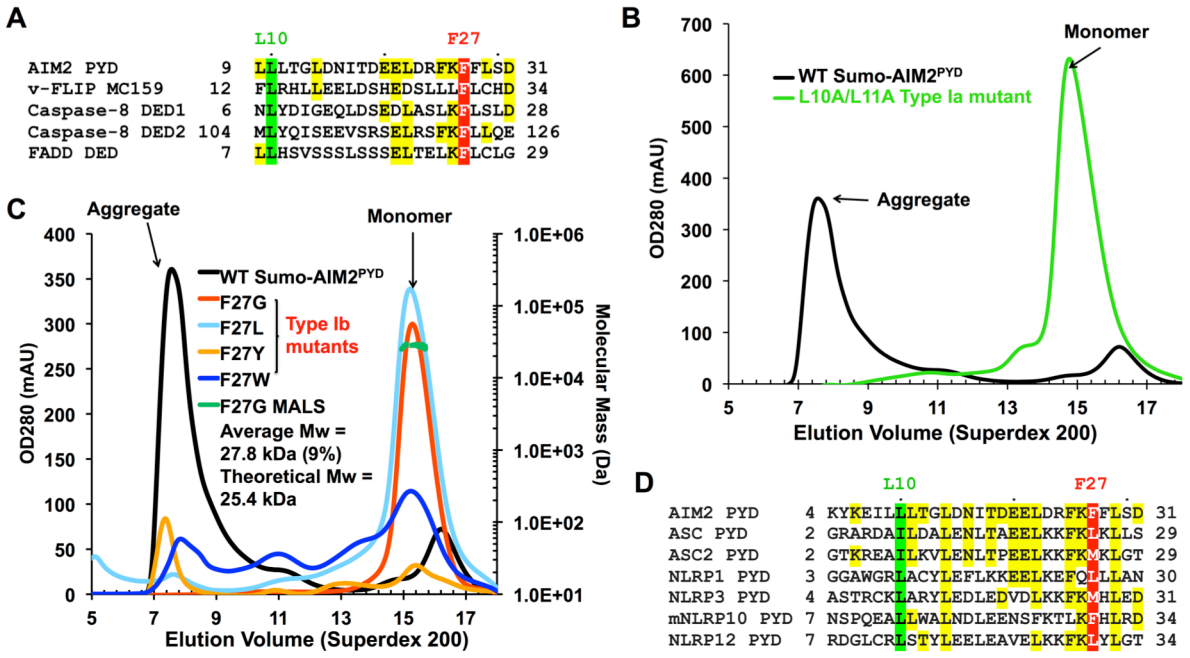

Figure 3.1. Sequence similarity between PYDs and DEDs, and identification of monomeric AIM2 PYD mutants.

A. Sequence alignment of human AIM2 PYD with human caspase-8 DED1 and DED2, and human FADD DED. The conserved hydrophobic positions are highlighted in red for that corresponding to type Ib and in green for that corresponding to type Ia interactions. F25 of FADD is analogous to F27 of AIM2, and has been shown to be important for apoptosis induction, self-association, and c-FLIP and caspase-8 interaction [1-3]. Additional residues that are identical with the AIM2 sequence are highlighted in yellow. Residue numbers are shown.

B. Gel filtration profiles of His-Sumo-AIM2^{PYD} WT and F25 mutant proteins expressed in *E. coli* using the pSMT3 vector. The proteins were purified using Ni-NTA columns. WT: mostly in the aggregation fraction; F27W, F27Y: in both aggregate and monomeric fractions; F27L: mostly in the monomeric fraction; F27G: only in the monomeric fraction.

C. Gel filtration profiles of His-Sumo-AIM2^{PYD} WT and the L10A/L11A mutant protein expressed in *E. coli* using the pSMT3 vector.

D. Sequence alignment among PYDs in the region around L10 and F27 of AIM2.

with the second DED (DED2) to form a rigid dumbbell shaped structure [30, 31]. In caspase-8, the analogous single site F122G mutant exhibited weakened interaction with FADD, while the double mutant, F122G and L123G, completely abolished its interaction with FADD [30].

To determine if F27 of AIM2^{PYD} also impacts its solubility and aggregation solution behavior, we generated the F27Y, F27L, F27W and F27G mutants on the His-Sumo-AIM2^{PYD} construct. All mutations caused the proteins to shift to the monomeric fraction, at least to some extent (**Figure 3.1B**). The more conserved substitutions F27W and F27Y showed a mixture of aggregated and monomeric proteins, while the F27L mutant is mostly monomeric and the F27G mutant is completely monomeric. Upon removal of the Sumo-tag, the F27G AIM2^{PYD} mutant showed solubility greater than 20 mg/ml. These data suggest that F27 is involved in self-association of AIM2^{PYD}.

Based on the definition of the three types of asymmetric interactions that have been observed in the DD fold superfamily [24, 26], F27 resides on a type Ib surface. Modeling and sequence alignment revealed that the corresponding type Ia surface likely includes residues L10 and L11 on the predicted helix H1 (**Figure 3.1A**). In previously reported interactions in the DD superfamily, the type Ia and the type Ib surfaces form a conserved asymmetric interaction pair [24]. Indeed, the mutant L10A/L11A of AIM2^{PYD} also showed almost all monomeric species (**Figure 3.1C**), revealing that the type Ia and Ib surfaces are both involved in AIM2 self-association. Both the type Ia and the type Ib residues are also conserved among the different PYDs (**Figure 3.1D**), suggesting that the type I interaction may be a common feature in PYD/PYD interactions.

AIM2^{PYD} form ordered filaments *in vitro* and in cells

To assess whether AIM2^{PYD} forms ordered aggregates, we first used negative stain EM to examine purified His-Sumo-AIM2^{PYD}, which elutes in the void position of a Supderdex 200 column (**Figure 3.1B**). The protein showed filamentous morphology (**Figure 3.2A**). To confirm

that AIM2^{PYD} also forms ordered aggregates in cells, we transiently transfected in 293T cells full-length, PYD domain, and HIN domain of AIM2 in fusion to eGFP at the C-terminus (AIM2^{FL}-eGFP, AIM2^{PYD}-eGFP and AIM2^{HIN}-eGFP). Confocal microscopy showed that while both AIM2^{FL}-eGFP and AIM2^{PYD}-eGFP formed filamentous structures, AIM2^{HIN}-eGFP did not, suggesting that PYD is responsible for the ordered aggregation (**Figure 3.2B**). We further transiently transfected in HeLa cells AIM2^{PYD} WT and Type I interface mutants identified above,

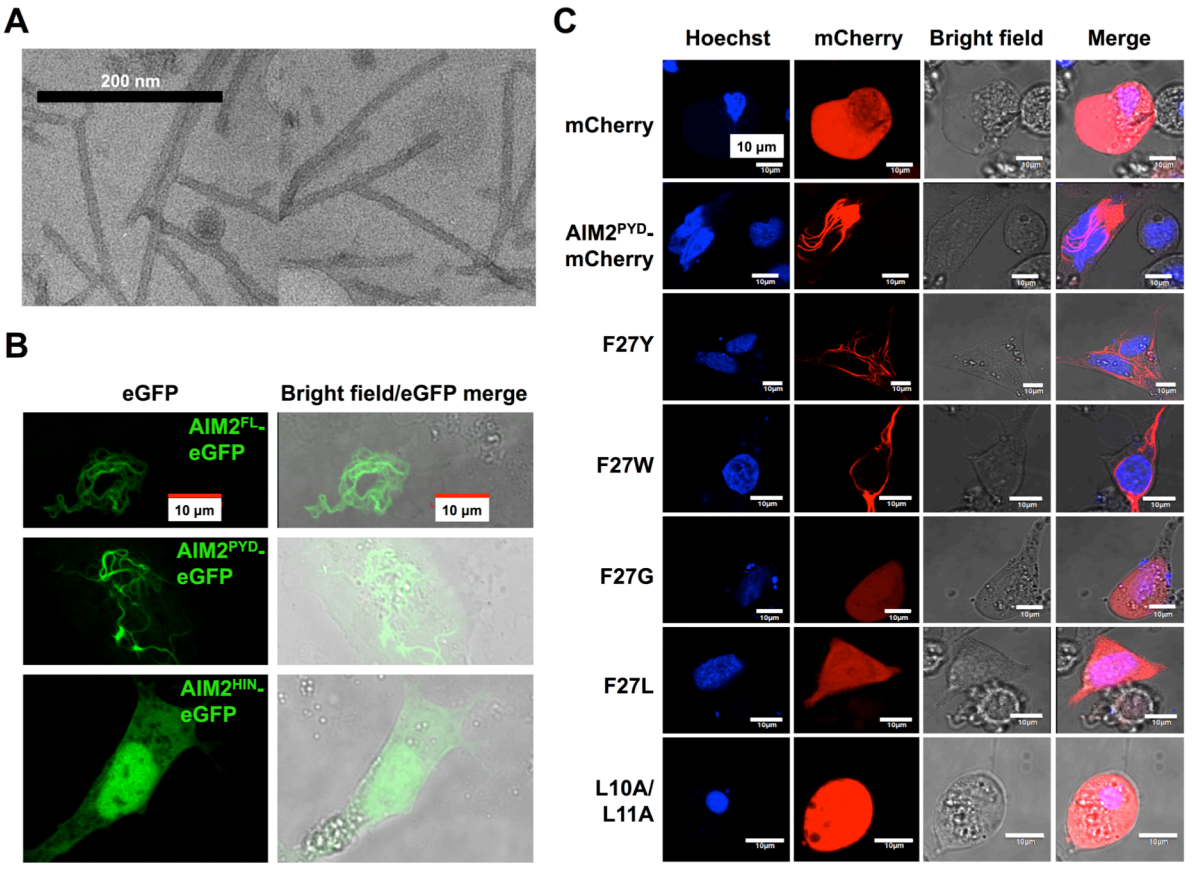

Figure 3.2. AIM2 PYD forms filamentous aggregates.

A. EM images of purified His-Sumo-AIM2^{PYD}, which showed ordered filamentous structures.

B-C. Confocal microscopy images of C-terminal eGFP tagged AIM2 constructs (**B**) and of mCherry tagged AIM^{PYD} WT and Type I interface mutants (**C**). 0.8 µg of recombinant DNA was transfected into cells using Lipofectamine 2000 (Invitroggen) accordining to manufacturer's instructions. Twenty-four hours post transfection, cells were fixed in 0.5% paraformaldehyde followed by nuclei staining using Hoechst 33342 (Molecular probes). The images were collected on an Olympus Fluoview FV1000 confocal microscope.

as fusions to C-terminal mCherry. Confocal microscopy images showed filamentous aggregates for WT, F27Y, and F27W AIM2^{PYD}-mCherry, while F27G, F27L, and L10A/L11A AIM2^{PYD}-mCherry distributed throughout the cells (**Figure 3.2C**). These cellular data correlate well with migration positions in gel filtration chromatography (**Figure 3.1B**). Together, they suggest that bulky hydrophobic residues at the predicted Type I interface are essential for filament formation.

Crystal structure of F27G of AIM2^{PYD}

We set up the F27G mutant of AIM2^{PYD} (residues 1-100) and obtained initial crystals that diffracted to ~4Å resolution. Using *in situ* proteolysis with trypsin, needle clusters grew within 3 days at 4 °C in the same condition with improved resolution to ~1.8 Å (**Figure 3.3A**). The structure was determined using molecular replacement in the program MOLREP [32]. A composite of several PYD structures was used as the search model because of the low sequence identity of AIM2^{PYD} to any known PYD structures. Model building and refinement at 1.82 Å was carried out using Coot [33] and PHENIX [34] (**Table S3.1**). The final atomic coordinates comprise one residue from the vector, and AIM2^{PYD} residues M1 to K93. It is likely that trypsin cleaved the C-terminal tail off at residue K93. This C-terminal region is involved in crystal packing and the cleavage must have facilitated crystal growth.

The structure revealed a six-helical bundle structure comprised of helices H1 to H6, which is conserved in the DD fold superfamily [24] (**Figure 3.3B**). Mutation to Gly at F27 did not dramatically alter the structure; it only created a minor kink in helix H2 (**Figure 3.3C**). In comparison with the WT AIM2^{PYD} structure that was crystallized as a fusion to N-terminal maltose binding protein (MBP) [15], helix H2 in the F27G mutant is in fact longer (**Figure 3.3D-E**). Most conspicuously, in the published WT AIM2^{PYD} structure, the H2-H3 region is highly disordered with high B-factors that go up to ~120 Å^2 while the remainder of the residues show B-factors of ~20-40 Å^2 (**Figure 3.3F**). In contrast, in our high-resolution F27G mutant AIM2^{PYD} structure, this region is ordered and well defined; the B-factors of residues in this region fall

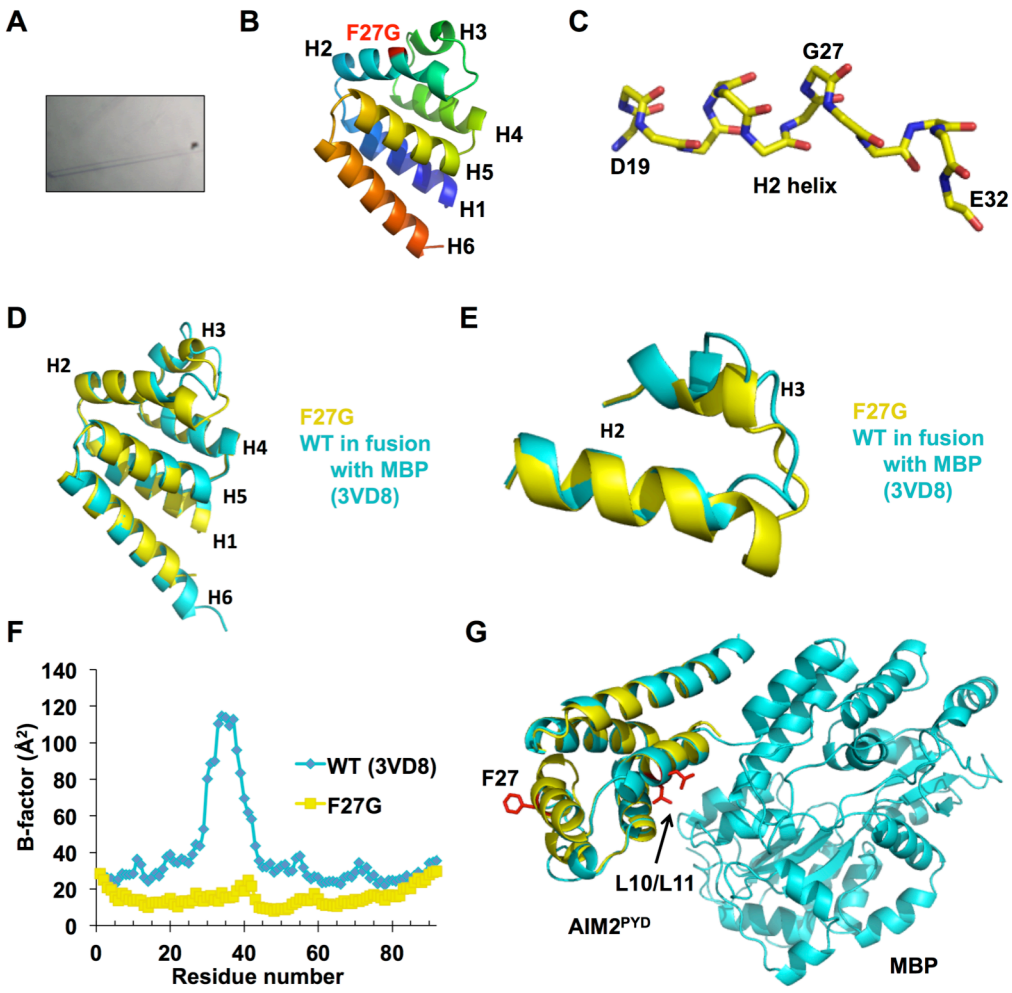

Figure 3.3. Crystal structure of the AIM2^{PYD} F27G mutant.

A. Photograph of a crystal under a transmission light microscope.

B. A ribbon diagram of the structure in rainbow colors. Helices 1-6 are labeled and the location of F27G is shown in red.

C. A stick model of helix H2 showing the kink at G27.

D. Superposition of the crystal structures of F27G (yellow) with the WT in fusion with the MBP tag (cyan).

E. Zoom-up of the superposition in the H2-H3 region, showing the longer H2 in the F27G structure and the different conformations in this region.

F. B-factors along the protein sequence for both the F27G (yellow) and the WT (Cyan) structures, showing the low values in F27G even in the H2-H3 region.

G. Superposition of the WT AIM2-MBP structure (cyan) with the F27G structure (yellow). L10/L11 and F27 residues are shown as red sticks, showing that L10/L11 are packed against MBP to avoid aggregation

within the average B-factor of 18.7 $Å^2$ in the whole protein chain (**Figure 3.3F**, **Table S3.1**). The protein conformation in the H2-H3 region is quite different in the WT and the F27G $AIM2^{PYD}$ (**Figure 3.3E**), suggesting that the ordered F27G mutant provides a clearer structure of this region of AIM2. In comparison with the WT structure, the F27G $AIM2^{PYD}$ structure shows differences in secondary structure boundaries (**Figure 3.4A**), offering an additional view on the intrinsic conformational flexibility of the molecule.

Modeled AIM2 PYD/PYD interaction: hydrophobic interactions may comprise the functional epitope

The locations of F27 on a type Ib surface and L10 on a type Ia surface, and the monomeric phenotypes of mutations on these residues, suggest that $AIM2^{PYD}$ oligomerizes through a type I interface. Consistent with this observation, residues L10 and L11 are positioned adjacent to the fusion partner MBP in the WT $AIM2^{PYD}$ structure [15] (**Figure 3.3G**). Therefore, MBP would inhibit the type I interaction of $AIM2^{PYD}$ in the fusion protein, explaining how MBP inhibits $AIM2^{PYD}$ aggregation.

We generated a PYD/PYD interaction model by superimposing $AIM2^{PYD}$ onto a type I interaction pair in the Myddosome [24, 26] (**Figure 3.4B**). It has been proposed previously that $AIM2^{PYD}$ interacts with ASC^{PYD} mainly through charge-charge interactions [15]. Previous extensive mutagenesis on ASC^{PYD} also suggested the involvement of charged interactions in ASC self-association and interaction with other PYD proteins such as NLRP3 and ASC2 [17, 35, 36]. In our model of the type I interaction in $AIM2^{PYD}$ oligomerization, both the F27 containing and the L10/L11 containing surfaces are highly charged (**Figure 3.4C-D**), consistent with these existing data.

In addition to charge interactions, it has also been proposed that hydrophobic surfaces may be involved in the interactions mediated by $AIM2^{PYD}$ [15]. Here we observe that the hydrophobic residues F27 and L10 appear to reside in the center of the charged patches and

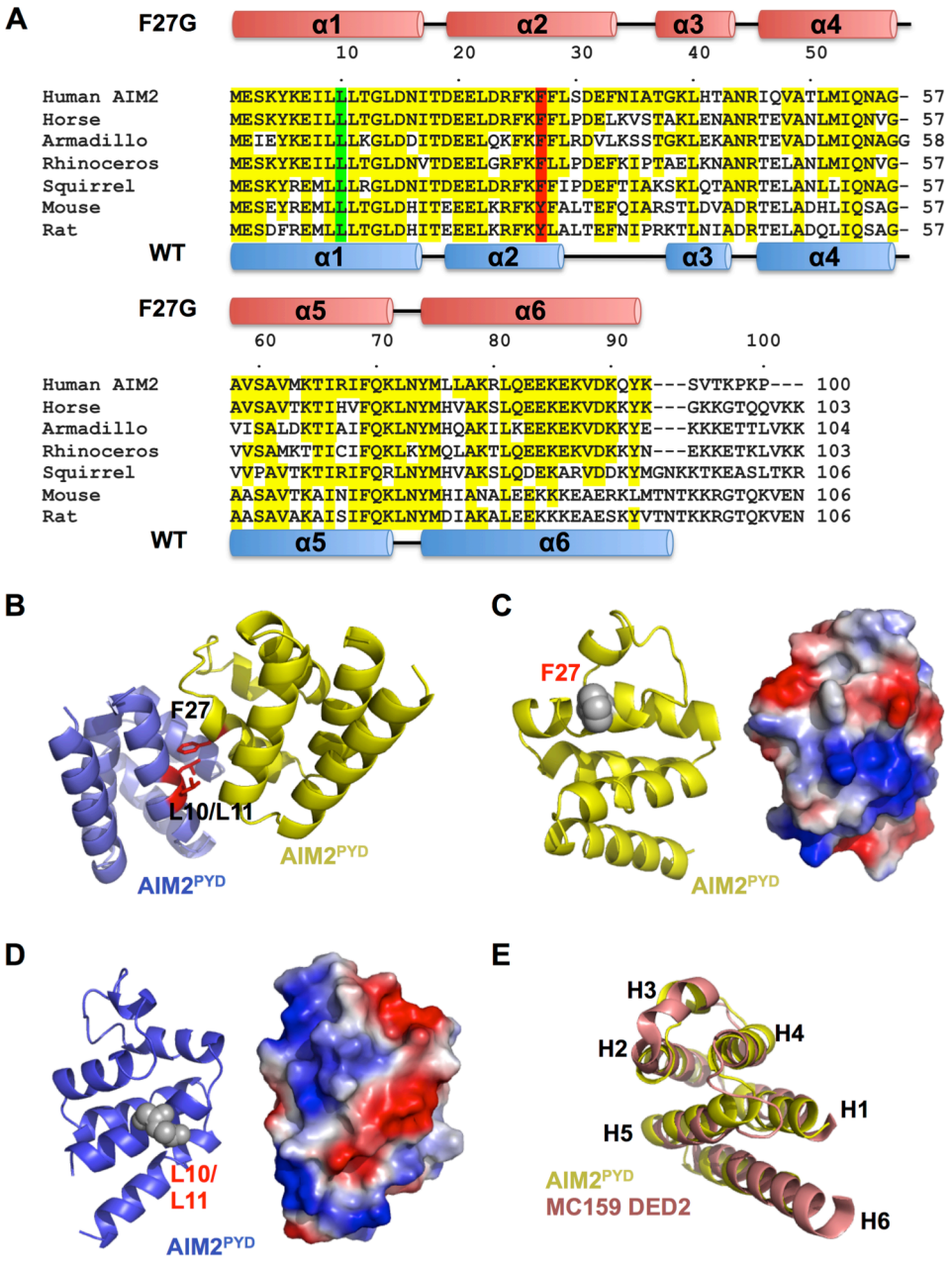

Figure 3.4. Sequence and structural comparisons of AIM2^{PYD}.

A. Sequence alignment among AIM2^{PYD} from different species, with secondary structures from the F27G structure (pink) and the WT structure (blue).

B. An AIM2^{PYD}/AIM2^{PYD} type I interaction model based on the Myddosome structure. The interaction residues F27, L10 and L11 are shown as red sticks.

C-D. Ribbon and electrostatic diagrams of the AIM2^{PYD} surfaces containing F27 (**C**) and L10/L11 (**D**), respectively.

E. Superposition between AIM2^{PYD} (yellow) and MC159 DED2 (pink).

are likely the major contributors of the interactions. The data provide additional structural and energetic insights because the strength of the hydrophobic interaction may be further enhanced by the local charges surrounding it. In addition, previous detailed mutational studies on protein-protein interfaces have shown that the buried hydrophobic contacts at the center of an interface may be responsible for a majority of the interfacial binding energy [37]. Therefore, the hydrophobic residues in $AIM2^{PYD}$ self-association may represent the hot spot or the functional epitope in the interaction, which has been mostly overlooked and not emphasized in the existing literature.

Structural similarities between PYDs and DEDs

In addition to the local sequence homology with DEDs (**Figure 3.1A**), $AIM2^{PYD}$ was also unexpectedly much more similar in structure to canonical DEDs, such as DED of FADD [1] and DED2 of vFLIP [30], than to CARDs and DDs. A DALI structural homology search [38] found that the top hits are all PYD or DED structures (**Table S3.2**, **Figure 3.4E**). This observation is in keeping with a phylogenetic analysis of DD superfamily, which suggests that DED and PYD share common ancestors with PYD derived latest in the evolution of these domains [39]. Therefore, the structural and evolutionary features dictate the similarities between DEDs and PYDs.

References

1. Eberstadt, M., Huang, B., Chen, Z., Meadows, R. P., Ng, S.-C., Zheng, L., J., L. M. & Fesik, S. W. (1998) NMR structure and mutagenesis of the FADD (Mort1) death-effector domain, *Nature.* **392**, 941-945.

2. Carrington, P. E., Sandu, C., Wei, Y., Hill, J. M., Morisawa, G., Huang, T., Gavathiotis, E. & Werner, M. H. (2006) The structure of FADD and its mode of interaction with procaspase-8, *Mol Cell.* **22**, 599-610.

3. Kaufmann, M., Bozic, D., Briand, C., Bodmer, J. L., Zerbe, O., Kohl, A., Tschopp, J. & Grutter, M. G. (2002) Identification of a basic surface area of the FADD death effector domain critical for apoptotic signaling, *FEBS Lett.* **527**, 250-4.

4. Lamkanfi, M. & Dixit, V. M. (2012) Inflammasomes and their roles in health and disease, *Annu Rev Cell Dev Biol.* **28**, 137-61.

5. Rathinam, V. A., Vanaja, S. K. & Fitzgerald, K. A. (2012) Regulation of inflammasome signaling, *Nat Immunol.* **13**, 333-2.

6. Strowig, T., Henao-Mejia, J., Elinav, E. & Flavell, R. (2012) Inflammasomes in health and disease, *Nature.* **481**, 278-86.

7. Hu, Z., Yan, C., Liu, P., Huang, Z., Ma, R., Zhang, C., Wang, R., Zhang, Y., Martinon, F., Miao, D., Deng, H., Wang, J., Chang, J. & Chai, J. (2013) Crystal structure of NLRC4 reveals its autoinhibition mechanism, *Science.* **341**, 172-5.

8. Fernandes-Alnemri, T., Yu, J. W., Datta, P., Wu, J. & Alnemri, E. S. (2009) AIM2 activates the inflammasome and cell death in response to cytoplasmic DNA, *Nature.* **458**, 509-13.

9. Hornung, V., Ablasser, A., Charrel-Dennis, M., Bauernfeind, F., Horvath, G., Caffrey, D. R., Latz, E. & Fitzgerald, K. A. (2009) AIM2 recognizes cytosolic dsDNA and forms a caspase-1-activating inflammasome with ASC, *Nature.* **458**, 514-8.

10. Burckstummer, T., Baumann, C., Bluml, S., Dixit, E., Durnberger, G., Jahn, H., Planyavsky, M., Bilban, M., Colinge, J., Bennett, K. L. & Superti-Furga, G. (2009) An orthogonal proteomic-genomic screen identifies AIM2 as a cytoplasmic DNA sensor for the inflammasome, *Nat Immunol.* **10**, 266-72.

11. Roberts, T. L., Idris, A., Dunn, J. A., Kelly, G. M., Burnton, C. M., Hodgson, S., Hardy, L. L., Garceau, V., Sweet, M. J., Ross, I. L., Hume, D. A. & Stacey, K. J. (2009) HIN-200 proteins regulate caspase activation in response to foreign cytoplasmic DNA, *Science.* **323**, 1057-60.

12. Kerur, N., Veettil, M. V., Sharma-Walia, N., Bottero, V., Sadagopan, S., Otageri, P. & Chandran, B. (2011) IFI16 acts as a nuclear pathogen sensor to induce the inflammasome in response to Kaposi Sarcoma-associated herpesvirus infection, *Cell Host Microbe.* **9**, 363-75.

13. Jin, T., Perry, A., Jiang, J., Smith, P., Curry, J. A., Unterholzner, L., Jiang, Z., Horvath, G., Rathinam, V. A., Johnstone, R. W., Hornung, V., Latz, E., Bowie, A. G., Fitzgerald, K. A. & Xiao, T. S. (2012) Structures of the HIN domain:DNA complexes reveal ligand binding and activation mechanisms of the AIM2 inflammasome and IFI16 receptor, *Immunity.* **36**, 561-71.

14. Yuan, S. & Akey, C. W. (2013) Apoptosome structure, assembly, and procaspase activation, *Structure.* **21**, 501-15.

15. Jin, T., Perry, A., Smith, P. T., Jiang, J. & Xiao, T. S. (2013) Structure of the AIM2 pyrin domain provides insights into the mechanisms of AIM2 autoinhibition and inflammasome assembly, *The Journal of biological chemistry*.

16. Liepinsh, E., Barbals, R., Dahl, E., Sharipo, A., Staub, E. & Otting, G. (2003) The death-domain fold of the ASC PYRIN domain, presenting a basis for PYRIN/PYRIN recognition, *Journal of molecular biology.* **332**, 1155-63.

17. de Alba, E. (2009) Structure and interdomain dynamics of apoptosis-associated speck-like protein containing a CARD (ASC), *The Journal of biological chemistry.* **284**, 32932-41.

18. Hiller, S., Kohl, A., Fiorito, F., Herrmann, T., Wider, G., Tschopp, J., Grutter, M. G. & Wuthrich, K. (2003) NMR structure of the apoptosis- and inflammation-related NALP1 pyrin domain, *Structure (Camb).* **11**, 1199-205.

19. Natarajan, A., Ghose, R. & Hill, J. M. (2006) Structure and dynamics of ASC2, a pyrin domain-only protein that regulates inflammatory signaling, *The Journal of biological chemistry.* **281**, 31863-75.

20. Su, M. Y., Kuo, C. I., Chang, C. F. & Chang, C. I. (2013) Three-dimensional structure of human NLRP10/PYNOD pyrin domain reveals a homotypic interaction site distinct from its mouse homologue, *PLoS One.* **8**, e67843.

21. Pinheiro, A. S., Proell, M., Eibl, C., Page, R., Schwarzenbacher, R. & Peti, W. (2010) Three-dimensional structure of the NLRP7 pyrin domain: insight into pyrin-pyrin-mediated effector domain signaling in innate immunity, *The Journal of biological chemistry.* **285**, 27402-10.

22. Pinheiro, A. S., Eibl, C., Ekman-Vural, Z., Schwarzenbacher, R. & Peti, W. (2011) The NLRP12 pyrin domain: structure, dynamics, and functional insights, *Journal of molecular biology.* **413**, 790-803.

23. Bae, J. Y. & Park, H. H. (2011) Crystal structure of NALP3 protein pyrin domain (PYD) and its implications in inflammasome assembly, *The Journal of biological chemistry.* **286**, 39528-36.

24. Ferrao, R. & Wu, H. (2012) Helical assembly in the death domain (DD) superfamily, *Current opinion in structural biology.* **22**, 241-7.

25. Park, H. H., Logette, E., Rauser, S., Cuenin, S., Walz, T., Tschopp, J. & Wu, H. (2007) Death domain assembly mechanism revealed by crystal structure of the oligomeric PIDDosome core complex, *Cell.* **128**, 533–546.

26. Lin, S. C., Lo, Y. C. & Wu, H. (2010) Helical assembly in the MyD88-IRAK4-IRAK2 complex in TLR/IL-1R signalling, *Nature.* **465**, 885-890.

27. Siegel, R. M., Martin, D. A., Zheng, L., Ng, S. Y., Bertin, J., Cohen, J. & Lenardo, M. J. (1998) Death-effector filaments: novel cytoplasmic structures that recruit caspases and trigger apoptosis, *The Journal of cell biology.* **141**, 1243-53.

28. Yuan, R. T., Young, S., Liang, J., Schmid, M. C., Mielgo, A. & Stupack, D. G. (2012) Caspase-8 isoform 6 promotes death effector filament formation independent of microtubules, *Apoptosis.* **17**, 229-35.

29. Qiao, Q., Yang, C., Zheng, C., Fontan, L., David, L., Yu, X., Bracken, C., Rosen, M., Melnick, A., Egelman, E. H. & Wu, H. (2013) Structural Architecture of the CARMA1/Bcl10/MALT1 Signalosome: Nucleation-Induced Filamentous Assembly, *Mol Cell.* **51**, 766-79.

30. Yang, J. K., Wang, L., Zheng, L., Wan, F., Ahmed, M., Lenardo, M. J. & Wu, H. (2005) Crystal structure of MC159 reveals molecular mechanism of DISC assembly and FLIP inhibition, *Mol Cell.* **20**, 939-49.

31. Li, F. Y., Jeffrey, P. D., Yu, J. W. & Shi, Y. (2006) Crystal structure of a viral FLIP: insights into FLIP-mediated inhibition of death receptor signaling, *The Journal of biological chemistry.* **281**, 2960-8.

32. Vagin, A. A. & Teplyakov, A. (1997) MOLREP: an Automated Program for Molecular Replacement, *J Appl Cryst.* **30**, 1022.

33. Emsley, P. & Cowtan, K. (2004) Coot: model-building tools for molecular graphics, *Acta crystallographica Section D, Biological crystallography.* **60**, 2126-32.

34. Adams, P. D., Afonine, P. V., Bunkoczi, G., Chen, V. B., Davis, I. W., Echols, N., Headd, J. J., Hung, L. W., Kapral, G. J., Grosse-Kunstleve, R. W., McCoy, A. J., Moriarty, N. W., Oeffner, R., Read, R. J., Richardson, D. C., Richardson, J. S., Terwilliger, T. C. & Zwart, P. H. (2010) PHENIX: a comprehensive Python-based system for macromolecular structure solution, *Acta crystallographica Section D, Biological crystallography.* **66**, 213-21.

35. Moriya, M., Taniguchi, S., Wu, P., Liepinsh, E., Otting, G. & Sagara, J. (2005) Role of charged and hydrophobic residues in the oligomerization of the PYRIN domain of ASC, *Biochemistry.* **44**, 575-83.

36. Vajjhala, P. R., Mirams, R. E. & Hill, J. M. (2012) Multiple binding sites on the pyrin domain of ASC protein allow self-association and interaction with NLRP3 protein, *The Journal of biological chemistry.* **287**, 41732-43.

37. Clackson, T. & Wells, J. A. (1995) A hot spot of binding energy in a hormone-receptor interface, *Science.* **267**, 383-6.

38. Holm, L. & Sander, C. (1995) Dali: a network tool for protein structure comparison, *Trends Biochem Sci.* **20**, 478-480.

39. Kersse, K., Verspurten, J., Vanden Berghe, T. & Vandenabeele, P. (2011) The death-fold superfamily of homotypic interaction motifs, *Trends Biochem Sci.* **36**, 541-52.

Chapter Four

Plasticity in PYD Assembly Revealed by Cryo-EM Structure of the PYD Filament of AIM2

Citation. This chapter has been assembled with minor modifications from the final version of the following published manuscript:

Cell Discovery **1**, 15013 (2015)

Plasticity in PYD assembly revealed by cryo-EM structure of the PYD filament of AIM2

Alvin Lu[1,2,†], Yang Li[1,2,†], Qian Yin[1,2], Jianbin Ruan[1,2], Xiong Yu[3], Edward Egelman[3] and Hao Wu[1,2,*]

[1]Department of Biological Chemistry and Molecular Pharmacology, Harvard Medical School, Boston, MA 02115

[2]Program in Cellular and Molecular Medicine, Boston Children's Hospital, Boston, MA 02115

[3]Department of Biochemistry and Molecular Genetics, University of Virginia, Charlottesville, VA 22908

[†]Co-first authors

*Corresponding author

Contributions. This study was the collaborative effort of several members of the Wu lab, as well as Dr. Yu, who collected the cryo-EM data, and Professor Egelman, who performed helical reconstruction. I would like to thank them for their contribution in various aspects of this project, as listed in the following description.

Professor Wu and I conceived this study, and together with Dr. Li, drafted the manuscript. All the authors of the published manuscript contributed to the revision of this

manuscript. I cloned, expressed, and purified the samples for helical reconstruction and biochemical studies, as shown in Figures 4.1B and 4.2C-D. I also performed initial screening of filament quality by negative-stain EM. Dr. Yu collected the cryo-electron micrographs as shown in Figure 4.1C, and Professor Egelman performed helical reconstruction to generate the cryo-EM density map as shown in Figure 4.1D-G. Dr. Li performed structure building and refinement, as shown in Figures 4.1D-G and 4.2A. Dr. Li and I together analyzed the structure, as shown in Figures 4.2B, 4.3, and 4.4. Dr. Ruan collected and analyzed the negative-stain electron micrographs of $AIM2^{HIN}$ with dsDNA, as shown in Figure 4.5A-D. Dr. Yin analyzed and generated the model of $AIM2^{HIN}$/dsDNA model as shown in Figure 4.5E-F. Professor Wu and I summarized the data presented in this study and proposed the model depicted in Figure 6.

Supplemental materials. Four supplemental figures (Figures S4.1-4.4), a Supplemental Movie (Movie S4.1), Materials and Methods, and Supplemental References can be found in Appendix III.

Abstract

Absent in melanoma 2 (AIM2) is an essential cytosolic double-stranded DNA receptor that assembles with the adaptor, apoptosis-associated speck-like protein containing a caspase recruitment domain (ASC), and caspase-1 to form the AIM2 inflammasome, which leads to proteolytic maturation of cytokines and pyroptotic cell death. AIM2 contains an N-terminal Pyrin domain (PYD) that interacts with ASC through PYD/PYD interactions and nucleates ASC^{PYD} filament formation. To elucidate the molecular basis of AIM2-induced ASC^{PYD} polymerization, we generated $AIM2^{PYD}$ filaments fused to green fluorescent protein (GFP) and determined its cryo-electron microscopic (cryo-EM) structure. The map showed distinct definition of helices, allowing fitting of the crystal structure. Surprisingly, the GFP-$AIM2^{PYD}$ filament is a 1-start helix with helical parameters distinct from those of the 3-start ASC^{PYD} filament. However, despite the apparent symmetry difference, helical net and detailed interface analyses reveal minimal changes in subunit packing. GFP-$AIM2^{PYD}$ nucleated ASC^{PYD} filament formation in comparable efficiency as untagged $AIM2^{PYD}$, suggesting assembly plasticity in both $AIM2^{PYD}$ and ASC^{PYD}. The DNA-binding domain of AIM2 is able to form AIM2/DNA filaments, within which the $AIM2^{PYD}$ is brought into proximity to template ASC^{PYD} filament assembly. Because ASC is able to interact with many PYD-containing receptors for the formation of inflammasomes, the observed structural plasticity may be critically important for this versatility in the PYD/PYD interactions.

Introduction

Inflammasomes are cytosolic supramolecular complexes assembled in response to pathogen- and other damage-associated stimuli to activate pro-inflammatory responses through the maturation of interleukin 1β (IL-1β) and interleukin 18 (IL-18) [1]. They typically consist of a sensor component, after which the names of the inflammasomes are given, an adaptor component, and an effector component such as caspase-1 and possibly caspase-11 (mouse), caspase-4 (human) and caspase-5 (human) [2]. Upon stimulation, the sensor components may

convert from an auto-inhibited state and oligomerize to recruit an adaptor protein, which in turn recruit and activate the caspase zymogens through auto-proteolysis. Activated caspases then target the pro-forms of IL-1β and IL-18 for proteolytic maturation. These pro-inflammatory cytokines are released outside of the cell to trigger the downstream interleukin receptor pathway and induce the transcription of pro-inflammatory genes. Another possible outcome of inflammasome activation is pyroptotic cell death, which strengthens the inflammatory response.

Canonical inflammasome sensors can be classified into two classes, nucleotide-binding and oligomerization domain (NOD)-like receptors (NLRs) and absent in *melanoma* 2 (AIM2)-like receptors (ALRs). NLRs contain an N-terminal domain such as caspase recruitment domain (CARD), Pyrin domain (PYD), or baculoviral IAP repeat (BIR) domain for the recruitment of other inflammasome components. Taking the initials from these recruitment domains, NLRs are named as NLRP, NLRC and NLRB (also known as NAIP), respectively. NLRs also consist of a central NOD, and a C-terminal leucine-rich repeat (LRR) domain [3]. NLR activation is thought to be the result of binding of the LRR domain to stimuli or partner molecules leading to a conformational change in the NOD-LRR region, which releases the auto-inhibition of the NOD domain. In the human genome, there are 22 putative NLRs [4].

ALRs comprise an N-terminal PYD and C-terminal HIN domains for dsDNA recognition. The two known ALRs, AIM2 and IFI16, are able to assemble functional inflammasomes [5, 6]. AIM2 was first identified in a proteomic-genomic screen that linked its role to IL-1β maturation [7-10]. The orthopoxvirus vaccinia virus and the beta-herpesvirus murine cytomegalovirus (MCMV) have been shown to directly trigger AIM2 activation in murine macrophages [6, 7]. While AIM2 assemble inflammasomes in the cytosol, IFI16 has been shown to shuttle between the cytosol and the nucleus, and functions as a nuclear pathogen sensor in Kaposi's sarcoma-associated herpesvirus (KSHV)-infected endothelial cells [5].

The HIN domain is composed of tandem oligonucleotide/oligosaccharide binding (OB) folds, as first revealed from the crystal structures of IFI16 HIN-A and HIN-B [11]. Each OB fold

conforms to the canonical OB domain architecture, which is a closed β-barrel with five twisted β-strands and an α-helix connecting the β3 and β4 strands [12]. Later, the structures for human AIM2 HIN and IFI16 HIN-B in complex with dsDNA were determined to show that the OB lobes and the in-between linker directly bind the dsDNA phosphate backbone [13]. Crystal structure of the mouse AIM2 in complex with dsDNA and related mutagenesis experiments showed the similar binding mode [14, 15]. The HIN domain of AIM2 was also shown to interact directly with the PYD of AIM2 to exert an auto-inhibition effect, and binding to dsDNA liberates PYD for inflammasome assembly [13, 16, 17]. The mouse ALR p202 without the N-terminal PYD is a specific inhibitor of AIM2 inflammasome activation [18].

ALRs and PYD-containing NLRPs recruit the bipartite adaptor ASC that contains both an N-terminal PYD and a C-terminal CARD. While the PYD of ASC (ASC^{PYD}) interacts with PYD in ALR and NLR sensors, the CARD of ASC (ASC^{CARD}) recruits CARD-containing effectors such as caspase-1. We and others have shown that ASC^{PYD} forms filamentous structures [17, 19, 20] with helical symmetry, which has emerged to be a conserved assembly mechanism for proteins in the death domain (DD) superfamily that includes both PYD and CARD [21]. The helical assembly involves three conserved types of asymmetric interactions. We found that ASC-dependent inflammasomes are formed through two-step nucleated polymerization [17]. For the AIM2 inflammasome, upon binding of the HIN domain to dsDNA, the $AIM2^{PYD}$ domain clusters to nucleate the formation of ASC^{PYD} filaments. Analogously, activated NLRPs contain clustered PYD that templates ASC^{PYD} filament polymerization. We determined the ASC^{PYD} filament structure through cryo-electron microscopy (cryo-EM) at a resolution of ~3.8 Å, which revealed the detailed molecular interactions between the ASC^{PYD} subunits [17]. Subsequently, the resulting clustered ASC^{CARD} domain outside of the central ASC^{PYD} filament acts to nucleate caspase-1 filaments through CARD/CARD interactions, leading to signal amplification from the AIM2 sensor, to the ASC adaptor and then to caspase-1 [17]. The formation of caspase-1 filaments initiates proximity-driven dimerization and auto-proteolysis, and hence caspase

activation.

How AIM2^{PYD} nucleates ASC^{PYD} filament formation is currently unclear. To resolve this question, we used cryo-EM to determine the filament structure of a GFP fused AIM2^{PYD}. The structure surprisingly revealed that the GFP-AIM2^{PYD} filament is a 1-start helix with helical parameters distinct from those of the 3-start ASC^{PYD} filament. However, despite the apparent symmetry difference, helical net and detailed interface analyses both showed minimal changes in subunit packing. The apparent ability of PYDs to adopt different helical symmetries indicates plasticity in their assembly. All ALRs and most members of the large NLR family have a PYD, which use the single adapter ASC for inflammasome formation. Because the ALR and NLR PYDs do not share high levels of sequence identity, there might be slight differences in their intrinsic filament forming symmetry, and yet all these PYDs have to interact with the same ASC^{PYD}. In this context, the observed plasticity must be important for this versatility in the PYD/PYD interactions. It is remarkable that a significant difference in helical symmetry only results in small local changes in subunit packing in these PYD filaments. Given the similar mode of interactions utilized for the entire death domain superfamily, the plasticity in symmetry and interaction may be general characteristics of the superfamily and likely underlie the wide evolutionary success of these domains in innate immunity.

Results

Structure determination of the GFP-AIM2^{PYD} filament by cryo-EM

AIM2 contains an N-terminal PYD and a C-terminal dsDNA-binding HIN domain (**Figure 4.1A**). The AIM2^{PYD} could be over-expressed in *E. coli* but was hardly soluble, likely due to formation of extensive filamentous aggregates. To overcome this problem, we first tried to express AIM2^{PYD} as a His-MBP fusion in a monomeric form, followed by removal of the His-MBP tag to allow AIM2^{PYD} polymerization. However, cleaved, untagged AIM2^{PYD} immediately

bundled (**Figure S4.1A**) and quickly precipitated. We therefore reasoned that a non-cleavable tag which still allows filament formation is required for obtaining soluble filaments for cryo-EM studies. We fused AIM2^{PYD} to an N-terminal non-cleavable His-GFP tag with only a two-residue linker (**Figure 4.1A**). GFP-AIM2^{PYD} was purified by Ni-NTA affinity chromatography (**Figure S4.1B**) followed by size exclusion chromatography (SEC). It formed soluble aggregates as shown by elution in the void fractions of SEC (**Figure 4.1B**). Cryo-EM images showed that GFP-AIM2^{PYD} mostly formed filaments of limited lengths, from ~200 nm to ~1 μm (**Figure 4.1C**), which likely contributed to their solubility. The diameter of the filaments is ~20 nm.

Starting with an averaged power spectrum (**Figure 4.1D**), it was evident that many different helical symmetries were possible [22]. The correct helical symmetry was determined by trial-and-error, searching for a solution using the iterative helical real space reconstruction (IHRSR) method [23] that yielded recognizable secondary structures [24]. The symmetry that was found, a rise of 6.0 Å and a right-handed rotation of 138.9° per subunit, generated a reconstruction where the PYD was seen to be largely α-helical. The AIM2^{PYD} subunit in the filament shows a six-helix bundle structure that is highly similar to the AIM2^{PYD} crystal structures in isolation [16, 19]. Thus, the reconstruction was taken to be correct. The calculated power spectrum from the reconstructed volume is consistent with the observed averaged power spectrum (**Figure 4.1D**).

In the filament, AIM2^{PYD} forms the core while the GFP tag packs tightly outside (**Figure 4.1E**, **Movie S4.1**). The AIM2^{PYD} crystal structure (PDB ID: 3VD8) can be readily fit into the central density (**Figure 4.1F**). Only minor adjustments of the individual helices were necessary, which were performed using the real space fitting tool in Coot [25]. In contrast to the clearly visible secondary structures in the AIM2^{PYD} region, the individual GFP density is essentially an ellipsoid that matches the size of a GFP molecule (PDB ID: 1EMA). We rotated the GFP molecule along its longer axis to place its C-terminus close to the N-terminus of AIM2^{PYD} to which the GFP is fused (**Figure 4.1G**). There is no clear density from the C-terminus of GFP to

Figure 4.1. Cryo-EM structure determination of the GFP-AIM2^{PYD} filament.

A. Domain organizations of AIM2 and its PYD construct used for cryo-EM.

B. Gel filtration profile of the GFP-AIM2^{PYD} protein on a Superdex 200 10/300 size-exclusion column, showing elution at the void position.

C. A representative cryo-EM image.

D. Comparison of experimental and simulated power spectra. A few indexed layer lines are labeled.

E. Helical reconstructed cryo-EM map in two orientations of the GFP-AIM2^{PYD} filament fitted with atomic models of GFP (green, PDB ID: 1EMA) and partially refined AIM2^{PYD} (magenta, starting PDB ID: 3VD8).

F. A side view of the cryo-EM map of the AIM2^{PYD} filament core with the GFP region removed, fitted with the partially refined AIM2^{PYD} model. A single subunit is shown in blue.

G. A close-up view of one GFP-AIM2^{PYD} subunit, showing that the C-terminus of GFP is close to the N-terminus of AIM2^{PYD}.

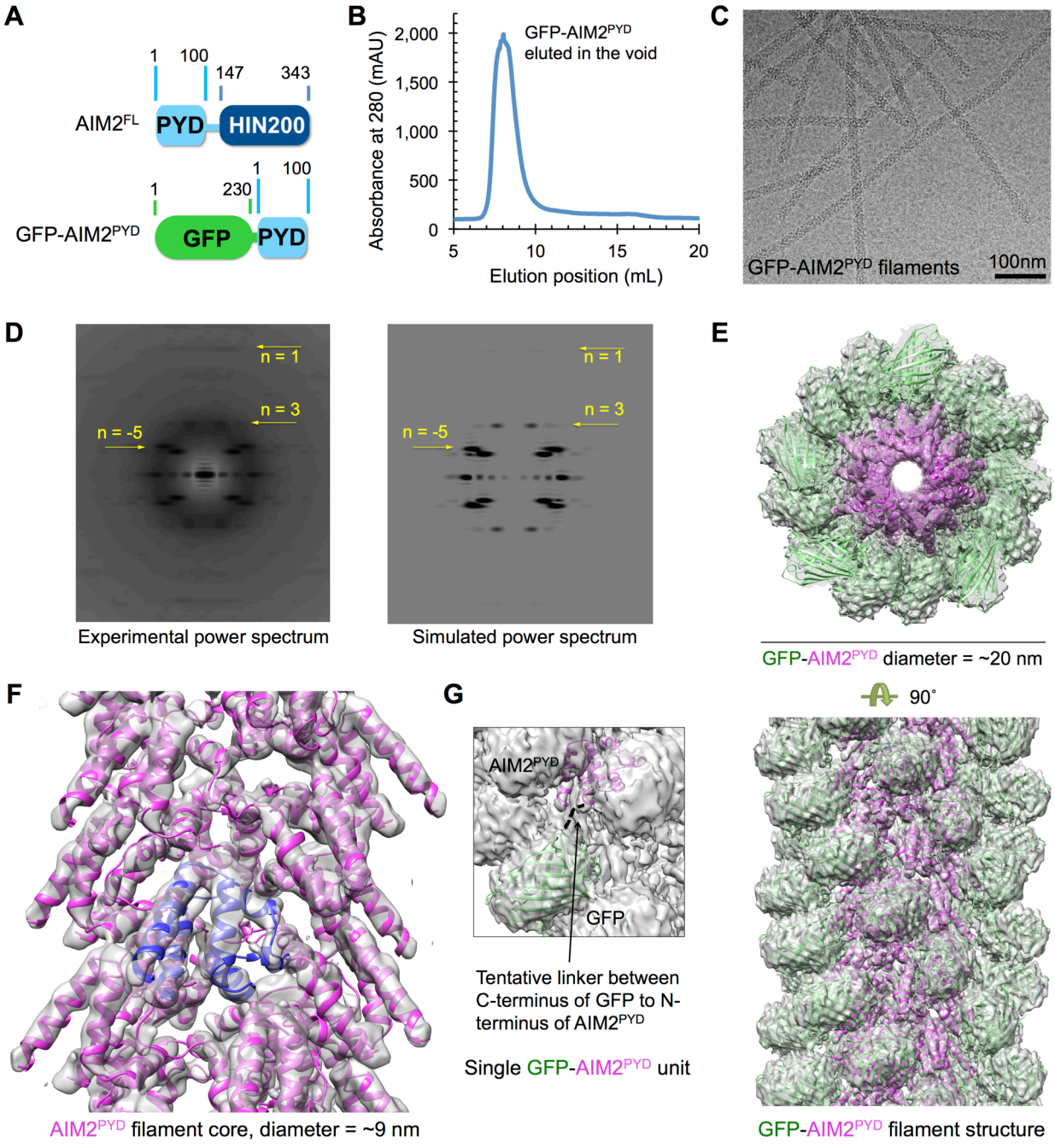

Figure 4.1 (Continued)

the fused N-terminus of AIM2^{PYD}, suggesting flexibility between these two entities and explaining the much poorer resolution for the GFP tag. Estimation of resolutions by Fourier shell correlation (FSC) between the densities and the fitted molecules gave ~5.0 Å for the AIM2^{PYD} region (**Figure S4.1C**) and ~11 Å if GFP is included (**Figure S4.1D**). The GFP density alone is probably resolved to only ~20 Å. The partially ordered GFP contributes to the doubling of the diameter of these filaments compared to the AIM2^{PYD} core, which is ~9 nm. Consistent with the estimation by FSC, the calculated model volumes filtered to 5 or 6 Å resolution showed features comparable to the experimental volume (**Figure S4.1E**).

The GFP-AIM2^{PYD} filament has a helical symmetry different from the ASC^{PYD} filament but retains the ability to nucleate ASC^{PYD} filament formation

Given that AIM2^{PYD} and the full-length AIM2 in complex with dsDNA nucleate ASC^{PYD} filament formation [17], it was surprising that the AIM2^{PYD} filament has an apparent, almost completely different symmetry from our previously determined ASC^{PYD} filament structure. The latter is a 3-start helical assembly with C3 point group symmetry, having a right-handed rotation of ~52.9˚ and an axial rise 13.9 Å per subunit along each of the 3-start strands [17]. Because the total axial rise per subunit of the ASC^{PYD} filament would be 13.9/3 = 4.6 Å, in comparison to 6.0 Å for the GFP-AIM2^{PYD} filament, within the same filament length, there would be (6.0-4.6)/6.0 = 23% fewer subunits in the GFP-AIM2^{PYD} filament. Since the diameters of the ASC^{PYD} filament and the GFP-AIM2^{PYD} core are almost identical, at ~ 9 nm, it dictates that the latter is packed significantly less densely, likely due to the fused GFP. If the modeled GFP-AIM2^{PYD} subunits are placed into a filament based on the ASC^{PYD} filament symmetry, one GFP molecule would be in a clash with an adjacent GFP molecule (**Figure 4.2A**). This exercise suggests that to accommodate the fairly large GFP tag (MW = 28.1 kDa), the intrinsic AIM2^{PYD} helical filament may have been altered, resulting in less dense packing. The altered packing may have also destabilized the AIM2^{PYD} filament so that the GFP-AIM2^{PYD} filaments are shorter and more

soluble than the AIM2^{PYD} filament without a large fusion tag, allowing *in vitro* reconstitution and cryo-EM structure determination.

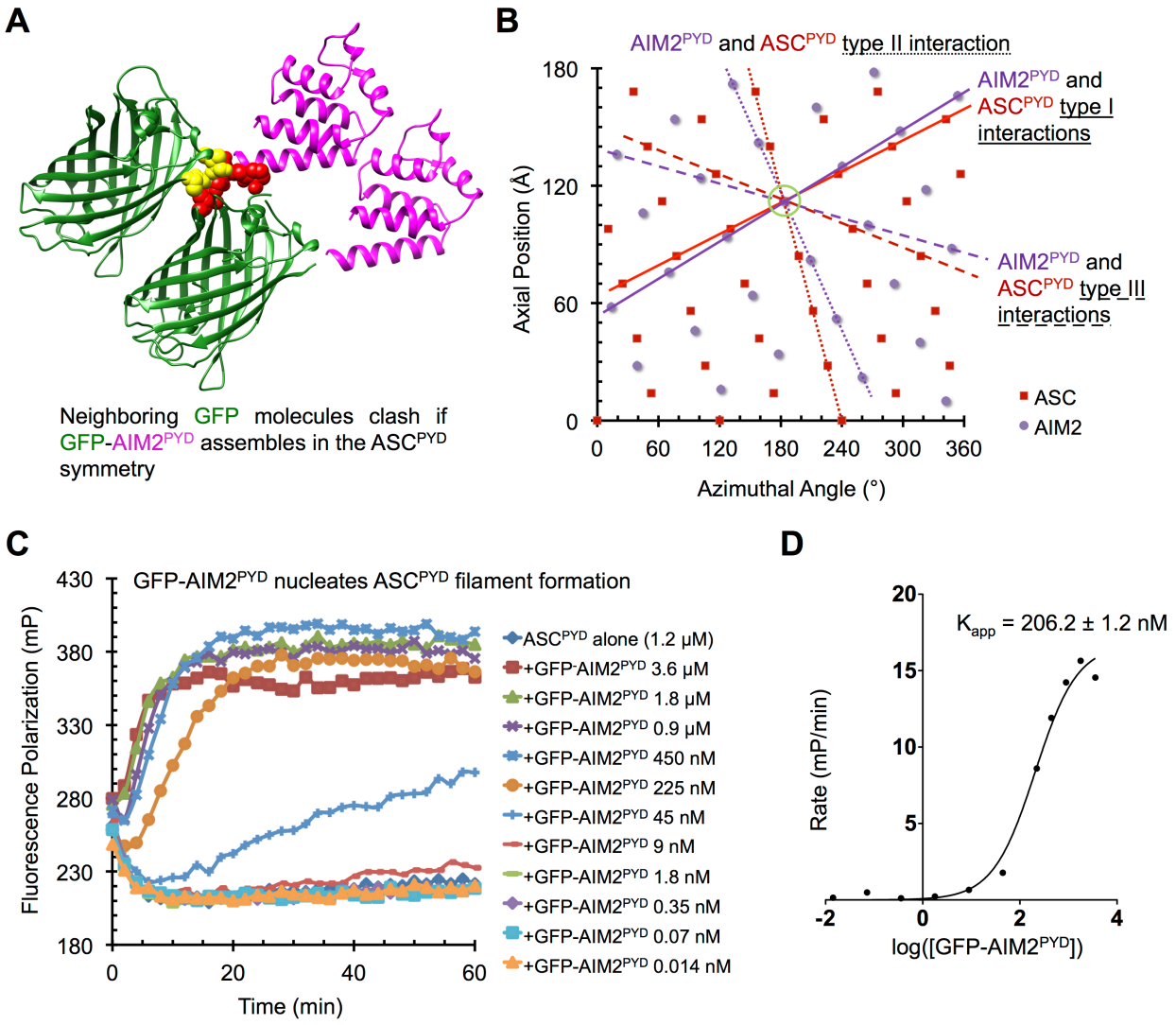

Figure 4.2. The GFP-AIM2^{PYD} filament has a different helical symmetry from ASC^{PYD} but retains the ability to nucleate ASC^{PYD} filaments.

A. GFP-AIM2^{PYD} subunits in the ASC^{PYD} filament symmetry, showing steric clash in the GFP region (red and yellow).

B. Superimposed helical net plots of GFP-AIM2^{PYD} and ASC^{PYD} filaments showing similar orientations of the interactions despite the different symmetries.

C. Potentiation of ASC^{PYD} filament formation by GFP-AIM2^{PYD}.

D. Initial slopes (mP/min) of (**C**) were plotted against the log of the concentrations (nM) of the added GFP-AIM2^{PYD} to extrapolate an apparent dissociation constant (K_{app}) of the GFP-AIM2^{PYD}/ASC^{PYD} interaction.

We asked if the difference in symmetry led to completely different packing in the AIM2^{PYD} and the ASC^{PYD} filaments. To compare the packing arrangements, we generated helical net plots for both filaments, in which each dot represents the location of a subunit, and aligned them using a subunit near the center as a reference (**Figure 4.2B**, **Figure S4.2A-B**). The aligned helical net plots showed that despite the completely different symmetry, the locations of subunits in AIM2 and ASC filaments are quite similar, suggesting comparable spatial packing arrangements. In the ASC^{PYD} filament structure, three types of interactions mediate the assembly, with type I interactions for intrastrand contacts, and type II and III interactions for interstrand contacts. In the AIM2^{PYD} filament structure, the lines connecting these interactions differ minimally from those in the ASC^{PYD} filament, further corroborating the similar subunit packing contacts in both filaments.

The altered symmetry and tweaked packing in the GFP-AIM2^{PYD} filament suggest plasticity in the assembly and tolerance to variability. Our previous cryo-EM reconstruction of the ASC^{PYD} filament has already indicated intrinsic variability, as shown by an approximate Gaussian distribution of rotation angles per subunit from 51.5 to 54.5 ° [17]. However, the magnitude of change observed here between the GFP-AIM2^{PYD} filament structure and the ASC^{PYD} filament structure is much larger. To determine whether GFP-AIM2^{PYD} filaments with altered symmetry could still nucleate ASC^{PYD} filaments, we utilized a fluorescence polarization (FP) assay to monitor enhanced polarization due to filament formation and reduced motion. ASC^{PYD} was expressed as a fusion to the large solubility tag MBP (MBP-ASC^{PYD}), which allowed purification of monomeric MBP-ASC^{PYD} on a size exclusion column. The protein was then labeled by the Alexa568 fluorophore via an engineered C-terminal Cys residue using maleimide chemistry. The polymerization reaction was initiated by addition of the TEV protease to remove the MBP tag, upon which ASC^{PYD} spontaneously formed filaments at a very slow rate. Inclusion of sub-stoichiometric amounts of GFP-AIM2^{PYD} greatly enhanced the rate of ASC^{PYD} polymerization (**Figure 4.2C**). The apparent affinity for GFP-AIM2^{PYD} to promote ASC^{PYD}

filament formation was determined to be ~0.21 μM by plotting the initial rates of ASC^{PYD} filament formation against the concentrations of the GFP-$AIM2^{PYD}$ seeds (**Figure 4.2D**). We also repeated a polymerization experiment published in our previous study [17] in which MBP-$AIM2^{PYD}$ and labeled MBP-ASC^{PYD} were used to assess nucleation of ASC^{PYD} filament formation by $AIM2^{PYD}$ upon removal of MBP from both proteins (**Figure S4.2C**).

We quantified the rate of potentiation of ASC^{PYD} filament formation, which gave an apparent $AIM2^{PYD}$/ASC^{PYD} affinity of ~0.68 μM (**Figure S4.2C**). Therefore, the GFP tag did not interfere with the nucleating capability of $AIM2^{PYD}$, suggesting that ASC^{PYD} filament could also be assembled by symmetry similar to that of the GFP-$AIM2^{PYD}$. The apparent slightly weaker interaction between untagged $AIM2^{PYD}$ and ASC^{PYD} may be due to instability of untagged $AIM2^{PYD}$. This tolerance of symmetry and packing variability in both $AIM2^{PYD}$ and ASC^{PYD} is notable and may contribute to the versatility of the death domain superfamily in mediating oligomerization.

To determine if this concept of variability tolerance is more general, we produced mCherry-tagged $NLRP6^{PYD}$ and confirmed its ability to nucleate ASC^{PYD} filaments (**Figure S4.2D**). The N-terminal mCherry tag is of similar size as the GFP-tag, and did not disrupt the interaction between $NLRP6^{PYD}$ and ASC^{PYD}. The measured apparent affinity for mCherry-$NLRP6^{PYD}$ to promote ASC^{PYD} filament formation is ~0.09 μM (**Figure S4.2D**).

Structural features of the $AIM2^{PYD}$ filament

We used the structure refinement program Phenix and electron scattering factors to assess the agreement between the atomic model of the filament and the cryo-EM density. The cropped cryo-EM density corresponding to 15 $AIM2^{PYD}$ subunits that has been adjusted in real space was placed into a crystallographic unit cell and back transformed to obtain the structure factors. Upon rigid body refinement at 5.0 Å resolution with fixed B-factors for each subunit, the R and R_{free} factors were 0.43 and 0.47, respectively. Almost all the main chain density was

observed, with part of the α2-α3 loop visible at a lower contour level (**Figure 4.3A**). Compared to the crystal structure of the monomeric MBP-fused wild-type AIM2^{PYD}, the filament conformation of AIM2^{PYD} shows main differences at this region (**Figure 4.3B**), suggesting that AIM2^{PYD} possesses intrinsic flexibility to allow for subtle conformational changes during oligomerization. The F27G mutant of AIM2^{PYD} also exhibits differences with the wild-type AIM2^{PYD} at this region (**Figure 4.3B**).

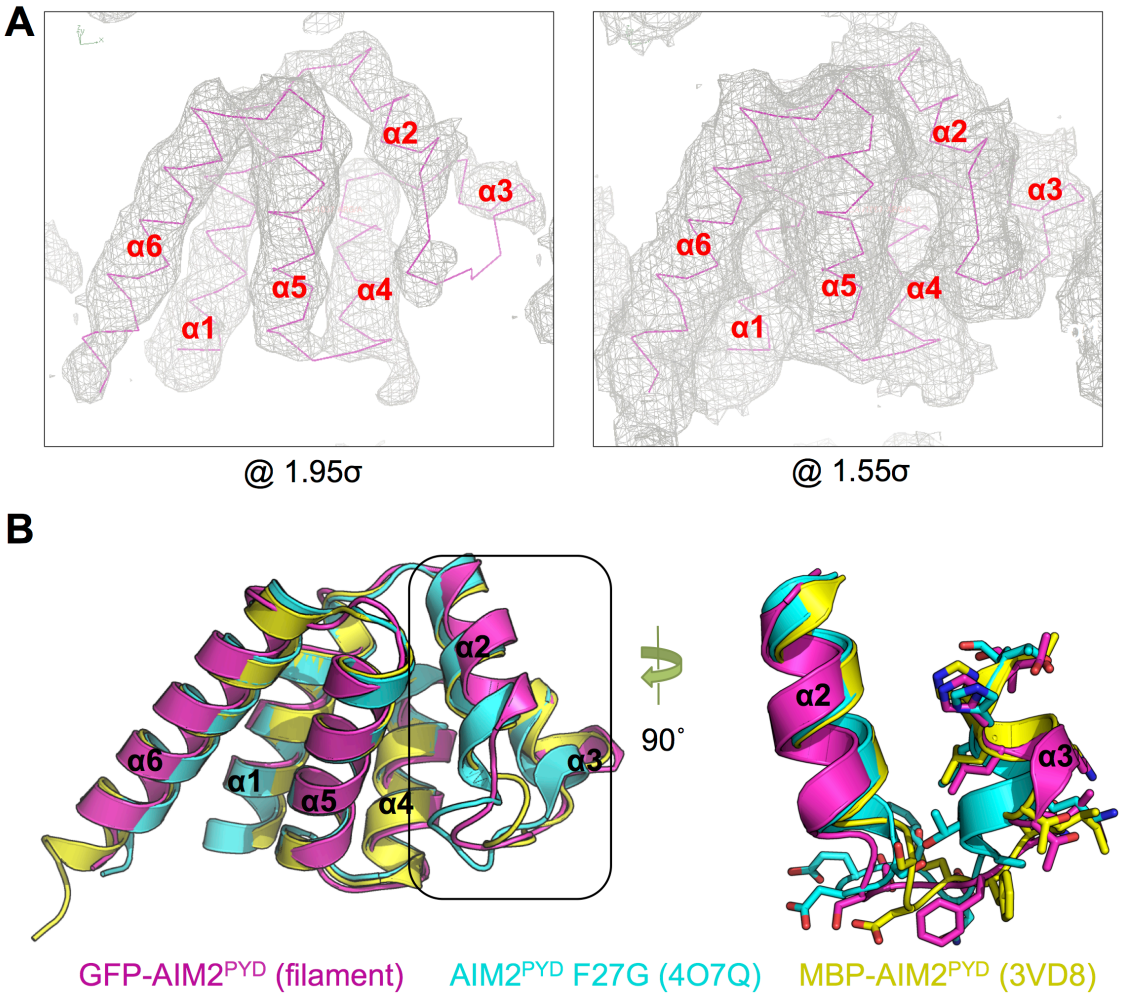

Figure 4.3. Conformational changes between AIM2^{PYD} structures in isolation and in the filament.

A. Cryo-EM maps at two contour levels showing that despite the lower density in the α2-α3 region, the trajectory of the loop is defined.

B. Comparison of AIM2^{PYD} structure in the filament (magenta) with that in isolation (yellow), and with the F27G mutant (cyan).

The AIM2^{PYD} filament core has an outer diameter of ~9 nm and an inner hole with a diameter of ~2 nm (**Figure 4.4A**), similar to dimensions of the ASC^{PYD} filament [17]. The filament has an apparent bumpy surface, in contrast to the smoother surface of the ASC^{PYD} filament due to the longer C-terminal helix in AIM2^{PYD}. While the GFP-AIM2^{PYD} filament has the symmetry of a right-handed 1-start helix with 138.9° rotation and 6.0 Å axial rise per subunit, the sequential intrastrand subunits do not make direct molecular contact (**Figure 4.4B**). If we sequentially label the AIM2^{PYD} subunits according to the helical operator, the three types of interactions that dictate helical assembly in the AIM2^{PYD} filament will be between the first (i) and the fourth (i+3) subunits for the type I contacts, between the first (i) and the sixth (i+5) subunits for the type II contacts, and between the first (i) and the third (i+2) for the type III contacts (**Figure 4.4B**). Orientation and position of the three types of interactions are conserved between the AIM2^{PYD} and ASC^{PYD} structures (**Figure 4.4C-H**). Similar to ASC^{PYD}, the type I interaction is the most extensive of the three types. Notably, type I interfaces in AIM2^{PYD} are mainly hydrophobic in nature, while that in ASC^{PYD} is formed by salt bridges between positively and negatively charged residues.

In the AIM2^{PYD} filament structure, the type I interaction is formed by Ser3, Lys6, Leu10, Leu11, Asp15, and Ile46 of the α1/α4 helixes of one subunit and Arg24, Phe27, Phe28, and Asp31 of the α2-α3 region of an adjacent subunit (**Figure 4.4C**). Gln54 and Asn55 at the end of the α4 helix interact with Asn73, Tyr74, and Leu76 in between α5-α6 of an adjacent molecule to form the type II contacts (**Figure 4.4D**). Type III interactions are mediated by Gly38 and Lys39 of α3 and the nearby Asp15, Asn16, and Ile17 residues of another subunit (**Figure 4.4E**). To determine whether there are significant changes in these interfacial contacts if the AIM2^{PYD} filament assumes the ASC^{PYD} filament symmetry, we superimposed the AIM2^{PYD} subunit structure onto the respective type I, II and III interaction pairs in the ASC^{PYD} filament (**Figure 4.4F-G**). This exercise shows that the orientation and position of the three types of interactions are highly similar with either the observed GFP-AIM2^{PYD} filament symmetry or the ASC^{PYD}

Figure 4.4. Detailed interactions in the AIM2^{PYD} filament structure.

A. A surface representation of the AIM2^{PYD} filament with subunits individually colored by chain in a rainbow gradient.

B. A schematic diagram of the helical assembly of the AIM2^{PYD} filament. The red dotted arrow indicates the direction of the helical spiral as defined by a rise of 6.0 Å and a right-handed rotation of 138.9° per subunit. It should be noted that adjacent subunits i and i+1 do not directly contact. The right panel shows locations of the three types of asymmetric interactions.

C-E. Detailed interactions in the type I (**C**), type II (**D**), and type III (**E**) interfaces. Subunit colors match those in the schematic (**B**).

F-H. AIM2^{PYD} subunits were aligned onto the ASC^{PYD} filament, and the thus generated AIM2/AIM2 interactions are shown in the same color schemes as in **C-E**. Grays ribbons show the corresponding AIM2/AIM2 interactions in the GFP-AIM2^{PYD} filament structure.

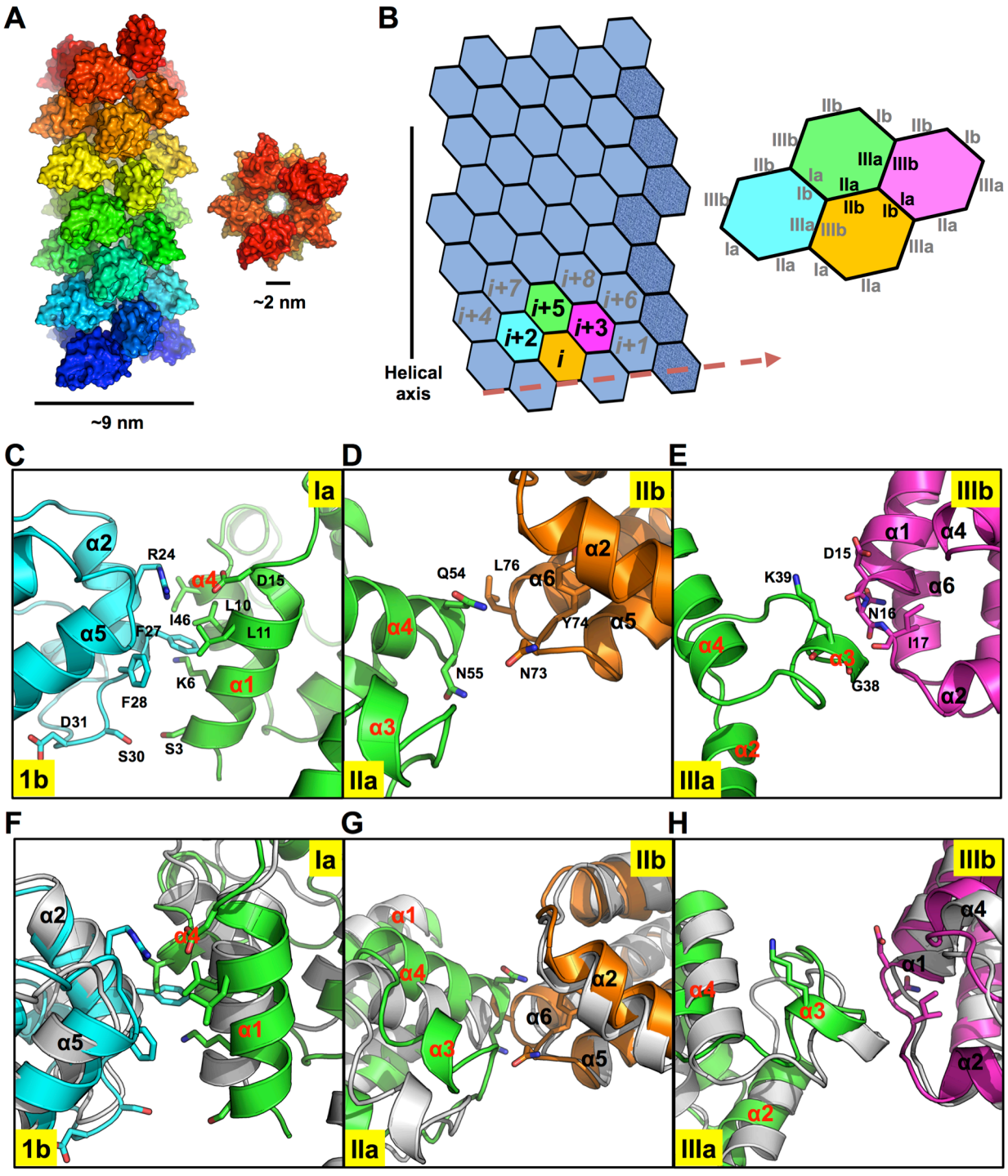

Figure 4.4 (Continued)

filament symmetry (**Figure 4.4F-G**). There are minimal adjustments of the interfacial contacts, further supporting the helical net analysis (**Figure 4.2B**). Like the ASC^{PYD} filament, the type I interaction in the $AIM2^{PYD}$ filament is the most extensive of the three types of interactions. However, the type I interface in the $AIM2^{PYD}$ filament is mainly hydrophobic in nature, while that in the ASC^{PYD} filament is formed by salt bridges between positively and negatively charged residues.

$AIM2^{HIN}$ forms a filamentous complex with dsDNA

Previous studies have shown that full-length IFI16, an ALR, cooperatively assembles filaments with dsDNAs [26]. IFI16 has an N-terminal PYD followed by two HIN domains. Cooperative binding and filament formation require the PYD, while the individual HIN domains or the two HIN domains together did not show significant dsDNA binding at the close to physiological salt concentration used in the assays [26], consistent with the observed salt-dependence of IFI16 HIN in interaction with dsDNAs [13]. We asked if AIM2 also forms filaments with dsDNAs. It has been shown previously that AIM2 activation in cells is dependent on transfected dsDNA length [10, 13]. Under one assay condition, in human PBMCs, an 80-bp dsDNA, in comparison with dsDNA of 50-bp or less, was a better inducer of cell death [13]. Under another condition, in mouse BMDMs, a 44-bp dsDNA could kill mouse BMDMs when transfected at high concentrations (≥20ug) and even longer dsDNA, 100-500 bp in lengths, induced progressively more killing when transfected [10]. In contrast, shorter dsDNA did not efficiently induce cell death [10].

Because a 44-bp or 80-bp dsDNA is too short to be visualized reliably using negative staining electron microscopy, we used polymerase chain reaction to generate longer dsDNA fragments. We first tried $AIM2^{HIN}$, which was expressed as a His-Sumo-fusion with the tag cleaved off during purification. In contrast to IFI16, we found that $AIM2^{HIN}$ is able to form filaments with 300 bp, 1 kbp and 2 kbp gel purified dsDNA fragments under close to

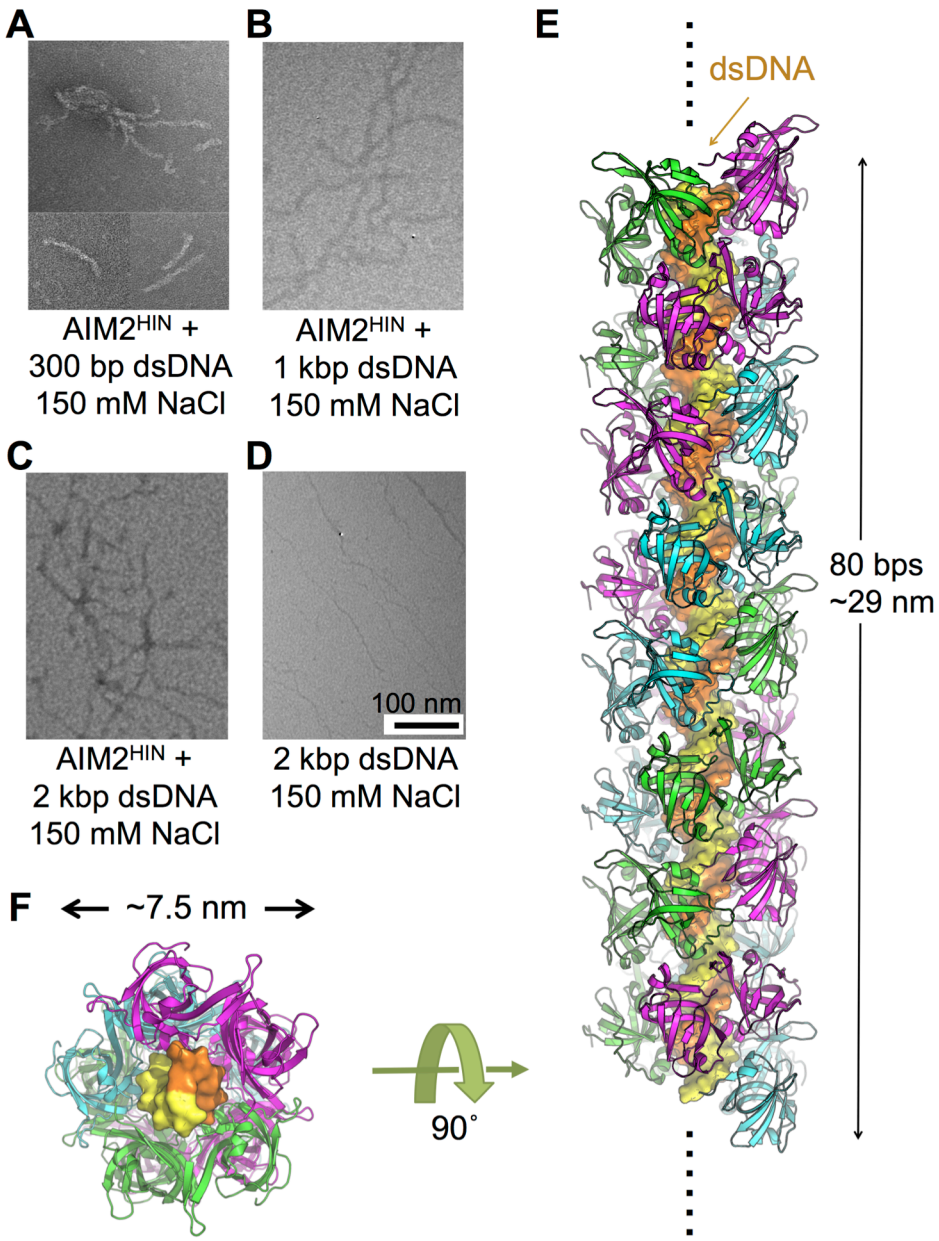

Figure 4.5. AIM2^{HIN} forms filaments with dsDNA.

A-C. EM images of negatively stained AIM2^{HIN} (0.05 mg/ml) mixed with 300 bp dsDNA (**A**), 1 kbp dsDNA (**B**), and 2 kbp dsDNA (**C**). The molar ratios of AIM2^{HIN} to dsDNA are 60:1, 200:1 and 400:1, respectively, for 300 bp, 1 kbp and 2 kbp dsDNAs.

D. An EM image of negatively stained 2 kbp dsDNA.

E-F. A model of the AIM2^{HIN}/ dsDNA filament, shown along (**E**) and down (**F**) the helical axis. The dsDNA is illustrated as a surface diagram with the two helical strands colored in orange and yellow, respectively. AIM2^{HIN} domains are colored in green, cyan, and magenta.

physiological pH and salt concentrations (**Figure 4.5A-C**). The diameter of the $AIM2^{HIN}$/dsDNA filaments is measured to be close to but less than 10 nm. The dsDNA alone control showed much thinner threads (**Figure 4.5D**), confirming that the filaments in the presence of $AIM2^{HIN}$ are the $AIM2^{HIN}$/dsDNA complexes. With increasing dsDNA lengths, the $AIM2^{HIN}$/dsDNA filaments become curvier and more convoluted. The calculated linear lengths for 300 bp, 1 kbp and 2 kbp dsDNA fragments are 108 nm, 360 nm and 720 nm, respectively.

Formation of a full-length AIM2/dsDNA complex is hampered by the insolubility of full-length AIM2 when overexpressed in *E. coli* as a His-Sumo-tagged protein, in contrast to the soluble nature of full-length IFI16 [26]. This difference is most likely due to the PYD domain, as the PYD of IFI16 is much less aggregated than $AIM2^{PYD}$ when expressed alone (**Figure S4.3**). Unlike AIM2 that was shown to be auto-inhibited [13, 16], IFI16 appears to exist in an extended conformation in the absence of dsDNA stimulation [11]. Overexpression of full-length AIM2 may relieve this auto-inhibition and therefore lead to aggregation and insolubility. To overcome this difficulty, we expressed AIM2 as a fusion to the large solubility tag His-MBP to inhibit self-oligomerization. Purified monomeric His-MBP-AIM2 was then mixed with dsDNA, to which the TEV protease was added to remove the His-MBP tag. In contrast to formation of IFI16/dsDNA filaments [26], full-length AIM2 precipitated upon encountering dsDNA and TEV, suggesting large-scale aggregation upon activation. This apparent higher aggregation tendency of AIM2 than IFI16 may correlate with the need to sense small amounts of dsDNA in the cytosol.

To model the $AIM2^{HIN}$/dsDNA filament complex, we used an existing human $AIM2^{HIN}$/dsDNA complex crystal structure (PDB ID: 3RN5) [13]. We used 80 bps as one optimal dsDNA length for AIM2 activation, and first aligned one complex to an ideal 80-bp B-form dsDNA by superimposing the dsDNA molecules. We reasoned that a most plausible way to model a dsDNA coated with $AIM2^{HIN}$ is by aligning the same complex to different segments in the 80 bp dsDNA. We attempted different DNA step sizes. Remarkably, a step size of every 4 bps generated an $AIM2^{HIN}$/dsDNA filament complex in which the $AIM2^{HIN}$ molecules are in

extensive contact, but with no significant steric clash (**Figure 4.5E**). In contrast, a step of 3 bps or 5 bps generated $AIM2^{HIN}$ molecules on dsDNA that are either in severe clash or with no contact, suggesting that the 4 bps step is optimal. Assuming that each HIN domain occupies 4 bps, the molar ratio of protein to DNA-binding sites would have been 0.8:1 for all the EM experiments (**Figure 4.5A-C**). In this predicted $AIM2^{HIN}$/dsDNA filament model, each HIN molecule is in contact with 6 adjacent HINs. The diameter of the model with dsDNA decorated by an outer layer of $AIM2^{HIN}$ molecules is ~7.5 nm (**Figure 4.5F**), consistent with the EM observation. The ~50-residue linker between the PYD and HIN domains may allow the PYDs to swing around the dsDNA core to form a short helical assembly of $AIM2^{PYD}$ molecules for interacting with and nucleating ASC^{PYD} filaments.

Discussion

AIM2 is a critically important cytoplasmic dsDNA sensor that activates caspase-1 to provide host defense against pathogens. Here we present the cryo-EM structure of the PYD domain of AIM2 in its activated, filamentous form. The cryo-EM images and the low-resolution power spectrum are both dominated by the GFP tag, which is poorly ordered. Despite this difficulty, we were able to obtain a map of the central $AIM2^{PYD}$ filament at a resolution that is clearly interpretable.

We and others have previously identified numerous $AIM2^{PYD}$ mutants that are defective in their abilities to self-aggregate and/or to nucleate ASC^{PYD} filaments [16, 17, 19] (**Figure S4.4A**). Strikingly, when these mutation sites are mapped onto the $AIM2^{PYD}$ structure, almost all mutations are exactly at the observed interfacial contacts in the $AIM2^{PYD}$ filament structure (**Figure S4.4B**). The type I interface $AIM2^{PYD}$ mutants F27G, F27L, L10A/L11A, and D31K did not self-aggregate [19]. F27G, L10A/L11A, and R24E mutations abolished the ability of $AIM2^{PYD}$ to nucleate ASC^{PYD} filaments [17]. The type II mutant, Y74R, lost the ability to nucleate ASC^{PYD} [17]. Located at the edge of both type Ia and type IIIb interfaces, D15R was also completely

defective. Type III mutants, G38E and K39E, appeared to have partially lost their ability to interact with ASC^{PYD}. The quadruple mutant D19A/E20A/E21A/D23A near the type Ib interface also showed compromised ability to interact with ASC^{PYD} [16]. These existing mutational data confirmed the validity of the observed interactions in the AIM2^{PYD} filament. Human AIM2^{PYD} and IFI16^{PYD} share 31 % sequence identity. Sequence alignment of IFI16^{PYD} to AIM2^{PYD} shows that the interfacial residues important for AIM2^{PYD} filament formation and function are mostly conserved in IFI16^{PYD} (**Figure S4.4C**), suggesting that IFI16^{PYD} uses a similar assembly mechanism for initiating inflammasome formation and signaling.

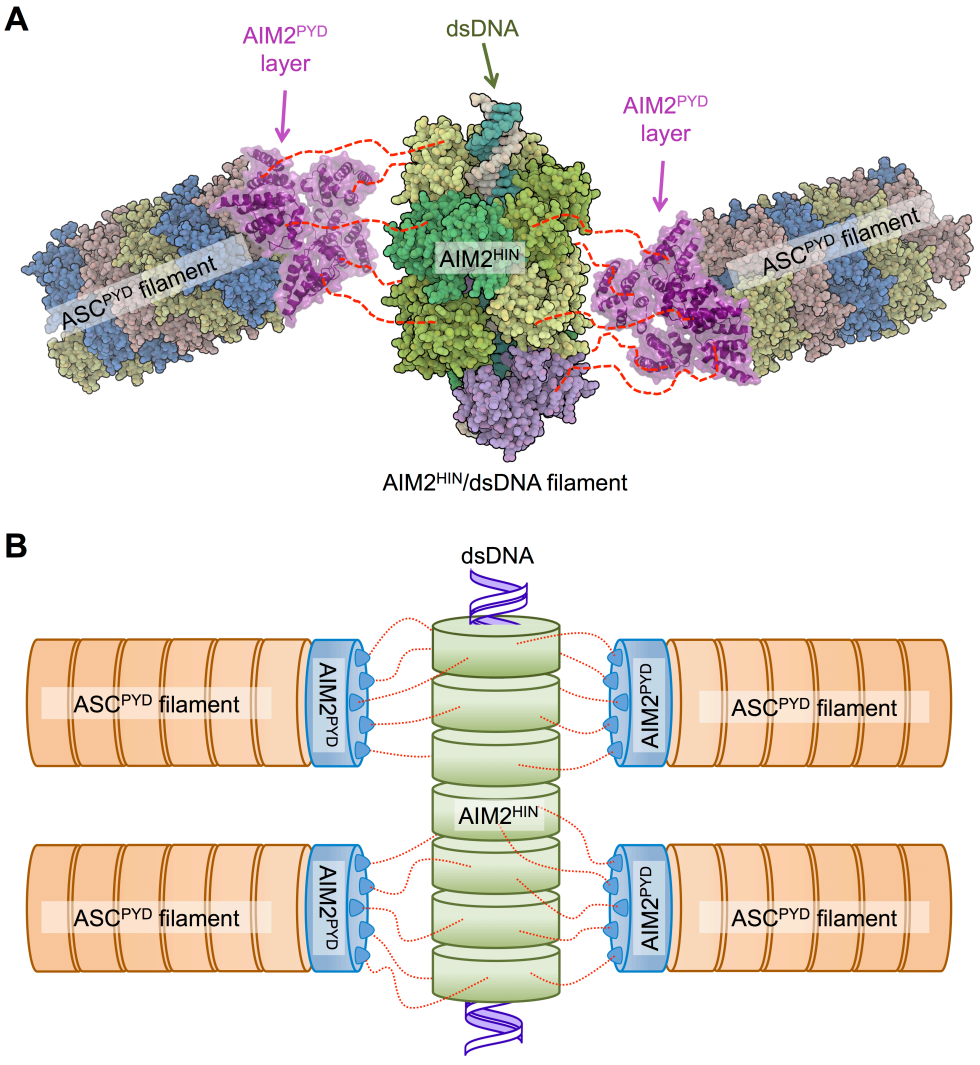

Figure 4.6. A conceptual model of ASC^{PYD} nucleation by the AIM2/dsDNA complex, shown as an atomic model (**A**) and a schematic (**B**)

Our structure and the EM analysis on AIM2^{HIN}/dsDNA interaction provide a conceptual model in dsDNA-induced AIM2 activation (**Figure 4.6A-B**). First, cytoplasmic dsDNA of sufficient length from invading pathogens will recruit AIM2 through HIN/dsDNA interactions. Wrapping of the HIN domain around the dsDNA not only overcomes AIM2 auto-inhibition, but also brings the attached AIM2^{PYD} into proximity to form helical assemblies. There is a fairly long, ~50 residue linker between the PYD and the HIN, which can be as long as ~19 nm when completely stretched. Since the AIM2^{HIN}/dsDNA filament is ~7.5 nm in diameter, it takes ~12 nm to reach from one side of the filament to the opposing side, shorter than what the linker could theoretically reach. The AIM2^{PYD} filaments in turn act as the platforms to nucleate ASC^{PYD} filaments, resulting in inflammasome assembly and caspase-1 activation. How exactly AIM2^{PYD} assembles on the side of dsDNA still remains to be illustrated. The linker between HIN and PYD, albeit long, may impose a spatial restrain on the length of the PYD helical assembly, and promote formation of short local AIM2^{PYD} filaments. Despite the likelihood of being short, the helical nature of AIM2^{PYD} on the side of dsDNA is supported by previous mutagenesis data and cellular activation assays, which showed the importance of the interfacial residues in the AIM2^{PYD} helical assembly for activation of the AIM2 inflammasome [1] [17] [19].

The significantly less dense packing in the GFP-AIM2^{PYD} filament relative to the ASC^{PYD} filament suggests plasticity in PYD filament assembly. Although the GFP fused to AIM2^{PYD} via a mere two-residue linker most likely affected the symmetry of the filament, the much longer PYD-HIN linker would allow AIM2^{PYD} to assume its natural helical symmetry without being perturbed by the attached HIN domain. The HIN domain is of similar size to GFP. One possibility is that AIM2^{PYD} does have a natural symmetry identical to ASC^{PYD}. Another possibility is that AIM2^{PYD} forms filaments using a symmetry somewhat different from ASC^{PYD}. Conversely, ASC^{PYD} may be able to assume different symmetries depending which binding partner it interacts with. It is worth noting that ALRs and most members of the large NLR family have a PYD, which use the single adapter ASC for inflammasome formation. The minimal changes in subunit interactions in

an altered symmetry should allow successful PYD/PYD interaction despite the symmetry difference. Therefore, the observed structural plasticity must be important for the functional requirement of ASC in interacting with multiple PYDs in inflammasome formation. In addition, the $AIM2^{PYD}$ filament structure reported here represents the first case in which adaptability has been observed for the entire superfamily of death domain-containing proteins.

Many other filamentous systems have also been known to possess variability. For example, tubulin can be polymerized *in vitro* to form microtubules with 9 to 15 or more protofilaments, and transitions between these can be seen in the same microtubule [27]. F-actin possesses considerably variable and randomized twist but a relatively constant rise per subunit [28]. The death domain fold superfamily represents the most abundant domain in innate immune signaling pathways. These domains are versatile modules for both homotypic and heterotypic molecular interactions that afford the scaffolds for their respective signaling complexes. Given the conserved mode of interactions in the death domain fold superfamily, this observed plasticity in PYD assembly may contribute to the adaptability of the death domain fold in general, and likely explain the omnipresence of these domains in innate immune pathways.

References

1. Lamkanfi, M. & Dixit, V. M. (2014) Mechanisms and functions of inflammasomes, *Cell.* **157**, 1013-22.

2. Lu, A. & Wu, H. (2014) Structural mechanisms of inflammasome assembly, *FEBS J.* **282**, 435-44.

3. Hu, Z., Yan, C., Liu, P., Huang, Z., Ma, R., Zhang, C., Wang, R., Zhang, Y., Martinon, F., Miao, D., Deng, H., Wang, J., Chang, J. & Chai, J. (2013) Crystal structure of NLRC4 reveals its autoinhibition mechanism, *Science.* **341**, 172-5.

4. Ting, J. P., Lovering, R. C., Alnemri, E. S., Bertin, J., Boss, J. M., Davis, B. K., Flavell, R. A., Girardin, S. E., Godzik, A., Harton, J. A., Hoffman, H. M., Hugot, J. P., Inohara, N., Mackenzie, A., Maltais, L. J., Nunez, G., Ogura, Y., Otten, L. A., Philpott, D., Reed, J. C., Reith, W., Schreiber, S., Steimle, V. & Ward, P. A. (2008) The NLR gene family: a standard nomenclature, *Immunity.* **28**, 285-7.

5. Kerur, N., Veettil, M. V., Sharma-Walia, N., Bottero, V., Sadagopan, S., Otageri, P. & Chandran, B. (2011) IFI16 acts as a nuclear pathogen sensor to induce the inflammasome in response to Kaposi Sarcoma-associated herpesvirus infection, *Cell Host Microbe.* **9**, 363-75.

6. Rathinam, V. A., Jiang, Z., Waggoner, S. N., Sharma, S., Cole, L. E., Waggoner, L., Vanaja, S. K., Monks, B. G., Ganesan, S., Latz, E., Hornung, V., Vogel, S. N., Szomolanyi-Tsuda, E. & Fitzgerald, K. A. (2010) The AIM2 inflammasome is essential for host defense against cytosolic bacteria and DNA viruses, *Nat Immunol.* **11**, 395-402.

7. Hornung, V., Ablasser, A., Charrel-Dennis, M., Bauernfeind, F., Horvath, G., Caffrey, D. R., Latz, E. & Fitzgerald, K. A. (2009) AIM2 recognizes cytosolic dsDNA and forms a caspase-1-activating inflammasome with ASC, *Nature.* **458**, 514-8.

8. Fernandes-Alnemri, T., Yu, J. W., Datta, P., Wu, J. & Alnemri, E. S. (2009) AIM2 activates the inflammasome and cell death in response to cytoplasmic DNA, *Nature.* **458**, 509-13.

9. Burckstummer, T., Baumann, C., Bluml, S., Dixit, E., Durnberger, G., Jahn, H., Planyavsky, M., Bilban, M., Colinge, J., Bennett, K. L. & Superti-Furga, G. (2009) An orthogonal proteomic-genomic screen identifies AIM2 as a cytoplasmic DNA sensor for the inflammasome, *Nat Immunol.* **10**, 266-72.

10. Roberts, T. L., Idris, A., Dunn, J. A., Kelly, G. M., Burnton, C. M., Hodgson, S., Hardy, L. L., Garceau, V., Sweet, M. J., Ross, I. L., Hume, D. A. & Stacey, K. J. (2009) HIN-200 proteins regulate caspase activation in response to foreign cytoplasmic DNA, *Science.* **323**, 1057-60.

11. Liao, J. C., Lam, R., Brazda, V., Duan, S., Ravichandran, M., Ma, J., Xiao, T., Tempel, W., Zuo, X., Wang, Y. X., Chirgadze, N. Y. & Arrowsmith, C. H. (2011) Interferon-Inducible Protein 16: Insight into the Interaction with Tumor Suppressor p53, *Structure.* **19**, 418-29.

12. Theobald, D. L., Mitton-Fry, R. M. & Wuttke, D. S. (2003) Nucleic acid recognition by OB-fold proteins, *Annual Review of Biophysics and Biomolecular Structure.* **32**, 115-133.

13. Jin, T., Perry, A., Jiang, J., Smith, P., Curry, J. A., Unterholzner, L., Jiang, Z., Horvath, G., Rathinam, V. A., Johnstone, R. W., Hornung, V., Latz, E., Bowie, A. G., Fitzgerald, K. A. & Xiao,

T. S. (2012) Structures of the HIN domain:DNA complexes reveal ligand binding and activation mechanisms of the AIM2 inflammasome and IFI16 receptor, *Immunity.* **36**, 561-71.

14. Ru, H., Ni, X., Zhao, L., Crowley, C., Ding, W., Hung, L. W., Shaw, N., Cheng, G. & Liu, Z. J. (2013) Structural basis for termination of AIM2-mediated signaling by p202, *Cell Res.* **23**, 855-8.

15. Sung, M. W., Watts, T. & Li, P. (2012) Crystallographic characterization of mouse AIM2 HIN-200 domain bound to a 15 bp and an 18 bp double-stranded DNA, *Acta Crystallogr Sect F Struct Biol Cryst Commun.* **68**, 1081-4.

16. Jin, T., Perry, A., Smith, P., Jiang, J. & Xiao, T. S. (2013) Structure of the absent in melanoma 2 (AIM2) pyrin domain provides insights into the mechanisms of AIM2 autoinhibition and inflammasome assembly, *The Journal of biological chemistry.* **288**, 13225-35.

17. Lu, A., Magupalli, V. G., Ruan, J., Yin, Q., Atianand, M. K., Vos, M. R., Schroder, G. F., Fitzgerald, K. A., Wu, H. & Egelman, E. H. (2014) Unified polymerization mechanism for the assembly of ASC-dependent inflammasomes, *Cell.* **156**, 1193-206.

18. Yin, Q., Sester, D. P., Tian, Y., Hsiao, Y. S., Lu, A., Cridland, J. A., Sagulenko, V., Thygesen, S. J., Choubey, D., Hornung, V., Walz, T., Stacey, K. J. & Wu, H. (2013) Molecular mechanism for p202-mediated specific inhibition of AIM2 inflammasome activation, *Cell reports.* **4**, 327-39.

19. Lu, A., Kabaleeswaran, V., Fu, T., Magupalli, V. G. & Wu, H. (2014) Crystal structure of the F27G AIM2 PYD mutant and similarities of its self-association to DED/DED interactions, *Journal of molecular biology.* **426**, 1420-7.

20. Cai, X., Chen, J., Xu, H., Liu, S., Jiang, Q. X., Halfmann, R. & Chen, Z. J. (2014) Prion-like polymerization underlies signal transduction in antiviral immune defense and inflammasome activation, *Cell.* **156**, 1207-22.

21. Ferrao, R. & Wu, H. (2012) Helical assembly in the death domain (DD) superfamily, *Current opinion in structural biology.* **22**, 241-7.

22. Egelman, E. H. (2010) Reconstruction of helical filaments and tubes, *Methods Enzymol.* **482**, 167-83.

23. Egelman, E. H. (2000) A robust algorithm for the reconstruction of helical filaments using single-particle methods, *Ultramicroscopy.* **85**, 225-34.

24. Egelman, E. H. (2014) Ambiguities in helical reconstruction, *eLife.* **3**.

25. Emsley, P. & Cowtan, K. (2004) Coot: model-building tools for molecular graphics, *Acta crystallographica Section D, Biological crystallography.* **60**, 2126-32.

26. Morrone, S. R., Wang, T., Constantoulakis, L. M., Hooy, R. M., Delannoy, M. J. & Sohn, J. (2014) Cooperative assembly of IFI16 filaments on dsDNA provides insights into host defense strategy, *Proceedings of the National Academy of Sciences of the United States of America.* **111**, E62-71.

27. Chretien, D., Metoz, F., Verde, F., Karsenti, E. & Wade, R. H. (1992) Lattice defects in microtubules: protofilament numbers vary within individual microtubules, *The Journal of cell biology.* **117**, 1031-40.

28. Egelman, E. H., Francis, N. & DeRosier, D. J. (1982) F-actin is a helix with a random variable twist, *Nature.* **298**, 131-5.

Chapter Five

A VHH Defines Mechanism of Inflammasome Assembly

Citation. This chapter has been assembled with minor modifications from the following manuscript in press:

Journal of Experimental Medicine (accepted manuscript)

A Single Domain Antibody Fragment that Recognizes the Adaptor ASC Defines the Role of ASC Domains in Inflammasome Assembly

Florian I. Schmidt,[1,†] Alvin Lu,[2,3,†] Jeff W. Chen,[1] Jianbin Ruan,[2,3] Catherine Tang,[2,3] Hao Wu,[2,3,*] and Hidde L. Ploegh[1,4*]

[1]Whitehead Institute for Biomedical Research, Cambridge, MA 02142

[2]Department of Biological Chemistry and Molecular Pharmacology, Harvard Medical School, Boston, MA 02115

[3]Program in Cellular and Molecular Medicine, Boston Children's Hospital, Boston, MA 02115

[4]Department of Biology, Massachusetts Institute of Technology, Cambridge, MA 02139

[†]Co-first authors

*Co-corresponding authors

Contributions. This study was a collaborative effort of the Ploegh lab and the Wu lab. I am grateful for such close collaboration. I would like to specially thank Dr. Schmidt for his wonderful personalities and great curiosity on the subject matter, as well as his persistence and passion in research. I am also honored to receive guidance and supervision from Professor Ploegh and Professor Wu as brilliant scientists and mentors.

Dr. Schmidt, Mr. Chen, and I performed the majority of the experiments. Dr. Schmidt and Mr. Chen were responsible for generating the nanobody library, identification and cloning of the ASC-binding nanobody, and all subsequent cellular experiments. I provided the purified ASC proteins for immunization, performed crystallization of the nanobody alone and in complex with mutant ASC^{CARD}, structure determination and analysis, and *in vitro* experiments with purified proteins, including size-exclusion and fluorescence polarization assays. Ms. Tang is a summer student who provided help with the initial crystallization screen of the nanobody alone crystal. Dr. Ruan identified and provided the monomeric ASC^{CARD} mutant construct that eventually yielded the complex crystal. Dr. Schmidt, Professor Ploegh, Professor Wu, and I conceived the study and together wrote the manuscript.

Supplemental materials. One Supplemental Table (Table S5.1), Materials and Methods, and Supplemental References can be found in Appendix IV.

Abstract

Myeloid cells assemble inflammasomes in response to infection or cell damage: cytosolic sensors activate pro-caspase-1 mostly indirectly, via the adaptor ASC and/or NLRC4. This leads to secretion of pro-inflammatory cytokines and pyroptosis. To explore complex formation under physiological conditions, we generated an alpaca single domain antibody, VHH_{ASC}, which specifically recognizes the CARD of human ASC via its type II interface. VHH_{ASC} not only impairs ASC^{CARD} interactions *in vitro,* but also inhibits inflammasome activation in response to NLRP3, AIM2, and NAIP triggers when expressed in living cells, highlighting a role of ASC in all three types of inflammasomes. VHH_{ASC} leaves the Pyrin domain of ASC functional and stabilizes a filamentous intermediate of inflammasome activation. Incorporation of VHH_{ASC}-EGFP into these structures allowed the visualization of endogenous ASC^{PYD} filaments for the first time. These data revealed that cross-linking of ASC^{PYD} filaments via ASC^{CARD} mediates the assembly of ASC foci.

Introduction

The innate immune system employs a diverse set of genetically encoded sensors to detect evidence of infection or cell damage in the different compartments of the cell. Cytosolic sensors and adaptors in myeloid cells integrate information to initiate a strong inflammatory response through the assembly of macromolecular protein complexes termed inflammasomes. Activation of inflammasomes culminates in the activation of caspase-1, which enables the maturation and release of pro-inflammatory cytokines such as IL-1β and IL-18, as well as cell death by pyroptosis [1].

The sensor involved determines the specificity of the inflammasome and is typically a member of two conserved protein families: NLRs (nucleotide-binding domain [NBD]- and leucine-rich repeat [LRR]-containing proteins), and ALRs (AIM2-like receptors). These sensors recruit caspase recruitment domain (CARD)-containing pro-caspase-1 indirectly via the

interposition of CARD-containing ASC or NLRC4. A diverse array of cell damage signals, including potassium efflux, activates NLRP3 inflammasomes through an unknown mechanism, which then recruit ASC via interactions between Pyrin domains (PYD). AIM2 directly binds to DNA with its HIN domain and also engages ASC via PYD/PYD interactions. Human NAIP/NLRC4 inflammasomes contain two NLRs: NAIP, which senses components of bacterial type III secretion systems or flagellin, and NLRC4, which – once activated by NAIP – can recruit pro-caspase-1, although ASC enhances cytokine secretion in mice [2-5]. Recent cryo-electron microscopy experiments showed that a single NAIP family member primes the self-propagated incorporation of 9-11 NLRC4 monomers into a wheel-like structure [6, 7].

Local polymerization of PYD and CARD domains, both members of the death domain family, determines activation thresholds and amplifies the signal [8-10]. In their active conformation, the PYD of NLRP3 and AIM2 nucleate the formation of ASC^{PYD} filaments, while locally concentrated ASC^{CARD} induces the polymerization of pro-caspase-1 CARD. These structures have so far been shown only *in vitro*, or in cells that (over)express single domains of ASC fused to fluorescent proteins. Their presence therefore demands verification at physiological protein levels in the relevant cell type [11]. Local concentration of pro-caspase-1 autocatalytically activates caspase-1, which in turn catalyzes the conversion of pro-cytokines into mature IL-1β and IL-18.

While we understand some of the molecular triggers and consequences of inflammasome activation, the underlying cell biology and the molecular interactions involved require further study. Reconstitution of defined steps of inflammasome activation *in vitro* or in unrelated control cells has been quite informative, but –short of their deletion, mutation or overexpression– inflammasome components in their physiological context are challenging targets for molecular perturbations. Many inflammasome components are prone to oligomerization or self-activate when artificially overexpressed [12, 13], emphasizing the need

for functional studies in relevant cell types with endogenous expression levels of inflammasome components.

Antibodies are valuable tools to perturb protein function *in vitro*, or when microinjected into living cells [14, 15]. Nonetheless, application of full-sized antibodies has been limited to a few select cases mostly because of technical challenges. These include the time required to generate and produce antibodies, their bulk, inefficient delivery methods, and sensitivity to the reducing environment of the cytosol.

The description of heavy chain-only antibodies in camelids was a landmark discovery [16, 17], that provided a means to overcome many of these challenges. Heavy chain-only antibodies are comprised of two identical heavy chains and recognize their antigen by means of a single, heavy chain variable domain (VHH). These VHH segments can be expressed as stand-alone fragments and exhibit affinities comparable to conventional antibodies. VHHs are stable in the absence of disulfide-bonds or glycosylation and can thus be easily produced in bacteria, or expressed in the cytosol of eukaryotic cells [18]. VHHs have been used as crystallization chaperones owing to their ability to stabilize protein structures [19, 20]. VHHs can induce or selectively bind distinct conformations, mask epitopes required for protein-protein interactions, or inhibit enzymatic activities [21-23]. VHHs directed against distinct inflammasome components would thus constitute excellent tools to probe and molecularly analyze distinct steps of inflammasome activation.

We generated a VHH against the adaptor protein ASC to elucidate the molecular mechanism that allows ASC to greatly amplify the signaling response to many inflammasome triggers. We show that VHH_{ASC} specifically blocks CARD/CARD interactions of ASC^{CARD} and thus inhibits inflammasome activation by agents that trigger NLRP3, AIM2, and NAIP in human macrophage-like cells. By stabilizing an intermediate step of inflammasome activation, VHH_{ASC} confirmed the formation of ASC^{PYD} filaments at endogenous ASC levels, and revealed that ASC

CARD mediates the coalescence of multiple ASC filaments into a single macromolecular ASC focus per cell.

Results

Identification of an Alpaca VHH Specific for Human ASC

To study molecular interactions in the course of inflammasome activation, we generated alpaca VHHs that bind to the adaptor protein ASC. We immunized an alpaca with purified ASC, produced as a fusion with maltose binding protein (MBP). After five booster immunizations, we isolated peripheral blood lymphocytes from the immunized alpaca, extracted RNA, prepared cDNA, and amplified VHH-coding sequences by PCR. The amplified VHH cDNAs were cloned into a phagemid vector to yield a plasmid library that encodes the VHH repertoire contained in the collected lymphocytes.

To identify VHHs that bind human ASC, we immobilized MBP-ASC to beads and selected ASC-binding phage by two rounds of phage display. Since we observed a strong immune response to MBP, we depleted phages displaying MBP-binding VHHs prior to each round of phage display and panned for ASC-specific VHHs in the presence of excess soluble MBP. 96 VHH clones obtained by this procedure were sequenced and tested by ELISA for binding to the fusion protein MBP-ASC and MBP alone. Of these 96 clones, 43 bound to MBP-ASC, but not to MBP, and all encoded the same VHH, VHH_{ASC}.

To test its specificity, we expressed VHH_{ASC} in *Escherichia coli (E. coli)* and coupled the purified VHH_{ASC} to cyanogen bromide-activated Sepharose beads. Incubation of this VHH_{ASC} matrix with lysates of THP-1 cells that overexpress EGFP allowed recovery of a single predominant polypeptide with an apparent molecular weight of 20 kDa (**Figure 5.1A**). The identity of this polypeptide as ASC was confirmed by mass spectrometry (80% sequence coverage, data not shown). A similarly immobilized GFP-specific VHH, $VHH_{Enhancer}$ [23],

Figure 5.1. VHH_{ASC} Specifically Binds Human ASC CARD

A. Resins with covalently coupled VHH_{ASC} and $VHH_{Enhancer}$ were used to immunoprecipitate the respective VHH targets from THP-1 cells expressing EGFP. Proteins bound to the resin were eluted with acidic buffers, separated by SDS-PAGE, and stained with colloidal Coomassie. The highlighted protein bands were cut out and subjected identification by mass spectrometry.

B. Differentiated THP-1 cells were left untreated or treated with LPS and nigericin to trigger NLRP3 inflammasome activation. Cells were subjected to immunofluorescence staining with rabbit anti-ASC and Alexa Fluor 647-coupled VHH_{ASC} or VHH NP1. Maximum intensity projections of representative images of at least three experiments are presented. Scale bars represent 10 µm.

C. A549 cells transiently expressing HA-tagged VHHs and the designated bait proteins fused to Renilla luciferase were lysed to immunoprecipitate VHHs with immobilized anti-HA. Renilla luciferase activity of the co-immunoprecipitated bait proteins was measured and normalized by the activity in the input. Mean values ± SEM from three independent experiments are displayed.

D. MBP-ASC^{CARD} was incubated with an excess of VHH_{ASC} and complexes separated from monomeric VHH_{ASC} by size exclusion chromatography. MBP was cleaved off purified complexes with TEV protease and the yielded protein samples subjected to size exclusion chromatography as well. Samples of the fractions were analyzed by SDS-PAGE and Coomassie staining.

E. A549 cells were transiently transfected with expression vectors for EGFP, EGFP-ASC, EGFP-ASC^{PYD}, or EGFP-ASC^{CARD}. 24 h post transfection, cells were lysed and subjected to SDS-PAGE and immunoblot with anti-EGFP, anti-ASC (raised against the PYD of ASC), and VHH_{ASC} combined with the respective HRP-coupled secondary antibodies. Representative immunoblots of at least three experiments are shown.

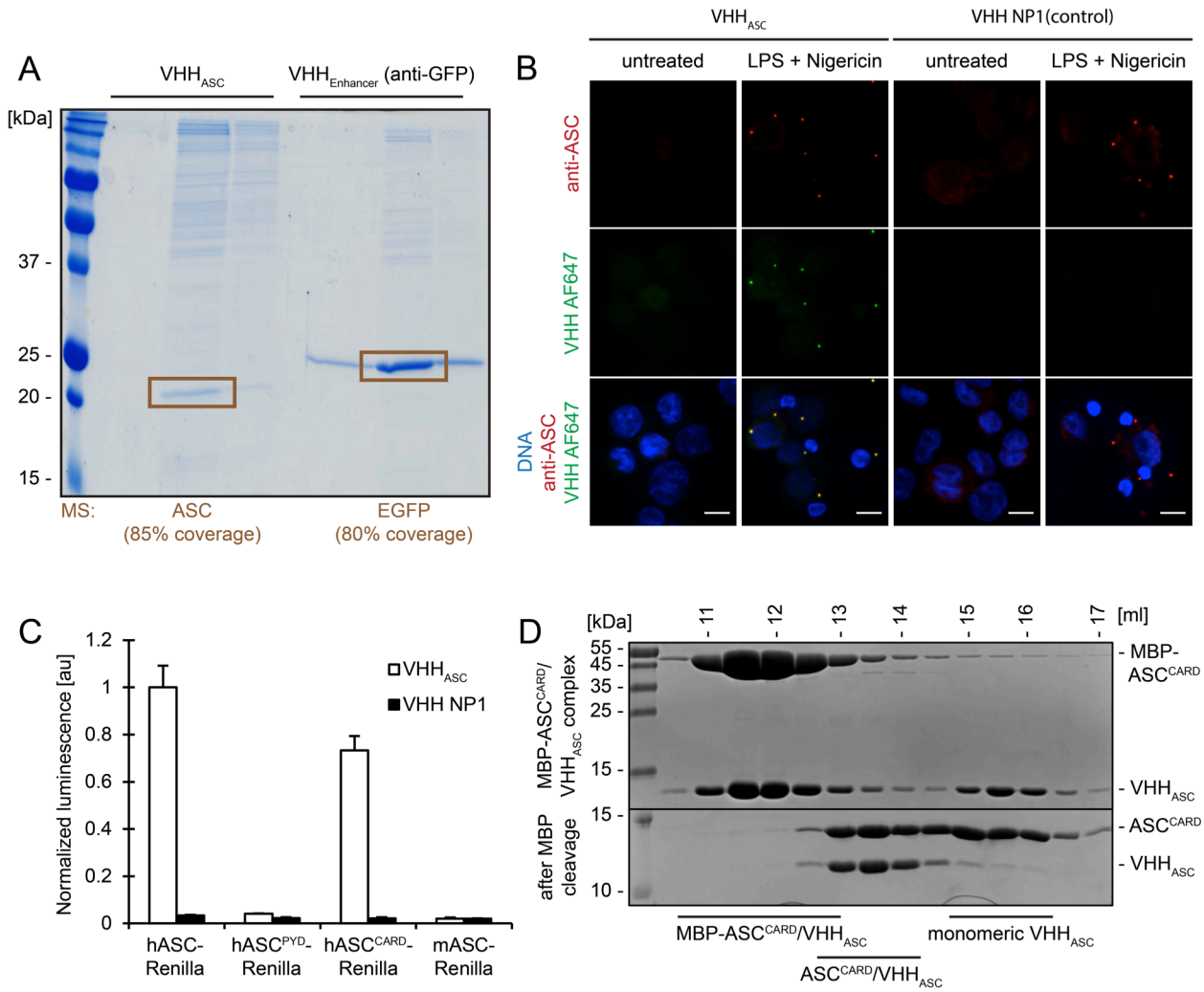

Figure 5.1 (Continued)

recovered EGFP but not ASC from the same THP-1 lysates. VHH_{ASC} thus interacts specifically with ASC in THP-1 cell lysates.

The VHH expression vectors encode VHHs equipped with a sortase motif to facilitate site-specific labeling with organic fluorophores. Fluorescently labeled VHH_{ASC} specifically stained ASC foci in THP-1 cells evoked by treatment with the NLRP3 activators LPS and nigericin, but did not stain any distinct structures in untreated cells (**Figure 5.1B**). A fluorescently labeled control VHH specific for the influenza A virus nucleoprotein NP, VHH NP1 [24], did not stain ASC foci.

We applied the LUMIER assay [25] to test interactions of HA-tagged VHH_{ASC} with Renilla luciferase fused to human and mouse full length ASC, as well as fusions of Renilla with the individual domains of human ASC: ASC^{PYD} and ASC^{CARD}. Full length human ASC and ASC^{CARD} interacted with VHH_{ASC}, while murine ASC and the PYD of human ASC did not (**Figure 5.1C**). We concluded that VHH_{ASC} recognizes the CARD of human ASC. VHH_{ASC} also recognized ASC CARD in immunoblots **(Figure 5.1E)**, indicating that the epitope recognized by VHH_{ASC} is retained in SDS-treated ASC^{CARD}. Moreover, purified VHH_{ASC}, when mixed with MBP-ASC^{CARD}, engaged in complex formation and co-eluted with MBP-ASC^{CARD} upon size exclusion chromatography (**Figure 5.1D**). Size exclusion chromatography showed co-elution of ASC^{CARD} and VHH_{ASC} at an estimated 1:1 stoichiometry. We concluded that VHH_{ASC} specifically binds to the CARD of human ASC, but not mouse ASC.

Structures of VHH_{ASC} Alone and the ASC^{CARD}/VHH_{ASC} Complex

To map the molecular interactions between VHH_{ASC} and ASC, we determined the crystal structures of VHH_{ASC} alone and in complex with ASC^{CARD} at 1.9 Å and 4.2 Å resolution, respectively (**Table S5.1**). The VHH_{ASC} structure shows the typical features of a V domain fold, comprised of 9 β-strands stacked into a four-stranded β-sheet and a five-stranded β-sheet (**Figure 5.2A**). The four-stranded β-sheet is formed by β-strands A/A', B, E, and D, and the five-

stranded β-sheet is formed by β-strands C, C', C'', F, and G, which are connected by intervening loops. The loop regions connecting β-strands B and C, strands C' and C'', and strands F and G correspond to complementarity-determining regions CDR1, CDR2, and CDR3, respectively. Compared to other VHHs, VHH_{ASC} exhibits an unusually short CDR3. We inferred that the very short CDR3 in VHH_{ASC} is unlikely to make a major contribution to binding its target.

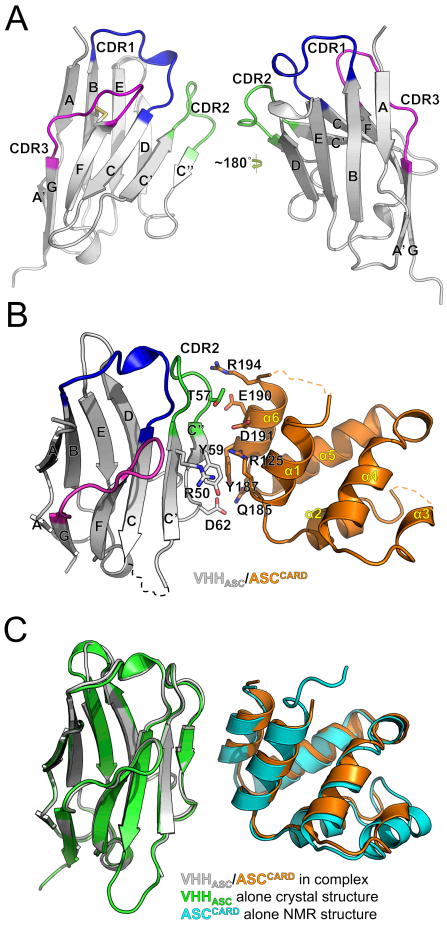

Figure 5.2. VHH_{ASC} Binds to an Interface of ASC^{CARD} Required for Homotypic Interactions

A. Structure of VHH_{ASC} at 1.9 Å resolution.

B. Structure of VHH_{ASC} in complex with the N128A/E130R monomeric mutant of ASC^{CARD} at 4.2 Å resolution. Residues at the interaction interface are indicated. Because the resolution of the complex was not sufficient to resolve the displayed amino acid side chains, we used the side chain conformations from the VHH crystal structure at 1.9 Å resolution and the full-length ASC NMR structure.

C. Comparisons of the structures of the complex of VHH_{ASC}/ASC^{CARD} N128A/E130R with VHH_{ASC} and ASC^{CARD} alone.

To determine the binding interface with ASC, we determined the crystal structure of VHH_{ASC} in complex with ASC^{CARD}. We were not successful in crystallizing the wild-type ASC^{CARD}/VHH_{ASC} complex, and instead turned to a monomeric mutant (N128A/E130R) of ASC^{CARD}. These mutations were predicted to impair CARD/CARD interactions via the type IIb interface based on the rather conserved interaction surfaces in the death domain family [26, 27]. The mutant ASC^{CARD} indeed remained monomeric, could still form a complex with VHH_{ASC}, and crystallized into needle-shaped crystals, which allowed us to solve the structure (**Figure 5.2B**).

Compared to the crystal structure of VHH_{ASC} alone and the NMR structure of ASC (PDB:2KN6) [28], neither VHH_{ASC} nor ASC^{CARD} in the VHH_{ASC}/ASC^{CARD} complex shows significant conformational changes (**Figure 5.2C**). Even though the structure of the complex was determined only to near atomic resolution, it nonetheless allowed identification of residues in contact. Surprisingly, among the CDRs, only the CDR2 loop participates in ASC recognition (**Figure 5.2B**). In addition, the C' strand and the C'' strand of VHH_{ASC}, which correspond to framework (FR) 2 and 3 of the domain, respectively, constitute the majority of the interface with ASC (**Figure 5.2B**). On the side of ASC^{CARD}, the last helix α6, and less extensively α1, directly contact VHH_{ASC}. Residues Thr57, Tyr59, Arg50, and Asp62 of VHH_{ASC} interact with residues Arg194, Glu190, Asp191, Arg125, Tyr187, and Gln185 of ASC^{CARD} to form the binding interface. Importantly, the exposed Tyr187 on ASC^{CARD} is completely masked by VHH_{ASC}, and this hydrophobic interaction with a large buried surface area presumably contributes significantly to the binding affinity (**Figure 5.2B, Figure 5.3A**). Taken together, our structural analysis shows that VHH_{ASC} mostly binds to the C-terminal region of human ASC, using an unusual combination of CDR2 and FR residues.

Binding of VHH_{ASC} to ASC^{CARD} Sterically Occludes ASC^{CARD} Type II Interface

In order to understand the molecular interaction between ASC^{CARD} and VHH_{ASC}, as well as the implications for the effect of VHH_{ASC} in inhibiting ASC^{CARD}-mediated interactions, we

Figure 5.3. Binding of VHH_{ASC} to ASC^{CARD} Sterically Occludes ASC^{CARD} Type II Interface

A. Electrostatic surface representation of the VHH_{ASC}/ASC^{CARD} complex, highlighting tyrosine 59 in VHH_{ASC} and tyrosine 187 in ASC^{CARD}.

B. The MBP-ASC^{CARD}-SUMO fusion protein was incubated with TEV protease to cleave off the MBP protein, which led to polymerization of ASC^{CARD}-SUMO. A representative electron micrograph of the resulting fibers subjected to negative staining is shown. The scale bar represents 100 nm.

C. Representation of the ASC^{CARD} filament modeled using the known $MAVS^{CARD}$ filament structure (left), a zoomed view of the type II interface of two highlighted ASC^{CARD} subunits (middle), and illustration of the complex of VHH_{ASC} with ASC^{CARD} subunit 1 (right). The VHH sterically clashes with ASC^{CARD} subunit 2 bound via the type II interface (shown in transparent cyan).

D. Interaction of ASC wt and type II mutant Y187A with His-tagged caspase-1. The indicated combinations of His_6-GFP-caspase-1^{CARD} and wild-type or mutant His_6-MBP-ASC were incubated. Where indicated, His_6-MBP was cleaved off ASC using TEV protease, and His-tagged proteins were purified using Ni-NTA resin. Samples of the protein mixtures were analyzed by SDS-PAGE and Coomassie staining. Positions of the indicated proteins are marked on the right. The intensity of the ASC^{FL} bands was determined from the scanned gel and normalized by the band intensity of GFP-caspase-1^{CARD}.

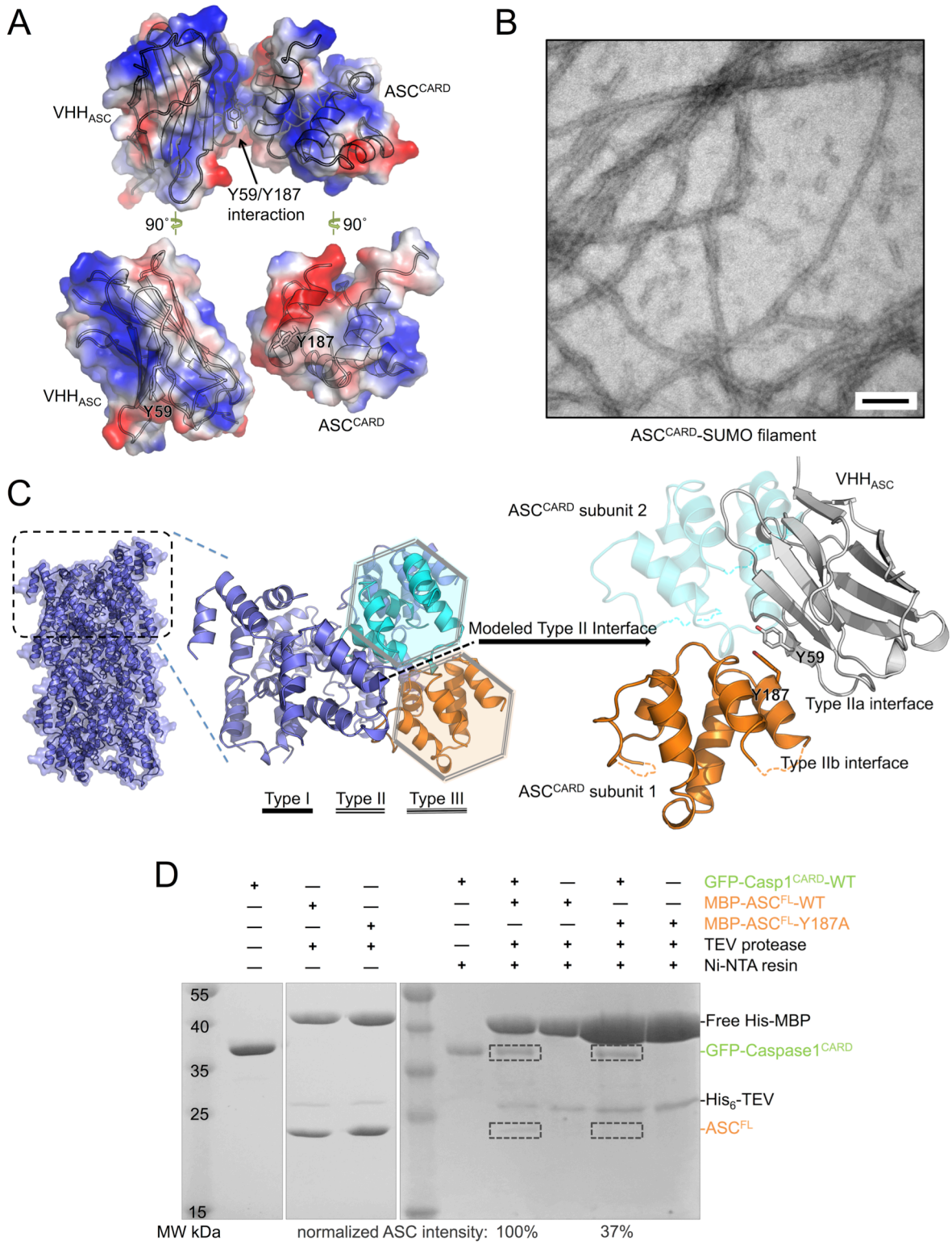

Figure 5.3 (Continued)

attempted to identify the surfaces of ASC^{CARD} that mediate interactions with itself and with caspase-1^{CARD}. We first investigated the quaternary structure assumed by oligomers of ASC^{CARD}. We constructed a sandwich-tagged MBP-ASC^{CARD}-SUMO fusion protein. Upon removal of MBP, ASC^{CARD}-SUMO oligomerized into extended filaments (**Figure 5.3B**). The SUMO fusion prevents aggregation of filaments and increased overall solubility after oligomerization. Irrespective of whether endogenous ASC^{CARD} forms extended filaments or short filamentous assemblies under physiological conditions in cells, the ASC^{CARD} filaments formed *in vitro* serve as a proxy that helps reveal structural details of CARD/CARD interactions. No structural information on the filamentous structure of ASC^{CARD} exists, but CARD domains exhibit a sufficient degree of conservation to allow meaningful structural predictions based on other CARD structures. We therefore modeled the structure of an ASC^{CARD} filament based on the 3.6 Å resolution cryo-EM structure of the $MAVS^{CARD}$ filament [29]. We aligned copies of ASC^{CARD} to each unit of the $MAVS^{CARD}$ filament, effectively imposing the 1-stranded helical parameters (101.1° twist angle and 5.13 Å axial rise per unit) onto ASC^{CARD}. We then superimposed the VHH_{ASC}/ASC^{CARD} complex structure on the predicted ASC^{CARD} filament structure (**Figure 5.3C**). Thus, the surface of ASC^{CARD} used in the VHH_{ASC} interaction overlaps with its type IIb surface; the bound VHH_{ASC} sterically clashes with the adjacent subunit in the ASC^{CARD} filament along the type II direction, suggesting that binding of VHH_{ASC} to ASC^{CARD} interferes with CARD/CARD interactions in ASC^{CARD} self-oligomerization via the type II interface.

ASC^{CARD} and Caspase-1^{CARD} also Interact Through Type II Interfaces

To probe the importance of the type II interface of ASC^{CARD}, we analyzed the effect of mutations at this interface on ASC^{CARD} interaction with pro-caspase-1^{CARD}. The VHH_{ASC}/ASC^{CARD} complex structure shows a hydrophobic surface patch near α6, primarily contributed by the exposed Tyr187 (**Figure 5.3A**). We generated the Y187A mutant in full-length ASC fused to the C-terminus of solubilizing MBP, and cleaved off MBP in the presence of His_6-GFP-caspase-

1^{CARD}. When we purified His_6-GFP-caspase-1^{CARD} with Ni-NTA resin, the amount of the ASC mutant co-purified was reduced by 63% compared to wild-type ASC (**Figure 5.3D**). We concluded that type II interactions are essential in mediating the ASC^{CARD}/caspase-1^{CARD} association. Blocking this interface by VHH_{ASC} was thus expected to abolish ASC^{CARD} self-oligomerization, as well as its ability to recruit pro-caspase-1.

VHH_{ASC} Directly Inhibits ASC^{CARD}-nucleated Caspase-1^{CARD} and ASC^{CARD} Polymerization

We can reconstitute the polymerization of inflammasome components *in vitro* using purified proteins, including the ASC^{CARD}-nucleated polymerization of caspase-1^{CARD} [8]. We used a fluorescence polarization assay to monitor nucleation of caspase-1^{CARD} filaments by oligomeric ASC^{CARD} in the presence and absence of VHH_{ASC} (**Figure 5.4A**). This assay exploits the fact that fluorescence anisotropy increases when a fluorescent monomeric species polymerizes. In short, we labeled monomeric caspase-1^{CARD} (N-terminal MBP, C-terminal SUMO) by means of a sortase reaction [30], followed by purification of the labeled monomers [8]. We added sub-stoichiometric amounts of oligomeric GFP-ASC^{CARD} to seed the growth of caspase-1^{CARD} filaments upon TEV cleavage of the MBP fusion partner. We pre-incubated the GFP-ASC^{CARD} seeds with either VHH_{ASC} or the anti-GFP $VHH_{Enhancer}$. Incubation of the GFP-ASC^{CARD} seeds with equimolar amounts of VHH_{ASC} abolished their ability to nucleate caspase-1^{CARD} filament formation (**Figure 5.4A**). Incubation of GFP-ASC^{CARD} with $VHH_{Enhancer}$ did not affect caspase-1^{CARD} polymerization. Binding of ASC^{CARD} by VHH_{ASC} thus directly and specifically interferes with the ASC^{CARD}/capase-1^{CARD} interaction.

To determine the stoichiometry of inhibition by VHH_{ASC}, we pre-incubated a fixed, sub-stoichiometric amount of ASC^{CARD} with various amounts of VHH_{ASC}, and subsequently monitored caspase-1^{CARD} filament formation (**Figure 5.4B**). We fitted a single-site antagonist model to the obtained initial slopes of the fluorescence polarization traces and determined the apparent binding constant (K_{app}) between VHH_{ASC} and GFP-ASC^{CARD} to be 159.5 ± 1.5 nM

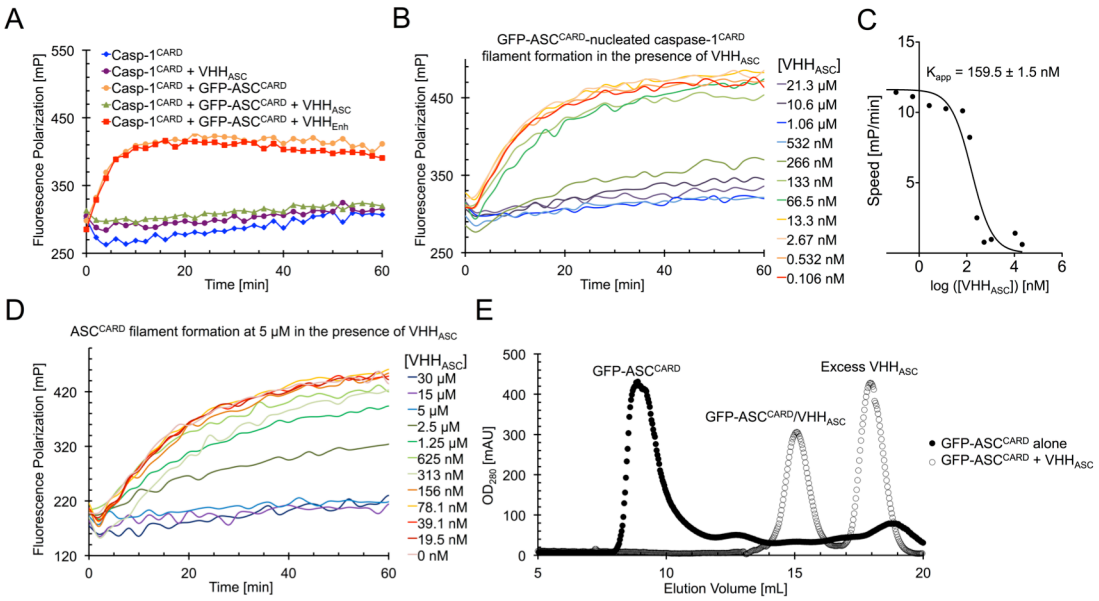

Figure 5.4. VHH_{ASC} Prevents ASC^{CARD}-nucleated Polymerization of Caspase-1^{CARD} and ASC^{CARD}

A. ASC-nucleated caspase-1^{CARD} polymerization in the presence of VHH_{ASC} and $VHH_{Enhancer}$. Fluorescently labeled monomeric MBP-caspase-1^{CARD}-SUMO (4 µM) was mixed with oligomeric GFP-ASC^{CARD} (1.1 µM) preincubated with VHH_{ASC} or $VHH_{Enhancer}$ (1.1 µM) where indicated. MBP was cleaved from fluorescent caspase-1^{CARD}-SUMO to allow ASC^{CARD}-nucleated polymerization of caspase-1^{CARD}. Polymerization was followed by measuring fluorescence polarization over time.

B. ASC-nucleated caspase-1^{CARD} polymerization in presence of different VHH_{ASC} concentration. Polymerization of caspase-1^{CARD}-SUMO by oligomeric GFP-ASC^{CARD} was measured by fluorescence polymerization assays as described in (**A**), except that GFP-ASC^{CARD} was pre-incubated with the indicated concentrations of VHH_{ASC}.

C. Apparent inhibition constant of VHH_{ASC}. The initial slope of the fluorescence polarization processes in (**B**) was plotted against the logarithm of the VHH_{ASC} concentration.

D. ASC^{CARD} polymerization. Fluorescently labeled monomeric MBP-ASC^{CARD}-SUMO (5 µM) was preincubated with VHH_{ASC} at the indicated concentrations. MBP was cleaved off fluorescent ASC^{CARD}-SUMO to self-nucleated polymerization of ASC^{CARD}. Polymerization was followed by measuring fluorescence polarization over time.

E. Stability of ASC^{CARD} oligomers in presence of VHH_{ASC}. Oligomeric GFP-ASC^{CARD} was incubated with excess VHH_{ASC} for 30 min at room temperature or left untreated. Protein samples were subjected to size exclusion chromatography, OD_{280} profiles are displayed.

(**Figure 5.4C**). K_{app} is of the same order of magnitude as the concentration of GFP-ASC^{CARD}, suggesting that 1:1 binding of VHH_{ASC} inhibits ASC^{CARD}/caspase-1^{CARD} interaction.

In addition, we assayed the effect of VHH_{ASC} directly on ASC^{CARD} oligomerization. We used fluorescently labeled monomeric MBP-ASC^{CARD}-SUMO in an experiment similar to the caspase-1^{CARD} polymerization assay, but exploited the fact that at sufficient concentrations, ASC^{CARD}-SUMO polymerizes in the absence of any nucleators. Addition of an approximately equimolar amount of VHH_{ASC} to the polymerizing ASC^{CARD} was required to block polymerization (**Figure 5.4D**), suggesting that 1:1 binding of VHH_{ASC} to ASC^{CARD} also inhibits its self-oligomerization. To compare the affinity of VHH_{ASC} for ASC^{CARD} with the affinities of ASC CARD/CARD interactions, we incubated oligomeric GFP-ASC^{CARD} with excess VHH_{ASC}. GFP-ASC^{CARD} on its own behaves as an oligomer as assayed by size-exclusion chromatography. After incubation with excess VHH_{ASC}, however, only smaller dimeric complexes of ASC^{CARD}:VHH_{ASC} as well as monomeric VHH_{ASC} were observed (**Figure 5.4E**), suggesting that VHH_{ASC} may even disassemble already activated inflammasome complexes by competing with ASC CARD/CARD interactions. Taken together, the data demonstrate that VHH_{ASC} –by occluding the type IIb interface of ASC^{CARD}– perturbs CARD/CARD interactions of ASC^{CARD} with both ASC^{CARD} and caspase-1^{CARD}.

VHH_{ASC} Blocks NLRP3- and AIM2-dependent Inflammasome Activation

In contrast to conventional antibodies, VHHs can retain their binding properties in the reducing milieu of the cytosol. VHHs can therefore be expressed cytosolically to perturb protein function under physiological conditions and at endogenous concentrations of the wild-type form of a VHH target [17, 24]. In this sense, VHH-mediated perturbations are fundamentally distinct from analyses of mutant forms of the target protein, or from siRNA or Cas9/CRISPR-based approaches where the goal is a reduction in expression levels of the target protein.

Figure 5.5. VHH_{ASC} Prevents NLRP3 and AIM2 Inflammasome Activation in THP-1 Cells

A. THP-1 cell lines inducibly expressing VHH_{ASC}-HA or VHH NP1-HA were cultivated for 24h in the absence or presence of doxycycline, fixed, stained for HA, and analyzed by flow cytometry.

B-E. Wild-type THP-1 cells and the cell lines described in (**A**) were differentiated and VHH expression induced for 24h. (**B**) Cells were treated with 200 ng/mL LPS for 3 h, harvested and cell lysates analyzed by immunoblot with anti-ASC, anti-HA, and anti-GAPDH. (**C**) Cells were treated with 200 ng/mL LPS for 4 h or left untreated. Supernatants were analyzed by TNF ELISA. (**D-E**) Cells were treated with LPS for 3 h and nigericin for 45 min, or left untreated. Supernatants were analyzed by IL-1β ELISA (**D**) and by immunoblots with anti-IL-1β and anti-caspase-1 p10 (**E**). Immunoblots representative of three experiments are shown. The asterisk indicates a statistically significant difference (Student‘s t-test $P<0.001$).

F-G. Cells treated as in (**D**) were fixed and stained for DNA and ASC; images were recorded by wide field fluorescence microscopy (**F**) and the fraction of cells containing ASC foci was quantified (**G**). Data from three independent experiments with at least 500 cells per condition ± SEM is shown. Scale bars represent 20 µm.

H. THP-1 cell lines cultivated as described in (**B**) were treated with LPS for 3 h and transfected with poly (dA:dT) or transfection agent only. Supernatants were harvested after 4 h and IL-1β levels quantified by ELISA. The asterisk indicates a statistically significant difference (Student’s t-test $P=0.002$). Data from three independent experiments was quantified for all ELISA results and average values ± SEM are shown.

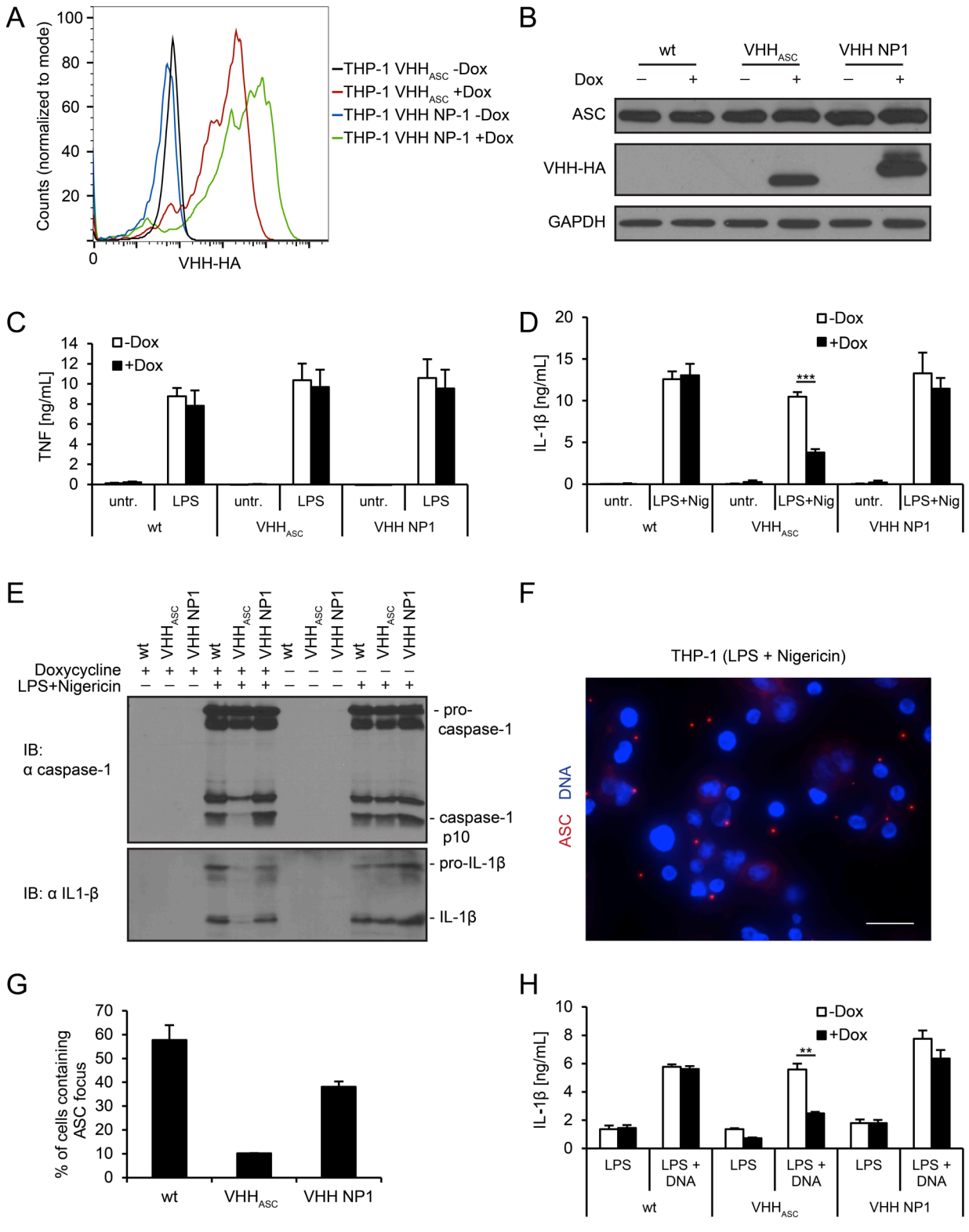

Figure 5.5 (Continued)

To study the role of ASC CARD during inflammasome assembly in human cells, we generated derivatives of the human monocyte-like cell line THP-1 that inducibly express HA-tagged VHH_{ASC} or the control VHH NP1 [24] upon addition of doxycycline. Both VHHs were induced to similar levels of expression (**Figure 5.5A**), did not alter levels of ASC (**Figure 5.5B**), and did not affect LPS-induced TNF secretion in phorbol-12-myristate-13-acetate (PMA)-differentiated cells (**Figure 5.5C**). To test the effect of VHH_{ASC} on NLRP3 inflammasome activation, we differentiated THP-1 cells with PMA (o/n) and then induced VHH expression for 24 h. For activation, doxycycline-induced cells were treated with LPS for 3 h and with the potassium ionophore nigericin for 45 min, both in the absence of doxycycline.

Potassium efflux activates the NLRP3 inflammasome. This involves the recruitment and polymerization of ASC and pro-caspase-1, auto-catalytic activation of caspase-1, and subsequent maturation of IL-1β and IL-18. As assessed by immunoblot and ELISA, parental THP-1 cells secreted processed caspase-1 and IL-1β in response to NLRP3 triggers (**Figure 5.5D-E**). Doxycycline treatment did not affect caspase-1 activation or IL-1β conversion. Moreover, on average 58% of the cells contained an ASC focus as detected by immunofluorescence microscopy using anti-ASC antibodies (**Figure 5.5F-G**). While VHH_{ASC} cell lines behaved like unmodified THP-1 cells in the absence of doxycycline, caspase-1 cleavage and IL-1β secretion were substantially reduced in cells induced to express VHH_{ASC}. Only 10% of the treated cells contained an ASC focus when expression of VHH_{ASC} was induced. Induction of the control VHH NP1 neither changed secretion of caspase-1 and IL-1β, nor substantially impaired ASC focus formation. VHH_{ASC} thus specifically reduces the assembly of ASC foci, perturbs the recruitment and autocatalytic cleavage of pro-caspase-1 and consequently IL-1β secretion.

When activated by DNA, AIM2 employs ASC to recruit and activate pro-caspase-1 similar to NLRP3. When THP-1 cell lines were transfected with poly(dA:dT), IL-1β release was substantially reduced by expression of VHH_{ASC}, but not by the control VHH NP1 (**Figure 5.5H**).

Consistent with our interpretation of the *in vitro* data, VHH_{ASC} masks the CARD of soluble ASC molecules in living cells and thus prevents CARD/CARD interactions between ASC molecules and recruitment of pro-caspase-1.

VHH_{ASC} Blocks NAIP/NLRC4-dependent Inflammasome Activation

While NLRP3 and AIM2 receptors depend on ASC to recruit pro-caspase-1 to nascent inflammasomes, NAIP/NLRC4 inflammasome complexes can directly engage pro-caspase-1 via homotypic CARD/CARD interactions. In mouse cells, NLRC4-dependent secretion of IL-1β is more efficient in the presence of ASC [31]. To investigate the role of ASC in NAIP/NLRC4 inflammasomes in human cells, we differentiated THP-1 cell lines as before and activated NAIP/NLRC4 inflammasomes with the *Shigella flexneri* needle protein MxiH, which directly binds to NAIP and thus activates NAIP/NLRC4 inflammasomes [2]. MxiH was delivered into the cytosol using the anthrax toxin delivery system [32, 33]. In brief, cells were treated with the anthrax toxin protective antigen (PA) and a fusion protein of MxiH and the N-terminus of the anthrax lethal factor, LFn. PA binds to the anthrax receptor at the cell surface, is proteolytically activated to form the pre-pore, and then recruits LFn-MxiH. The complex is endocytosed and LFn-MxiH is translocated into the cytosol through the PA pore upon acidification of endosomes.

In parental THP-1 cells, translocation of MxiH to the cytosol induced robust IL-1β secretion and pyroptotic cell death, as judged by release of cytosolic LDH (**Figure 5.6A-B**). To show that the observed IL-1β secretion and pyroptotic cell death were indeed dependent on MxiH, and not caused by bacterial contaminants contained in our protein preparations, we used a mutant version of MxiH. The mutant MxiH 2A, in which two conserved hydrophobic residues in the needle-protein helical hairpin region were changed to alanine [2], was indeed substantially less potent than MxiH in activating IL-1β secretion and cell death. In cells expressing VHH_{ASC}, cytokine secretion was clearly diminished in response to MxiH delivery, while control cells that expressed VHH NP1 behaved like the parental THP-1 line. Human NAIP/NLRC4 inflammasome

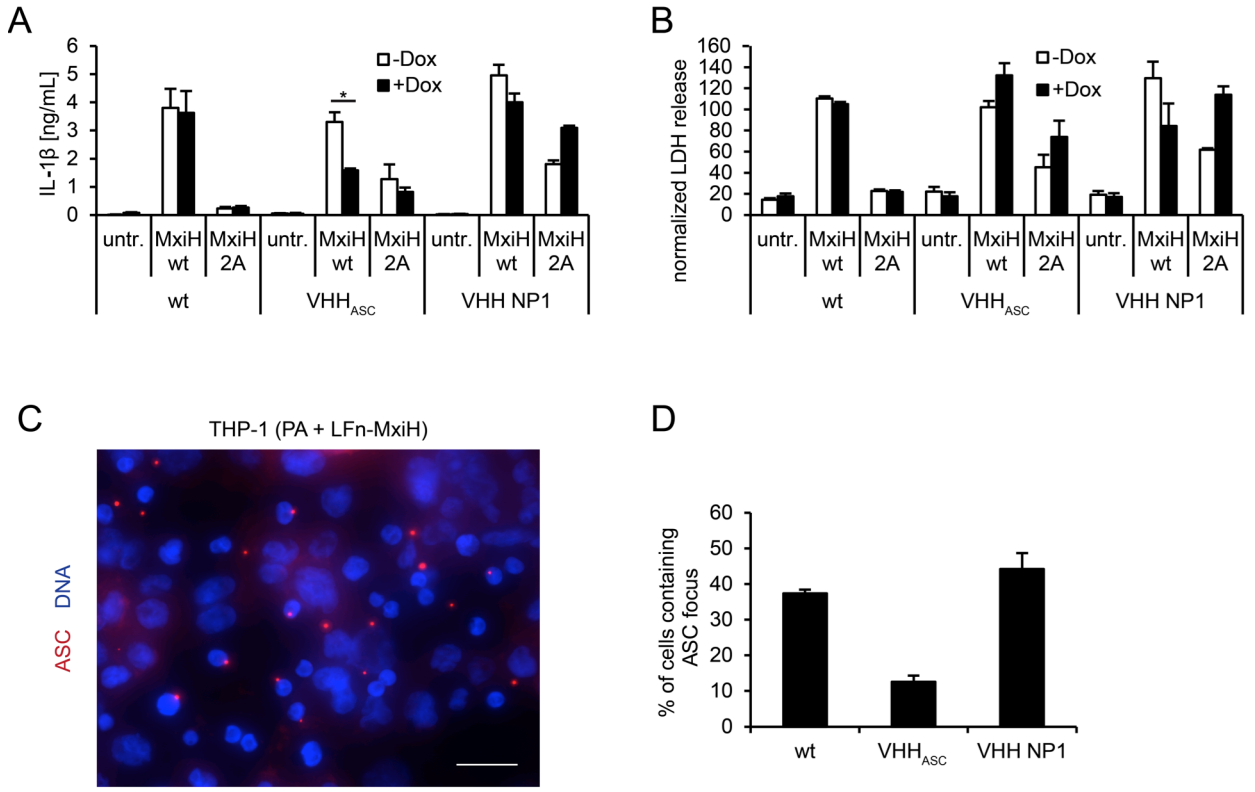

Figure 5.6. VHH$_{ASC}$ Prevents IL-1β Secretion, but not Cell Death, by NAIP/NLRC4 Inflammasomes in THP-1 Cells

A and B. Wild-type THP-1 cells and cell lines inducibly expressing VHH$_{ASC}$-HA or VHH NP1-HA were differentiated and VHH expression induced for 24 h. Cells were treated with PA and LFn-MxiH wt or 2A for 3 h, or left untreated. IL-1β in the supernatants was quantified by ELISA (**A**), LDH activity was quantified and normalized to cells lysed in 1% Triton X-100 (**B**). Data from three independent experiments was quantified and average values ± SEM are shown. The asterisk indicates a statistical significant difference (Student's t-test P=0.039).

C and D. THP-1 cell lines were differentiated and induced as described in (**A**), and subsequently treated with PA and MxiH wt or 2A for 2 h in the presence of 50 µM z-YVAD-cmk. Cells were fixed and stained for DNA and ASC; images were recorded by wide field fluorescence microscopy (**C**) and the fraction of cells containing ASC foci was quantified (**D**). Scale bars represent 20 µm. Data from three independent experiments with at least 500 cells per condition ± SEM is shown.

activation thus requires ASC for efficient cytokine maturation. IL-1β secretion was diminished slightly in THP-1 VHH_{ASC} cells in which VHH expression was not induced. This is most likely due to leakiness of the inducible expression system.

In parental THP-1 cells and THP-1 cell lines expressing VHH NP1, we observed ASC foci in 37 and 44% of the treated cells (**Figure 5.6C-D**). In THP-1 cells that express VHH_{ASC}, the fraction of cells containing ASC foci was reduced to 13%. As is the case for NLRP3 inflammasomes, VHH_{ASC} acted both at the level of ASC focus formation and in the recruitment of pro-caspase-1, to perturb activation of NAIP/NLRC4 inflammasomes.

In contrast to cytokine secretion, cell death by pyroptosis occurred at comparable levels in THP-1, THP VHH_{ASC}, and THP VHH NP1, irrespective of whether VHH expression was induced or not. This suggests that human ASC is dispensable for pyroptosis. Direct pro-caspase-1 recruitment to NLRC4 may be sufficient for cell death, as has been proposed for mouse macrophages infected with *Salmonella* [4]. In summary, our data suggest that NLRC4-dependent IL-1β maturation and secretion requires ASC. Caspase-1 activation very likely takes place at the macromolecular assemblies visualized as ASC foci. In contrast, cell death by pyroptosis does not require ASC or ASC foci, and is presumably initiated in smaller assemblies.

VHH_{ASC}-EGFP Assembles Along ASC Filaments in Response to NLRP3 and AIM2 Activators

In the presence of VHH_{ASC}-HA, we observed reduced numbers of ASC foci in response to NLRP3 triggers. Given that VHH_{ASC} binds to the CARD of ASC, and that NLRP3 activation induces the formation of ASC^{PYD} filaments *in vitro*, we were surprised that we were unable to stain any macromolecular structures containing ASC or VHH_{ASC}-HA in cells that lacked ASC foci. Since we used conventional indirect immunofluorescence microscopy with primary antibodies against the PYD of ASC or against HA in combination with fluorescently-labeled

Figure 5.7. VHH_{ASC}-EGFP Assembles Along ASC Filaments in Response to Inflammasome Triggers

A-D. THP-1 cell lines inducibly expressing VHH_{ASC}-EGFP or VHH NP1-EGFP were differentiated and VHH expression induced for 24 h. Cells were left untreated (**A**), treated with LPS for 3 h and nigericin for 45 min to trigger NLRP3 inflammasomes (**B**), treated with LPS for 3 h and transfected with DNA for 4 h to trigger AIM2 inflammasomes (**C**), or treated with PA and LFn-MxiH wt in the presence of 30 µM z-YVAD-cmk for 2 h to trigger NAIP/NLRC4 inflammasomes (**D**). Cells were fixed and stained for DNA and ASC; images of single planes were recorded by spinning disc confocal microscopy. Scale bars represent 10 µm. Representative images from at least 3 experiments are shown.

E-G. THP-1 cell lines were differentiated, VHH expression induced, and NLRP3, AIM2, and NLRC4 inflammasomes activated or cells left untreated as in (**A-D**), but in the presence of 50 µM z-YVAD-cmk. Cells were fixed and mounted with mounting medium containing DAPI; Z stacks were recorded by spinning disc confocal microscopy. At least 300 cells per condition were analyzed and cells containing green-fluorescent filaments or foci were manually counted. One typical experiment representative of at least 3 independent experiments was quantified.

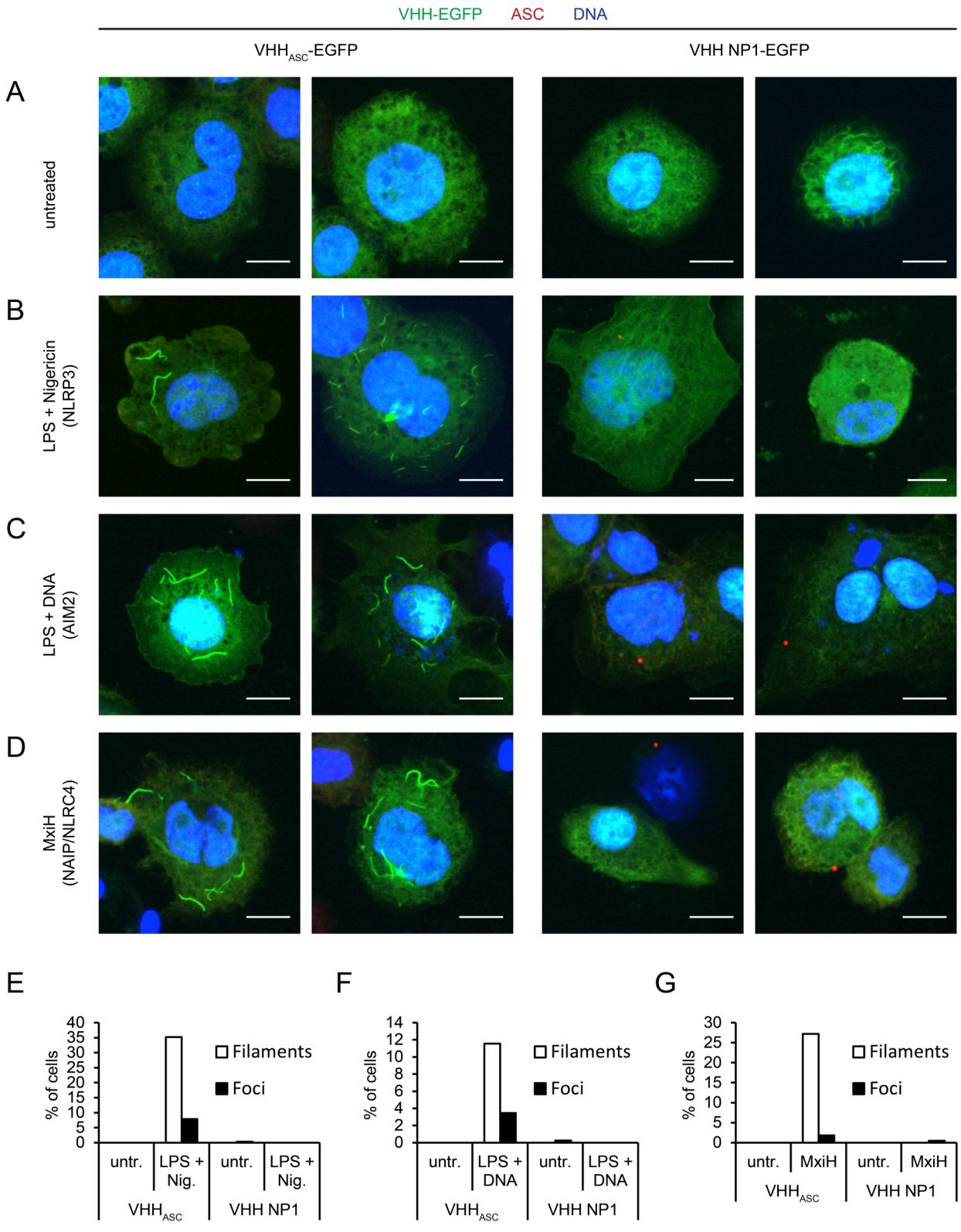

Figure 5.7 (Continued)

secondary antibodies, we reasoned that impaired accessibility of antigens for staining with conventional antibodies, or the small number of molecules involved might be the explanation.

To address these issues, we generated THP-1 cell lines that inducibly expressed a VHH_{ASC}-EGFP fusion protein or the control VHH NP1-EGFP. When THP-1 VHH_{ASC}-EGFP cells were treated with LPS and nigericin to activate NLRP3 inflammasomes, we observed two different outcomes (**Figure 5.7B and E**): Few cells contained ASC foci that could be stained with conventional anti-ASC antibodies and that were EGFP positive – they presumably represent the fraction of cells in which VHH levels were too low to impair ASC focus formation, but in which VHH_{ASC} may still impair pro-caspase-1 recruitment. We also observed many cells that exhibited one, a few, or multiple filamentous EGFP structures of variable length which could not be stained with ASC PYD antibodies. In the absence of inflammasome triggers, cells that expressed VHH_{ASC}-EGFP lacked such structures (**Figure 5.7A and E**). Filamentous structures were absent also from cells that expressed the control VHH NP1-EGFP, even when treated with NLRP3 inflammasome triggers. Filamentous EGFP was thus observed only upon meeting two conditions: 1. when ASC^{PYD} could build filaments in response to inflammasome triggers, and 2. when VHH_{ASC}-EGFP was expressed. We conclude that these EGFP-positive structures were formed along endogenous ASC filaments, assembled upon NLRP3-nucleated polymerization of ASC^{PYD}. An excess of VHH_{ASC}-EGFP we hypothesize thus masked ASC^{CARD}, but still permitted the formation of ASC^{PYD} filaments. This is the first time that ASC filaments could be visualized at physiological ASC levels and therefore cannot be attributed to overexpression artifacts. These filaments must represent an intermediate phenotype, since ASC^{CARD} was masked by VHH_{ASC} and could not complete its physiological function. That ASC formed long, unbranched filaments, as opposed to densely packed ASC foci, suggests that the organization of multiple ASC filaments into a single focus requires accessible ASC^{CARD}. The ASC^{CARD}, beyond its role in the recruitment of pro-caspase-1, thus serves a function in the organization of multiple ASC

filaments into a single dense ASC focus, possibly by cross-linking ASC filaments assembled through the ASC^{PYD}.

In vitro, full length ASC assembles into highly cross-linked filaments, while ASC^{PYD} assembled into long, linear filaments [8, 9]. If VHH_{ASC}-EGFP indeed prevented cross-linking of full length ASC filaments (vide supra), VHH_{ASC} should also prevent cross-linking of ASC filaments *in vitro*. To test the effect of VHH_{ASC} on the quaternary structure of full-length ASC, we formed a complex of VHH_{ASC} and recombinantly expressed full-length ASC fused to MBP, in which MBP prevents ASC oligomerization. When MBP was removed from the complex by TEV cleavage, ASC/VHH_{ASC} polymerized into long, linear filaments as observed by negative-stain EM after only 5 min (**Figure 5.8A**). These filaments have a diameter of >20 Å, corresponding to a core PYD filament (≈9Å [8]) decorated by ASC^{CARD}/VHH_{ASC} monomers. Importantly, these filaments are not cross-linked, and thus resemble ASC^{PYD} filaments. When MBP was cleaved from MBP-ASC in the absence of VHH_{ASC}, ASC polymerized as well, but formed highly cross-linked bundled structures which precipitated over time. After 20 min, essentially no more filamentous structures were recognized and ASC formed an amorphous, dense mass. By masking the ASC^{CARD}, VHH_{ASC} therefore may prevent crosslinking of full length ASC filaments *in vitro*, and thus supports the model deduced from our microscopy studies.

To more directly visualize ASC in the observed filamentous assemblies, we took advantage of the propensity of overexpressed EGFP-ASC to assemble into ASC foci when overexpressed in epithelial cells [34]. Although nucleation of EGFP-ASC foci themselves is artificial and does not depend on any upstream nucleators, formation of the macromolecular structures seems to be governed by the PYD/PYD and CARD/CARD interactions that are assumed to underlie the assembly of endogenous ASC foci [8, 35]. This includes the finding that EGFP-ASC^{PYD} assembles into filaments, as it does *in vitro*. When EGFP-ASC or EGFP-ASC^{PYD} was overexpressed in epithelial A549 cells, we observed foci and filaments, respectively (**Figure 5.8B**). When full length EGFP-ASC was expressed in the presence of VHH_{ASC},

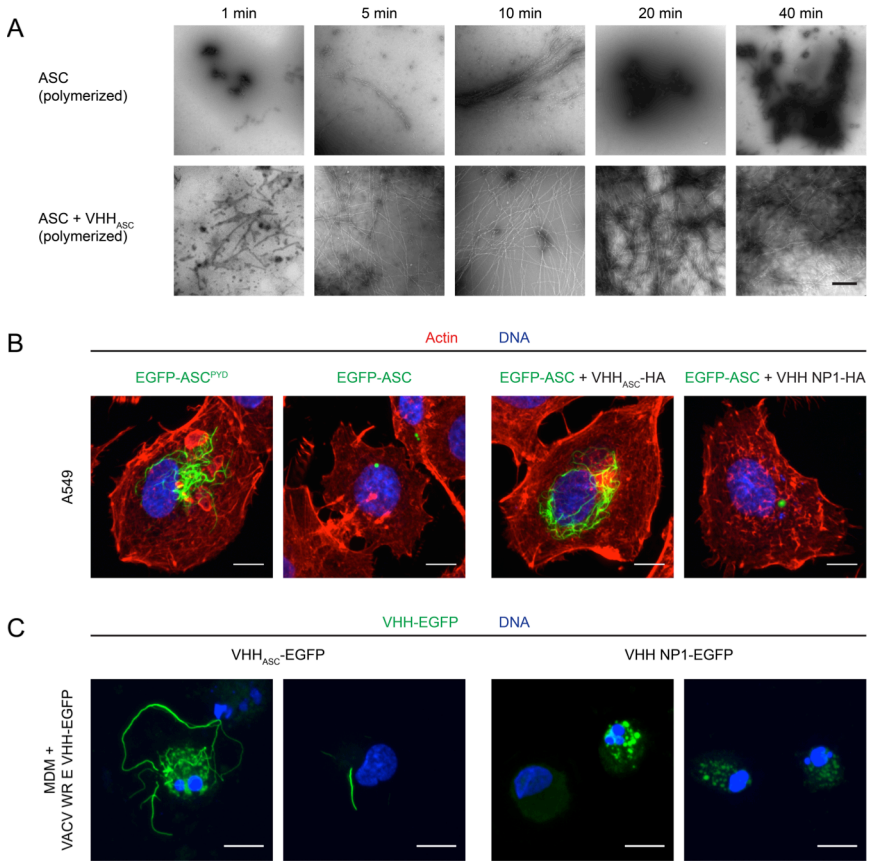

Figure 5.8. VHH$_{ASC}$ Stabilizes ASC Filaments formed through ASC^{PYD} polymerization *in vitro* and in cells

A. MBP-ASC or MBP-ASC preincubated with VHH$_{ASC}$ were incubated with TEV protease to remove the MBP fusion and allow polymerization. At the indicated times, the reaction was stopped and the resulting macromolecular structures were visualized by negative stain electron microscopy. Scale bars represent 500 nm.

B. A549 cells were transiently transfected with expression vectors for EGFP-ASC^{PYD} or EGFP-ASC in the absence or presence of expression vectors for VHH$_{ASC}$ or VHH NP1. 24 h post transfection, cells were fixed and stained for DNA and filamentous actin. Z-stacks of representative cells were recorded by spinning disc confocal microscopy and maximum intensity projections are displayed. Scale bars represent 10 µm.

C. Human monocyte-derived macrophages were differentiated in the presence of 10% FBS and 100 ng/mL M-CSF for 5 days and subsequently infected with mature virions of vaccinia virus WR E VHH$_{ASC}$-EGFP L mCherry or WR E VHH NP1-EGFP L mCherry at an MOI of 20. Cells were fixed 18 h post infection and stained for DNA. Z stacks of representative cells were recorded by spinning disc confocal microscopy and images of maximum intensity projections are shown. Scale bars represent 10 µm.

however, we did observe EGFP-ASC filaments but no ASC foci. These filaments resembled the EGFP-ASC^{PYD} filaments, indicating that in masking ASC^{CARD}, VHH$_{ASC}$ indeed blocked further compaction of ASC filaments formed by PYD polymerization.

Activation of AIM2 by DNA-binding nucleates the formation of ASC PYD filaments *in vitro* as well [8]. To validate our model, we tested whether DNA –as an alternative activator of ASC PYD filaments– would also lead to the assembly of VHH$_{ASC}$-EGFP along endogenous ASC structures in a cellular context (**Figure 5.7C and F**). Indeed, we observed filamentous EGFP in poly(dA:dT)-transfected THP-1 cells expressing VHH$_{ASC}$-EGFP, but not in cells expressing the control VHH NP1-EGFP. The occurrence of filamentous VHH$_{ASC}$-EGFP structures in response to two different activators of ASC PYD polymerization thus confirmed that filamentous VHH$_{ASC}$-EGFP assemblies are readouts for ASC PYD filament formation.

VHH$_{ASC}$-EGFP Assembles Along ASC Filaments in Response to NAIP/NLRC4 Triggers

Efficient cytokine maturation in response to the NAIP/NLRC4 trigger MxiH involves multimolecular ASC complexes because ASC foci accrued upon stimulation and VHH$_{ASC}$ reduced IL-1β secretion. Unlike NLRP3 and AIM2, NLRC4 does not contain a PYD and therefore cannot directly nucleate the oligomerization of ASC filaments by PYD/PYD interactions. Two scenarios that allow NLRC4 to induce the formation of ASC filaments are conceivable: NLRC4 may directly nucleate the formation of ASC filaments via the ASC^{CARD}. Indeed, both overexpressed ASC^{CARD} in cells [36], as well as purified ASC^{CARD} *in vitro* (**Figure 5.3B**), can oligomerize into filament-like structures. Alternatively, NLRC4 may bind one or several ASC molecules through its CARD, which in turn changes the conformation of the bound ASC molecules, so that ASC itself can nucleate the formation of ASC filaments using its PYD. This scenario would resemble the situation observed for NLRP3 and AIM2. To test which of the two possibilities applies, we triggered THP-1 VHH$_{ASC}$-EGFP and THP-1 VHH NP1-EGFP with cytosolically delivered MxiH in the presence of the caspase-1 inhibitor z-YVAD-cmk to reduce

pyroptotic cell death. When cells expressing VHH_{ASC}-EGFP were treated with MxiH, we observed filamentous EGFP structures in many cells (**Figure 5.7D and G**). The EGFP structures were similar to those found when NLRP3 was activated by K^+ efflux (nigericin), or when AIM2 was activated by DNA. Filamentous assemblies did not occur in the absence of inflammasome triggers and were never observed in cells expressing VHH NP1-EGFP. Based on the specificity of VHH_{ASC} for ASC^{CARD}, the EGFP structures seen upon NLRP3/AIM2 activation must be comprised of VHH_{ASC}-EGFP molecules aligned along ASC^{PYD} filaments, by binding to the free ASC^{CARD}. We therefore reasoned that NAIP/NLRC4 activation also involves the formation of ASC filaments polymerized via ASC^{PYD}. In that case, one or several initiator ASC molecules are presumably 'activated' by NLRC4 and turned into nucleators of ASC^{PYD} polymerization.

In summary, our data on VHH_{ASC}-EGFP filament formation demonstrate that the activation of NAIP/NLRC4 inflammasomes involves the formation of ASC filaments that assemble by polymerization of ASC^{PYD}. As in case of NLRP3, the ASC^{CARD} is likely to also have a dual role in inflammasome activation: it mediates cross-linking of linear ASC fibers, and recruits the effector pro-caspase-1 to the macromolecular complex.

VHH_{ASC}-EGFP Assembles Along ASC Filaments in Vaccinia Virus-infected Human Macrophages

To rule out that the observed VHH_{ASC}-EGFP assemblies along ASC^{PYD} filaments constitute an artifact of the monocytic leukemia cell line THP-1, we analyzed inflammasome activation in differentiated human macrophages derived from peripheral blood monocytes. To express VHH_{ASC}-EGFP in macrophages and at the same time activate inflammasomes, we generated a recombinant vaccinia virus (VACV) strain, which expresses VHH_{ASC}-EGFP or VHH NP1-EGFP under the control of an early viral promoter and mCherry under the control of a late viral promoter. Infection of mouse macrophages and THP-1 cells with this DNA virus induces

inflammasome activation in an AIM2 or NLRP3-dependent manner [37, 38]. Consistently, THP-1 cells infected with mature virions of VACV E VHH_{ASC}-EGFP exhibited filamentous EGFP-positive assemblies (data not shown). Many monocyte-derived macrophages infected with VACV E VHH_{ASC}-EGFP contained filamentous assemblies of EGFP, while control cells infected with VACV E VHH NP1-EGFP did not (**Figure 5.8C**). We did not observe mCherry expression in the vast majority of cells, suggesting that virus entry or early gene expression is sufficient for inflammasome activation. Of note, most VACV-infected human monocyte-derived macrophages exhibited signs of pyroptotic or apoptotic cell death, including nuclear fragmentation.

In conclusion, we found that VHH_{ASC}-EGFP assemblies along ASC^{PYD} filaments also occur in primary human macrophages and therefore visualize a genuine intermediate in inflammasome activation.

Discussions

Inflammasomes are critical information hubs of the innate immune system. A lack of appropriate tools to perturb inflammasomes in physiological conditions has hampered a more complete molecular understanding of the underlying cell biology and of the molecular interactions involved. We generated and characterized VHH_{ASC}, an alpaca single domain antibody that recognizes the CARD of the human inflammasome adapter ASC. Its introduction into the cytoplasm of living cells allowed us to occlude a key interaction interface of ASC, while leaving the function of its ASC^{PYD} unperturbed. This approach proved to be more informative than genetic ablation of ASC altogether. The application of VHHs to explore events in the cytoplasm complements more conventional genetic approaches: without having to resort to deletions or point mutations, protein-protein interactions can be perturbed conditionally. The ability of VHHs to serve as crystallization chaperones, also for proteins that have proven difficult to crystallize, allows identification of the exact molecular interfaces concerned. VHHs thus provide new mechanistic insights.

Using VHH_{ASC} we demonstrated the role of ASC in NLRP3, AIM2, and NAIP/NLRC4-dependent IL-1β secretion. VHH_{ASC} also allowed us to tease apart the functions of the ASC domains involved: ASC^{PYD} forms filaments in response to its direct nucleation by $NLRP3^{PYD}$ and $AIM2^{PYD}$, or in response to the engagement of linker ASC molecules by $NLRC4^{CARD}$ (**Figure 5.9A**). ASC^{CARD} appears critical in cross-linking the multiple ASC^{PYD} filaments formed (**Figure 5.9B**), which consolidates all ASC molecules into a single supramolecular organizing center (SMOC) [39, 40], also known as ASC speck or focus. Moreover, we confirmed the role of ASC^{CARD} in the recruitment and subsequent activation of pro-caspase-1.

Identification and characterization of VHH_{ASC} included solving the structure of the VHH_{ASC} alone and in complex with ASC^{CARD}. We thus established that VHH_{ASC} occludes the type II interface of the ASC^{CARD}. Immunoprecipitation experiments demonstrate that VHH_{ASC} readily interacts with ASC from unstimulated cells, suggesting that co-expressed VHH_{ASC} likely forms stable complexes with ASC in cells. We further showed that the type II interface of ASC is required for homotypic CARD/CARD interactions with other ASC molecules and pro-caspase-1, and that both interactions were perturbed by VHH_{ASC} in well-defined *in vitro* polymerization assays.

Our findings –*in* vitro, in cell lines, and in primary cells – expand a model of inflammasome activation that involves the local polymerization of inflammasome components, recently put forward based on *in vitro* studies and yeast prion assays [8, 9]. We demonstrate that endogenous ASC can form ASC^{PYD} filaments at endogenous ASC levels in the relevant cell type, ruling out any artifacts that may be caused by overexpression or by a lack of regulatory factors. Once NLRP3 is activated, $NLRP3^{PYD}$ directly nucleates ASC^{PYD} filaments by inducing an ASC conformation that drives polymerization. Assembly of NAIP/NLRC4 inflammasomes is a more intriguing case: activation of NAIP/NLRC4 by bacterial needle proteins yields ASC^{PYD} filaments as well. We therefore reasoned that $NLRC4^{CARD}$ must employ linker molecules of ASC via its CARD. This is in line with yeast prion assays, in which $NLRC4^{CARD}$-triggered formation of

Figure 5.9. Molecular Model of Inflammasome Activation

A. Mechanism of ASC filament formation nucleated by NLRP3 (left) and NAIP/NLRC4 (right).

B. Model of ASC filament cross-linking mediated by ASC^{CARD}.

C. Modeled structure of ASC filament covered with VHH_{ASC}. Relative arrangement of ASC^{PYD}, ASC^{CARD}, and VHH_{ASC} is shown. ASC^{CARD}/VHH_{ASC} unlikely follows the exact helical symmetry of the PYD filament core due to the flexible linker between PYD and CARD.

D. Schematic representation of ASC focus formation in unperturbed conditions, and formation of ASC filaments coated with VHH_{ASC}-EGFP.

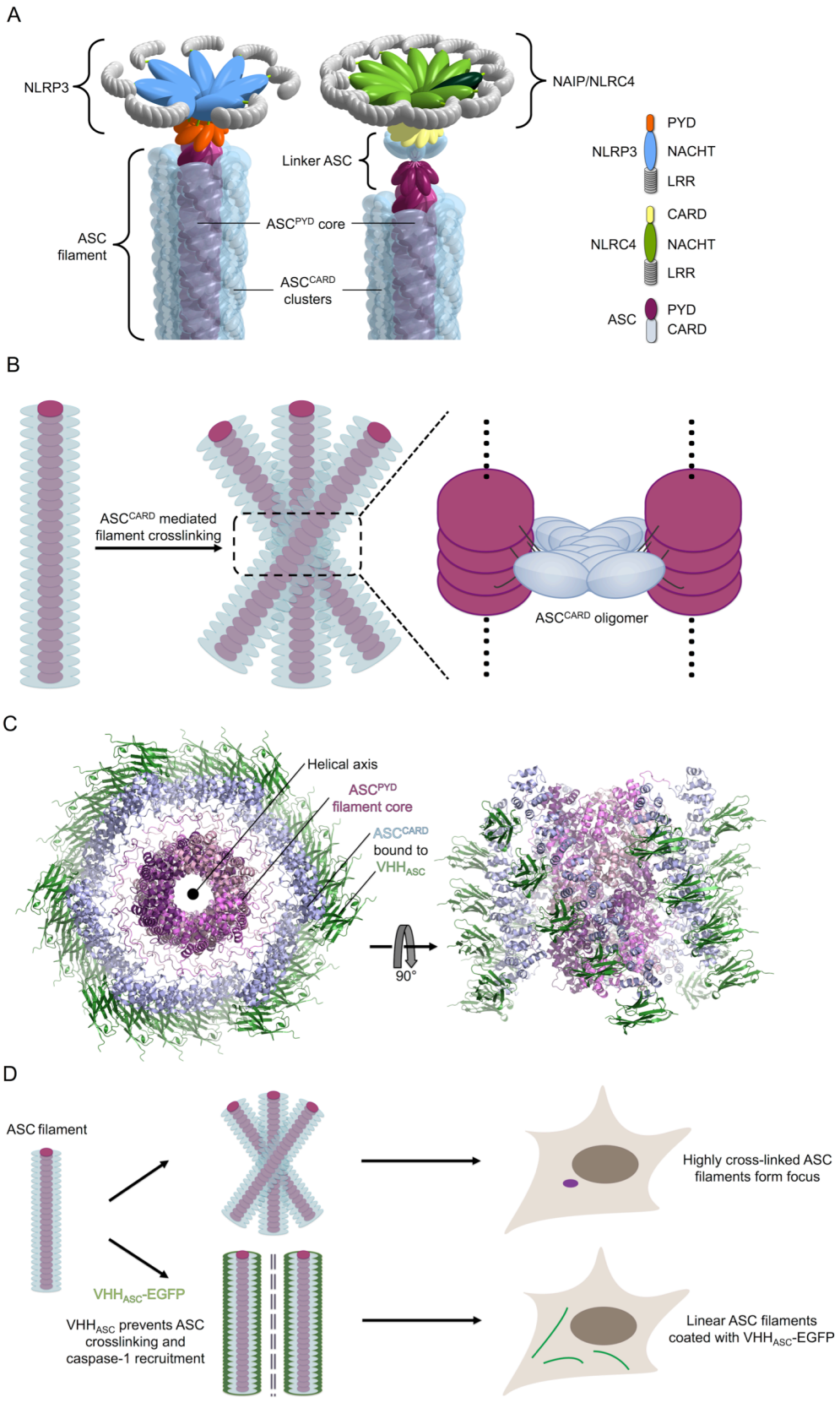

Figure 5.9 (Continued)

ASC–Sup35C prions was dependent on both oligomerization-competent PYD and CARD [9]. In a mechanism that requires further structural characterization, $NLRC4^{CARD}$ induces an active conformation of ASC by binding its ASC^{CARD}, which then nucleates PYD-mediated ASC filaments (**Figure 5.9A**). Mere engagement of the ASC CARD was not sufficient for activation, since binding of ASC^{CARD} by VHH_{ASC} neither induced the formation of filaments, nor led to IL-1β secretion. Similarly, in yeast experiments, $caspase\text{-}1^{CARD}$ was insufficient to induce polymerization of ASC–Sup35C prions [9]. In light of our structural understandings, the VHH_{ASC}/ASC complex would presumably retain its ability to interact with NLRC4. Since complex formation occludes only the type IIb interface, the intact type I, III, and IIa interfaces would allow the VHH_{ASC}-bound ASC to interact with activated NLRC4 by forming a small layer of ASC to nucleate ASC^{PYD} filament formation (**Figure 5.10**).

ASC is dispensable for NAIP/NLRC4-dependent pyroptosis in human cells, because VHH_{ASC} does not impair LDH release in response to MxiH treatment. Similarly, *Salmonella*-induced pyroptosis of mouse macrophages does not require ASC, while critical for efficient cytokine release [4]. Direct recruitment of pro-caspase-1 by NLRC4 may be sufficient to trigger caspase-1-dependent cell death. However, neutrophils are insensitive to pyroptosis when NAIP/NLRC4-dependent cytokine secretion was induced by *Salmonella* infection [41]. The fact that pyroptosis did not occur in neutrophils from $ASC^{-/-}$ mice, despite the presence of activated NLRC4 and pro-caspase-1, shows that regulation of pyroptosis is more complex than currently understood.

By masking the type II interface of ASC^{CARD}, but not ASC^{PYD}, we stabilized an intermediate state in inflammasome activation (**Figure 5.9C**). We often observed multiple ASC^{PYD} filaments at the same time, indicating that nucleation can occur at multiple sites. Typically, only a single ASC focus is observed per cell, which suggests that several ASC filaments coalesce into a single microscopical structure during inflammasome assembly. This requires ASC^{CARD}, which is in line with our observation that *in vitro* inclusion of VHH_{ASC} prevents

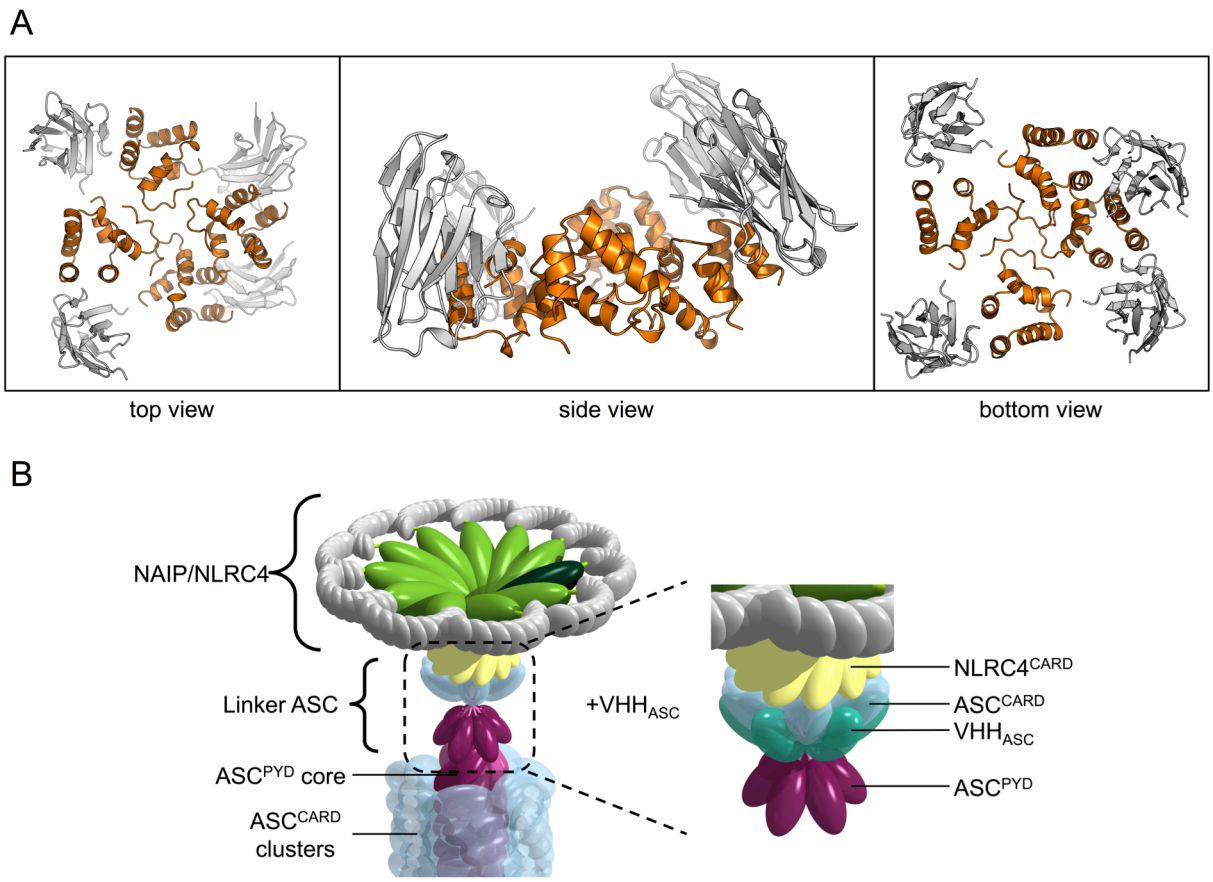

Figure 5.10. Model of Small Oligomer of ASC^{CARD} Complexed by VHH$_{ASC}$

A. An ASC^{CARD} oligomer (orange) with bound VHH$_{ASC}$ (gray) was modeled based on the MAVS^{CARD} filament symmetry and the ASC^{CARD}/VHH$_{ASC}$ structure. VHH$_{ASC}$ occludes type IIb interface of ASC^{CARD}, but does not interfere with small oligomer assembly.

B. A few ASC molecules bound to activated NLRC4 are sufficient to nucleate the formation of ASC^{PYD} filaments even in the presence of VHH$_{ASC}$.

ASC CARD/CARD interactions and blocks the cross-linking of full-length ASC filaments (**Figure 5.9D**). We cannot rule out that ASC^{CARD} might also facilitate a transport mechanism that brings multiple ASC filaments together. A coalescence step involving the crosslinking of multiple ASC filaments would elegantly explain the formation of inflammasomes involving different NLRs, such as the mixed NLRP3/NLRC4 inflammasomes observed in *Salmonella*-infected mouse macrophages [42]. Activation of different NLRs may trigger polymerization of individual ASC filaments that later join to form a single ASC focus. Lastly, masking ASC^{CARD} with VHH$_{ASC}$ also

prevents the recruitment of caspase-1 and therefore prevents the ultimate outcome of inflammasome activation, the autocatalytic activation of caspase-1. This work has implications for the development of anti-inflammatory agents that could work by targeting the type II interaction face on ASC^{CARD} and may pave the way for further perturbation studies using single domain antibodies as research tools.

References

1. Vanaja, S. K., Rathinam, V. A. & Fitzgerald, K. A. (2015) Mechanisms of inflammasome activation: recent advances and novel insights, *Trends in cell biology.* **25**, 308-315.

2. Yang, J., Zhao, Y., Shi, J. & Shao, F. (2013) Human NAIP and mouse NAIP1 recognize bacterial type III secretion needle protein for inflammasome activation, *Proceedings of the National Academy of Sciences of the United States of America.* **110**, 14408-13.

3. Vance, R. E. (2015) The NAIP/NLRC4 inflammasomes, *Curr Opin Immunol.* **32**, 84-9.

4. Broz, P., von Moltke, J., Jones, J. W., Vance, R. E. & Monack, D. M. (2010) Differential requirement for Caspase-1 autoproteolysis in pathogen-induced cell death and cytokine processing, *Cell Host Microbe.* **8**, 471-83.

5. Kortmann, J., Brubaker, S. W. & Monack, D. M. (2015) Cutting Edge: Inflammasome Activation in Primary Human Macrophages Is Dependent on Flagellin, *J Immunol.* **195**, 815-9.

6. Zhang, L., Chen, S., Ruan, J., Wu, J., Tong, A. B., Yin, Q., Li, Y., David, L., Lu, A., Wang, W. L., Marks, C., Ouyang, Q., Zhang, X., Mao, Y. & Wu, H. (2015) Cryo-EM structure of the activated NAIP2-NLRC4 inflammasome reveals nucleated polymerization, *Science.* **350**, 404-9.

7. Hu, Z., Zhou, Q., Zhang, C., Fan, S., Cheng, W., Zhao, Y., Shao, F., Wang, H. W., Sui, S. F. & Chai, J. (2015) Structural and biochemical basis for induced self-propagation of NLRC4, *Science.* **350**, 399-404.

8. Lu, A., Magupalli, V. G., Ruan, J., Yin, Q., Atianand, M. K., Vos, M. R., Schroder, G. F., Fitzgerald, K. A., Wu, H. & Egelman, E. H. (2014) Unified polymerization mechanism for the assembly of ASC-dependent inflammasomes, *Cell.* **156**, 1193-206.

9. Cai, X., Chen, J., Xu, H., Liu, S., Jiang, Q. X., Halfmann, R. & Chen, Z. J. (2014) Prion-like polymerization underlies signal transduction in antiviral immune defense and inflammasome activation, *Cell.* **156**, 1207-22.

10. Sborgi, L., Ravotti, F., Dandey, V. P., Dick, M. S., Mazur, A., Reckel, S., Chami, M., Scherer, S., Huber, M., Bockmann, A., Egelman, E. H., Stahlberg, H., Broz, P., Meier, B. H. & Hiller, S. (2015) Structure and assembly of the mouse ASC inflammasome by combined NMR spectroscopy and cryo-electron microscopy, *Proceedings of the National Academy of Sciences of the United States of America*.

11. Lechtenberg, B. C., Mace, P. D. & Riedl, S. J. (2014) Structural mechanisms in NLR inflammasome signaling, *Current opinion in structural biology.* **29**, 17-25.

12. Fernandes-Alnemri, T., Wu, J., Yu, J. W., Datta, P., Miller, B., Jankowski, W., Rosenberg, S., Zhang, J. & Alnemri, E. S. (2007) The pyroptosome: a supramolecular assembly of ASC dimers mediating inflammatory cell death via caspase-1 activation, *Cell Death Differ.* **14**, 1590-604.

13. Shenoy, A. R., Wellington, D. A., Kumar, P., Kassa, H., Booth, C. J., Cresswell, P. & MacMicking, J. D. (2012) GBP5 promotes NLRP3 inflammasome assembly and immunity in mammals, *Science.* **336**, 481-5.

14. Doxsey, S. J., Brodsky, F. M., Blank, G. S. & Helenius, A. (1987) Inhibition of endocytosis by anti-clathrin antibodies, *Cell.* **50**, 453-63.

15. Antonin, W., Holroyd, C., Fasshauer, D., Pabst, S., Von Mollard, G. F. & Jahn, R. (2000) A SNARE complex mediating fusion of late endosomes defines conserved properties of SNARE structure and function, *The EMBO journal.* **19**, 6453-64.

16. Hamers-Casterman, C., Atarhouch, T., Muyldermans, S., Robinson, G., Hamers, C., Songa, E. B., Bendahman, N. & Hamers, R. (1993) Naturally occurring antibodies devoid of light chains, *Nature.* **363**, 446-8.

17. Helma, J., Cardoso, M. C., Muyldermans, S. & Leonhardt, H. (2015) Nanobodies and recombinant binders in cell biology, *The Journal of cell biology.* **209**, 633-644.

18. Muyldermans, S. (2013) Nanobodies: natural single-domain antibodies, *Annual review of biochemistry.* **82**, 775-97.

19. Pardon, E., Laeremans, T., Triest, S., Rasmussen, S. G., Wohlkonig, A., Ruf, A., Muyldermans, S., Hol, W. G., Kobilka, B. K. & Steyaert, J. (2014) A general protocol for the generation of Nanobodies for structural biology, *Nature protocols.* **9**, 674-93.

20. Burg, J. S., Ingram, J. R., Venkatakrishnan, A. J., Jude, K. M., Dukkipati, A., Feinberg, E. N., Angelini, A., Waghray, D., Dror, R. O., Ploegh, H. L. & Garcia, K. C. (2015) Structural biology. Structural basis for chemokine recognition and activation of a viral G protein-coupled receptor, *Science.* **347**, 1113-7.

21. Irannejad, R., Tomshine, J. C., Tomshine, J. R., Chevalier, M., Mahoney, J. P., Steyaert, J., Rasmussen, S. G., Sunahara, R. K., El-Samad, H., Huang, B. & von Zastrow, M. (2013) Conformational biosensors reveal GPCR signalling from endosomes, *Nature.* **495**, 534-8.

22. Paalanen, M. M., Ekokoski, E., El Khattabi, M., Tuominen, R. K., Verrips, C. T., Boonstra, J. & Blanchetot, C. (2011) The development of activating and inhibiting camelid VHH domains against human protein kinase C epsilon, *European journal of pharmaceutical sciences : official journal of the European Federation for Pharmaceutical Sciences.* **42**, 332-9.

23. Kirchhofer, A., Helma, J., Schmidthals, K., Frauer, C., Cui, S., Karcher, A., Pellis, M., Muyldermans, S., Casas-Delucchi, C. S., Cardoso, M. C., Leonhardt, H., Hopfner, K. P. & Rothbauer, U. (2010) Modulation of protein properties in living cells using nanobodies, *Nature structural & molecular biology.* **17**, 133-8.

24. Ashour, J., Schmidt, F. I., Hanke, L., Cragnolini, J., Cavallari, M., Altenburg, A., Brewer, R., Ingram, J., Shoemaker, C. & Ploegh, H. L. (2015) Intracellular expression of camelid single-domain antibodies specific for influenza virus nucleoprotein uncovers distinct features of its nuclear localization, *Journal of virology.* **89**, 2792-800.

25. Barrios-Rodiles, M., Brown, K. R., Ozdamar, B., Bose, R., Liu, Z., Donovan, R. S., Shinjo, F., Liu, Y., Dembowy, J., Taylor, I. W., Luga, V., Przulj, N., Robinson, M., Suzuki, H., Hayashizaki, Y., Jurisica, I. & Wrana, J. L. (2005) High-throughput mapping of a dynamic signaling network in mammalian cells, *Science.* **307**, 1621-5.

26. Lin, S. C., Lo, Y. C. & Wu, H. (2010) Helical assembly in the MyD88-IRAK4-IRAK2 complex in TLR/IL-1R signalling, *Nature.* **465**, 885-890.

27. Ferrao, R. & Wu, H. (2012) Helical assembly in the death domain (DD) superfamily, *Current opinion in structural biology.* **22**, 241-7.

28. de Alba, E. (2009) Structure and interdomain dynamics of apoptosis-associated speck-like protein containing a CARD (ASC), *The Journal of biological chemistry.* **284**, 32932-41.

29. Wu, B., Peisley, A., Tetrault, D., Li, Z., Egelman, E. H., Magor, K. E., Walz, T., Penczek, P. A. & Hur, S. (2014) Molecular imprinting as a signal-activation mechanism of the viral RNA sensor RIG-I, *Mol Cell.* **55**, 511-23.

30. Guimaraes, C. P., Witte, M. D., Theile, C. S., Bozkurt, G., Kundrat, L., Blom, A. E. & Ploegh, H. L. (2013) Site-specific C-terminal and internal loop labeling of proteins using sortase-mediated reactions, *Nature protocols.* **8**, 1787-99.

31. Broz, P., Newton, K., Lamkanfi, M., Mariathasan, S., Dixit, V. M. & Monack, D. M. (2010) Redundant roles for inflammasome receptors NLRP3 and NLRC4 in host defense against Salmonella, *J Exp Med.* **207**, 1745-55.

32. Arora, N. & Leppla, S. H. (1993) Residues 1-254 of anthrax toxin lethal factor are sufficient to cause cellular uptake of fused polypeptides, *The Journal of biological chemistry.* **268**, 3334-41.

33. Young, J. A. & Collier, R. J. (2007) Anthrax toxin: receptor binding, internalization, pore formation, and translocation, *Annual review of biochemistry.* **76**, 243-65.

34. Masumoto, J., Taniguchi, S., Nakayama, J., Shiohara, M., Hidaka, E., Katsuyama, T., Murase, S. & Sagara, J. (2001) Expression of apoptosis-associated speck-like protein containing a caspase recruitment domain, a pyrin N-terminal homology domain-containing protein, in normal human tissues, *The journal of histochemistry and cytochemistry : official journal of the Histochemistry Society.* **49**, 1269-75.

35. Sahillioglu, A. C., Sumbul, F., Ozoren, N. & Haliloglu, T. (2014) Structural and dynamics aspects of ASC speck assembly, *Structure.* **22**, 1722-34.

36. Masumoto, J., Taniguchi, S. & Sagara, J. (2001) Pyrin N-terminal homology domain- and caspase recruitment domain-dependent oligomerization of ASC, *Biochem Biophys Res Commun.* **280**, 652-5.

37. Hornung, V., Ablasser, A., Charrel-Dennis, M., Bauernfeind, F., Horvath, G., Caffrey, D. R., Latz, E. & Fitzgerald, K. A. (2009) AIM2 recognizes cytosolic dsDNA and forms a caspase-1-activating inflammasome with ASC, *Nature.* **458**, 514-8.

38. Delaloye, J., Roger, T., Steiner-Tardivel, Q. G., Le Roy, D., Knaup Reymond, M., Akira, S., Petrilli, V., Gomez, C. E., Perdiguero, B., Tschopp, J., Pantaleo, G., Esteban, M. & Calandra, T. (2009) Innate immune sensing of modified vaccinia virus Ankara (MVA) is mediated by TLR2-TLR6, MDA-5 and the NALP3 inflammasome, *PLoS pathogens.* **5**, e1000480.

39. Kagan, J. C., Magupalli, V. G. & Wu, H. (2014) SMOCs: supramolecular organizing centres that control innate immunity, *Nature reviews Immunology.* **14**, 821-6.

40. Hauenstein, A. V., Zhang, L. & Wu, H. (2015) The hierarchical structural architecture of inflammasomes, supramolecular inflammatory machines, *Current opinion in structural biology.* **31**, 75-83.

41. Chen, K. W., Gross, C. J., Sotomayor, F. V., Stacey, K. J., Tschopp, J., Sweet, M. J. & Schroder, K. (2014) The neutrophil NLRC4 inflammasome selectively promotes IL-1beta maturation without pyroptosis during acute Salmonella challenge, *Cell reports.* **8**, 570-82.

42. Man, S. M., Hopkins, L. J., Nugent, E., Cox, S., Gluck, I. M., Tourlomousis, P., Wright, J. A., Cicuta, P., Monie, T. P. & Bryant, C. E. (2014) Inflammasome activation causes dual recruitment of NLRC4 and NLRP3 to the same macromolecular complex, *Proceedings of the National Academy of Sciences of the United States of America.* **111**, 7403-8.

Chapter Six

A Filament Capping Mechanism Underlies Homotypic CARD-CARD Interaction

Citation. This chapter has been assembled with minor modifications from the longer version of the accepted manuscript:

Nature Structure & Molecular Biology (accepted manuscript)

Molecular basis of caspase-1 polymerization and its inhibition by a new capping mechanism

Alvin Lu[1,2,†], Yang Li[1,2,†], Florian I. Schmidt[3], Qian Yin[1,2], Shuobing Chen[4,5], Tian-Min Fu[1,2], Alexander B. Tong[1,2], Hidde L. Ploegh[3,6], Youdong Mao[4,5,7], and Hao Wu[1,2,*]

[1]Department of Biological Chemistry and Molecular Pharmacology, Harvard Medical School, Boston, MA 02115

[2]Program in Cellular and Molecular Medicine, Boston Children's Hospital, Boston, MA 02115

[3]Whitehead Institute for Biomedical Research, Cambridge, MA 02142

[4]Center for Quantitative Biology, Peking-Tsinghua Joint Center for Life Sciences, Academy for Advanced Interdisciplinary Studies, State Key Laboratory for Artificial Microstructures and Mesoscopic Physics, School of Physics, Peking University, Beijing 100871, China

[5]Department of Cancer Immunology and Virology, Intel Parallel Computing Center for Structural Biology, Dana-Farber Cancer Institute, Boston, MA 02215

[6]Department of Biology, Massachusetts Institute of Technology, Cambridge, MA 02139

[7]Department of Microbiology and Immunobiology, Harvard Medical School, Boston, MA 02115

[†]Co-first authors

*Corresponding author

Contributions. This study was the collaborative effort of several Wu lab members, with the help from the Mao lab and the Ploegh lab. I am grateful to have worked in such collaborative environment and would like to thank everyone for contribution in various aspects of this project.

Dr. Li, Dr. Schmidt, Dr. Yin, Mr. Chen, Dr. Fu, Professor Mao, and I performed the experiments and analyzed the data. I purified the recombinant proteins and performed biochemical experiments, with the help of Dr. Yin and Dr. Fu. Mr. Chen, under the supervision of Professor Mao, prepared the cryo-EM grids of purified caspase-1^{CARD} filaments and collected the cryo-electron micrographs. Dr. Li processed the cryo-EM data and completed the helical reconstruction. Mr. Tong provided help on Rosetta refinement of the capase-1^{CARD} structure. Dr. Schmidt generated stable cell lines and performed cellular assays under the supervision of Professor Ploegh. Professor Wu and I together analyzed the caspase-1^{CARD} filament structure, performed homology modeling of CARD-only proteins, proposed the capping model of inhibition, and wrote the manuscript.

Supplemental materials. Eight Supplemental Figures (Figures S6.1-6.8), Materials and Methods, and Supplemental References can be found in Appendix V.

Abstract

Inflammasomes are cytosolic caspase-1 activation complexes that sense intrinsic and extrinsic danger signals to trigger inflammatory responses and pyroptotic cell death. Homotypic interactions by Pyrin domains (PYD) and caspase recruitment domains (CARD) in inflammasome component proteins mediate oligomerization into filamentous assemblies. Several cytosolic proteins consisting of only the interaction domains exert inhibitory effects on inflammasome assembly. In this study, we determined the structure of caspase-1^{CARD} filament by cryo-electron microscopy and investigated the biophysical properties of two caspase-1-like CARD-only proteins, inhibitor of CARD (INCA or CARD17) and ICEBERG (or CARD18). Our results show that INCA caps caspase-1 filament, thereby exerting potent inhibition with low nanomolar K_i on caspase-1^{CARD} polymerization *in vitro* and inflammasome activation in cells. While caspase-1^{CARD} uses six complementary surfaces of three types for filament assembly, INCA is defective in two of the six interfaces to terminate caspase-1 filament.

Introduction

As the first line of defense, supramolecular assemblies known as inflammasomes activate inflammatory caspases in response to pathogenic invasion and cellular perturbation [1]. These elaborate complexes in the cytosol typically consist of an upstream sensor component, an adaptor component, and a downstream effector component, including caspase-1, caspase-11 (mouse), and caspase-4 and -5 (human). The sensor proteins, such as absent in melanoma 2 (AIM2)-like receptors (ALRs) and nucleotide-binding domain (NBD) and leucine-rich repeat (LRR) containing proteins (NLRs) [2], respond to a variety of pathogen-associated molecular patterns (PAMPs) including cytosolic dsDNA and bacterial flagellin, as well as danger-associated molecular patterns (DAMPs) such as an abrupt increase in extracellular ATP level, uric acid crystals, or generation of reactive oxygen species. Once activated, a sensor protein interacts with an adaptor molecule that links the sensor to inflammatory caspase recruitment,

dimerization, and auto-proteolytic activation. Activated caspases proteolytically process pro-interleukin-1β (pro-IL-1β) and pro-interleukin-18 (pro-IL-18). The mature cytokines, once released, can initiate downstream signaling events leading to the transcription of many pro-inflammatory and antiviral genes [3]. Inflammatory caspase activation can also lead to pyroptotic cell death characterized by spillage of cellular contents.

Sensor proteins in the ALR family typically contain an N-terminal Pyrin domain (PYD) and a C-terminal DNA binding domain known as hematopoietic expression, interferon-inducibility, nuclear localization (HIN) domain [4, 5]. Most NLRs consist of an N-terminal interaction domain (e.g. a PYD), a central NBD, and a C-terminal LRR domain. Through homotypic PYD-PYD interactions, the sensor proteins with a PYD domain recruit the bipartite apoptosis-associated speck-like protein containing a CARD (ASC), which contains an N-terminal PYD and a C-terminal caspase recruitment domain (CARD). ASC is responsible for recruitment of caspase-1 by CARD-CARD interactions. Both PYD and CARD belong to the death domain (DD) fold superfamily and have a six-helix bundle structure [6]. In contrast, the NLR family proteins NLRBs (also known as NAIPs) do not contain a PYD or CARD and signal through the recruitment of the CARD containing NLRC4 as an adaptor [7, 8]. The NAIP/NLRC4 complexes recruit caspase-1 in a manner similar to the ASC/caspase-1 interaction, using CARD-CARD interactions [7, 9, 10]. Hence, CARD-CARD interactions are essential for the assembly of all inflammasomes. Recent studies support that both PYD-PYD and CARD-CARD interactions are mediated by nucleated polymerization and filament formation [11, 12]. Sensor PYDs nucleate ASC^{PYD} filament formation, which in turn clusters ASC^{CARD} to template the polymerization of $caspase\text{-}1^{CARD}$ filaments [13]. Nucleated polymerization elegantly explains the mechanism of signal amplification in inflammasome activation [14].

Inflammasomes are regulated by a set of inhibitory molecules to prevent their over-activation [15]. Some of these endogenous inhibitors mimic the interaction domains in inflammasome components and use disctinctive inhibitory mechanisms. For example, mouse

p202 lacks a PYD, but contains two HIN domains of which the first HIN domain interacts with dsDNA. We previously found that the second HIN domain in p202 specifically interacts with the AIM2 HIN domain, resulting in preferential co-recruitment of p202 and AIM2 to the same dsDNA. This co-recruitment dilutes the local concentration of AIM2 PYD to suppress AIM2 activation, a phenomenon that is associated with lupus-like diseases in mice [5].

A number of PYD-only proteins (POPs) and CARD-only proteins (COPs) have been identified to inhibit inflammasome formation and cytokine maturation [16-22]. Regulation by COPs is proposed to arise because of selective pressure and the need for higher tolerance for inflammatory stimuli. Interestingly, rodents and primates all have caspase-1, but COPs are only found in higher primates, suggesting that the emergence of these genes must originate after the human/mouse divergence [22]. The genes of proposed CARD-only inhibitors, COP1 (also known as Pseudo-ICE and CARD16), INCA (also known as CARD17), and ICEBERG (also known as CARD18), are close to the caspase-1 locus as a result of a series of gene duplication events [23]. New stop codons led to transcripts missing several downstream exons, resulting in the translation of CARDs lacking the caspase domain [24, 25]. COP1 has a shorter isoform that is nearly identical to caspase-1 CARD, suggesting that it mediates the same interactions that caspase-1 does, thereby acting as a decoy to inhibit caspase-1 activation. The longer isoform of COP1 contains an additional ~100 residues C-terminal to the CARD, suggesting that there might be additional mechanisms at play. INCA and ICEBERG have 83% and 53% identity to caspase-1 CARD respectively and may have evolved new mechanisms of action. Additionally, INCA and caspase-1 are simultaneously upregulated by INF-γ in human monocytic cell lines THP-1 and U937, and ICEBERG, but not INCA, is induced by LPS and TNF-α [19, 20]. Therefore, INCA and ICEBERG may play distinct roles in different biological settings.

To determine how CARD-CARD interactions activate and regulate the inflammasome assembly, we determined the caspase-1^{CARD} filament structure by cryo-electron microscopy (cryo-EM), and performed detailed biochemical analyses to understand the mechanisms of

inhibition by INCA and ICEBERG. Our results define the role of a CARD complex in the pathway and uncover differential functional effects of ICEBERG and INCA. ICEBERG can nucleate caspase-1 filament formation and incorporate into caspase-1 filaments, but it fails to inhibit inflammasome activation. As previously suggested, ICEBERG may function by interfering with the interaction of caspase-1 with other CARD-containing proteins [21]. In contrast to ICEBERG, we find that INCA caps caspase-1^{CARD} oligomers to prevent their polymerization, and hence robustly inhibits inflammasome assembly *in vitro* at low nM concentrations. Induced expression of INCA in the THP-1 cell line strongly inhibits inflammasome activation.

Results

Cryo-EM reconstruction of the caspase-1^{CARD} filament

To visualize the molecular interactions critical for inflammasome assembly, we determined the structure of caspase-1^{CARD}, which is the first oligomeric CARD structure in the inflammasome pathway. Similar to ASC^{PYD}, caspase-1^{CARD} exhibited a high tendency to self-oligomerize into filaments. Because the question of whether these CARD filaments show any structural similarity to the PYD filaments remained to be addressed, we set out to purify soluble caspase-1^{CARD} filaments suitable for cryo-EM study. Our previous studies on death domain fold proteins suggested that filaments formed *in vitro* upon removal of a solubility tag from purified monomeric fusion proteins are more homogenous than those formed in *E. coli* during protein expression [26]. Therefore, we used this strategy and first generated a fusion construct with maltose binding protein (MBP), His-MBP-caspase-1^{CARD}. However, this construct appeared to be aggregated on a size-exclusion column, and removal of the MBP tag resulted in bundled filaments (data not shown). We then generated a His-MBP-caspase-1^{CARD}-SUMO fusion construct (termed sandwich-tagged) in order to disrupt caspase-1^{CARD} self-oligomerization during over-expression in *E. coli* (**Figure 6.1A**). The fusion protein was purified by size-

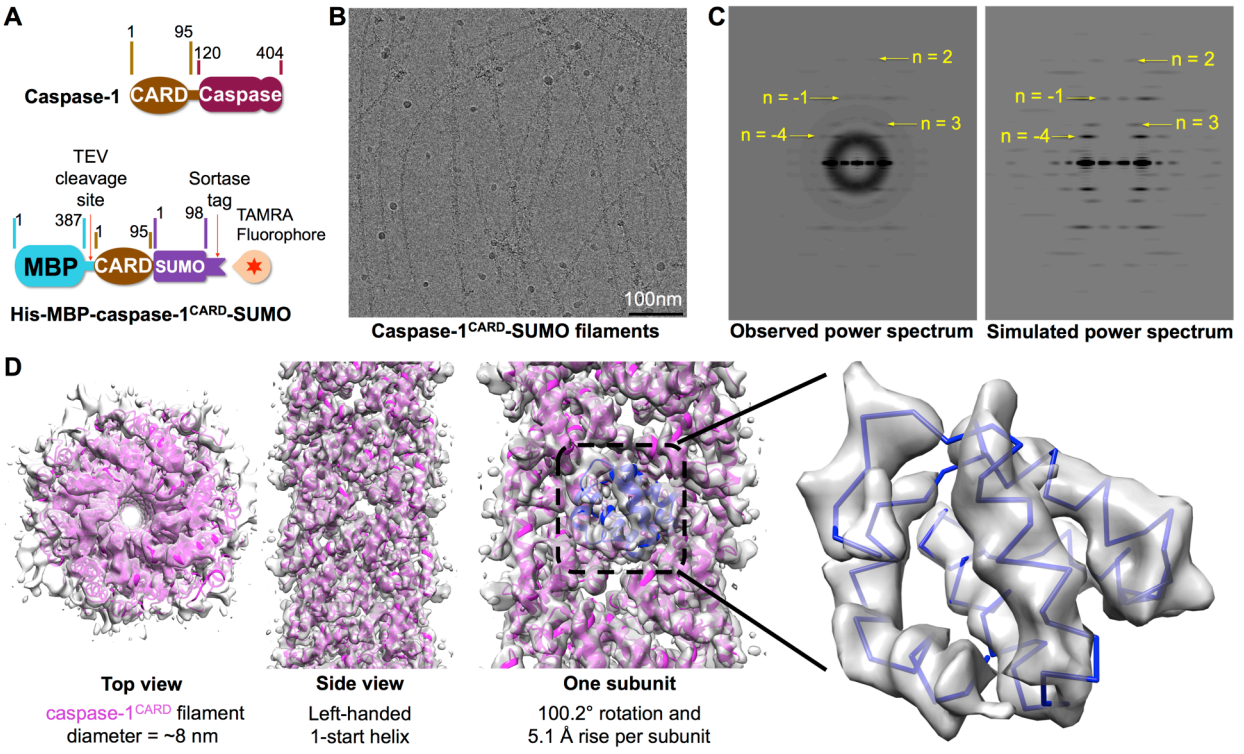

Figure 6.1. Cryo-EM structure determination of the caspase-1^{CARD} filament.

A. Domain organizations of pro-caspase-1 and its CARD construct for reconstruction and *in vitro* fluorescence polarization assay.

B. A representative cryo-EM image.

C. Close agreement between experimental and simulated power spectra. Selective layer lines are labeled.

D. Reconstructed cryo-EM map fitted with caspase-1^{CARD} model in magenta with one subunit highlighted in blue. At the right, cryo-EM density is shown in zoom and superimposed with a fitted caspase-1^{CARD} molecule.

exclusion as a monomer, and upon removal of the N-terminal His-MBP tag by the Tobacco Etch Virus (TEV) protease, spontaneously formed extended individual filaments of a few hundred nanometers in length, as seen on cryo-electron micrographs (**Figure 6.1B**).

An averaged power spectrum exhibited clear layer lines but lacked a meridional maximum (**Figure 6.1C, Figure S6.1A**). The absence of the first meridional reflection might be due to sample heterogeneity or insignificant image quality. Because the visible layer lines bear

close resemblance to those of the MAVS^{CARD} filament in the RIG-I pathway [27], we tested the assumption that the rise per subunit would be similar, about 5.1 Å. We found that the hypothetical helical parameters fitted well with the rest of the visible layer lines, leading to a calculated initial 1-start helical symmetry of -100.23° and 5.06 Å in rotation and rise per subunit respectively (**Figure 6.1C**). Beginning from a solid cylinder model and using iterative helical real-space reconstruction (IHRSR) [28], we obtained a final volume containing mostly α-helices with refined helical parameters of -100.21° and 5.10 Å (**Figure 6.1D**). A homology structure model of caspase-1^{CARD} that we derived from the NMR structure of ICEBERG [20] could readily be positioned into the density, indicating the correctness of the reconstruction (**Figure 6.1D, Figure S6.1B-C**). The reconstructed volume also had disordered density outside the caspase-1^{CARD} filament core, which may correspond to the flexible C-terminal SUMO-tag (**Figure 6.1D**). We estimated the reconstruction as ~4.8 Å using both gold standard and model versus map Fourier shell correlation plots, with resolved density for some large side chains (**Figure S6.1B-E**), including many at the interface (see below). The final caspase-1^{CARD} model is very similar to the ICEBERG structure (**Figure S6.1F-G**).

Structure of the caspase-1^{CARD} filament reveals CARD-CARD interactions in inflammasome assemblies

Caspase-1^{CARD} forms a left-handed 1-start helical assembly that resembles the crystal structure of the Myddosome death domain complex [29]. The diameter of the filament is approximately 8 nm, with an inner hole of < 1 nm (**Figure 6.2A**). This is in contrast to the more loosely packed ASC^{PYD} filament with a larger inner hole [11] and the more tightly packed MAVS^{CARD} filament with virtually no inner hole [27]. Within this helical assembly, caspase-1^{CARD} subunits pack into an arrangement similar to the Myddosome DD complex and the MAVS^{CARD} filament consisting of roughly four subunits per turn (**Figure 6.2B**), using the previously defined three types of asymmetric interactions [6, 30]. The type III interface harbors interactions in the

helical strand direction. The Type I and type II interfaces provide interaction between the helical turns (**Figure 6.2C**). The type I interface is the most extensive of the three types, with electrostatic complementarity (**Figure 6.2D**). Because of the potential inaccuracies in side chain conformations at this resolution, we describe the type Ia patch as collectively involving residues in helices α1 and α4 (such as K11, R10, R15, R55, and D52), which interact with residues in helix α2 (such as Q31, E28, D27, and N23) (**Figure 6.2E**). In contrast, the type II interaction requires an exposed hydrophobic residue, Y82 in the α5-α6 loop of one subunit, to be inserted into the α2-α3 loop of the adjacent subunit (**Figure 6.2F**). The type III interface appears to be the least extensive and may contribute less binding energy during filament formation (**Figure 6.2G**).

In order to validate the importance of these interfacial residues, we generated site-directed mutants and compared their properties with wild-type (WT) caspase-1^{CARD} using two different methods (**Figure 6.2H-I**). We used GFP-tagged caspase-1^{CARD} for these experiments because the fusion protein mostly formed soluble short filaments, similar to the GFP-$AIM2^{PYD}$ protein [31]. We first analyzed whether the mutations reduced the aggregation tendency of GFP-tagged caspase-1^{CARD} using size-exclusion chromatography. We then determined whether the mutations decreased the ability of GFP-tagged caspase-1^{CARD} to promote filament formation of wild-type monomeric caspase-1^{CARD} using fluorescence polarization (FP). For the second experiment, we added a C-terminal sortase motif to the His-MBP-caspase-1^{CARD}-SUMO construct used for cryo-EM. The fusion protein was labeled with the fluorophore TAMRA using recombinant sortase A (**Figure 6.1A**) [32], and caspase-1^{CARD} polymerization was initiated upon removal of the His-MBP tag by the TEV protease. In the absence of a potent nucleator, the caspase-1^{CARD} self-polymerization rate was low at the 4 μM concentration used in the experiment (**Figure S6.2**). The presence of an aggregated nucleator such as GFP-tagged caspase-1^{CARD}, which forms short filaments [11], greatly enhanced the rate of polymerization, as indicated by increases of FP values (**Figure S6.2)**. The apparent nucleation potency of wild-type

Figure 6.2. Structural analysis of the caspase-1^{CARD} filament.

A. Surface representation of the caspase-1^{CARD} filament structure. Different subunits are shaded with colors from warm to cold.

B. A schematic diagram of the helical filament, with three neighboring subunits highlighted in magenta, green, and cyan.

C. Relative orientations of the type Ia, Ib, IIa, IIb, IIIa, and IIIb patches.

D. Electrostatic surface renderings of a tetrameric turn showing complementary charges.

E-G. The type I, II, and III interfaces, respectively. Given the current resolution, the precise side chain conformations are not implied in the representation.

H. Size-exclusion chromatography analysis showing void and soluble fractions of wild-type and mutant capsase-1^{CARD}.

I. Void fractions of WT and mutants were further assayed for their potency to nucleate monomeric wild-type caspase-1^{CARD} to form filaments. Approximately 140 nM of each nucleator sample and TEV protease were added to 4 μM of TAMRA-labeled His-MBP-caspase-1^{CARD}-SUMO for polymerization.

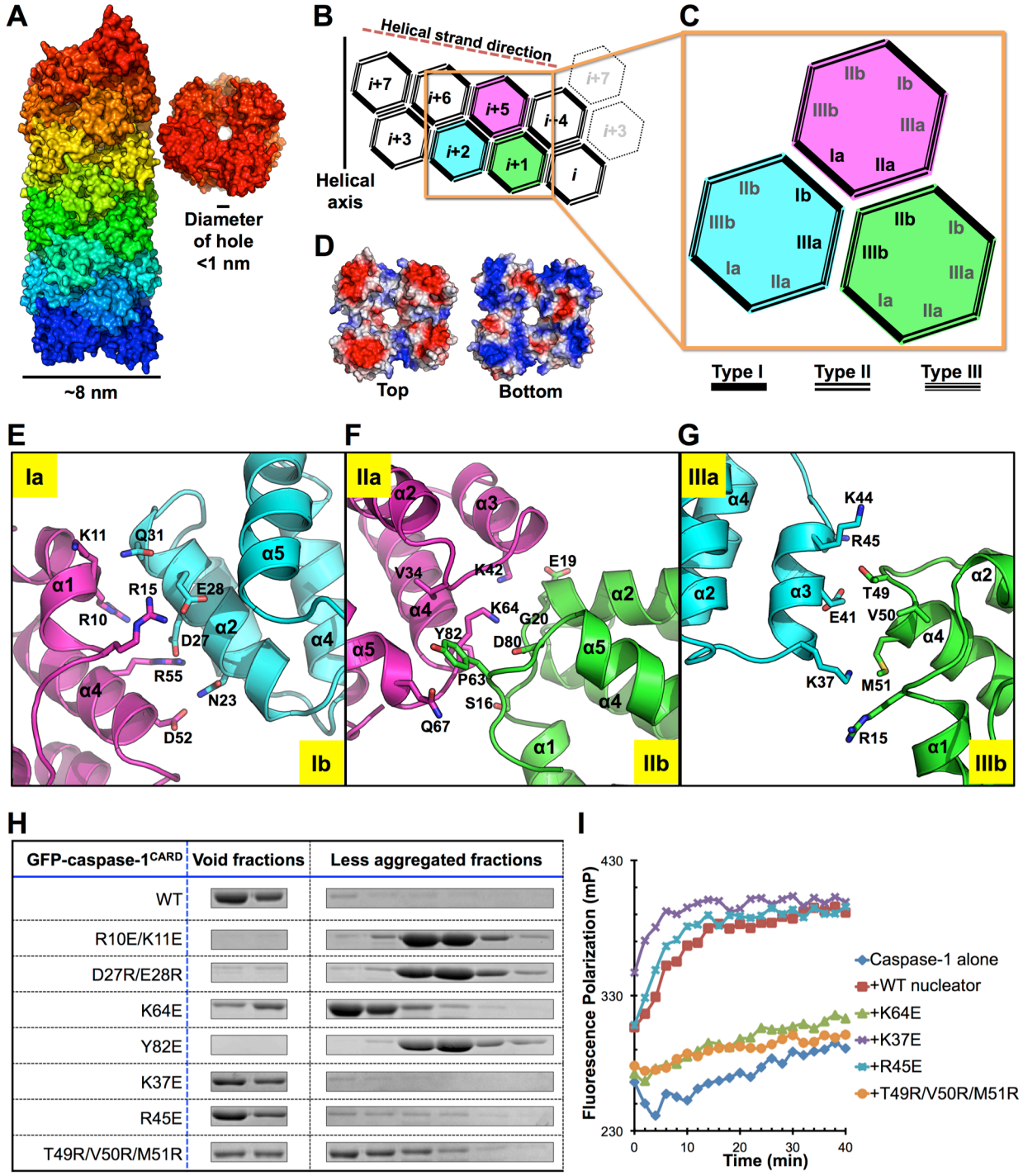

Figure 6.2 (Continued)

GFP-tagged caspase-1^{CARD} was shown to be ~283.0 ± 1.4 nM (**Figure S6.2**). This assay allowed us to test the effects of caspase-1^{CARD} mutations on caspase-1/caspase-1 interactions, as well as on caspase-1^{CARD} interactions with other proteins in later parts of this study.

While GFP-tagged wild-type caspase-1^{CARD} eluted exclusively at the void volume of a Superdex 200 gel filtration column, charge-reversal mutants of type Ia (R10E/K11E) and Ib (D27R/E28R) patches abolished caspase-1^{CARD} filament formation, which reflected the importance of electrostatic interactions at the type I interface (**Figure 6.2H**). The Y82E mutant at the type IIb patch also completely abolished filament formation. In contrast, the charge reversal mutant on the type IIa patch, K64E, only impaired, but did not eliminate, filament formation, suggesting that the type II interface is likely contributed predominately by hydrophobic interactions. In the caspase-1^{CARD} polymerization assay, K64E was completely incapable of nucleating wild-type caspase-1^{CARD} filament formation (**Figure 6.2I**). Charge reversal mutants at the type IIIa patch (K37E or R45E) did not affect either filament formation or nucleation. Only a more drastic triple mutant (T49R/V50R/M51R) at the type IIIb surface impaired aggregation and nucleation potency (**Figure 6.2H-I**), consistent with the small surface contact at the type III interface. These results correlate well with our analysis of the caspase-1^{CARD} cryo-EM structure.

Comparison of the casepase-1^{CARD} structure to other death domain complexes

Our caspase-1^{CARD} structure provides molecular details of a signaling filament in the inflammasome pathway. The crystal and cryo-EM structures of the RIG-I^{CARD}/MAVS^{CARD} system revealed critical details of the CARD-CARD interaction in that system [27]. However, despite being in the same death domain fold subfamily, caspase-1^{CARD} and MAVS^{CARD} have very little sequence similarity. In our hands, structural modeling by sequence comparison failed to accurately predict the interfaces. Therefore, the caspase-1^{CARD} structure enables us to identify the interfacial residues as well as the locations of the characteristic three types of interactions.

We compared the caspase-1^{CARD} filament structure to other existing DD fold complexes by pairwise structural alignment between isolated dimers of caspase-1^{CARD} and dimers of other DD fold complexes. Within the CARD subfamily, MAVS^{CARD} is the only other high-resolution filament structure recently determined by cryo-EM. Despite having very low sequence identity, the helical parameters of MAVS^{CARD} and caspase-1^{CARD} are similar, which might have been determined by the relative orientations of the interfaces (**Figure S6.3A-C**). We also compared the buried residues in respect to each type of interaction, showing that the relative location of these residues indeed correlates very well between the two CARDs (**Figure S6.3D**). To have a quantitative comparison, we aligned one subunit of each interface type and measured how much rotation was required to overlap the other subunit (**Figure S6.3E**). Between MAVS^{CARD} and caspase-1^{CARD}, rotations for type I, II, and III were 10.2˚, 8.1˚, and 14.1˚, respectively. For comparisons of caspase-1^{CARD} interactions with those of MyD88^{DD} and RAIDD^{DD}, the rotations were respectively 14.1˚/8.3˚/13.3˚ and 10.6˚/11.3˚/21.8˚, indicating the more dissimilar quaternary structures. Overall, these angular differences were smaller than the relative rotations between interactions in the caspase-1^{CARD} filament and the ASC^{PYD} filament (14.8˚/32.5˚/42.3˚). Caspase-1^{CARD} filament, MAVS^{CARD} filament, and the Myddosome are all left-handed 1-start helical assembly, while the ASC^{PYD} filament is a right-handed three-start helical assembly [11].

INCA displays distinct properties from caspase-1^{CARD} and ICEBERG

To compare behavior of INCA, ICEBERG, and caspase-1^{CARD}, we expressed 6x-Histidine-tagged (His) human INCA and ICEBERG in *E. coli*. While INCA was soluble and could be purified by Ni-NTA affinity chromatography, ICEBERG remained in the insoluble fraction after centrifugation of the lysate (**Figure 6.3A**). Furthermore, INCA eluted as a monomer from size-exclusion chromatography (**Figure 6.3B**). To investigate the biochemical properties of ICEBERG, it was fused to the C-terminus of His-MBP to increase the solubility. His-MBP-ICEBERG was soluble and could be purified using Ni-NTA affinity chromatography. The fusion

protein eluted from the void fraction of a Superdex 200 size-exclusion column. Removal of the His-MBP tag using the TEV protease resulted in long and bundled filaments, shown by negative-stain electron microscopy (EM) (**Figure 6.3C**). These initial observations led us to ponder why INCA would behave so differently from ICEBERG and caspase-1^{CARD}.

The NMR structure of ICEBERG determined at pH 3.8 [20] to prevent aggregation shows a typical CARD structure with a six-helix bundle fold that is also very similar to that of ASC^{CARD} [33]. INCA has 55% sequence identity to ICEBERG with no gaps in the alignment and its predicted secondary structures are identical to those of ICEBERG (**Figure 6.3D**). Yet, ICEBERG and INCA have contrasting biophysical properties in solution. Sequence comparisons revealed identities of 53% for ICEBERG and caspase-1^{CARD}, and 83% for INCA and caspase-1^{CARD} (**Figure 6.3D**). Therefore, it is the less homologous ICEBERG that shares the filament forming ability of caspase-1^{CARD}, while INCA is monomeric. These observations suggest that the biochemical mechanisms of inflammasome inhibition by these two COPs may be quite distinct and require further investigation.

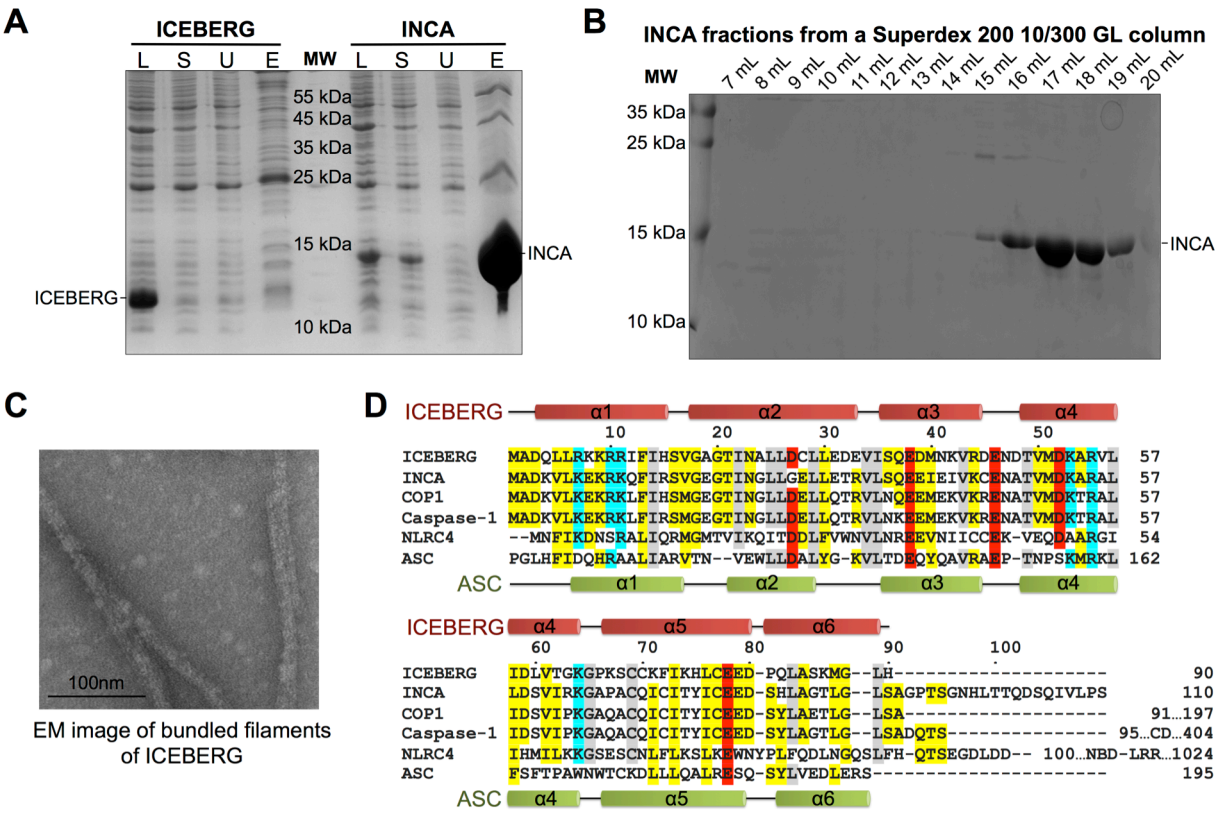

EM image of bundled filaments of ICEBERG

Figure 6.3. ICEBERG is filamentous while INCA is monomeric.

A. Coomassie Blue-stained SDS-PAGE gel for Ni-NTA affinity purification of *E. coil* expressed 6xHis-tagged ICEBERG and INCA. L: whole cell lysate. S: soluble fraction. U: Ni-NTA unbound fraction. E: Ni-NTA elution. ICEBERG appeared as aggregate (at ~12kDa) and INCA (at ~15kDa) could bind to Ni-NTA beads.

B. Superdex 200 size exclusion chromatography profile of His-tagged INCA. INCA eluted at monomeric position.

C. Negative-stain electron micrograph of MBP-tagged ICEBERG after MBP cleavage. Untagged ICEBERG formed bundled filaments.

D. Sequence alignment of ICEBERG, INCA, COP1, ASC^{CARD}, NLRC4^{CARD}, and caspase-1^{CARD}. Secondary structures are labeled for ICEBERG and ASC^{CARD}. Regions outside of the aligned CARDs are indicated by residue numbers at the end of the alignment. Caspase-1 has a caspase domain (CD) ending with residue 404. COP-1 has a C-terminal region spanning roughly 100 residues with an unknown fold. NLRC4 has a nucleotide-binding domain (NBD) followed by leucine-rich repeats (LRR) which ends with residue 1024.

ICEBERG enhances caspase-1^{CARD} filament formation while INCA inhibits nucleated caspase-1^{CARD} polymerization

We used the caspase-1^{CARD} polymerization assay to probe the effects of the COPs on caspase-1 polymerization. Upon removal of the His-MBP tag by addition of the TEV protease, caspase-1^{CARD}-SUMO formed filaments at a negligibly slow rate as shown by the minimal change in FP (**Figure 6.4A**). ICEBERG greatly enhanced formation of caspase-1^{CARD} filaments, suggesting that oligomeric ICEBERG provided seeds for polymerization of monomeric caspase-1^{CARD}. In contrast, addition of INCA did not have significant effects on caspase-1^{CARD} filament formation at its low basal rate.

In ASC-dependent inflammasomes, it is the CARD of the adaptor ASC that nucleates caspase-1^{CARD} polymerization [11]. To recapitulate this *in vitro*, we expressed His-GFP fused to ASC^{CARD}, the majority of which eluted at the void volume of a Superdex 200 size-exclusion column (**Figure 6.4B**). Negative-stain EM indicated that the protein formed short His-GFP-ASC^{CARD} filaments (**Figure 6.4C**). Addition of these ASC^{CARD} filaments at levels well below stoichiometry robustly potentiated caspase-1^{CARD} polymerization, with an apparent dissociation constant (K_{app}) of 108.0 ± 1.4 nM (**Figure 6.4D**). Using fixed His-GFP-ASC^{CARD} and caspase-1^{CARD} concentrations, we added sub-stoichiometric amounts of INCA, and measured the rates of filament formation. Strikingly, very low concentrations of INCA were sufficient to greatly inhibit caspase-1^{CARD} filament formation (**Figure 6.4E**). The apparent inhibitory constant (K_i) was measured at 9.4 ± 1.4 nM (**Figure 6.4E**).

To address the question whether ICEBERG could interact with ASC^{CARD}, we designed an ASC^{CARD} polymerization assay similar to the caspase-1^{CARD} assay. We expressed and purified monomeric His-MBP-ASC^{CARD}-SUMO with a C-terminal sortase motif and labeled the protein with the TAMRA fluorophore *in vitro* using recombinant sortase A. Upon addition of the TEV protease, filamentous His-GFP-ASC^{CARD} acted as a nucleator to polymerize the labeled, His-MBP removed monomeric ASC^{CARD}-SUMO, indicated by increasing FP as a function of

time. In contrast, ICEBERG failed to promote ASC^{CARD} filament formation (**Figure S6.4A**). Moreover, ICEBERG did not inhibit His-GFP-ASC^{CARD} nucleated ASC^{CARD} polymerization (**Figure S6.4B**). We conclude that there is no apparent interaction between ICEBERG and ASC^{CARD}.

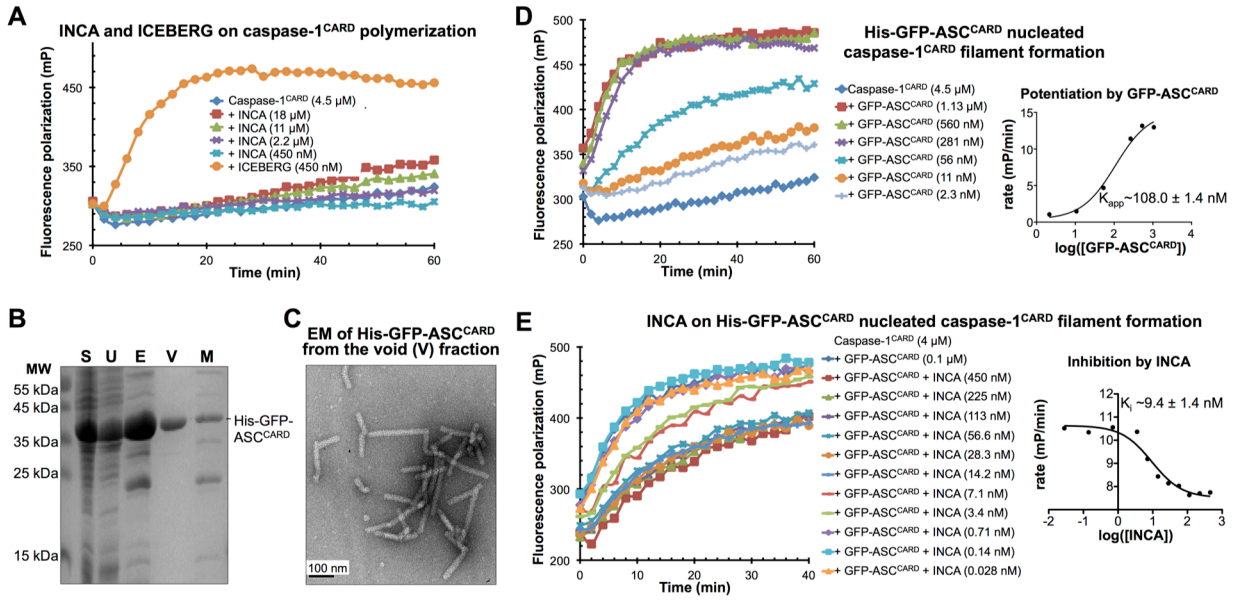

Figure 6.4. INCA inhibits ASC^{CARD} nucleated caspase-1^{CARD} filament formation.

A. ICEBERG but not INCA nucleated caspase-1^{CARD} filament formation. Averages of triplicate experiments were plotted.

B. Ni-NTA affinity purification and size exclusion chromatography of His-GFP-tagged ASC^{CARD}. S: soluble fraction of bacterial lysate. U: Ni-NTA unbound fraction. E: Ni-NTA elution. V: void fraction on gel filtration. M: monomer fraction on gel filtration.

C. Negative-stain electron micrograph of the His-GFP-ASC^{CARD} void fraction. Scale bar at 100 nm.

D. Effect of GFP-tagged ASC^{CARD} on caspase-1^{CARD} filament formation. Different amounts of ASC^{CARD} were added to promote caspase-1^{CARD} filament formation. Averages of triplicate experiments were plotted. The initial rates of caspase-1^{CARD} polymerization were plotted against the His-GFP-ASC^{CARD} concentrations to derive an apparent dissociation constant between ASC and caspase-1.

E. Different amounts of INCA were added to determine its inhibitory effect on His-GFP-ASC^{CARD} nucleated caspase-1^{CARD} filament formation. The initial rates of caspase-1^{CARD} polymerization were plotted against the INCA concentrations to derive an apparent inhibitory constant.

INCA interacts with caspase-1^{CARD} and directly inhibits its polymerization

The inhibitory effect of INCA with low nM potency in ASC^{CARD}-induced caspase-1^{CARD} polymerization was remarkable. To determine whether INCA directly interacts with ASC or caspase-1, we co-expressed the proteins in pairs. INCA was cloned into the pDW363 vector with an N-terminally fused biotin acceptor peptide (BAP), which allows biotinylation in *E. coli* by the biotin ligase BirA expressed from the same vector [34]. Biotinylated INCA was first co-expressed with His-GFP-ASC^{CARD}. Ni-NTA affinity purification and gel filtration chromatography yielded strong Coomassie Blue-stained bands of His-GFP-ASC^{CARD}, but no bands of co-purified INCA (**Figure 6.5A**). Streptavidin Western detected a weak band of biotinylated INCA co-purified with His-GFP-ASC^{CARD} (**Figure 6.5A**). To clarify if the apparent weak interaction has any functional importance, we used the ASC^{CARD} polymerization assay to determine if INCA can inhibit this process. Over-stoichiometric amounts of INCA, at up to 10 μM, did not inhibit His-GFP-ASC^{CARD} nucleated ASC^{CARD} filament formation (**Figure 6.5B**), suggesting that the ASC^{CARD}/INCA interaction, if at all, does not exert a significant functional effect.

To determine if INCA interacts with caspase-1^{CARD}, we co-expressed the BAP-INCA fusion with His-GFP-caspase-1^{CARD}. Unlike His-GFP-ASC^{CARD}, His-GFP-caspase-1^{CARD} co-purified with sufficient amounts of INCA to be visible on Coomassie Blue-stained SDS-PAGE (**Figure 6.5C**, lanes E, 7 mL and 8mL). Streptavidin Western further confirmed that the bands were biotinylated INCA, demonstrating the direct interaction between INCA and caspase-1^{CARD}. CARD domains of both ASC and caspase-1 were present in the assays that we used to demonstrate inhibition of caspase-1 polymerization by INCA (**Figure 6.4E**). The assay was thus not suitable to determine whether INCA acts on CARD domains of ASC or caspase-1. We therefore performed an alternative experiment using His-GFP-caspase-1^{CARD} as the nucleator. As mentioned earlier, His-GFP-caspase-1^{CARD} and His-GFP-ASC^{CARD} were similarly potent in nucleating monomeric caspase-1^{CARD} into extended filaments (**Figure 6.4D, Figure S6.2**). Addition of INCA at very low concentrations strongly inhibited His-GFP-caspase-1^{CARD}

Figure 6.5. INCA preferentially interacts with caspase-1^{CARD}.

A. His-GFP-ASC^{CARD} and biotinylated INCA were co-expressed in BL21(DE3) cells. Streptavidin-AP Western blot showed no significant interaction between INCA and ASC^{CARD}.

B. Over-stoichiometric amounts of INCA did not inhibit His-GFP-ASC^{CARD} nucleated ASC^{CARD} filament formation. Averages of triplicate experiments were plotted.

C. His-GFP-caspase-1^{CARD} and biotinylated INCA were co-expressed in BL21(DE3) cells. Streptavidin-AP Western blot confirmed the interaction between INCA and caspase-1^{CARD} seen on the PAGE gel. The complex eluted from the void position of a Superdex 200 column.

D. Sub-stoichiometric amounts of INCA inhibited His-GFP-caspase-1^{CARD} nucleated caspase-1^{CARD} filament formation. Averages of triplicate experiments were plotted. The initial rates of caspase-1^{CARD} polymerization were plotted against the INCA concentrations to derive an apparent inhibitory constant.

E-F. The void fraction at 7 mL of the His-GFP-caspase-1^{CARD}/biotinylated INCA complex shown in (**C**) was subjected to streptavidin-gold labeling (**E**) and Ni-NTA-gold labeling (**F**), which suggested an end location of INCA in caspase-1 filaments. Scale bar at 100 nm.

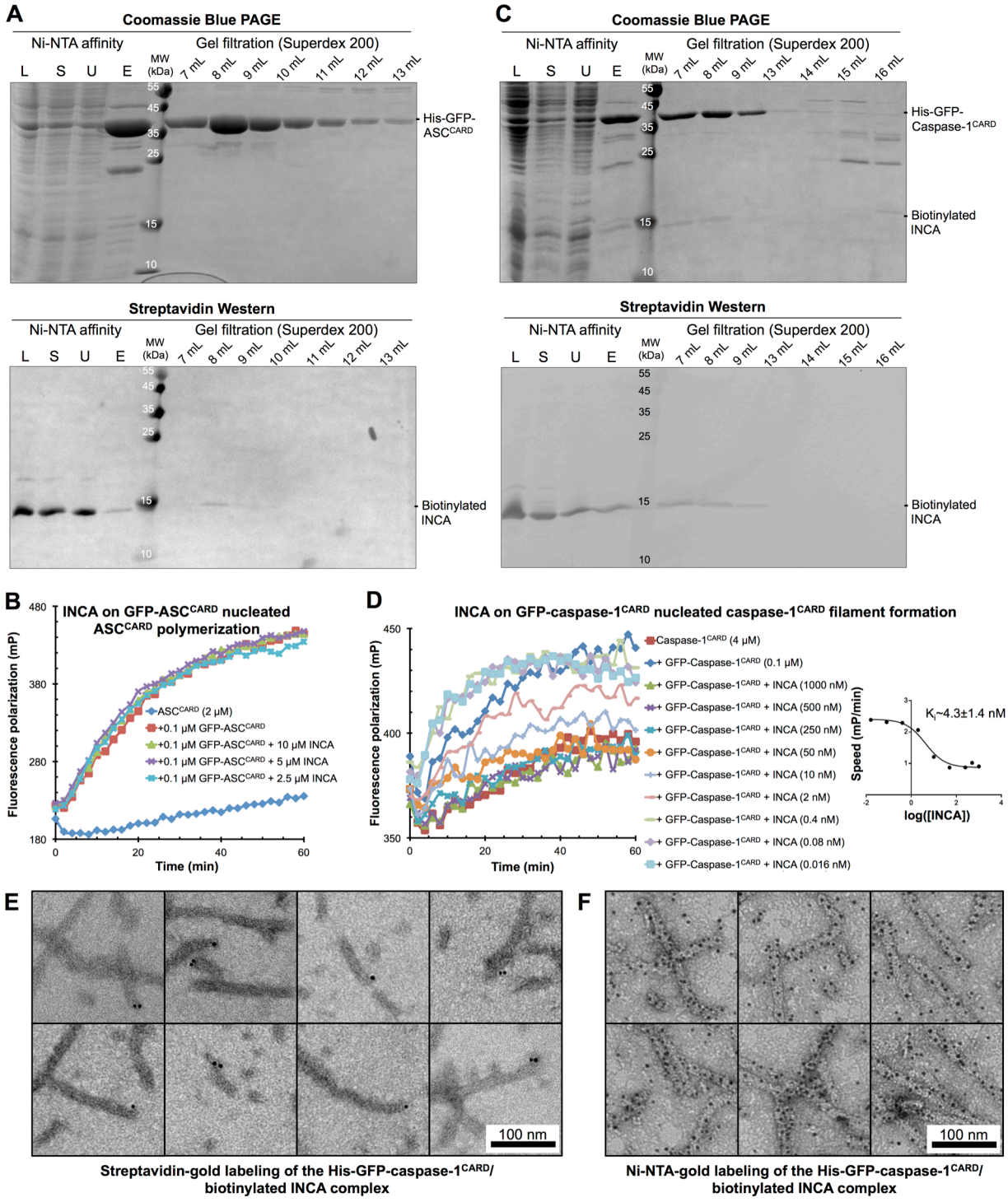

Figure 6.5 (Continued)

induced caspase-1^{CARD} polymerization (**Figure 6.5D**). The apparent inhibitory constant (K_i) is 4.3 ± 1.4 nM, similar to that obtained in His-GFP-ASC^{CARD} induced caspase-1^{CARD} polymerization (**Figure 6.4E**). We subjected the His-GFP-caspase-1^{CARD}/biotinylated INCA complex (**Figure 6.5C**) to Streptavidin-gold and Ni-NTA-gold labeling and observed that INCA exclusively localized at the tip of caspase-1^{CARD} filaments (**Figure 6.5E-F**).

The concentrations of monomeric caspase-1^{CARD} and the pre-formed filamentous nucleators used in the polymerization assays were 4.0 μM and 0.1 μM, respectively. At this assay condition, INCA inhibits the polymerization reactions with low nM K_i. The inhibitory constant is about three orders of magnitude lower than the concentration of monomeric caspase-1 and about 10-25 fold lower than the concentrations of the filamentous nucleators. Therefore, a plausible explanation is that INCA interacts only with the filamentous form of caspase-1. This interaction can occur directly on the His-GFP-caspase-1^{CARD} filaments. When His-GFP-ASC^{CARD} filaments are used, monomeric caspase-1 will polymerize on these nucleators. Then the His-GFP-ASC^{CARD}/caspase-1^{CARD} complex filaments can interact directly with INCA.

From the gold labeling experiment (**Figure 6.5E-F**), we quantitatively estimated this strength of inhibition by capping. The average length of the His-GFP-caspase-1^{CARD} filaments was estimated to be ~150 nm based on the electron micrographs. A similar length estimate was derived for His-GFP-ASC^{CARD} filaments (**Figure 6.4C**). Given the observed axial rise per subunit of 5.1 Å for the caspase-1^{CARD} filament, the total number of subunit per filament was approximately 30 (**Figure 6.1D**). This suggests that the effective concentration of His-GFP-caspase-1^{CARD} nucleator would be ~30-fold lower, about 3 nM, which brings K_i of INCA inhibition in the same order of magnitude. Collectively, these data are consistent with the conclusion that INCA inhibits caspase-1^{CARD} filament formation by capping small caspase-1^{CARD} containing nucleators.

To test this hypothesis, we performed gel filtration analysis to investigate whether His-MBP-caspase-1^{CARD}-SUMO formed complexes with INCA. At a concentration equivalent to the FP assays, caspase-1^{CARD} was incubated with TEV for 90 minutes at room temperature to remove the N-terminal His-MBP in the presence or absence of slightly over-stoichiometric amount of INCA. As in the experiment shown in **Figure 6.4A,** we expected caspase-1^{CARD}-SUMO to remain mostly monomeric in the absence of a nucleator. Upon completion of the polymerization reaction, the mixtures of MBP-cleaved caspase-1 and INCA were injected to a Superdex 200 column in order to determine if a stable complex was formed. No apparent shift in the elution position was observed when the two proteins were run individually or as a mixture (**Figure S6.5**). this result suggests that INCA does not form a stable complex with caspase-1^{CARD} to sequester the monomeric form, but rather caps the oligomeric form.

ICEBERG interacts with caspase-1^{CARD} filaments by co-mixing

To test whether ICEBERG interacts directly with caspase-1^{CARD}, we used a similar strategy as for INCA and co-expressed biotinylated ICEBERG and His-GFP-caspase-1^{CARD}. Ni-NTA pulldown showed co-purified biotinylated ICEBERG, though sub-stoichiometric to His-GFP-caspase-1^{CARD}, as confirmed by streptavidin Western (**Figure 6.6A**). In size-exclusion chromatography, the complex eluted from the void fraction (**Figure 6.6B**). The complex was then labeled with Ni-NTA-gold and streptavidin-gold conjugates separately and subjected to negative-stain EM analysis to probe the locations of the two proteins in the complex (**Figure 6.6C-D**). The labeling results showed that both gold conjugates randomly labeled the body of the filaments, indicating that ICEBERG co-polymerized with caspase-1^{CARD} into filaments. Therefore, despite the fact that both INCA and ICEBERG have been described as CARD-only proteins, INCA clearly functions through a mechanism different from ICEBERG.

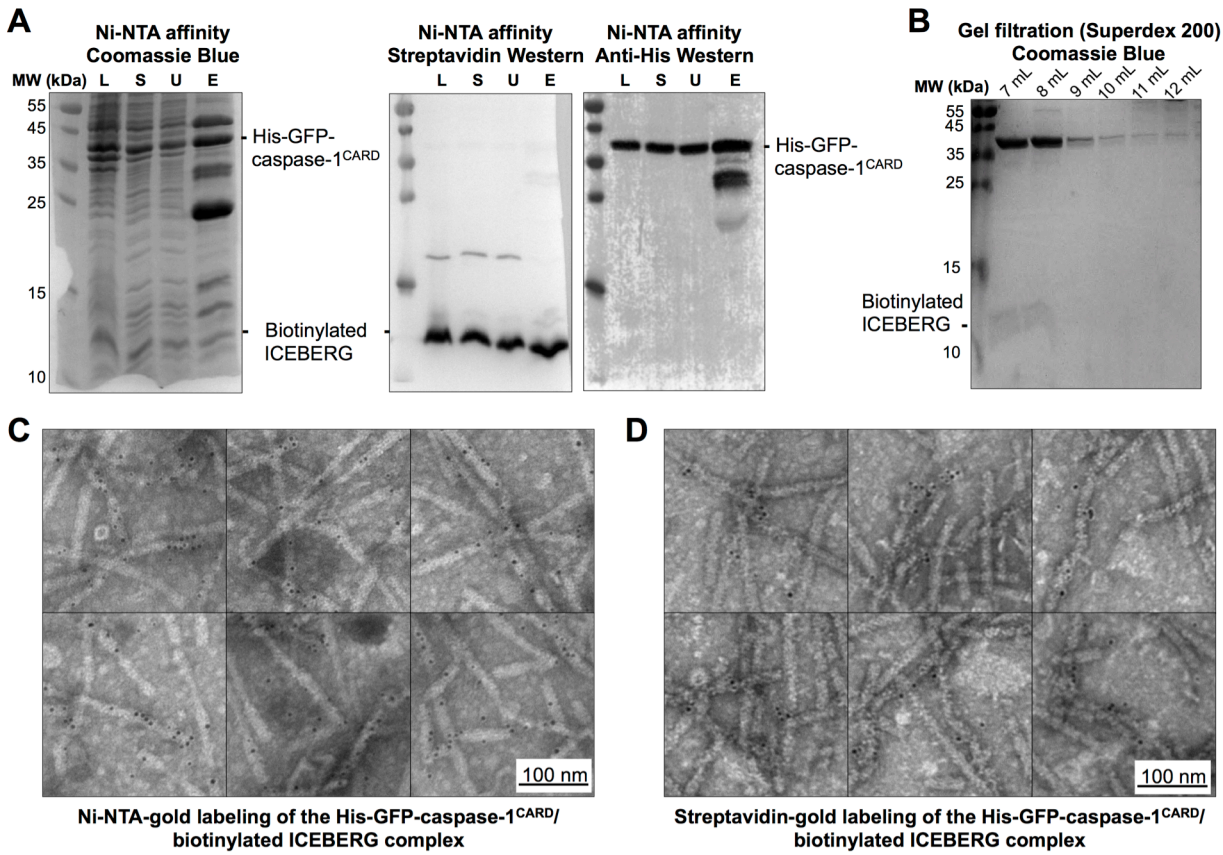

Figure 6.6. ICEBERG interacts with caspase-1^{CARD} by co-mixing.

A. His-GFP-caspase-1^{CARD} and biotinylated ICEBERG were co-expressed in BL21(DE3) cells. Streptavidin-AP and anti-6xHis-tag Western blots were shown to confirm the presence of ICEBERG in complex with His-GFP-caspase-1^{CARD} after Ni-NTA affinity chromatography. L: Whole cell lysate. S: Soluble fraction. U: Ni-NTA unbound. E: Ni-NTA elute.

B. The complex eluted from the void of a Superdex 200 column.

C-D. The void fraction at 7 mL was subjected to negative-stain EM after labeling with Ni-NTA-gold conjugate (5 nm gold) (**C**) and streptavidin-gold conjugate (6 nm gold) (**D**), which suggested co-mixing. Scale bar at 100 nm.

INCA but not ICEBERG efficiently inhibits NLRP3 inflammasome activation in THP-1 cells

Caspase-1 processing and IL-1β secretion are hallmarks of inflammasome activation. We assayed both to monitor the effect of inducible expression of ICEBERG or INCA in THP-1 cells under physiological conditions (**Figure 6.7**). We generated THP-1 cell lines expressing either INCA or ICEBERG. Expression of the transgenes was induced by the addition of

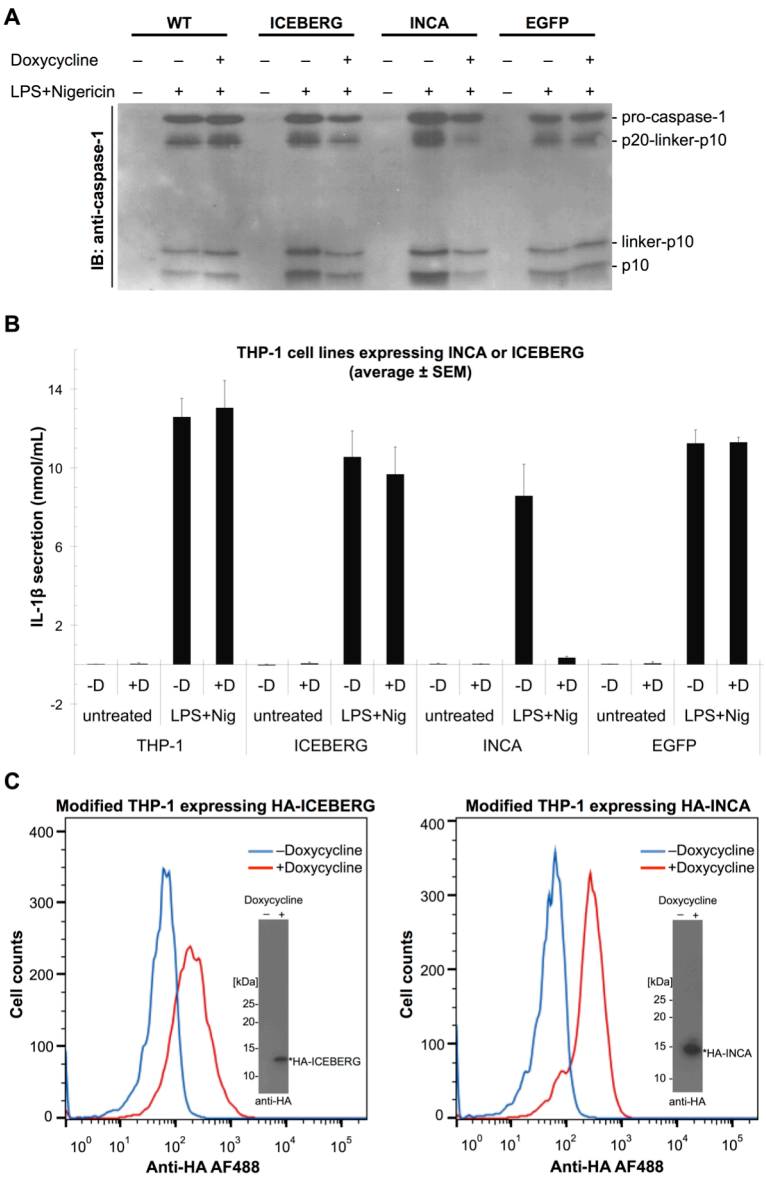

Figure 6.7. Inducible expression of ICEBERG and INCA on NLRP3 inflammasome activation in modified THP-1 cells treated by LPS and nigericin (Nig).

A. Caspase-1 processing was studied in WT (unmodified THP-1) and modified THP-1 cells carrying the ICEBERG or INCA transgene.

B. ELISA assay for IL-1β secretion for unmodified and modified THP-1 cells carrying ICEBERG or INCA transgenes. Doxycycline (D) served to induce the expression of transgene. THP-1 cells carrying the EGFP transgene were used as a control. Averaged results ± SEM from 3 experiments are shown.

C. Control experiment showing the inducible expression of HA-ICEBERG and HA-INCA in modified THP-1 cell lines as detected by anti-HA alexafluor488 antibody.

doxycycline (D) for 24h before the experiments. Importantly, doxycycline was withdrawn before inflammasome activation because we noticed that expression of any transgene during inflammasome activation impaired IL-1β secretion (data not shown). Cells were then treated for 3h with LPS and for 45 min with nigericin to induce NLRP3 inflammasome assembly. We first analyzed the processing of caspase-1 by an immunoblot, which showed that expression of INCA efficiently inhibited the appearance of the processed forms, while ICEBERG expression had minimal effects (**Figure 6.7A**). Consistent with the above, secretion of IL-1β in wild-type THP-1 cells and un-induced cell lines (-D) was comparable as quantified by ELISA (**Figure 6.7B**). Expression of INCA efficiently inhibited IL-1β secretion in LPS/nigericin-treated cells, while expression of EGFP did not impair IL-1β secretion. Expression of ICEBERG did not have any significant effect on IL-1β secretion (**Figure 6.7B**).

Therefore consistent with our *in vitro* data, the cellular experiments support a model in which INCA efficiently perturbs caspase-1 cleavage and activity, presumably due the inhibition of caspase-1 polymerization. In contrast, ICEBERG did not seem to inhibit NLRP3-dependent inflammasome activation, caspase-1 oligomerization, and caspase-1 activity. However, the situation in cells is substantially more complex, and it is conceivable that ICEBERG levels are insufficient, or that ICEBERG binding to caspase-1^{CARD} is subject to regulation by cellular proteins. The question whether ICEBERG is, if at all, a genuine inflammasome inhibitor remains to be answered. Even though it physically interacts with caspase-1, the exact molecular mechanism of regulation is unclear.

Structural mechanism of caspase-1 inhibition by INCA

The tendency of death domain fold family proteins to oligomerize into helical oligomers has been shown extensively. Examples of DD helical structures include the PIDDosome (DD) [30], the Myddosome (DD) [29], ASC filament (PYD) [11] and MAVS filament (CARD) [27]. We present the first CARD filament structure in the inflammasome pathway. For INCA to interact

with caspase-1, we predict that it must use the similar CARD-CARD interaction surfaces observed in the caspase-1^{CARD} filament structure. By this notion, we superimposed a predicted INCA monomer model based on the NMR structure of ICEBERG onto the caspase-1^{CARD} filament structure, in order to visualize the subtle differences between INCA and caspase-1^{CARD} underlying INCA's inhibitory mechanism (**Figure 6.8, Figure S6.6**).

For the type I interaction, INCA has a very similar type Ia interface, marked by the conserved R15 and R55 between caspase-1 and INCA. Asp27 on the caspase-1 type Ib surface is changed to Gly27 in INCA (**Figure 6.8A**). Such change probably reduces the strength of type Ib interface in INCA. According to our mutagenesis studies on caspase-1, type Ib mutation (D27R/E28R) completely disrupted filament formation and resulted in the monomeric form of caspase-1 (**Figure 6.2H**). The type II interface is primarily hydrophobic in caspase-1, which relies on Tyr82 for the interaction (**Figure 6.2F, H**). The corresponding residue in INCA is His82 (**Figure 6.8B**). This will probably reduce the strength of its type IIb interface. Type III interface represents the least extensive interface and is mostly conserved between INCA and caspase-1^{CARD} (**Figure 6.8C**).

As a result, we propose a model of how INCA inhibits caspase-1^{CARD} via a capping mechanism, based on the defective type Ib and IIb interfaces and the intact type Ia, IIa, IIIa, and IIIb interfaces (**Figure S6.6**). During inflammasome activation by filament formation and in the absence of the inhibitory protein INCA, oligomerized ASC^{CARD} domains seed caspase-1^{CARD} filaments (**Figure S6.6A**). But in the presence of INCA, a small caspase-1^{CARD} oligomer can stochastically recruit one or a few subunits of INCA through its intact type Ia, IIa, IIIa, and IIIb patches, thereby capping the growing caspase-1 filament. Due to the defective type Ib and IIb patches in INCA, the capped filament then loses the ability to further recruit inactive, monomeric caspase-1 (**Figure S6.6B**). This capping mechanism explains the high inhibitory potency of INCA in blocking caspase-1^{CARD} filament formation in our biochemical assay.

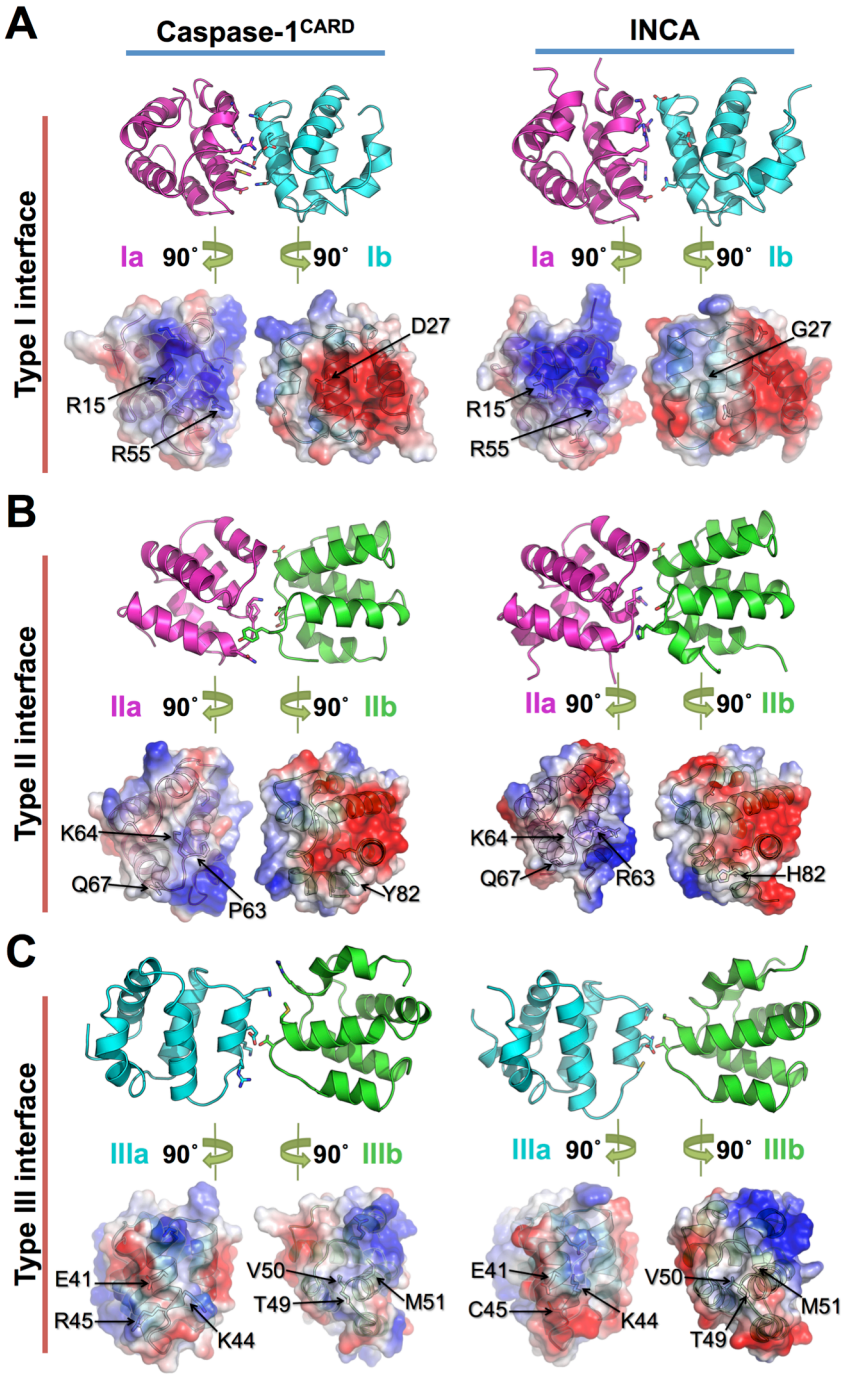

Figure 6.8. Comparison of critical interfacial residues between caspase-1^{CARD} and INCA. Model of an INCA monomer was generated using ICEBERG NMR structure as template (PDB: 1DGN). It was superimposed on each of the subunit in the caspase-1^{CARD} filament cryo-EM structure using the Dali pairwise structural alignment online server. Type I, II, and III interfaces of caspase-1^{CARD} and INCA are compared side by side, as shown in (**A**), (**B**), and (**C**) respectively.

In order to test this model, we generated a charge-reversal mutant, R55E, on the type Ia interface of INCA and tested its ability to inhibit GFP-caspase-1 nucleated caspase-1^{CARD} filament formation. Type Ia harbors basic residues that are essential for forming the electrostatic interactions between neighboring CARDs. Therefore, this mutation in INCA is expected to lower its affinity to caspase-1^{CARD} oligomer and thereby abolishes its ability to cap the growing caspase-1^{CARD} filament. Predictably, the R55E mutation significantly reduced the inhibition potency (**Figure S6.7**). When we increased the concentrations of R55E in the polymerization assay to drive the inhibition, a K_i of ~1.7 μM for R55E was derived, which is ~400 fold higher than that of wild-type INCA. This result supports our proposed capping mechanism.

Discussions

An emerging theme in the field of innate immunity involves the discovery of higher-order signalosomes in ligand binding and signal transduction [14]. The inflammasome assemblies, in particular, have a nucleated polymerization mechanism [11]. Through the formation of filaments and elaborate aggregates in the cell, component proteins come together for efficient activation and signal amplification [11, 12]. This mechanism has also been observed in the RIG-I pathway [27, 35] and the CARMA1/Bcl10/MALT1 pathway [26], and can be further generalized to related death domain fold containing proteins in other pathways. Extending the initial discovery of INCA as an inhibitor of LPS-induced and caspase-1-dependent IL-1β secretion [1], we investigated its mechanism of inhibition in the context of higher-order inflammasome assemblies. We found that INCA is a strikingly efficient inhibitor of caspase-1^{CARD} oligomerization, with an apparent inhibitory constant in the nanomolar range. We conclude from our biochemical and structural analyses that INCA caps small oligomers of caspase-1^{CARD} through CARD-CARD interactions to prevent the further recruitment of inactive caspase-1 monomers and the elongation of the CARD filaments (**Figure S6.8**). INCA also has a ~20-residue C-terminal tail (**Figure 6.3D**), which is predicted to be disordered. When bound to the caspase-1 filament, the C-terminus of $INCA^{CARD}$

should point to the outside and likely interfere with caspase-1 monomers from approaching the filament (**Figure S6.8**).

Unlike for INCA, future studies are required to elucidate the functional mechanisms of ICEBERG and COP1. ICEBERG oligomerizes and comingles with caspase-1. COP1 has two isoforms, a short isoform with CARD only and a longer isoform with an additional ~100 residues at the C-terminal end. $COP1^{CARD}$ differs from $caspase\text{-}1^{CARD}$ in only three residues, two of which, H15 and Q37, reside at the predicted filamentous interface (**Figure 6.3D**). However, H15 and Q37 are identical in ICEBERG and therefore these differences should not affect the interaction of COP1 with caspase-1. Hence, like ICEBERG, COP1 may also comingle with caspase-1 filaments. It remains to be determined whether ICEBERG and COP1 are bona fide inflammasome inhibitors because our cellular assay failed to show any inhibition of NLRP3 inflammasome activation by ICEBERG.

Numerous studies suggest that inflammasomes may represent important therapeutic targets against human diseases. For example, genetic evidence in the inflammasome sensor proteins NLRP3 (172 known disease variants), Pyrin/MEFV (297 known disease variants), PSTPIP1 (22 known disease variants) and NLRP12 (32 known disease variants) links inflammasomes to hereditary periodic fevers (HPFs), inflammation and autoimmunity. More importantly, over-activation of inflammasomes is causal for or associated with highly prevalent inflammatory diseases within and outside the immune system [1, 2, 36], including gout, rheumatoid arthritis, dermatitis, lung fibrosis [37], irritable and inflammatory bowel diseases [38], neuropathic pain, sepsis, obesity, atherosclerosis [39], diabetes [40, 41], and gastric carcinoma. Many of these diseases have limited treatment options, in particular, those that specifically address the root of the inflammatory response. The capping mechanism by INCA which we discovered here permits interference of inflammasome assembly at a vastly substoichiometric ratio, and provides a new potential therapeutic strategy in inhibition of inflammasomes, as well

as the many other innate immune signaling complexes that utilize the death fold domains as the main scaffolding architectures.

Our studies also made a mechanistic connection to capping proteins that dynamically regulate cellular cytoskeletal networks. For instance, the dimeric protein CapZ seals the barbered end of actin filaments to prevent their elongation [42-44]. Human CapZ has an apparent dissociation constant of ~3 nM in actin elongation and depolymerization assays [44]. This is comparable to what we report here for INCA in a caspase-1 polymerization assay. Fungal metabolites known as cytochalasins, which have the ability to bind actin filaments to block their polymerization, offer another example [45]. The effective concentrations of these molecules can range between hundreds of pM to several μM in cells [46]. The apparent equilibrium dissociation constant of cytochalasin D for ADP-actin is ~1-2 nM [47]. Our studies suggest that INCA may very well be the CapZ or cytochalasin-equivalent inhibitor of caspase-1 filament elongation, and illustrate a potential novel therapeutic mechanism for inflammasome-associated diseases.

References

1. Lamkanfi, M. & Dixit, V. M. (2014) Mechanisms and functions of inflammasomes, *Cell.* **157**, 1013-22.

2. Martinon, F., Mayor, A. & Tschopp, J. (2009) The inflammasomes: guardians of the body, *Annual review of immunology.* **27**, 229-65.

3. Vezzani, A., Maroso, M., Balosso, S., Sanchez, M. A. & Bartfai, T. (2011) IL-1 receptor/Toll-like receptor signaling in infection, inflammation, stress and neurodegeneration couples hyperexcitability and seizures, *Brain Behav Immun.* **25**, 1281-9.

4. Lu, A., Kabaleeswaran, V., Fu, T., Magupalli, V. G. & Wu, H. (2014) Crystal structure of the F27G AIM2 PYD mutant and similarities of its self-association to DED/DED interactions, *Journal of molecular biology.* **426**, 1420-7.

5. Yin, Q., Sester, D. P., Tian, Y., Hsiao, Y. S., Lu, A., Cridland, J. A., Sagulenko, V., Thygesen, S. J., Choubey, D., Hornung, V., Walz, T., Stacey, K. J. & Wu, H. (2013) Molecular mechanism for p202-mediated specific inhibition of AIM2 inflammasome activation, *Cell reports.* **4**, 327-39.

6. Ferrao, R. & Wu, H. (2012) Helical assembly in the death domain (DD) superfamily, *Current opinion in structural biology.* **22**, 241-7.

7. Zhang, L., Chen, S., Ruan, J., Wu, J., Tong, A. B., Yin, Q., Li, Y., David, L., Lu, A., Wang, W. L., Marks, C., Ouyang, Q., Zhang, X., Mao, Y. & Wu, H. (2015) Cryo-EM structure of the activated NAIP2-NLRC4 inflammasome reveals nucleated polymerization, *Science*.

8. Hu, Z., Zhou, Q., Zhang, C., Fan, S., Cheng, W., Zhao, Y., Shao, F., Wang, H. W., Sui, S. F. & Chai, J. (2015) Structural and biochemical basis for induced self-propagation of NLRC4, *Science*.

9. Qu, Y., Misaghi, S., Izrael-Tomasevic, A., Newton, K., Gilmour, L. L., Lamkanfi, M., Louie, S., Kayagaki, N., Liu, J., Komuves, L., Cupp, J. E., Arnott, D., Monack, D. & Dixit, V. M. (2012) Phosphorylation of NLRC4 is critical for inflammasome activation, *Nature.* **490**, 539-42.

10. Kofoed, E. M. & Vance, R. E. (2011) Innate immune recognition of bacterial ligands by NAIPs determines inflammasome specificity, *Nature.* **477**, 592-5.

11. Lu, A., Magupalli, V. G., Ruan, J., Yin, Q., Atianand, M. K., Vos, M. R., Schroder, G. F., Fitzgerald, K. A., Wu, H. & Egelman, E. H. (2014) Unified polymerization mechanism for the assembly of ASC-dependent inflammasomes, *Cell.* **156**, 1193-206.

12. Cai, X., Chen, J., Xu, H., Liu, S., Jiang, Q. X., Halfmann, R. & Chen, Z. J. (2014) Prion-like polymerization underlies signal transduction in antiviral immune defense and inflammasome activation, *Cell.* **156**, 1207-22.

13. Lu, A. & Wu, H. (2014) Structural mechanisms of inflammasome assembly, *FEBS J.* **282**, 435-44.

14. Wu, H. (2013) Higher-order assemblies in a new paradigm of signal transduction, *Cell.* **153**, 287-92.

15. Latz, E., Xiao, T. S. & Stutz, A. (2013) Activation and regulation of the inflammasomes, *Nature reviews Immunology.* **13**, 397-411.

16. Stehlik, C., Krajewska, M., Welsh, K., Krajewski, S., Godzik, A. & Reed, J. C. (2003) The PAAD/PYRIN-only protein POP1/ASC2 is a modulator of ASC-mediated nuclear-factor-kappa B and pro-caspase-1 regulation, *Biochem J.* **373**, 101-13.

17. Bedoya, F., Sandler, L. L. & Harton, J. A. (2007) Pyrin-only protein 2 modulates NF-kappaB and disrupts ASC:CLR interactions, *J Immunol.* **178**, 3837-45.

18. Dorfleutner, A., Talbott, S. J., Bryan, N. B., Funya, K. N., Rellick, S. L., Reed, J. C., Shi, X., Rojanasakul, Y., Flynn, D. C. & Stehlik, C. (2007) A Shope Fibroma virus PYRIN-only protein modulates the host immune response, *Virus Genes.* **35**, 685-94.

19. Lamkanfi, M., Denecker, G., Kalai, M., D'Hondt, K., Meeus, A., Declercq, W., Saelens, X. & Vandenabeele, P. (2004) INCA, a novel human caspase recruitment domain protein that inhibits interleukin-1beta generation, *The Journal of biological chemistry.* **279**, 51729-38.

20. Humke, E. W., Shriver, S. K., Starovasnik, M. A., Fairbrother, W. J. & Dixit, V. M. (2000) ICEBERG: a novel inhibitor of interleukin-1beta generation, *Cell.* **103**, 99-111.

21. Druilhe, A., Srinivasula, S. M., Razmara, M., Ahmad, M. & Alnemri, E. S. (2001) Regulation of IL-1beta generation by Pseudo-ICE and ICEBERG, two dominant negative caspase recruitment domain proteins, *Cell Death Differ.* **8**, 649-57.

22. Le, H. T. & Harton, J. A. (2013) Pyrin- and CARD-only Proteins as Regulators of NLR Functions, *Front Immunol.* **4**, 275.

23. Kersse, K., Vanden Berghe, T., Lamkanfi, M. & Vandenabeele, P. (2007) A phylogenetic and functional overview of inflammatory caspases and caspase-1-related CARD-only proteins, *Biochem Soc Trans.* **35**, 1508-11.

24. Lee, S. H., Stehlik, C. & Reed, J. C. (2001) Cop, a caspase recruitment domain-containing protein and inhibitor of caspase-1 activation processing, *The Journal of biological chemistry.* **276**, 34495-500.

25. da Cunha, J. P., Galante, P. A. & de Souza, S. J. (2008) Different evolutionary strategies for the origin of caspase-1 inhibitors, *Journal of molecular evolution.* **66**, 591-7.

26. Qiao, Q., Yang, C., Zheng, C., Fontan, L., David, L., Yu, X., Bracken, C., Rosen, M., Melnick, A., Egelman, E. H. & Wu, H. (2013) Structural Architecture of the CARMA1/Bcl10/MALT1 Signalosome: Nucleation-Induced Filamentous Assembly, *Mol Cell.* **51**, 766-79.

27. Wu, B., Peisley, A., Tetrault, D., Li, Z., Egelman, E. H., Magor, K. E., Walz, T., Penczek, P. A. & Hur, S. (2014) Molecular Imprinting as a Signal-Activation Mechanism of the Viral RNA Sensor RIG-I, *Mol Cell.* **55**, 511-23.

28. Egelman, E. H. (2007) The iterative helical real space reconstruction method: surmounting the problems posed by real polymers, *Journal of structural biology.* **157**, 83-94.

29. Lin, S. C., Lo, Y. C. & Wu, H. (2010) Helical assembly in the MyD88-IRAK4-IRAK2 complex in TLR/IL-1R signalling, *Nature.* **465**, 885-890.

30. Park, H. H., Logette, E., Raunser, S., Cuenin, S., Walz, T., Tschopp, J. & Wu, H. (2007) Death domain assembly mechanism revealed by crystal structure of the oligomeric PIDDosome core complex, *Cell.* **128**, 533-46.

31. Lu, A., Li, Y., Yin, Q., Ruan, J., Yu, X., Egelman, E. & Wu, H. (2015) Plasticity in PYD assembly revealed by cryo-EM structure of the PYD filament of AIM2, *Cell Discov.* **1**.

32. Guimaraes, C. P., Witte, M. D., Theile, C. S., Bozkurt, G., Kundrat, L., Blom, A. E. & Ploegh, H. L. (2013) Site-specific C-terminal and internal loop labeling of proteins using sortase-mediated reactions, *Nature protocols.* **8**, 1787-99.

33. de Alba, E. (2009) Structure and interdomain dynamics of apoptosis-associated speck-like protein containing a CARD (ASC), *The Journal of biological chemistry.* **284**, 32932-41.

34. Tsao, K. L., DeBarbieri, B., Michel, H. & Waugh, D. S. (1996) A versatile plasmid expression vector for the production of biotinylated proteins by site-specific, enzymatic modification in Escherichia coli, *Gene.* **169**, 59-64.

35. Hou, F., Sun, L., Zheng, H., Skaug, B., Jiang, Q. X. & Chen, Z. J. (2011) MAVS forms functional prion-like aggregates to activate and propagate antiviral innate immune response, *Cell.* **146**, 448-61.

36. Lopez-Castejon, G. & Pelegrin, P. (2012) Current status of inflammasome blockers as anti-inflammatory drugs, *Expert Opin Investig Drugs.* **21**, 995-1007.

37. Brusselle, G. G., Provoost, S., Bracke, K. R., Kuchmiy, A. & Lamkanfi, M. (2014) Inflammasomes in respiratory disease: from bench to bedside, *Chest.* **145**, 1121-33.

38. Aguilera, M., Darby, T. & Melgar, S. (2014) The complex role of inflammasomes in the pathogenesis of Inflammatory Bowel Diseases - Lessons learned from experimental models, *Cytokine Growth Factor Rev.* **25**, 715-730.

39. Ridker, P. M. & Luscher, T. F. (2014) Anti-inflammatory therapies for cardiovascular disease, *Eur Heart J.* **35**, 1782-1791.

40. Esser, N., Legrand-Poels, S., Piette, J., Scheen, A. J. & Paquot, N. (2014) Inflammation as a link between obesity, metabolic syndrome and type 2 diabetes, *Diabetes Res Clin Pract.* **105**, 141-150.

41. Robbins, G. R., Wen, H. & Ting, J. P. (2014) Inflammasomes and metabolic disorders: old genes in modern diseases, *Mol Cell.* **54**, 297-308.

42. Caldwell, J. E., Heiss, S. G., Mermall, V. & Cooper, J. A. (1989) Effects of CapZ, an actin capping protein of muscle, on the polymerization of actin, *Biochemistry.* **28**, 8506-14.

43. Lin, Y. H., Li, J., Swanson, E. R. & Russell, B. (2013) CapZ and actin capping dynamics increase in myocytes after a bout of exercise and abates in hours after stimulation ends, *J Appl Physiol (1985).* **114**, 1603-9.

44. Maun, N. A., Speicher, D. W., DiNubile, M. J. & Southwick, F. S. (1996) Purification and properties of a Ca(2+)-independent barbed-end actin filament capping protein, CapZ, from human polymorphonuclear leukocytes, *Biochemistry.* **35**, 3518-24.

45. Cooper, J. A. (1987) Effects of cytochalasin and phalloidin on actin, *The Journal of cell biology.* **105**, 1473-8.

46. Wakatsuki, T., Schwab, B., Thompson, N. C. & Elson, E. L. (2001) Effects of cytochalasin D and latrunculin B on mechanical properties of cells, *J Cell Sci.* **114**, 1025-36.

47. Carlier, M. F., Criquet, P., Pantaloni, D. & Korn, E. D. (1986) Interaction of cytochalasin D with actin filaments in the presence of ADP and ATP, *The Journal of biological chemistry.* **261**, 2041-50.

Chapter Seven

Conclusions and Future Directions

This dissertation is focused on the assembly and regulation mechanisms of inflammasomes. Using structural and biochemical approaches, I investigated the filamentous structures underlying ASC-dependent inflammasomes. In particular, I elucidated the homotypic interactions mediated by the PYD and CARD domains during self-oligomerization of component proteins, sensor-adaptor nucleation, adaptor-effector nucleation, and effector inhibition. These interactions took advantage of the multiple interfaces that were typical of death domains and shared striking structural and biophysical commonalities. This dissertation also describes how a filamentous scaffold plays an important functional role in signaling. Recognition of supramolecular signaling complexes, such as the Myddosome complex, the PIDDosome complex, the CBM complex, and now the inflammasome complexes, provides the structural basis to explain many previously poorly understood cellular phenomena [1, 2].

Inflammasome activation is a critical yet dangerous cellular response

Controlled inflammasome activation is essential to the survival of an organism. It provides the first line of defense against bacterial and viral infection by sensing a multitude of endogenous and exogenous stimuli. Activation of the inflammasome decides the fate of the infected cell as well as the fate of surrounding cells by triggering pyroptotic cell death. Normally, this response is critical for clearance of pathogens and for host protection. In other cases, dysregulation of inflammasomes causes many acute and chronic diseases. Pathogenesis mechanisms may include genetic mutations in the sensor proteins causing over-activation of the inflammasomes, or metabolic dysfunction of the host that generates cellular stresses.

Autoinflammatory disorders resulting from deregulated activation of the NLRP3 inflammasome are grouped under the name cryopyrin-associated periodic syndromes (CAPS). Cryopyrin is the gene name given to NLRP3. CAPS include three subtypes – familial cold autoinflammatory syndrome (FCAS), the Muckle-Wells syndrome (MWS), and neonatal-onset multisystem inflammatory disease (NOMID) – which share many clinical features such as fever

and urticarial skin rash but differ in the severity of manifestation [3]. FACS is the least severe form of CAPS, which is triggered by exposure to cold, resulting in recurrent attacks of a maculopapular rash associated with fever and chills, as well as swelling of the extremities, but severe amyloidosis is rare (OMIM#120100). Hereditary analysis has identified three missense mutations in NLRP3 (A439V, V198M, and E627G) that caused FACS [4]. MWS is a dominantly inherited syndrome that is best characterized by late-onset progressive hearing loss and severe renal amyloidosis (OMIM#191900). Several missense mutations (A352V, R260W, and G569R) of NLRP3 have been linked to MWS [4, 5]. Animal study further confirmed that the R258W mutation in mouse NLRP3 drove inflammasome hyperactivation resulting in MWS-like symptoms [6]. NOMID is the most severe form of FCAS, which is characterized by chromic inflammation of the central nervous system resulting in hearing and vision loss, recurrent joint flares leading to bone deformities and growth retardation, and polymorphonuclear cell infiltration causing chronic meningitis (OMIM#607115). Two NLRP3 mutations, D303N and F573S, have been identified in NOMID patients [5, 7].

Familial Mediterranean Fever (FMF) is caused by mutation of the MEFV gene that encodes the protein pyrin. FMF is characterized by recurrent episodes of fever lasting 1 to 3 days with serositis, synovitis, or skin rash, and long-term complications may include systematic amyloidosis (OMIM#249100). More than 90 MEFV mutations have been linked to FMF, with most of them concentrated at the C-terminal portion of the pyrin protein [8]. Pyrin has an N-terminal PYD domain reported to interact other inflammasome components and a C-terminal B30.2 domain which is another protein interaction module found in tripartite motif (TRIM) proteins [9]. It remains debatable whether pyrin forms a functional inflammasome or acts as a negative regulator. Co-immunoprecipitation experiments showed that the C-terminal B30.2 domain interacted with caspase-1 protease domain [10]. This interaction was proposed to block inflammasome activation because mouse macrophages carrying mutations in the B30.2 domain had an increased level of IL-1β secretion in response to inflammatory stimuli [11]. The anti-

inflammatory role of pyrin is reinforced by the observation that RNAi knockdown of pyrin in THP-1 cells caused elevated IL-1β secretion [12]. On the other hand, reconstitution experiments in HEK293 cells showed that pyrin could oligomerize ASC and activate caspase-1 [13]. In addition, the interaction between pyrin and the cytoskeleton-organizing protein, PSTPIP1, was shown to release pyrin's N-terminal PYD for ASC recruitment [14]. This interaction may explain how PSTPIP1 causes pyogenic sterile arthritis with pyoderma gangrenosum and acne (PAPA) syndrome (OMIM#604416). The exact molecular link between pyrin and FMF remains to be elucidated due to the lack of structural and biochemical evidence – it might very well act as a molecular sensor that tips the balance between pro- and anti-inflammatory responses.

Other inflammasome sensor proteins are also implicated in the development of autoinflammatory diseases. Animal studies linked activating mutations of NLRC4 to a macrophage-activation syndrome-like (MAV-like) illness and enterocolitis [15, 16]. DNA-induced over-activation of AIM2 facilitates the development of psoriasis (OMIM#177900), which is a chronic dermatosis characterized by red skin patches on the scalp, elbows, and knees [17]. NLRP7 is genetically linked to the development of familial hydatidiform mole (OMIM#231090), which is an autosomal recessive disorder that causes abnormal pregnancy and recurrent pregnancy losses [18]. The molecular mechanisms of these diseases are not as well understood.

Moreover, deregulated inflammasomes are also responsible for the pathogenesis of autoimmune disorders. Genetic variants of NLRP1 have been identified to cause vitiligo [19], which is an autoimmune disease characterized by depigmentation of skin and hair due to the loss of melanocytes (OMIM#606579). Other genetic studies have also linked NLRP1 to its susceptibility to Addison's disease (AAD) [20], autoimmune thyroid disease [21], and type 1 diabetes [22]. Elevated IL-1β processing has been found in individuals with vitiligo and associated autoimmune diseases [22]. In addition, the high expression level of AIM2 in mice has been correlated to the development of systemic lupus erythematosus (SLE) [23], which is a

disease characterized by the production of autoantibodies that cause macrophage-mediated organ inflammation, particularly in the kidney (OMIM#152700).

Contrary to the genetic predisposition to autoinflammatory and autoimmune disorders, metabolic diseases may arise in individuals with normal inflammasome variants. These diseases are often chronic and age-related. For instance, aberrant NLRP3 inflammasome activation mediates the development of gout [8], which is a form of arthritis characterized by stiffness and swelling of joints. Gout arises from diseases that cause increased uric acid level in the blood stream (hyperuricemia) and the deposition of monosodium urate (MSU) crystals within the joints [8]. MSU crystals activate the NLRP3 inflammasome to cause joint inflammation [24]. IL-1β blockade in gout patients helps ameliorate acute gout attacks [25]. In addition, NLRP3 has been shown to mediate the innate immune response to metabolic stressors such as β-amyloid, which indicates a potential role in the development of Alzheimer's disease [26]. NLRP3- and caspase-1-deficient mice have been shown to gain protection against learning disabilities associated with Alzheimer's disease [27]. Moreover, NLRP3 activation is associated with the pathogenesis of atherosclerosis [28]. Cholesterol crystal deposition in atherosclerosis plaques has been shown to serve as an endogenous danger signal for Nrf2-dependent NLRP3 inflammasome activation and IL-1β production [29].

Targeting the inflammasomes as therapeutic strategy

The mechanistic understandings of the inflammasome assembly and regulation may lead to the development of novel therapeutic strategies for inflammasome-mediated diseases. Current inflammasome modulators exert their effects either upstream of inflammasome assembly (*e.g.,* reducing activating triggers), or downstream of caspase activation (*e.g.,* antagonizing IL-1). These include drugs that curb NLRP3 inflammasome activation: antioxidants, inhibitors of uric acid synthesis, and small molecule inhibitors of the ATP receptor P2X7, as well as anti-IL-1 biologics [30]. Anti-IL-1 therapy has shown substantial clinical

success, despite of the need for frequent injection and side effects such as liver toxicity. Clinical success of “indirect” inflammasome inhibitors proves the potential in targeting this pathway. Caspase-1 has been another well pursued target but with limited success, likely due to the acidic nature of caspase substrate-like molecules and the participation of multiple caspases in the pathway [30].

IL-1β inhibition is currently the most widely used therapy for autoinflammatory disorders. Anakinra is an IL-1 receptor antagonist used in the treatment of CAPS and rheumatoid arthritis. Canakinumab is a neutralizing IL-1β antibody, which is approved for the treatment of CAPS and Systemic Juvenile Idiopathic Arthritis (SJIA). Rilonacept is also approved for the treatment of CAPS [31]. It is a dimeric fusion protein of the extracellular domains of the IL-1 receptor I and the IL-1 adaptor protein, which acts as a decoy for IL-1β [32]. These medications also have experimental uses in gout, pseudogout, FMF, and other inflammatory syndromes [30].

A microtubule-disrupting drug, colchicine, has become the main therapy for FMF patients [30]. The clinical success of colchicine as an anti-inflammatory agent has been known for many years [33], and has the additional benefit of preventing amyloidosis [34]. Colchicine has been reported to prevent inflammasome activation by disrupting the colocalization of NLRP3 and ASC [34]. However, the exact relationship between the cytoskeletal network and inflammasome activation remains to be elucidated. Colchicine is also approved for the treatment of gout [35]. In addition to NLRP3 inflammasome inhibition, colchicine also has other beneficial effects. It curbs the number of TNF-α receptors on the surface of macrophages and endothelial cells to dampen NF-κB signaling [36]; it suppresses MSU crystal-induced tyrosine phosphorylation and reactive oxygen species production in neutrophils at low dosage [37, 38]; it interrupts mass cell degranulation process by the inhibition of calcium influx [39]; and it induces the expression of TGF-β1 during the resolution phase of MSU-induced inflammation [40]. Therefore, the pleiotropic effects of colchicine may underlie its clinical efficacy.

Other medications have also been used to modulate the inflammatory responses through different mechanisms. Antimalarial medications, such as hydroxychloroquine and chloroquine, have shown to be an effective treatment option for systemic lupus erythematosus (SLE) and rheumatoid arthritis patients [41]. This group of compounds was found to block TLR7 and TLR9 activation in the lysosomal compartment in order to prevent aberrant NLRP3 inflammasome activation during infection [42]. Glyburide, a common medication to treat type II diabetes, has off-target effects in blocking NLRP3 inflammasome [43]. However, the dosage required for inflammasome inhibition is high enough to cause hypoglycemia *in vivo* [44]. Nevertheless, optimization of this lead may provide another potential therapeutic strategy.

The nucleated polymerization model is now being widely accepted as part of an overarching paradigm of filamentous signaling complexes [45]. The studies presented in this dissertation may have identified novel therapeutic strategies, which had been largely dismissed due to the lack of structural and biophysical understanding of the inflammasome pathway. For example, the interactions mediated by PYDs and CARDs of inflammasome components are attractive drug targets. The rationale is that these protein domains must work cooperatively to provide signal amplification during inflammasome activation [1]. Inhibitors of death domain interaction may curb inflammasome signaling by preventing the oligomerization of component proteins, which is necessary for activation. In addition, compounds that mimic the effect of INCA through a filament capping mechanism could prove highly effective for inflammasome inhibition. Moreover, other regulatory mechanisms hidden in the inflammasome system itself are yet to be discovered – it is not well understood how ICEBERG, COP1, NLRP10, ASC2, and many other inflammasome regulators exert their inhibitory effects. Therefore, structural and biochemical studies in the future will guide the design of novel therapeutic strategies.

Remaining mysteries of the inflammasome pathway

There are several unanswered questions to be addressed in the field of inflammasome signaling. Firstly, it remains debatable if pyroptosis is the major pathway of cytokine release, or whether there is another general secretory mechanism. In addition, the non-canonical inflammasome pathway has just been recognized as a response mechanism for intracellular LPS, but whether this pathway has any implication in IL-1β secretion requires further investigation. Moreover, the relationship between inflammasome activation and the cytoskeletal network is evident from the inhibitory effect of colchicine *in vivo* and in cells, but the exact molecular mechanism is unknown. Lastly, the autophagy pathway is shown to play a regulatory role during inflammasome activation, but it is unclear whether autophagy is inhibitory or facilitates inflammasome activation.

Over the years, researchers have proposed several mechanisms for the secretion of mature IL-1β [46]. During conventional protein secretion, signal recognition particles translocate nascent proteins by carrying a signal sequence to the lumen of endoplasmic reticulum. After receiving post-translational modification from the Golgi, the nascent proteins then maneuver through the cell in coated vesicles, which eventually release the cargo proteins by exocytosis [46]. However, IL-1β lacks the required signal sequence, and studies have reported that IL-1β does not follow the conventional secretory pathway [47]. Immunoelectron microscopy showed that the cytosol contained most of the IL-1β pool, and a small fraction of the IL-1β could be found in the endolysosome [48]. These observations led to the proposal of the “rescue and redirect” mechanism in which the autophagy pathway would recycle the activated IL-1β for secretion [46]. In addition, IL-1β could also be released by microvesicle shedding from the plasma membrane of THP-1 monocytes upon P2X7 receptor stimulation [49]. Alternatively, it could also be secreted within the smaller vesicles called exosomes (<80 nm) upon P2X7R activation, but independent of caspase-1 activation [50]. Inflammasome activation also triggers caspase-1-dependent pyroptotic cell death for rapid clearance of infected macrophages. During

the response to *S. typhimurium* infection, osmotic lysis occurred upon formation of the 1.1-2.4 nm pores [51]. The presence of glycine blocked osmotic lysis but not pore formation or IL-1β release, suggesting that pore formation might be another secretory pathway for IL-1β [51]. Moreover, a recent study has confirmed the role of autophagy in IL-1β secretion – with the help of the chaperone protein HSP90, IL-1β enters the lumen of a vesicular carrier and later intercalates between inner and the outer membranes of an autophagosome for secretion upon plasma membrane fusion [52]. Ultimately, these proposed secretory mechanisms are not mutually exclusive and may be cell-type specific [46].

Recent studies on caspase-4/5/11 have re-defined the non-canonical inflammasomes as intracellular LPS sensors [53]. Caspase-11 does not efficiently cleaves pro-IL-1β, suggesting that the non-canonical inflammasomes are not a functional replacement for canonical inflammasomes [54]. Caspase-1, on the other hand, can cleave and activate the caspase-11 substrate, gasdermin D, which presumably damages the cell membrane and causes pyroptosis [55]. However, gasdermin D activation seems to be upstream of NLRP3 inflammasome activation, because the loss of NLRP3, ASC, or caspase-1 did not dramatically affect gasdermin D maturation by caspase-11 [55]. It is not clear how gasdermin D activates the NLRP3 inflammasome and where the canonical and non-canonical inflammasome pathways would converge. Therefore, structural and biochemical studies of gasdermin D in the future may be able to address these questions.

The cell cytoskeleton has an intimate relationship with inflammasomes in many aspects. Phagocytosis of particulate agonists, including MSU crystals and calcium pyrophosphate dehydrate (CPPD), requires the actin network [56]. Inhibition of actin dynamics by cytochalasin D abolished NLRP3 activation by MSU crystals [34]. In addition, tubulin polymerization inhibitors, including colchicine, nocodazole, and podophyllotoxin, have been shown to specifically inhibit the activation of NLRP3 inflammasome, but not AIM2 or NAIP/NLRC4 inflammasomes [34]. One hypothesis is that the microtubule network mediates the

colocalization of mitochondria-resident ASC and ER-resident NLRP3 for colocalization at the perinuclear region in response to NLRP3 inflammasome triggers [34]. However, evidence supporting this hypothesis lacks spatial and temporal resolution, which does not explain the exact transport mechanism or molecular interactions [34]. Moreover, ASC is ubiquitously expressed and localizes throughout the cell, and it is unclear why only the mitochondrial fraction of ASC is used for inflammasome activation.

Cellular stresses – such as nutrient deprivation, organelle damage, accumulation of misfolded proteins, and oxidative damage – may trigger autophagy, which is a catabolic process to maintain cellular homeostasis in a lysosome-dependent manner [57]. Engulfment of damaged cellular components and stress signals by the double-membrane autophagosomes target them for lysosomal degradation [58]. Autophagy has been reported to play a regulatory role during inflammasome activation via several proposed mechanisms. Damaged mitochondria, if not promptly removed by autophagy, have been shown to increase ROS production and release mtDNA into the cytosol, which may serve as inflammasome triggers [57]. Alternatively, autophagy targets ubiquitinated inflammasomes for degradation to dampen inflammasome activation, which may also explain the enhancement of inflammasome activation with autophagy inhibition [59]. On the other hand, a more recent study has shown that NLRP3 inflammasome activation caused the release of ASC specks that served as a danger signal in the extracellular space for proinflammatory responses [60]. As mentioned earlier, autophagosomes have been found to provide a non-canonical pathway for IL-1β release, which reaffirms the proinflammatory role of autophagy [52]. Therefore, the effect of autophagy on inflammasome activation is complex – it probably plays distinct roles during various stages of inflammasome activation. By initially inhibiting activation at low levels of stress, autophagy may be able to coordinate a more dramatic inflammatory response when the stimulatory threshold is reached.

Future structural studies on inflammasomes

This dissertation presents studies that have addressed several questions regarding the activation and regulation of inflammasomes. The assembly process relies on homotypic interactions amongst component proteins. Structural properties of PYD and CARD domains allow for the formation of signaling filaments, which are essential for inflammasome formation. Nucleated polymerization governs the assembly of inflammasomes, which may be inhibited via a capping mechanism. Meanwhile, there remain several unanswered questions that need to be addressed by future structural studies.

Recent studies on the NAIP/NLRC4 inflammasome have nicely illustrated the molecular interactions and the conformational changes of NAIP/NLRC4 oligomerization [61-63]. However, molecular details of NAIP activation are yet to be captured. The C-terminal 35 amino acids of bacterial flagellin were shown to be necessary and sufficient to trigger the NAIP5/NLRC4 inflammasome activation [64]. A comprehensive truncation study showed that the LRR domains of NAIP2 and NAIP5 were dispensable for the recognition of PrgJ and flagellin, respectively, while the central NBD-associated helical domains (HD1-WHD-HD2) were sufficient for ligand recognition [65]. The structural basis for ligand recognition and specificity determinant is largely unknown.

Unlike the AIM2 and NAIP/NLRC4 inflammasomes with well-defined ligands, direct ligands or protein binders of NLRP3 have been poorly characterized. Over the years, numerous studies have identified NLRP3 inflammasome triggers including a wide spectrum of stress signals. DHX33, a member of the DExD/H-box RNA helicase family, has been shown to mediate inflammasome assembly in response to viral double-stranded RNA [66]. Co-immunoprecipitation experiments showed that the DEAD domain of DHX33 was necessary to interact with the NACHT domain of NLRP3 [66]. Molecular details of this interaction require future structural studies. In addition, a member of the NIMA-related kinase, NEK7, has recently been reported to activate NLRP3 inflammasome in response to potassium efflux [67, 68]. The

catalytic domain of NEK7 was reported to directly bind to NLRP3, but its kinase activity was dispensable for binding [69]. The NLRP3/NEK7 interaction required both the NACHT and LRR domains of NLRP3 [69]. Therefore, it may not be too radical to consider NLRP3 as an adaptor rather than a sensor component – NLRC4 was also originally identified as the IPAF inflammasome until the identification of NAIP proteins were identified as the real sensors. Structural details of NLRP3 oligomerization and ligand binding remain to be deciphered.

References

1. Wu, H. (2013) Higher-order assemblies in a new paradigm of signal transduction, *Cell.* **153**, 287-92.

2. Kagan, J. C., Magupalli, V. G. & Wu, H. (2014) SMOCs: supramolecular organizing centres that control innate immunity, *Nature reviews Immunology.* **14**, 821-6.

3. Heymann, M. C. & Rosen-Wolff, A. (2013) Contribution of the inflammasomes to autoinflammatory diseases and recent mouse models as research tools, *Clinical immunology.* **147**, 175-84.

4. Hoffman, H. M., Mueller, J. L., Broide, D. H., Wanderer, A. A. & Kolodner, R. D. (2001) Mutation of a new gene encoding a putative pyrin-like protein causes familial cold autoinflammatory syndrome and Muckle-Wells syndrome, *Nature genetics.* **29**, 301-5.

5. Dode, C., Le Du, N., Cuisset, L., Letourneur, F., Berthelot, J. M., Vaudour, G., Meyrier, A., Watts, R. A., Scott, D. G., Nicholls, A., Granel, B., Frances, C., Garcier, F., Edery, P., Boulinguez, S., Domergues, J. P., Delpech, M. & Grateau, G. (2002) New mutations of CIAS1 that are responsible for Muckle-Wells syndrome and familial cold urticaria: a novel mutation underlies both syndromes, *American journal of human genetics.* **70**, 1498-506.

6. Meng, G., Zhang, F., Fuss, I., Kitani, A. & Strober, W. (2009) A mutation in the Nlrp3 gene causing inflammasome hyperactivation potentiates Th17 cell-dominant immune responses, *Immunity.* **30**, 860-74.

7. Feldmann, J., Prieur, A. M., Quartier, P., Berquin, P., Certain, S., Cortis, E., Teillac-Hamel, D., Fischer, A. & de Saint Basile, G. (2002) Chronic infantile neurological cutaneous and articular syndrome is caused by mutations in CIAS1, a gene highly expressed in polymorphonuclear cells and chondrocytes, *American journal of human genetics.* **71**, 198-203.

8. Broderick, L., De Nardo, D., Franklin, B. S., Hoffman, H. M. & Latz, E. (2015) The inflammasomes and autoinflammatory syndromes, *Annual review of pathology.* **10**, 395-424.

9. Weinert, C., Grutter, C., Roschitzki-Voser, H., Mittl, P. R. & Grutter, M. G. (2009) The crystal structure of human pyrin b30.2 domain: implications for mutations associated with familial Mediterranean fever, *Journal of molecular biology.* **394**, 226-36.

10. Chae, J. J., Wood, G., Masters, S. L., Richard, K., Park, G., Smith, B. J. & Kastner, D. L. (2006) The B30.2 domain of pyrin, the familial Mediterranean fever protein, interacts directly with caspase-1 to modulate IL-1beta production, *Proceedings of the National Academy of Sciences of the United States of America.* **103**, 9982-7.

11. Chae, J. J., Komarow, H. D., Cheng, J., Wood, G., Raben, N., Liu, P. P. & Kastner, D. L. (2003) Targeted disruption of pyrin, the FMF protein, causes heightened sensitivity to endotoxin and a defect in macrophage apoptosis, *Molecular cell.* **11**, 591-604.

12. Papin, S., Cuenin, S., Agostini, L., Martinon, F., Werner, S., Beer, H. D., Grutter, C., Grutter, M. & Tschopp, J. (2007) The SPRY domain of Pyrin, mutated in familial Mediterranean fever patients, interacts with inflammasome components and inhibits proIL-1beta processing, *Cell death and differentiation.* **14**, 1457-66.

13. Yu, J. W., Wu, J., Zhang, Z., Datta, P., Ibrahimi, I., Taniguchi, S., Sagara, J., Fernandes-Alnemri, T. & Alnemri, E. S. (2006) Cryopyrin and pyrin activate caspase-1, but not NF-kappaB, via ASC oligomerization, *Cell death and differentiation.* **13**, 236-49.

14. Yu, J. W., Fernandes-Alnemri, T., Datta, P., Wu, J., Juliana, C., Solorzano, L., McCormick, M., Zhang, Z. & Alnemri, E. S. (2007) Pyrin activates the ASC pyroptosome in response to engagement by autoinflammatory PSTPIP1 mutants, *Molecular cell.* **28**, 214-27.

15. Canna, S. W., de Jesus, A. A., Gouni, S., Brooks, S. R., Marrero, B., Liu, Y., DiMattia, M. A., Zaal, K. J., Sanchez, G. A., Kim, H., Chapelle, D., Plass, N., Huang, Y., Villarino, A. V., Biancotto, A., Fleisher, T. A., Duncan, J. A., O'Shea, J. J., Benseler, S., Grom, A., Deng, Z., Laxer, R. M. & Goldbach-Mansky, R. (2014) An activating NLRC4 inflammasome mutation causes autoinflammation with recurrent macrophage activation syndrome, *Nature genetics.* **46**, 1140-6.

16. Romberg, N., Al Moussawi, K., Nelson-Williams, C., Stiegler, A. L., Loring, E., Choi, M., Overton, J., Meffre, E., Khokha, M. K., Huttner, A. J., West, B., Podoltsev, N. A., Boggon, T. J., Kazmierczak, B. I. & Lifton, R. P. (2014) Mutation of NLRC4 causes a syndrome of enterocolitis and autoinflammation, *Nature genetics.* **46**, 1135-9.

17. Dombrowski, Y., Peric, M., Koglin, S., Kammerbauer, C., Goss, C., Anz, D., Simanski, M., Glaser, R., Harder, J., Hornung, V., Gallo, R. L., Ruzicka, T., Besch, R. & Schauber, J. (2011) Cytosolic DNA triggers inflammasome activation in keratinocytes in psoriatic lesions, *Science translational medicine.* **3**, 82ra38.

18. Murdoch, S., Djuric, U., Mazhar, B., Seoud, M., Khan, R., Kuick, R., Bagga, R., Kircheisen, R., Ao, A., Ratti, B., Hanash, S., Rouleau, G. A. & Slim, R. (2006) Mutations in NALP7 cause recurrent hydatidiform moles and reproductive wastage in humans, *Nature genetics.* **38**, 300-2.

19. Jin, Y., Mailloux, C. M., Gowan, K., Riccardi, S. L., LaBerge, G., Bennett, D. C., Fain, P. R. & Spritz, R. A. (2007) NALP1 in vitiligo-associated multiple autoimmune disease, *The New England journal of medicine.* **356**, 1216-25.

20. Zurawek, M., Fichna, M., Januszkiewicz-Lewandowska, D., Gryczynska, M., Fichna, P. & Nowak, J. (2010) A coding variant in NLRP1 is associated with autoimmune Addison's disease, *Human immunology.* **71**, 530-4.

21. Alkhateeb, A., Jarun, Y. & Tashtoush, R. (2013) Polymorphisms in NLRP1 gene and susceptibility to autoimmune thyroid disease, *Autoimmunity.* **46**, 215-21.

22. Levandowski, C. B., Mailloux, C. M., Ferrara, T. M., Gowan, K., Ben, S., Jin, Y., McFann, K. K., Holland, P. J., Fain, P. R., Dinarello, C. A. & Spritz, R. A. (2013) NLRP1 haplotypes associated with vitiligo and autoimmunity increase interleukin-1beta processing via the NLRP1 inflammasome, *Proceedings of the National Academy of Sciences of the United States of America.* **110**, 2952-6.

23. Zhang, W., Cai, Y., Xu, W., Yin, Z., Gao, X. & Xiong, S. (2013) AIM2 facilitates the apoptotic DNA-induced systemic lupus erythematosus via arbitrating macrophage functional maturation, *Journal of clinical immunology.* **33**, 925-37.

24. Martinon, F., Petrilli, V., Mayor, A., Tardivel, A. & Tschopp, J. (2006) Gout-associated uric acid crystals activate the NALP3 inflammasome, *Nature.* **440**, 237-41.

25. So, A., De Smedt, T., Revaz, S. & Tschopp, J. (2007) A pilot study of IL-1 inhibition by anakinra in acute gout, *Arthritis research & therapy.* **9**, R28.

26. Halle, A., Hornung, V., Petzold, G. C., Stewart, C. R., Monks, B. G., Reinheckel, T., Fitzgerald, K. A., Latz, E., Moore, K. J. & Golenbock, D. T. (2008) The NALP3 inflammasome is involved in the innate immune response to amyloid-beta, *Nature immunology.* **9**, 857-65.

27. Heneka, M. T., Kummer, M. P., Stutz, A., Delekate, A., Schwartz, S., Vieira-Saecker, A., Griep, A., Axt, D., Remus, A., Tzeng, T. C., Gelpi, E., Halle, A., Korte, M., Latz, E. & Golenbock, D. T. (2013) NLRP3 is activated in Alzheimer's disease and contributes to pathology in APP/PS1 mice, *Nature.* **493**, 674-8.

28. Duewell, P., Kono, H., Rayner, K. J., Sirois, C. M., Vladimer, G., Bauernfeind, F. G., Abela, G. S., Franchi, L., Nunez, G., Schnurr, M., Espevik, T., Lien, E., Fitzgerald, K. A., Rock, K. L., Moore, K. J., Wright, S. D., Hornung, V. & Latz, E. (2010) NLRP3 inflammasomes are required for atherogenesis and activated by cholesterol crystals, *Nature.* **464**, 1357-61.

29. Freigang, S., Ampenberger, F., Spohn, G., Heer, S., Shamshiev, A. T., Kisielow, J., Hersberger, M., Yamamoto, M., Bachmann, M. F. & Kopf, M. (2011) Nrf2 is essential for cholesterol crystal-induced inflammasome activation and exacerbation of atherosclerosis, *European journal of immunology.* **41**, 2040-51.

30. Lopez-Castejon, G. & Pelegrin, P. (2012) Current status of inflammasome blockers as anti-inflammatory drugs, *Expert Opin Investig Drugs.* **21**, 995-1007.

31. Dinarello, C. A., Simon, A. & van der Meer, J. W. (2012) Treating inflammation by blocking interleukin-1 in a broad spectrum of diseases, *Nature reviews Drug discovery.* **11**, 633-52.

32. Grattagliano, I., Bonfrate, L., Ruggiero, V., Scaccianoce, G., Palasciano, G. & Portincasa, P. (2014) Novel therapeutics for the treatment of familial Mediterranean fever: from colchicine to biologics, *Clinical pharmacology and therapeutics.* **95**, 89-97.

33. Molad, Y. (2002) Update on colchicine and its mechanism of action, *Curr Rheumatol Rep.* **4**, 252-6.

34. Misawa, T., Takahama, M., Kozaki, T., Lee, H., Zou, J., Saitoh, T. & Akira, S. (2013) Microtubule-driven spatial arrangement of mitochondria promotes activation of the NLRP3 inflammasome, *Nature immunology.* **14**, 454-60.

35. Dalbeth, N., Lauterio, T. J. & Wolfe, H. R. (2014) Mechanism of action of colchicine in the treatment of gout, *Clinical therapeutics.* **36**, 1465-79.

36. Jackman, R. W., Rhoads, M. G., Cornwell, E. & Kandarian, S. C. (2009) Microtubule-mediated NF-kappaB activation in the TNF-alpha signaling pathway, *Experimental cell research.* **315**, 3242-9.

37. Roberge, C. J., Gaudry, M., de Medicis, R., Lussier, A., Poubelle, P. E. & Naccache, P. H. (1993) Crystal-induced neutrophil activation. IV. Specific inhibition of tyrosine phosphorylation by colchicine, *The Journal of clinical investigation.* **92**, 1722-9.

38. Chia, E. W., Grainger, R. & Harper, J. L. (2008) Colchicine suppresses neutrophil superoxide production in a murine model of gouty arthritis: a rationale for use of low-dose colchicine, *British journal of pharmacology.* **153**, 1288-95.

39. Oka, T., Hori, M. & Ozaki, H. (2005) Microtubule disruption suppresses allergic response through the inhibition of calcium influx in the mast cell degranulation pathway, *J Immunol.* **174**, 4584-9.

40. Yagnik, D. R., Evans, B. J., Florey, O., Mason, J. C., Landis, R. C. & Haskard, D. O. (2004) Macrophage release of transforming growth factor beta1 during resolution of monosodium urate monohydrate crystal-induced inflammation, *Arthritis and rheumatism.* **50**, 2273-80.

41. Wozniacka, A., Lesiak, A., Narbutt, J., McCauliffe, D. P. & Sysa-Jedrzejowska, A. (2006) Chloroquine treatment influences proinflammatory cytokine levels in systemic lupus erythematosus patients, *Lupus.* **15**, 268-75.

42. Shin, M. S., Kang, Y., Lee, N., Wahl, E. R., Kim, S. H., Kang, K. S., Lazova, R. & Kang, I. (2013) Self double-stranded (ds)DNA induces IL-1beta production from human monocytes by activating NLRP3 inflammasome in the presence of anti-dsDNA antibodies, *J Immunol.* **190**, 1407-15.

43. Lamkanfi, M., Mueller, J. L., Vitari, A. C., Misaghi, S., Fedorova, A., Deshayes, K., Lee, W. P., Hoffman, H. M. & Dixit, V. M. (2009) Glyburide inhibits the Cryopyrin/Nalp3 inflammasome, *The Journal of cell biology.* **187**, 61-70.

44. Marchetti, C., Chojnacki, J., Toldo, S., Mezzaroma, E., Tranchida, N., Rose, S. W., Federici, M., Van Tassell, B. W., Zhang, S. & Abbate, A. (2014) A novel pharmacologic inhibitor of the NLRP3 inflammasome limits myocardial injury after ischemia-reperfusion in the mouse, *Journal of cardiovascular pharmacology.* **63**, 316-22.

45. Sohn, J. & Hur, S. (2016) Filament assemblies in foreign nucleic acid sensors, *Current opinion in structural biology.* **37**, 134-144.

46. Lopez-Castejon, G. & Brough, D. (2011) Understanding the mechanism of IL-1beta secretion, *Cytokine & growth factor reviews.* **22**, 189-95.

47. Rubartelli, A., Cozzolino, F., Talio, M. & Sitia, R. (1990) A novel secretory pathway for interleukin-1 beta, a protein lacking a signal sequence, *The EMBO journal.* **9**, 1503-10.

48. Andrei, C., Dazzi, C., Lotti, L., Torrisi, M. R., Chimini, G. & Rubartelli, A. (1999) The secretory route of the leaderless protein interleukin 1beta involves exocytosis of endolysosome-related vesicles, *Molecular biology of the cell.* **10**, 1463-75.

49. MacKenzie, A., Wilson, H. L., Kiss-Toth, E., Dower, S. K., North, R. A. & Surprenant, A. (2001) Rapid secretion of interleukin-1beta by microvesicle shedding, *Immunity.* **15**, 825-35.

50. Qu, Y., Ramachandra, L., Mohr, S., Franchi, L., Harding, C. V., Nunez, G. & Dubyak, G. R. (2009) P2X7 receptor-stimulated secretion of MHC class II-containing exosomes requires the ASC/NLRP3 inflammasome but is independent of caspase-1, *J Immunol.* **182**, 5052-62.

51. Fink, S. L. & Cookson, B. T. (2006) Caspase-1-dependent pore formation during pyroptosis leads to osmotic lysis of infected host macrophages, *Cellular microbiology.* **8**, 1812-25.

52. Zhang, M., Kenny, S. J., Ge, L., Xu, K. & Schekman, R. (2015) Translocation of interleukin-1beta into a vesicle intermediate in autophagy-mediated secretion, *eLife.* **4**.

53. Shi, J., Zhao, Y., Wang, Y., Gao, W., Ding, J., Li, P., Hu, L. & Shao, F. (2014) Inflammatory caspases are innate immune receptors for intracellular LPS, *Nature.* **514**, 187-92.

54. Stowe, I., Lee, B. & Kayagaki, N. (2015) Caspase-11: arming the guards against bacterial infection, *Immunological reviews.* **265**, 75-84.

55. Kayagaki, N., Stowe, I. B., Lee, B. L., O'Rourke, K., Anderson, K., Warming, S., Cuellar, T., Haley, B., Roose-Girma, M., Phung, Q. T., Liu, P. S., Lill, J. R., Li, H., Wu, J., Kummerfeld, S., Zhang, J., Lee, W. P., Snipas, S. J., Salvesen, G. S., Morris, L. X., Fitzgerald, L., Zhang, Y., Bertram, E. M., Goodnow, C. C. & Dixit, V. M. (2015) Caspase-11 cleaves gasdermin D for non-canonical inflammasome signalling, *Nature.* **526**, 666-71.

56. Mostowy, S. & Shenoy, A. R. (2015) The cytoskeleton in cell-autonomous immunity: structural determinants of host defence, *Nature reviews Immunology.* **15**, 559-73.

57. Vural, A. & Kehrl, J. H. (2014) Autophagy in macrophages: impacting inflammation and bacterial infection, *Scientifica.* **2014**, 825463.

58. Netea-Maier, R. T., Plantinga, T. S., van de Veerdonk, F. L., Smit, J. W. & Netea, M. G. (2016) Modulation of inflammation by autophagy: Consequences for human disease, *Autophagy.* **12**, 245-60.

59. Shi, C. S., Shenderov, K., Huang, N. N., Kabat, J., Abu-Asab, M., Fitzgerald, K. A., Sher, A. & Kehrl, J. H. (2012) Activation of autophagy by inflammatory signals limits IL-1beta production by targeting ubiquitinated inflammasomes for destruction, *Nature immunology.* **13**, 255-63.

60. Baroja-Mazo, A., Martin-Sanchez, F., Gomez, A. I., Martinez, C. M., Amores-Iniesta, J., Compan, V., Barbera-Cremades, M., Yague, J., Ruiz-Ortiz, E., Anton, J., Bujan, S., Couillin, I., Brough, D., Arostegui, J. I. & Pelegrin, P. (2014) The NLRP3 inflammasome is released as a particulate danger signal that amplifies the inflammatory response, *Nature immunology.* **15**, 738-48.

61. Hu, Z., Yan, C., Liu, P., Huang, Z., Ma, R., Zhang, C., Wang, R., Zhang, Y., Martinon, F., Miao, D., Deng, H., Wang, J., Chang, J. & Chai, J. (2013) Crystal structure of NLRC4 reveals its autoinhibition mechanism, *Science.* **341**, 172-5.

62. Hu, Z., Zhou, Q., Zhang, C., Fan, S., Cheng, W., Zhao, Y., Shao, F., Wang, H. W., Sui, S. F. & Chai, J. (2015) Structural and biochemical basis for induced self-propagation of NLRC4, *Science*.

63. Zhang, L., Chen, S., Ruan, J., Wu, J., Tong, A. B., Yin, Q., Li, Y., David, L., Lu, A., Wang, W. L., Marks, C., Ouyang, Q., Zhang, X., Mao, Y. & Wu, H. (2015) Cryo-EM structure of the activated NAIP2-NLRC4 inflammasome reveals nucleated polymerization, *Science*.

64. Lightfield, K. L., Persson, J., Brubaker, S. W., Witte, C. E., von Moltke, J., Dunipace, E. A., Henry, T., Sun, Y. H., Cado, D., Dietrich, W. F., Monack, D. M., Tsolis, R. M. & Vance, R. E. (2008) Critical function for Naip5 in inflammasome activation by a conserved carboxy-terminal domain of flagellin, *Nature immunology.* **9**, 1171-8.

65. Tenthorey, J. L., Kofoed, E. M., Daugherty, M. D., Malik, H. S. & Vance, R. E. (2014) Molecular basis for specific recognition of bacterial ligands by NAIP/NLRC4 inflammasomes, *Molecular cell.* **54**, 17-29.

66. Mitoma, H., Hanabuchi, S., Kim, T., Bao, M., Zhang, Z., Sugimoto, N. & Liu, Y. J. (2013) The DHX33 RNA Helicase Senses Cytosolic RNA and Activates the NLRP3 Inflammasome, *Immunity.* **39**, 123-35.

67. Shi, H., Wang, Y., Li, X., Zhan, X., Tang, M., Fina, M., Su, L., Pratt, D., Bu, C. H., Hildebrand, S., Lyon, S., Scott, L., Quan, J., Sun, Q., Russell, J., Arnett, S., Jurek, P., Chen, D., Kravchenko, V. V., Mathison, J. C., Moresco, E. M., Monson, N. L., Ulevitch, R. J. & Beutler, B. (2016) NLRP3 activation and mitosis are mutually exclusive events coordinated by NEK7, a new inflammasome component, *Nature immunology.* **17**, 250-8.

68. Schmid-Burgk, J. L., Chauhan, D., Schmidt, T., Ebert, T. S., Reinhardt, J., Endl, E. & Hornung, V. (2016) A Genome-wide CRISPR (Clustered Regularly Interspaced Short Palindromic Repeats) Screen Identifies NEK7 as an Essential Component of NLRP3 Inflammasome Activation, *The Journal of biological chemistry.* **291**, 103-9.

69. He, Y., Zeng, M. Y., Yang, D., Motro, B. & Nunez, G. (2016) NEK7 is an essential mediator of NLRP3 activation downstream of potassium efflux, *Nature.* **530**, 354-7.

Appendix I

Supplemental Materials for Chapter Two:

A Structural and Mechanistic Study of the ASC^{PYD} Filament

This section contains the following 7 figures, 4 tables, caption for 1 movie, Material and Methods, and Supplemental References –

Supplemental Figures

Figure S2.1. Related to Figure 2.1;
Figure S2.2. Related to Figure 2.2;
Figure S2.3. Related to Figure 2.3;
Figure S2.4. Related to Figure 2.4;
Figure S2.5. Related to Figure 2.5;
Figure S2.6. Related to Figure 2.6;
Figure S2.7. Related to Figure 2.7.

Supplemental Tables

Table S2.1, related to Figure 2.4;
Table S2.2, related to Figure 2.5;
Table S2.3, related to Figure 2.5;
Table S2.4, related to Figure 2.7.

Supplemental Movie

Movie S2.1, related to Figure 2.3.

Material and Methods

Supplemental References

Supplemental Figures

Figure S2.1. ASC^{PYD} Forms filamentous Structures as Visualized by Electron Microscopy, Related to Figure 2.1

A. Size-exclusion chromatograph of the ASC^{PYD}/AIM2^{PYD} complex. ASC^{PYD} is fused with an N-terminal His-tag and co-expressed with untagged AIM2^{PYD}. The complex was first purified by Ni-affinity chromatography. It elutes in the void position on a Superdex 200 gel filtration column.

B. A negative stain EM image of Sumo-AIM2^{PYD} filaments.

C. Ni-NTA-gold (5 nm) labeling of Biotin-AIM2^{PYD}/His-ASC^{PYD} complex.

D. Size-exclusion chromatography of His-MBP tagged ASC^{PYD}. His-MBP-ASC^{PYD} fusion protein is monomeric on a Superdex200 column.

E. Proteolysis time course of MBP-tagged ASC^{PYD} labeled with Alexa488 by the TEV protease.

F. AIM2^{PYD} nucleated ASC^{PYD} filaments after the *in vitro* polymerization assay.

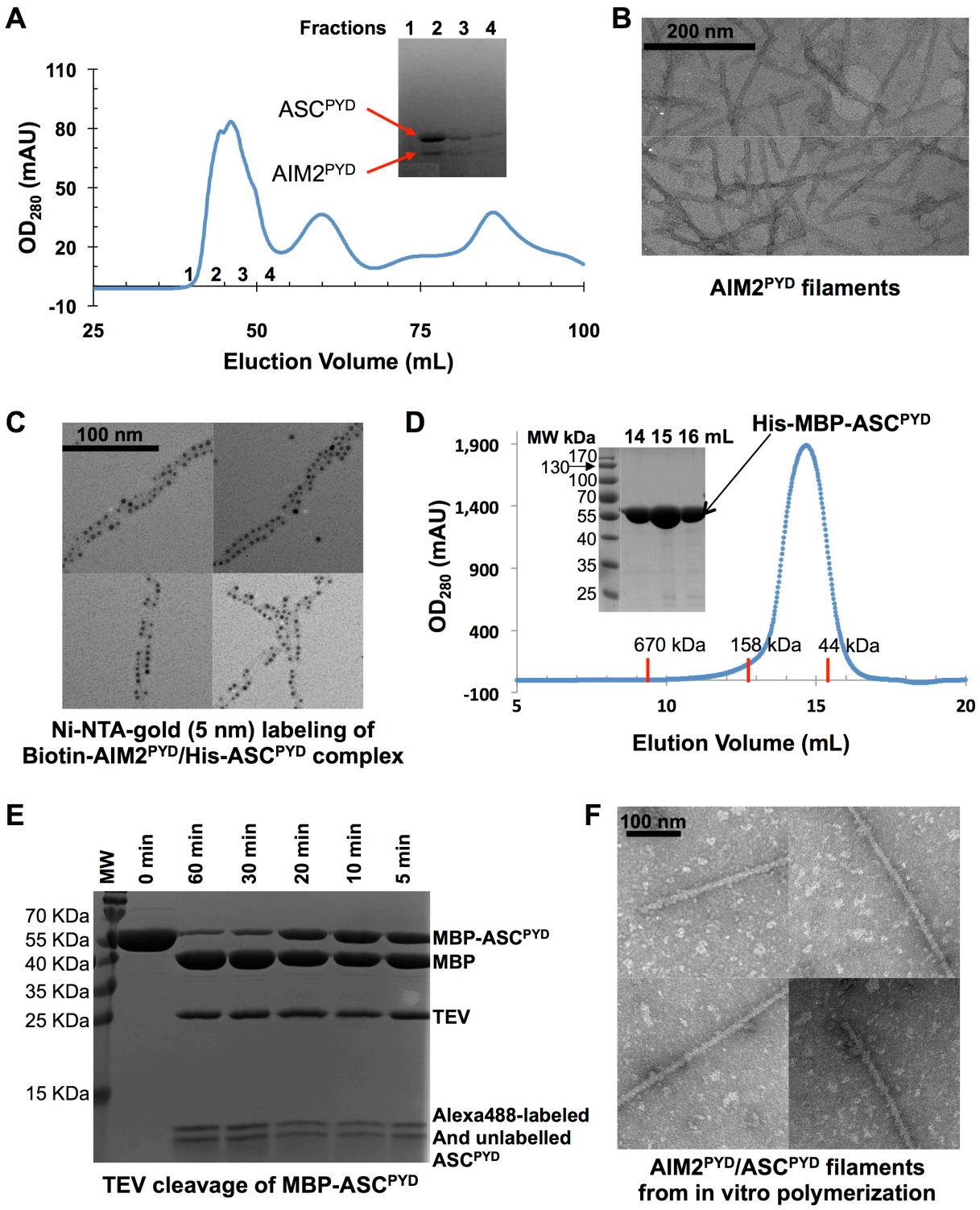

Figure S2.1 (Continued)

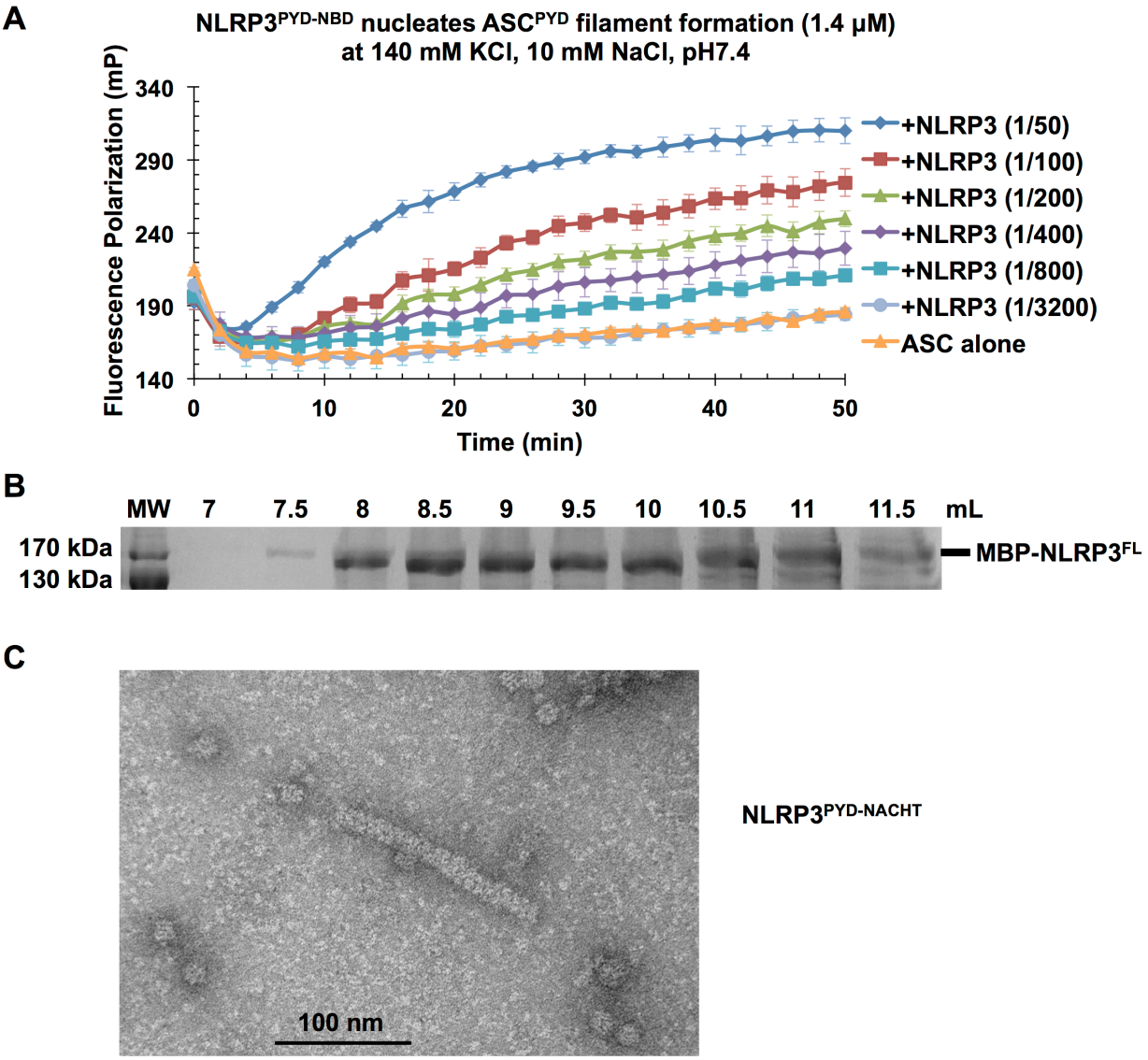

Figure S2.2. NLPR3^{FL} and NLRP3$^{PYD-NBD}$ but not NLRP3^{PYD} Promote ASC^{PYD} Filament Formation, Related to Figure 2.2

A. NLRP3$^{PYD-NBD}$ nucleates ASC^{PYD} filament formation (1.4 μM) at the physiological intracellular condition of 140 mM KCl and 10 mM NaCl at pH7.4. Data are represented as mean±SD (N=3).

B. SDS-PAGE of size-exclusion chromatography fractions of insect cell expressed MBP-NLRP3^{FL}.

C. A negative stain EM image of recombinant NLRP3$^{PYD-NBD}$.

Figure S2.3. Cryo-EM Structure of the ASC^{PYD} Filament at Near Atomic Resolution, Related to Figure 2.3

A. Fourier shell correlation (FSC) plot of the reconstruction, generated by dividing the images into two halves.

B. FSC plot of ASC^{PYD} filament reconstruction generated by comparison of the cryo-EM map with the final model, using DireX with occupancy refinement (solid line) and Phenix with TLS refinement (dashed line). The former gave a nominal resolution of 3.6 Å at FSC=0.143.

C. The actual EM reconstruction, filtered to 3.8 Å, is shown on the left as a transparent grey surface. Three adjacent subunits are shown as a ribbon model, each in a different color. On the right, the grey surface is that generated from the model when filtered to 3.8 Å and with refinement by DireX. The comparison shows that the 3.8 Å resolution, as claimed, is reasonable.

D. Structure-based sequence alignment of 11 PYDs with known structures. These include PYDs of ASC [1], NLRP1 [2], ASC2 [3, 4], hNLRP10 [5], mNLRP10 (PDB code 2DO9), NLRP7 [6], NLRP12 [7], NLRP3 [8], NLRP4 [9], MNDA (PDB code: 2DBG) and AIM2 [10]. Residues conserved in more than 7 proteins are shown in red. Yellow-highlighted residues indicate conservation with those in the ASC^{PYD} interfaces. The PYD of MEFV (also known as Pyrin), whose mutations are associated with FMF, is included at the bottom of the alignment. Locations of disease mutations in NLRP3 and pyrin are highlighted in green.

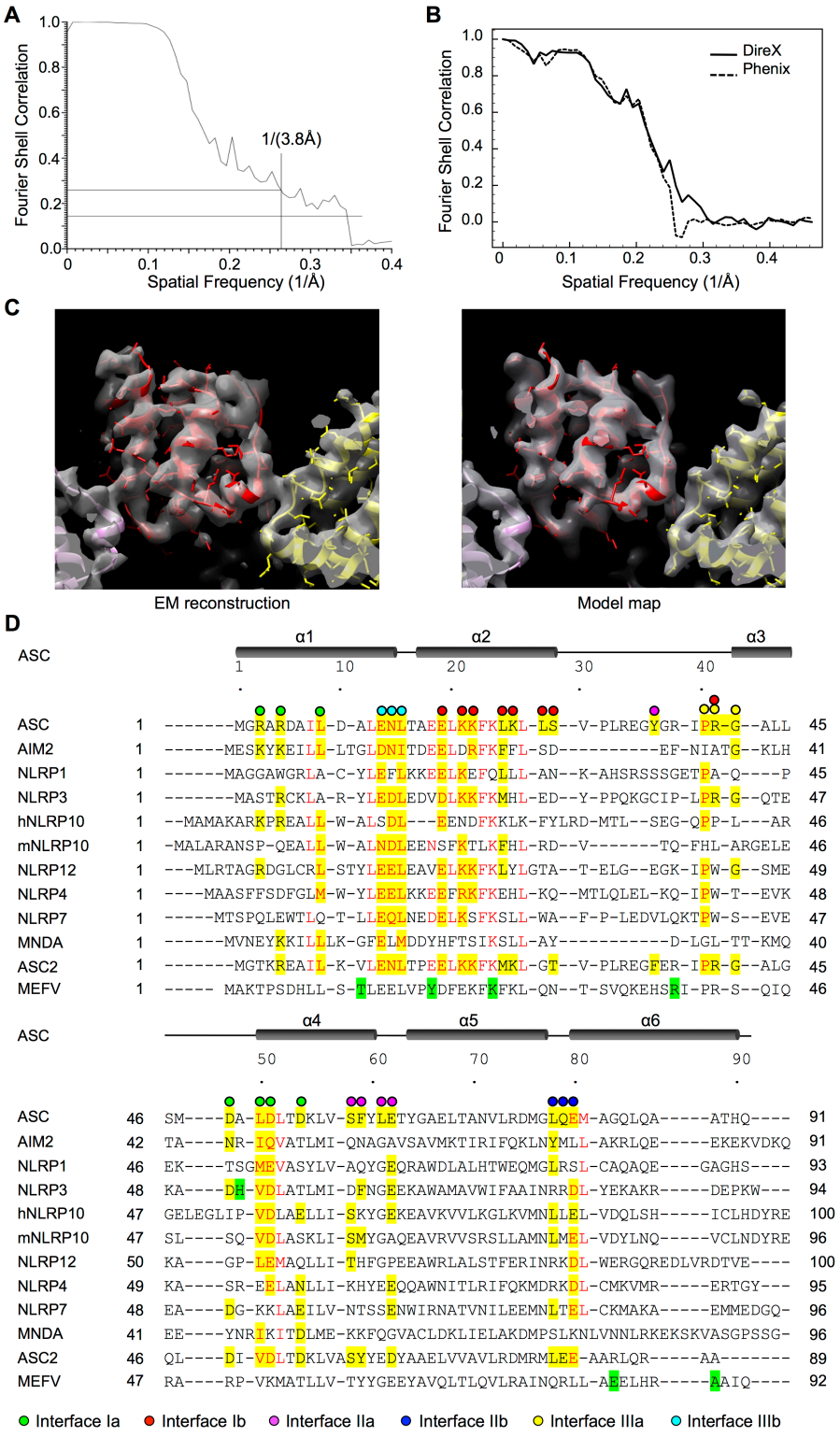

Figure S2.3 (Continued)

Figure S2.4. Detailed Cryo-EM Model of the ASC^{PYD} Filament, Related to Figure 2.4

A. Cryo-EM density superimposed with ASC^{PYD} structure in the filament in the α2-α3 region

B. Superposition of all 11 known PYD structures, showing the short α3 and the variation at the α2-α3 loop.

C, D, E. Superposition of the ASC/ASC dimers with RAIDD/PIDD dimers (top) and MyD88/MyD88 dimers (bottom) in the type I (**C**), type II (**D**) and type III (**E**) interactions.

F, G, H. Electrostatic surface representation of the interaction patches.

I. High salt significantly disrupts filament formation.

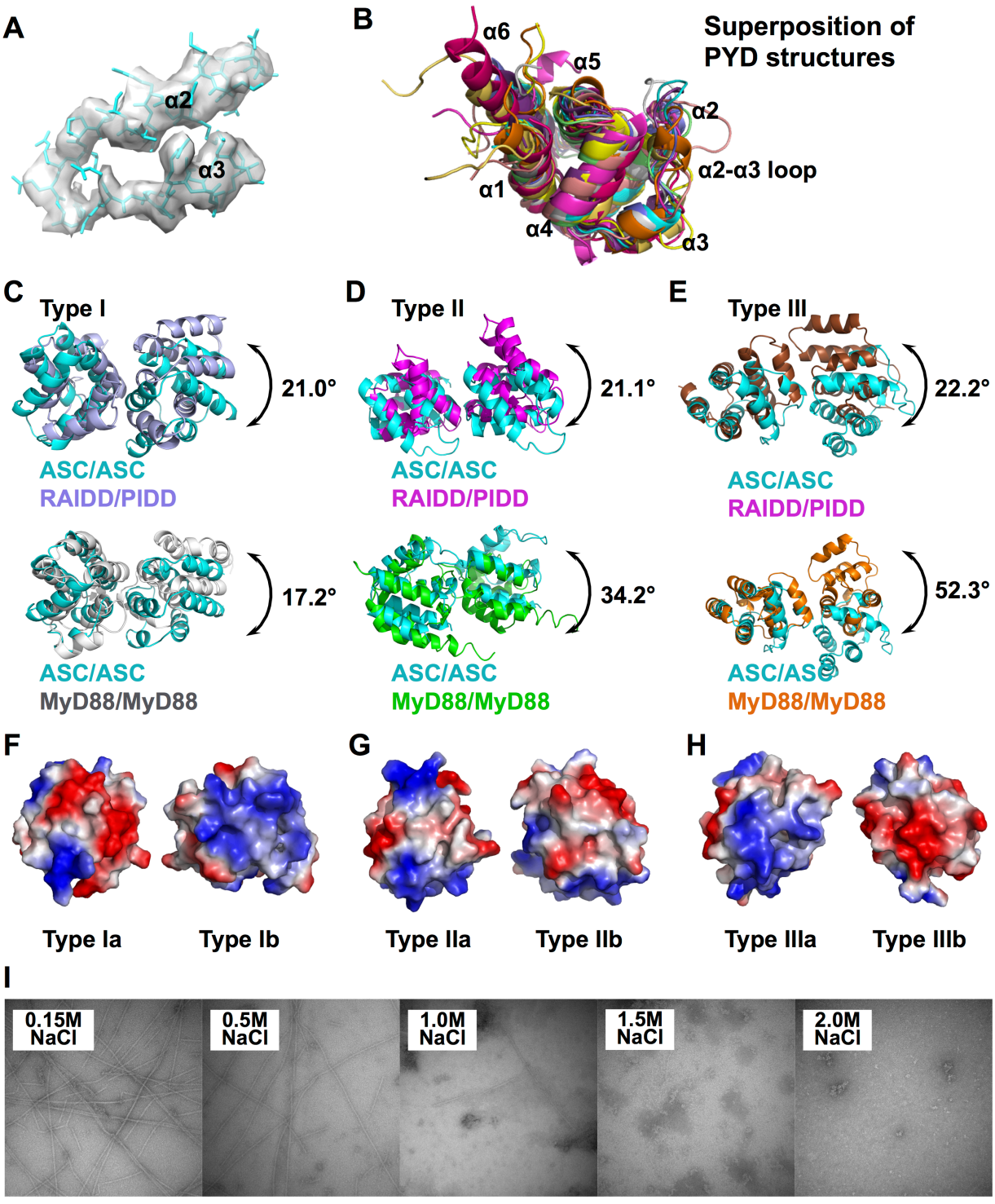

Figure S2.4 (Continued)

Figure S2.5. Structure-based Mutations Disrupts ASC Filament Formation and AIM2/ASC and NLRP3/ASC Interactions *in Vitro* and in Cells, Related to Figure 2.5

A. Morphology of ASC^{PYD} filaments visualized by fluorescence microscopy. eGFP control, WT (the arrowhead depicts filaments) and mutant (D48R, K21E/K22E, F59E, E13R and R41E) eGFP-tagged ASC^{PYD} (1-106) constructs were expressed in COS-1 cells. n: nucleus; scale bars = 10 μm.

B. Expression levels of depicted constructs shown by Western blotting using anti-ASC specific antibody.

C. Morphology of ASC^{PYD} filaments visualized by EM. eGFP control, WT and mutant (D48R, K21E/K22E, F59E, E13R and R41E) eGFP-tagged ASC^{PYD} constructs were expressed in HEK 293T cells. ASC immunoprecipitated complex was eluted followed by negative stain EM visualization. Scale bar = 100 nm.

D. ASC immunoprecipitated complex was eluted and analyzed by Western blotting using anti-ASC specific antibody. Lower band at ~40 kDa (denoted by arrowhead) represents eluted ASC, and upper band at ~55 kDa represents IgG heavy chain (denoted by asterisk).

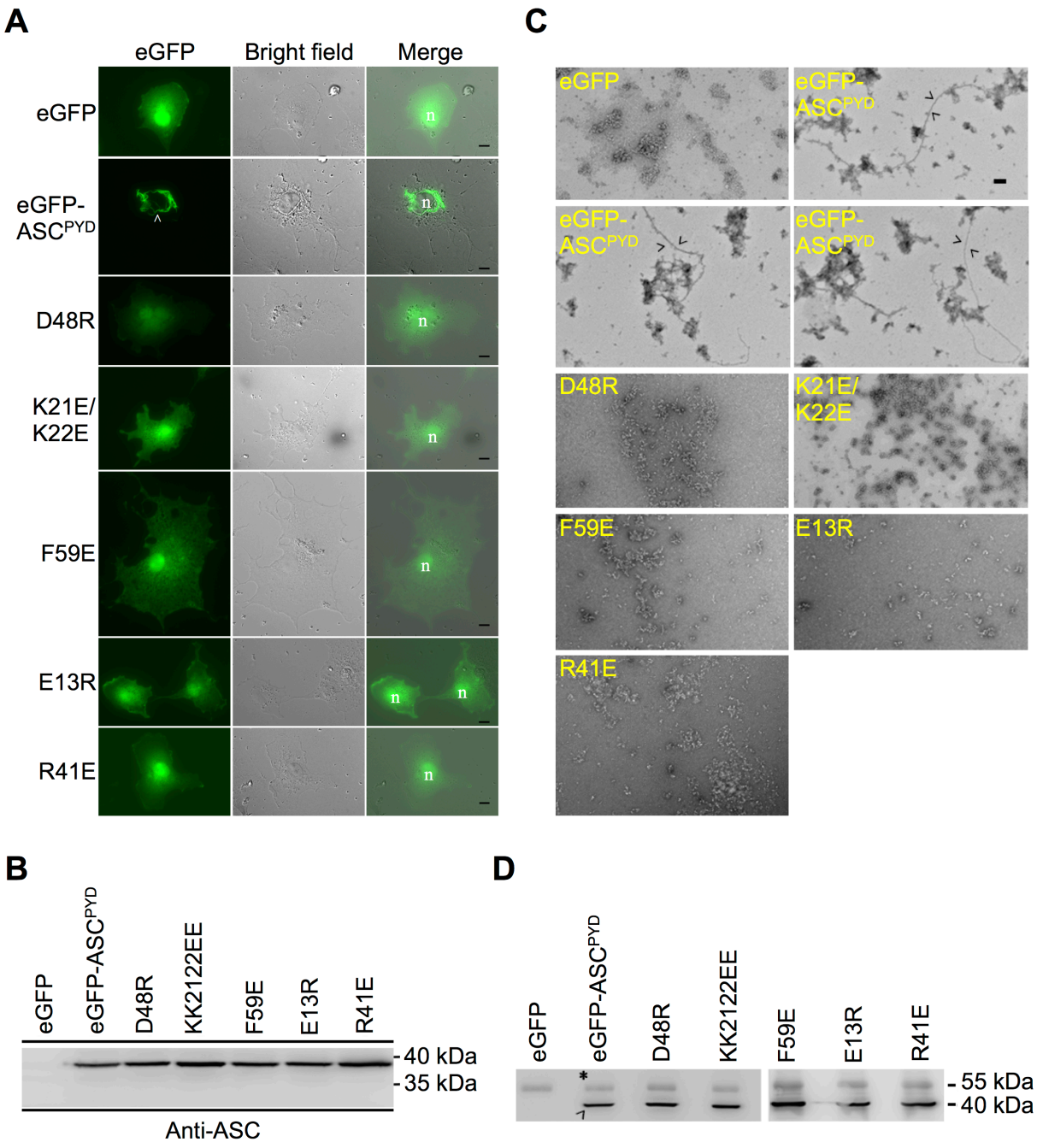

Figure S2.5 (Continued)

Figure S2.6. Reconstitution of Full AIM2 Inflammasome, Related to Figure 2.6

A. Kinetics of ASC^{FL} aggregation upon removal of the His-MBP tag.

B. Quantification of relative ASC^{PYD} (Mutant/WT) binding to ASC^{FL} using anti-eGFP antibody, shown as mean ± S.E. *** denotes $p < 0.001$ by Student's *t* test, n=4.

C. Ni-NTA pulldown of $AIM2^{PYD}$ by His-GFP-caspase-1^{CARD} through WT or mutant ASC^{FL} with mutations in the PYD. GFP-caspase-1^{CARD}, MBP-ASC^{FL}, and MBP-$AIM2^{PYD}$ were incubated on ice overnight with TEV protease. MBP and uncut MBP-$AIM2^{PYD}$ and MBP-ASC^{FL} were removed by incubating with amylose resin for 1 hr. Unbound fractions were incubated with Ni-NTA resin for 1 hr, washed 3 times, eluted and subjected to SDS-PAGE.

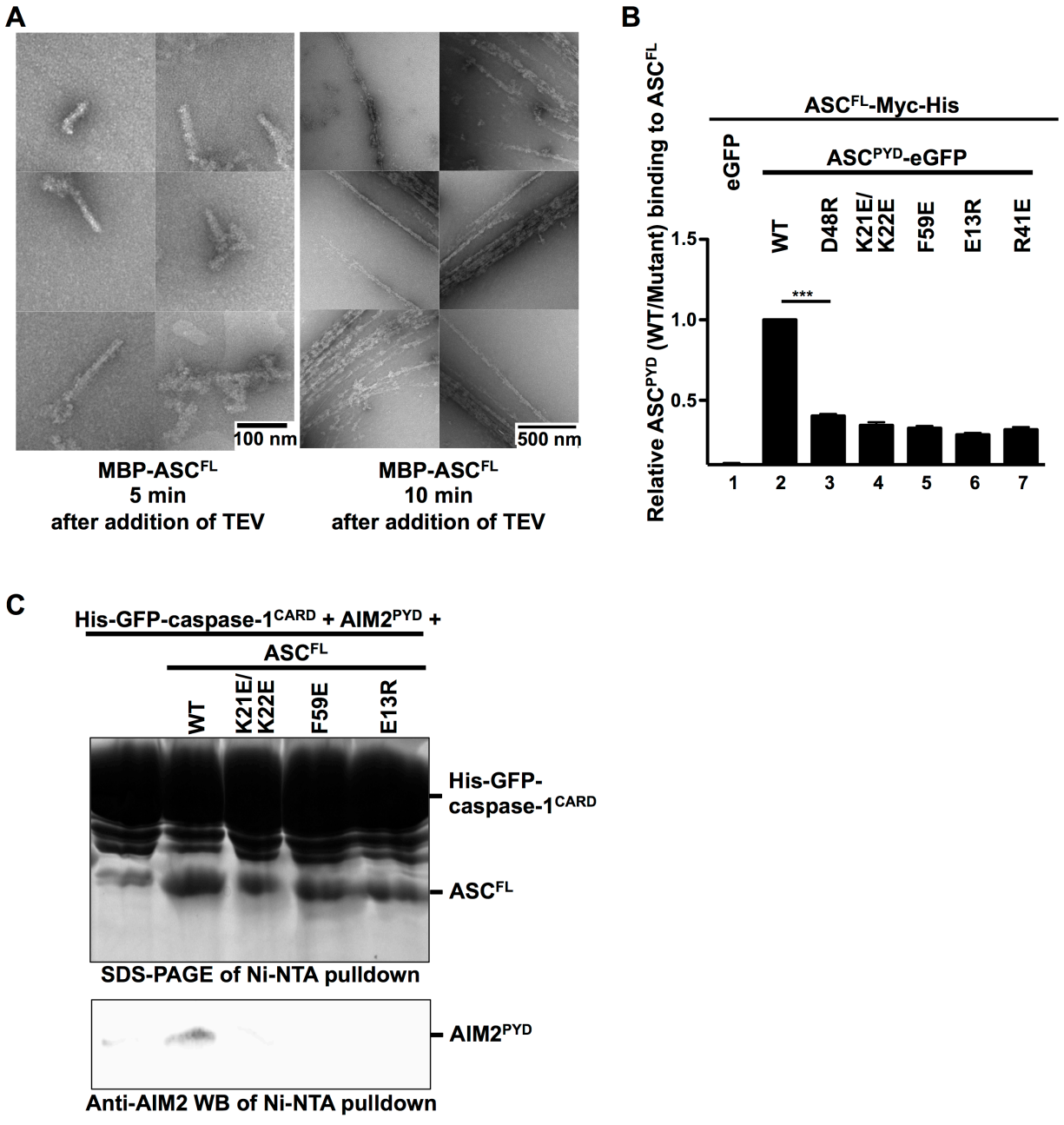

Figure S2.6 (Continued)

Figure S2.7. Morphology, Stoichiometry and ProIL-1β Processing in Inflammasomes, Related to Figure 2.7

A, B. Morphology of anti-ASC immunoprecipitated NLRP3 inflammasome clusters from uric acid crystal activated THP-1 cells analyzed by negative stain EM (A) in comparison with in vitro reconstituted inflammasomes incubated overnight (B).

C. Control images of immunogold EM on ultrathin cryosections. Left: Lack of labeling in the ASC-eGFP transfected cells in the absence of primary anti-ASC antibody. Arrowheads delineate perinuclear punctum. Right: eGFP alone transfected cells showed neither punctum nor anti-ASC gold labeling. Scale bar: 500 nm

D. Standard curve of quantitative Western blot of recombinant His-MBP-ASC.

E. Standard curve of quantitative Western blot of recombinant His-GFP-caspase-1.

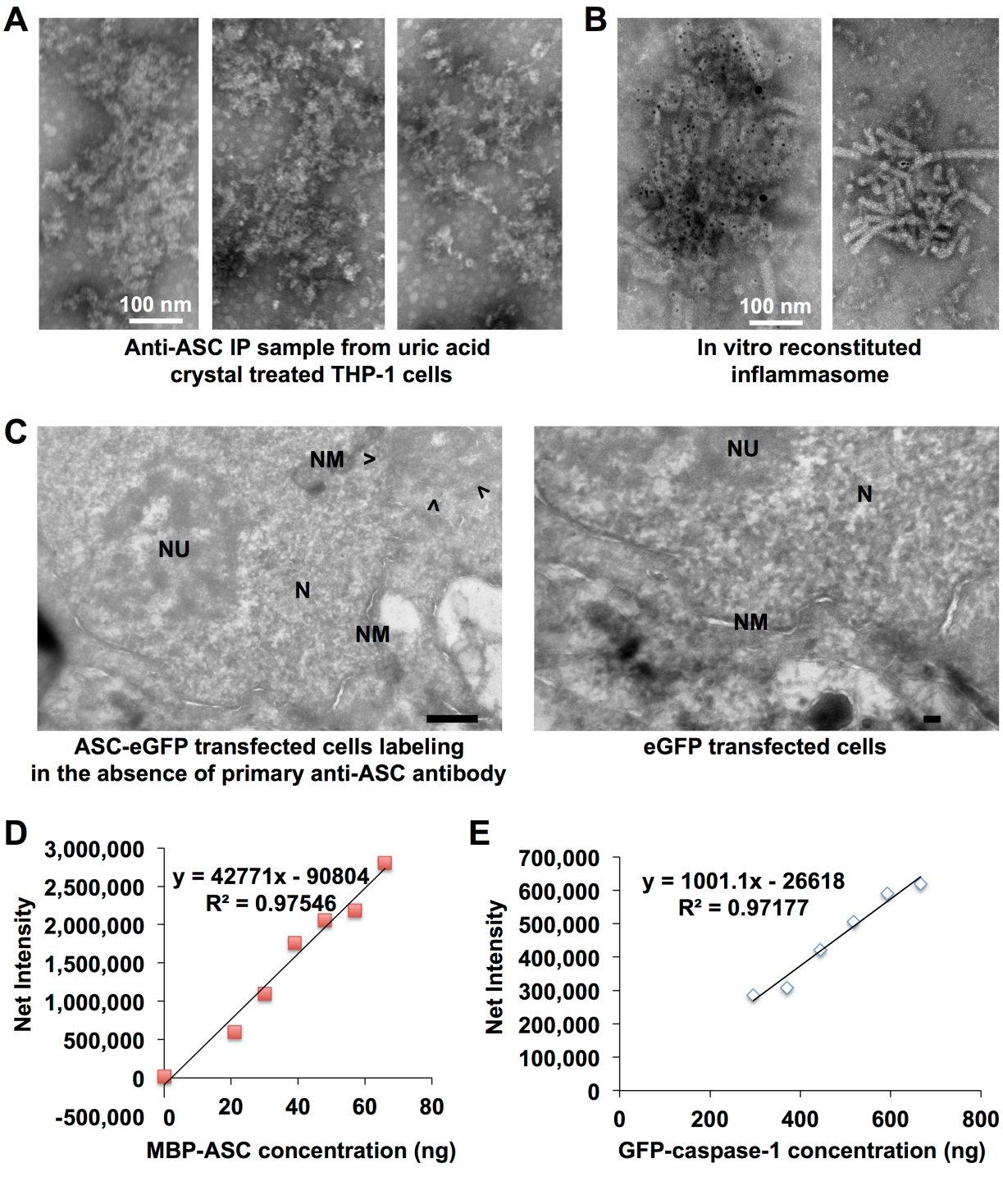

Figure S2.7 (Continued)

Supplemental Tables

Table S2.1. Comparison Between Interactions in the ASC^{PYD} Filament and Those in the PIDDosome and the Myddosome, Related to Figure 2.4. Shown are rotations needed to match the second subunit when the first subunit in the interaction pairs is aligned, Summary: 15-21° for type I, 21-35° for type II and 17-52° for type III interactions.

	ASC/ASC_Type I	ASC/ASC_Type II	ASC/ASC_Type III
PIDDosome			
RAIDD/RAIDD	16.2°	22.5°	33.2°
RAIDD/PIDD	21.0°	21.1°	22.2°
PIDD/PIDD	15.1°	N/A	17.9°
Myddosome			
MyD88/MyD888	17.2°	34.2°	52.3°
MyD88/IRAK4	25.5°	35.3°	35.4°
IRAK4/IRAK2	20.3°	22.4°	41.6°

Table S2.2. Summary of Mutagenesis Results on ASC^{PYD} Interfaces, Related to Figure 2.5.

-: disruption of filament formation; +/-: weakening of filament formation.

	Residues	Structure-based mutants *in vitro*	Structure-based mutants in cells	Existing defective mutants [11]
Type I				
Ia	R3	R3E (+/-)		
Ia	R5			
Ia	L9			
Ia	D48	D48R (-), D48N (-)	D48R (-)	D48A, D48N, D48E, D48R
Ia	L50	L50A (+/-)		
Ia	D51	D51R (-)		D51A, D51N, D51K
Ia	D54			
Ib	E19			E19A
Ib	K21	K21Q (-)		K21A, K21Q, K21E
Ib	K22	K21E/K22E (-)	K21E/K22E (-)	
Ib	L25			
Ib	K26	K26E (-)		K26A, K26Q
Ib	L28			
Ib	S29			
Ib	R41	R41E (-)	R41E (-)	R41A, R41Q, R41W
Type II				
IIa	Y36	Y36A (+/-)		
IIa	S58			
IIa	F59	F59E (-)	F59E (-)	
IIa	L61			
IIa	E62			E62A
IIb	L78			
IIb	Q79			
IIb	E80	E80R (+/-)		
Type III				
IIIa	P40			
IIIa	R41	R41E (-)	R41E (-)	R41A, R41Q, R41W
IIIa	G42			
IIIb	E13	E13R (-)	E13R (-)	
IIIb	N14			
IIIb	L15			

Table S2.3. Relative Rates of ASC^{PYD} Polymerization in the Presence of Sub-stoichiometric NLRP3 or AIM2, Related to Figure 2.5. Control rate: rate of ASC^{PYD} filament formation in the absence of nucleator. Nucleation rate: initial rate of filament formation in the presence of nucleator. +: indicates normal nucleation; +/-: indicates partially defective nucleation; -: indicates abolishment of nucleation

Activator	Mutation	Interface	Nucleation Ability	Polymerization rate ratio between with and without the activator
$NLRP3^{PYD-NBD}$	WT (@1/100 molar ratio)		+	10.61
	K23E,K24E	Type Ib	-	1.10
	M27E	Type Ib	-	0.88
	E64R	Type IIa	-	0.98
	D82R	Type IIb	-	1.02
	R43W	Type IIIa	-	1.11
	E15R	Type IIIb	-	0.98
$AIM2^{PYD}$	WT (@1/4 molar ratio)		+	4.91
	L10A,L11A	Type Ia	-	0.87
	R24E	Type Ib	-	0.95
	F27G	Type Ib	-	1.54
	Y74R	Type IIb	-	1.17
	G38E	Type IIIa	+/-	2.39
	K39E	Type IIIa	+/-	2.92
	D15R	Type IIIb	-	1.12

Table S2.4. Structure-based Sequence Alignment of PYDs Relative to ASC^{PYD} Shows Conservation and Variability at the Three Asymmetric Interfaces, Related to Figure 2.7. The number of residues conserved with ASC^{PYD} and the total number of residues at each interface are shown in the table and in parentheses, respectively. The total percentages of conservation are shown in the right column for those PYDs with ≥ 50% homology to ASC. See Figure S2.3C for the alignment.

	Ia (7)	Ib (7)	IIa (5)	IIb (3)	IIIa (3)	IIIb (3)	Total (28)
AIM2	6	3	0	1	1	3	14, 50%
NLRP1	2	3	1	1	1	2	10
NLRP3	4	4	2	1	3	3	17, 61%
hNLRP10	6	1	2	2	1	2	14, 50%
mNLRP10	3	2	2	2	0	3	12
NLRP12	4	4	1	1	2	3	15, 54%
NLRP4	3	3	1	1	1	3	12
NLRP7	2	2	1	2	1	3	11
MNDA	4	0	0	0	0	2	6
ASC2	6	6	4	3	3	3	25, 89%

Supplemental Movie

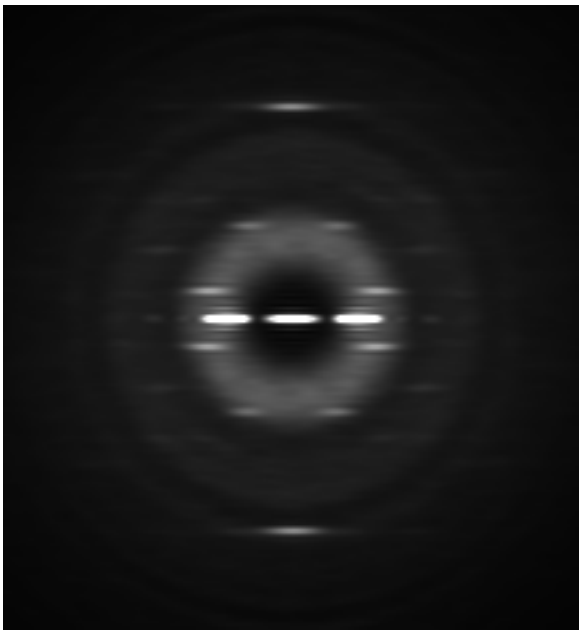

Movie S2.1. Averaged Power Spectrum Animation, Related to Figure 2.3

This three-frame animation was generated by computing the averaged power spectrum from filament segments in the central three bins of the histogram in Figure 2.3C. The large shifts of the near-equatorial layer line (n=-6) as well as the almost fixed meridional intensity (at ~ 1/14 $Å^{-1}$) arise from a variable twist with little variability in the axial rise per subunit. The power spectra, which are unbiased (due to the fact that they are invariant under translations of the images and do not require alignments of the images), demonstrate that the sorting in Figure 2.3C worked properly.

Materials and Methods

Recombinant Protein Expression and Purification

Various methods were attempted to obtain high quality filaments of ASC^{PYD}. The best results were obtained with ASC^{PYD} (residues 1-106), which was cloned into pDB-His-MBP vector (Berkeley Structural Genomics Center) using the NdeI and NotI cloning sites and expressed as an MBP-fusion protein with an additional N-terminal 6 x His tag. This construct was transformed and expressed in BL21(DE3) cells by growing the culture at 37 ˚C to OD of 0.8 and inducing with 0.5 mM IPTG overnight at 16 ˚C. The *E. coli* cells were harvested and lysed by sonication in a buffer containing 20 mM Tris at pH 8.0, 200 mM NaCl, 5 mM imidazole, 5 mM β-ME, and 10% glycerol. The cell lysate was centrifuged at 40,000 g for 40 minutes. The supernatant containing soluble MBP-ASC^{PYD} fusion protein was passed through a pre-equilibrated Ni-NTA column by gravity. The column was washed with 20 column-volume sonication buffer containing 20 mM imidazole. The fusion protein was eluted from the Ni-NTA beads with sonication buffer containing 300mM imidazole and passed through a Superdex 200 10/300 GL size-exclusion column with elution buffer containing 20 mM HEPES, 150 mM NaCl, and 1 mM TCEP. To avoid aggregation, all the purification steps were carried out at 4 ˚C.

The ASC^{PYD} filaments were formed by cleavage of the MBP tag with TEV protease at a molar ratio of 1/10 of the fusion protein. This reaction was left overnight at room temperature, which resulted in complete cutting and no precipitation. Cleaved MBP and TEV were removed by passing this mixture through a small Ni-NTA column. The flow-through, containing ASC^{PYD} filaments formed *in vitro,* was diluted accordingly for EM studies.

For nucleation assay, $NLRP3^{PYD\text{-}NBD}$ construct (residues 2-550) was over-expressed in BL21(DE3) cells with an N-terminal His-MBP tag and purified by Ni-NTA resin followed by gel filtration. The void peak (about 7-8 ml fractions) was concentrated for assay. All mutations in this construct were introduced using the QuikChange mutagenesis protocol. $NLRP3^{FL}$ was cloned

into a modified pFastBac HTa vector containing an N-terminal His-MBP tag. This construct was expressed in High Five cells (Invitrogen) with the Bac-to-Bac system using a manufacturer-recommended protocol. Lysis and purification steps were the same as above. $AIM2^{FL}$ and $AIM2^{PYD}$ (residues 1-100) were cloned into pDB-His-MBP vector and over-expressed in BL21(DE3) cells with an N-terminal MBP tag. Mutants for FP assay were generated by QuikChange mutagenesis. $AIM2^{FL}$ were purified by Ni-NTA resin followed by gel filtration. Only fractions corresponding to the monomeric position were used for assay. MBP-tagged $AIM2^{PYD}$ wildtype and mutant constructs were expressed as monomer for assay and pulldown purposes (see below).

ASC^{PYD} Polymerization Assay

Since ASC^{PYD} contains no cysteine residue for convenient labeling, a cysteine residue was introduced to C-terminus of the above MBP-ASC^{PYD} fusion construct (S106C) by QuikChange mutagenesis. This fusion protein was expressed and purified similarly to the wildtype except a buffer at pH 7.0 was used during the gel filtration step. About 30 nmol of the purified protein was incubated with a Cys-reactive fluorophore, Alexa Fluor 488 C_5 maleimide, with 2-fold excess. The reaction was left overnight on ice and passed through a Superdex 200 to remove excess dye. The fraction containing labeled fusion protein was diluted to about 2 to 3 μM for assay in a black round-bottom 384-well Greiner Bio-One plate.

For each well, three parts of labeled fusion protein was added to one part of reaction buffer containing 20 mM HEPES pH 8.0, 150 mM NaCl, 1 mM TCEP, 1 % Triton-X100, and other reaction components (such as TEV, nucleator proteins, DNA, and/or ATP). Data were collected with the SpectraMax M5e Multi-Mode Microplate Reader (Molecular Devices) using excitation at 495 nm and emission at 519 nm with an auto-cutoff filter at 515 nm.

Caspase-1^{CARD} Polymerization Assay

Labeling caspase-1^{CARD} by Alexa Fluor 488 C_5 maleimide abolished filament formation due to three exposed cysteine residues on the surface of the molecule. We used the sortase method [12] for labeling the monomeric "sandwich"-tagged caspase-1^{CARD} (N-terminal MBP, C-terminal Sumo). Labeling reagents, including an engineered, Ca^{2+}-independent sortase and the peptide-fluorophore conjugate Gly-Gly-Gly-TAMRA (GGG-TAMRA), were kindly provided by Dr. Hidde Ploegh. MBP-caspase-1^{CARD}-Sumo containing a C-terminal sortase motif, "LPETGG", was purified to homogeneity similar to the ASC^{PYD} construct. Two mg of the gel filtration monomer was incubated in a mixture containing protein: sortase: GGG-TAMRA = 50 μM: 30 μM: 500 μM at 4˚C overnight. The labeled MBP-casp1^{CARD}-Sumo was separate from free peptide-fluorophore by gel filtration in 20 mM HEPES pH 8.0, 150 mM NaCl, and 1 mM TCEP. MBP-tagged ASC^{PYD}, ASC^{CARD}, and ASC^{FL} in this assay were purified as monomer in the same buffer by gel filtration. Upon removal of the MBP tag, caspase-1^{CARD} polymerized into filaments and the C-terminal Sumo did not interfere with filament formation (as confirmed by EM). TAMRA labeled caspase-1 was used at ~4 μM in this assay. The same setup as the ASC^{PYD} polymerization assay was used with excitation/emission at 561 nm/585 nm.

Binary PYD/PYD Complexes and Nanogold Labeling

To form the AIM2^{PYD}/ASC^{PYD} binary complex, the two gene fragments (AIM2 1-100, ASC 1-106) were inserted into the pDW363 biotinylation vector [13] to co-express AIM2^{PYD} with an N-terminal biotin acceptor peptide (BAP) and ASC^{PYD} with an N-terminal 6 x His tag. The vector contains the BirA enzyme gene for AIM2^{PYD} biotinylation *in vivo.* The complex was expressed in BL21(DE3) cells. Similar expression protocol as above was used except that during overnight induction, 50 μM of biotin was supplemented. Since ASC^{PYD} forms filaments inside the *E. coli* cells resulting in reduced solubility compared to monomeric proteins, a lower speed (30,000 g for 30min) was used for clarifying the cell debris after sonication. The complex was purified by Ni-NTA resin with the batch method followed by gel filtration.

For the NLRP3$^{PYD\text{-}NACT}$/ASC^{PYD} complex, a different approach was used. NLRP3$^{PYD\text{-}NBD}$ (residues 2-550) was cloned into a modified pDB-His-MBP vector containing the biotin acceptor peptide. This construct was expressed with an N-terminal His-MBP tag and a C-terminal BAP and biotinylated *in vivo* by co-expressing with the empty pDW363 vector (harboring the BirA enzyme) using the co-transformation method. The biotinylated NLRP3$^{PYD\text{-}NBD}$ was mixed with 50-fold excess of the monomeric MBP-fused ASC^{PYD}. The polymerization of ASC^{PYD} was achieved by adding TEV to cleave off the MBP tag, forming the NLRP3$^{PYD\text{-}NBD}$/ASC^{PYD} complex.

Nanogold labeling for biotinylated binary complexes was done using streptavidin-gold conjugate (Electron Microscopy Sciences, 6 nm diameter gold). A carbon-coated copper EM grid was covered with 5 µl of sample and let sit for 1 minute. Excess sample was blotted with filter paper, and the grid was washed upside-down on 25 µl of incubation buffer (20 mM HEPES pH 8.0, 150 mM NaCl, 1 mM TCEP, and 0.1 % gelatin) three times of 1 minute each. The grid was floated for 60 minutes on 25 µl of 6 nm streptavidin-gold conjugate diluted in incubation buffer for 60 minutes. The grid was washed three times with incubation buffer and stained for 1 minute in 2 % uranyl acetate. Images were taken on a Tecnai G^2 Spirit BioTWIN Electron Microscope.

Ternary Complexes and Immunogold Labeling

MBP-fused ASC^{FL}, MBP-fused AIM2^{PYD}, and GFP-fused caspase-1^{CARD} were expressed separately in BL21(DE3) cells and purified by Ni-NTA resin and gel filtration chromatography. The ternary complex was formed *in vitro* by mixing AIM2/ASC/caspase-1 in a ratio of 1:1:3 and incubating with TEV for 2 hrs in room temperature to cleave off the MBP tag. The mixture was passed through amylose resin to remove cleaved MBP tag and uncut ASC^{FL} and AIM2^{PYD}. The complex was purified by Ni-NTA resin using 6 x His-GFP as a handle. Untagged ASC^{FL} and AIM2^{PYD} in the core ternary complex were detected by Western blot.

Visualization of AIM2 and ASC were achieved by immunogold labeling using appropriate commercially available primary antibodies (rabbit polyclonal IgG, against PYD). After applying 5 µL of samples, the grids were washed with incubation buffer (gel filtration buffer + 0.1 % gelatin) for three times of 1 minute each. The grids were floated on respective primary antibody diluted to appropriate concentrations recommended by EMS for immunogold labeling (for anti-AIM2, 0.5 µg/ml; for anti-ASC, 2 µg/ml). After 1 hr incubation, grids were washed three times with incubation buffer, then floated on 25 µL of secondary antibody-gold conjugate (goat anti-rabbit IgG, either 15 nm or 6 nm) diluted 1/20 in incubation buffer for 1 hr. The grids were washed and stained for 1 minute in uranyl acetate for visualization. For caspase-1 labeling, Ni-NTA-nanogold conjugate (Nanoprobes, 5nm) was incubated with the ternary complex on grid for 30 minutes (similar to the streptavidin-gold labeling).

Cryo-Electron Microscopy and Image Processing

Samples (2.5 µl) were applied to glow-discharged lacey carbon grids and vitrified using an FEI Vitrobot Mark IV. Grids were imaged using an FEI Titan Krios electron microscope operating at 300 keV, and recorded using a 4k x 4k Falcon II direct electron detector with a backthinned CMOS chip, with a sampling of 1.08 Å/px. The CTFFIND3 program [14] was used for determining the defocus, which ranged from ~ 1.0 µ to ~ 4.0 µ. A total of 370 images were used. The e2helixboxer routine from EMAN2 [15] was used for boxing filaments from the images. These long filaments were then cut into overlapping boxes, each 400 px (432 Å) long, with a shift of 20 px between adjacent boxes (an overlap of 380 px). The SPIDER software package [16] was used for most of the image processing, and the IHRSR algorithm [17] was implemented within SPIDER. The helical indexing was unambiguous [18] due to the strong meridional intensity at ~ 1/(13.9 Å) in averaged power spectra, showing that the rise per asymmetric unit in the filament was ~ 13.9 Å. The layer line at ~ 1/(31 Å) is n=3, and the near-equatorial layer line is n=-6. There is a C3 point-group symmetry, so every layer line contains a

Bessel order that is a multiple of three. An initial reconstruction was generated using this symmetry. The broadness of the n=-6 layer line in the averaged power spectrum, combined with the sharpness of the meridional layer line, suggested that the filaments had a fairly constant axial rise but a variable twist [19]. We therefore generated multiple references, having different values of the twist and axial rise, to use for a reference-based sorting of the images. The results showed that almost all of the variation was in the twist, as suspected, and power spectra generated from bins with different twists confirm the sorting (movie S1). Using references with a spacing of 0.3° in twist, the central bin (with a twist of 52.9°) had 24,665 segments among the ~80,000 total segments, and these were used for the final reconstruction.

Without treating out-of-plane tilt, the reconstruction reached a resolution of ~6-7 Å. The absolute hand of the reconstruction was unambiguous at this resolution given the comparison with the NMR structure (1UCP.PDB). Using references with out-of-plane tilt showed that the mode of the distribution was ~6° of tilt from the normal to the beam. The final cycles of the IHRSR algorithm involved generating references with azimuthal angle and out-of-plane tilt increments of 1.5°. The symmetry converged to a twist of 52.91° and an axial rise of 13.95 Å. The stated resolution of ~3.8 Å has been determined by comparison with the atomic model which provides a reality-check on any claims, absent from the Fourier Shell Correlation (FSC) approach [20]. It is clear, however, that the resolution is not uniform, and the helices on the inside of the filament that are more tightly packed are better resolved than those on the outside. The right-handed nature of the α-helices is clearly visible. The standard FSC method (dividing the data into two sets, aligned against the same reference) yielded FSC = 0.26 at 1/(3.8 Å), while the resolution at FSC = 0.143 [21] gave a resolution of 2.9 Å.

Structural Refinement

The ASC^{PYD} NMR structure (PDB ID 1UCP) [1] was chosen as the starting model for refinement. A region of the filament EM density with a length of 108 Å was extracted and 15

protomers were docked as a rigid-body into the EM density. The radial structure factor distribution of the EM density was then scaled to match that of the 15 subunit starting model. The density was then further sharpened with a B-factor of -60 $Å^2$ and a cosine shaped smooth cutoff at a resolution of 3.5 Å was applied.

The model was optimized by iterations over real-space refinement in DireX [22] and manual model building with Coot [23]. For the refinement, a mask was generated by computing a 15 Å density map from the initial atomic model. The edges of this low resolution density were steepened by applying a cosine mapping function with the program apply-cos-mapping, which is part of DireX, using the values 0.4 and 0.3 as upper and lower threshold values, respectively. A simple Babinet bulk solvent model with ksol = 0.65 and Bsol = 45 $Å^2$ was used.

A cross-validation approach was used to identify the optimally fitted model and to prevent over fitting [24]. In brief, only Fourier components of the cryo-EM density map lower than 3.7 Å were used for fitting, while Fourier components from the so called 'free' interval 3.5–3.7 Å were used for validation only. For this, the cross-correlation coefficient, C_{free}, is calculated between the model density map and the cryo-EM density map, both of which were band-pass filtered using the free interval, thus containing information that has not been used for fitting.

To further assist model building and correction a 20 ns MD simulation was performed using Gromacs [25] with the Amber99SB-ILDN force field [26]. The simulation included 12 protomers solvated in explicit water. From this simulation, 1200 snapshots of structures were extracted and refined with DireX into the EM density. The structure with the lowest C_{free} value was compared with the refined NMR model and the fragment between residues 31 to 53 fitted significantly better into the density was therefore used to replace the corresponding fragment in the model.

For final refinement, 20 iterations over DireX refinement and energy minimization with CNS [27] (without experimental data) were performed. The DireX refinement used grouped and restrained occupancy refinement. This final refinement procedure yields C_{work} and C_{free} values of

0.826 and 0.108, respectively. The Fourier Shell Correlation (FSC) between the final model and the EM density yields a cross-resolution of 3.6 Å, 4.8 Å, and 5.9 Å for FSC=0.143, 0.5, and 0.71 criteria. Phased reciprocal space refinement with Phenix [28] including TLS refinement resulted in a very similar FSC curve (Figure S2.3A). Resolution measurements have been much more problematic and controversial in the EM field than in X-ray crystallography, and attempts have been made to devise measures when there is no atomic model that can be compared to the reconstruction [29]. However, when near atomic resolution is achieved, we think that the ultimate measure of resolution is provided by the interpretability of the map and the comparison between the model and the map (Figure S2.3B, S2.3C). Therefore, based upon both the FSC (Figure S2.3A) and the comparisons of the map with the model (Figure S2.3B, S2.3C), we estimate the resolution of our reconstruction at ~3.8 Å.

Plasmids and Antibodies

Full length human ASC was cloned in EcoRI/XhoI sites of pCDNA3.1/myc-HisA and XhoI/HindIII sites of pEGFP-N1. ASC PYD (residues 1-106) (WT), encoding the PYD domain of human ASC, was amplified via PCR using full-length human ASC as template. The PCR product was cloned into the XhoI/HindIII sites of pEGFP-N1. Mutants (D48R, KK2122EE, F59E, E13R, R41E, K21E/D48K/D51K and E67R) of ASC^{PYD} (1-106) domain were generated by standard sit-directed mutagenesis kit (Stratagene). These mutants were cloned into the XhoI/HindIII sites of pEGFP-N1. All constructs were sequence verified.

The following antibodies were diluted and used as described below: anti-EGFP, 1:5,000 (polyclonal, Thermo Scientific); anti-ASC (N-15), 1:5,000 (polyclonal, Santa Cruz Biotechnology); anti-caspase-1 p12 subunit, 1:5,000 (monoclonal, Thermo Scientific).

Cell Culture and Transfection

The cells were grown in 100 mm dish and six-well plate containing coverslip for protein extraction and morphological studies respectively. HEK 293T cells were grown in DMEM with L-glutamine supplemented with 10 % fetal bovine serum. COS-1 cells were grown in DMEM supplemented with 10 % fetal bovine serum. THP-1 cells were maintained in RPMI with L-glutamine supplemented with 10 % fetal bovine serum, and 0.1 mM non-essential amino acids solution. All cells were maintained at 37 $^{\circ}$C with 5 % CO_2. COS-1 and HEK 293T cells were transfected using Lipofectamine 2000 (Invitrogen) according to the manufacture's instructions.

For NLRP3 inflammasome activation, THP-1 cells were treated overnight with PMA (300 ng/ml final concentration). This was followed by overnight LPS induction (10 µg/ml final concentration). Uric acid crystals (200 µg/ml final concentration) treatment was carried out for 6 hours. During whole procedure cells were maintained at 37 $^{\circ}$C with 5 % CO_2.

Protein Extraction, Immunoprecipitation, Immunoblotting, and Electron Microscopy

Wildtype and mutant (D48R, KK2122EE, F59E, E13R and R41E) human ASC^{PYD} domain (residue 1-106) constructs were expressed in HEK 293T cells, and were processed for recombinant protein extraction as follows. The Petri dishes were placed on ice, and cells were harvested with a rubber scraper and sedimented at ~2,600 g at 4 °C for 20 min. Cells were washed once with 20 ml of ice-cold PBS to remove serum proteins. The cell pellet was resuspended in 500 µl of lysis buffer (50 mM Tris-HCl, pH 7.5, 150 mM NaCl, 5 mM EGTA, 5 mM EDTA, and protease inhibitor) and pipetted up and down 10 times. The preparation was sedimented at ~500 g at 4 °C for 5 min to remove the nuclear fraction. The supernatant was collected and resedimented at 16,000 g at 4 °C for 30 min. The supernatant was measured for protein concentration with Bradford assay, and normalized to 1 mg/ml.

For immunoprecipitation, the precleared supernatant was immunoprecipitated with anti-ASC antibody overnight at 4 °C. The immobilized immune complex on protein A-sepharose was washed thrice using 1 ml of lysis buffer, and eluted using 0.2 M glycine at pH 2.6. Samples were

immediately neutralized with Tris-HCl at pH 8.0. The eluted immunopurified complex was resuspended in 5 µl of 5 x sample buffer and heated at 95 °C for 5 min. Proteins were resolved on 12.5 % SDS-PAGE gels, and immunoblotting was performed with anti-ASC and anti-eGFP antibodies.

Co-immunoprecipitation experiments were performed in transfected HEK 293T cells. Precleared supernatants were immunoprecipitated with monoclonal anti-His antibodies (Qiagen), overnight at 4 °C. The immobilized immune complex on protein A-sepharose was washed thrice using 1 ml of lysis buffer. The bound complex was eluted using 20 µl of 5 x sample buffer and heated at 95 °C for 5 min. Proteins were resolved on 12.5 % SDS-PAGE gels, and immunoblotting was performed with anti-His antibodies, and co-immunoprecipitated component was detected using polyclonal anti-eGFP antibodies (Thermo Scientific). Western blots (ECL detection) were documented using Chemidoc MP system (BioRad). Binding was quantified using densitometric measurement of band intensity using NIH ImageJ software.

For negative staining electron microscopy, glow discharged copper grids containing 2 µl of eluted immunopurified complex were stained with 5 % uranyl acetate for 1 minute and air-dried. Samples were imaged using JEOL 1200EX 80kV Transmission Electron Microscope (TEM) and images were recorded with an AMT 2k CCD camera (Harvard Medical School core facility).

Fluorescence and Confocal Laser Scanning Microscopy

COS-1 cells were seeded at a density of 2 x 10^5 for morphological studies. 12 hours post transfection cells were monitored by Zeiss Axiovert 135 fluorescence microscope (Carl Zeiss) at various time points. Cells were washed once with PBS, fixed with 4 % PFA for 5 minutes at room temperature, and were mounted in *N*-propyl gallate (NPG) antifade. Fluorescence microscopy was performed using a Zeiss Axiovert 200M microscope (Carl Zeiss) equipped for conventional epifluorescence microscopy with the respective filter sets for enhanced green

fluorescent protein (eGFP). Images were captured using a 40 x objective (0.75 numerical aperture) with AxioVision Rel. 4.6 software. Confocal sections were obtained with confocal laser scanning microscope FluoView FV1000 (Olympus). Images were captured using a 60 x objective (1.2 numerical aperture) with Olympus FluoView version 3.0 viewer software. The images were identically processed with Adobe Photoshop.

Immunogold EM on Ultrathin Cryosections

Transfected COS-1 cells (human ASC full length-eGFP and eGFP alone) were used for immunogold electron microscopy as previously described [30] and as detailed below. For preparation of cryosections the cells were rinsed once with PBS and were removed from the dish using 0.5mM EDTA (PBS). 800 µl of the cell suspension was layered on top of a 200 µl cushion of 8 % paraformaldehyde (in 0.1 M Sodium Phosphate buffer, pH 7.4) in an eppendorf tube and was sedimented at ~510 g for 3 minutes at room temperature (RT). The supernatant was carefully removed and fresh 4 % paraformaldehyde was added. Cells were fixed for 2 hours at room temperature and later fixative was replaced with PBS. Prior to freezing in liquid nitrogen the cell pellets were infiltrated with 2.3 M sucrose (PBS) (containing 0.2 M glycine to quench free aldehyde groups) for 15 minutes at RT. Frozen samples were sectioned at -120 °C, the sections were transferred to formvar-carbon coated copper grids. Grids were floated on 2 % gelatin dish at 4 °C until the immunogold labeling was carried out. The gold labeling was carried out at RT on a piece of parafilm. Grids were floated on drops of 1 % BSA for 10 minutes to block for unspecific labeling, transferred to 5 µl drops of primary antibody (anti-ASC, 1:50) and was incubated for overnight at 4 °C. The grids were then washed in 4 drops of PBS for a total of 15 minutes, transferred to 5 µl drops of Protein-A gold (10 nm) for 20 minutes, washed in 4 drops of PBS for 15 minutes and 6 drops of double distilled water at RT. Protein-A gold (10 nm) labeling alone served as a control. The labeled sections were contrasted by floating the grids on drops of 0.3% uranyl acetete in 2% methyl cellulose for 10 minutes, the excess liquid was

removed with a filterpaper (Whatman #1), leaving a thin coat of methyl cellulose (bluish interference color when dry). The grids were examined in a JEOL 1200EX-80kV Transmission electron microscope (TEM) and images were recorded with an AMT 2k CCD camera (Harvard Medical School core facility).

AIM2 Inflammasome Reconstitution

Transient reconstitution of the human AIM2 inflammasome was performed as previously described [31-33]. In brief, HEK293T cells were transfected with pEFBOS-C-term-Guassia luciferase/Flag pro-IL-1β (~54 kDa), pro-caspase-1, HA-ASC, and the full-length wildtype or mutant Flag-AIM2 expression constructs using GeneJuice (Novagen). Cell lysates were probed with mouse anti-IL1β monoclonal antibody (clone 3zD, National Cancer Institute, NIH). Expression of ASC and AIM2 was detected using anti-Flag (Sigma) and anti-HA antibodies (Roche Applied Biosystems), respectively.

Supplemental References

1. Liepinsh, E., Barbals, R., Dahl, E., Sharipo, A., Staub, E. & Otting, G. (2003) The death-domain fold of the ASC PYRIN domain, presenting a basis for PYRIN/PYRIN recognition, *Journal of molecular biology.* **332**, 1155-63.

2. Hiller, S., Kohl, A., Fiorito, F., Herrmann, T., Wider, G., Tschopp, J., Grutter, M. G. & Wuthrich, K. (2003) NMR structure of the apoptosis- and inflammation-related NALP1 pyrin domain, *Structure (Camb).* **11**, 1199-205.

3. Natarajan, A., Ghose, R. & Hill, J. M. (2006) Structure and dynamics of ASC2, a pyrin domain-only protein that regulates inflammatory signaling, *The Journal of biological chemistry.* **281**, 31863-75.

4. Espejo, F. & Patarroyo, M. E. (2006) Determining the 3D structure of human ASC2 protein involved in apoptosis and inflammation, *Biochem Biophys Res Commun.* **340**, 860-4.

5. Su, M. Y., Chang, C. I. & Chang, C. F. (2013) (1)H, (13)C and (15)N resonance assignments of the pyrin domain from human PYNOD, *Biomol NMR Assign*.

6. Pinheiro, A. S., Proell, M., Eibl, C., Page, R., Schwarzenbacher, R. & Peti, W. (2010) Three-dimensional structure of the NLRP7 pyrin domain: insight into pyrin-pyrin-mediated effector domain signaling in innate immunity, *The Journal of biological chemistry.* **285**, 27402-10.

7. Pinheiro, A. S., Eibl, C., Ekman-Vural, Z., Schwarzenbacher, R. & Peti, W. (2011) The NLRP12 pyrin domain: structure, dynamics, and functional insights, *Journal of molecular biology.* **413**, 790-803.

8. Bae, J. Y. & Park, H. H. (2011) Crystal structure of NALP3 protein pyrin domain (PYD) and its implications in inflammasome assembly, *The Journal of biological chemistry.* **286**, 39528-36.

9. Eibl, C., Grigoriu, S., Hessenberger, M., Wenger, J., Puehringer, S., Pinheiro, A. S., Wagner, R. N., Proell, M., Reed, J. C., Page, R., Diederichs, K. & Peti, W. (2012) Structural and Functional Analysis of the NLRP4 Pyrin Domain, *Biochemistry.* **51**, 7330-41.

10. Jin, T., Perry, A., Smith, P. T., Jiang, J. & Xiao, T. S. (2013) Structure of the AIM2 pyrin domain provides insights into the mechanisms of AIM2 autoinhibition and inflammasome assembly, *The Journal of biological chemistry*.

11. Moriya, M., Taniguchi, S., Wu, P., Liepinsh, E., Otting, G. & Sagara, J. (2005) Role of charged and hydrophobic residues in the oligomerization of the PYRIN domain of ASC, *Biochemistry.* **44**, 575-83.

12. Theile, C. S., Witte, M. D., Blom, A. E., Kundrat, L., Ploegh, H. L. & Guimaraes, C. P. (2013) Site-specific N-terminal labeling of proteins using sortase-mediated reactions, *Nature protocols.* **8**, 1800-7.

13. Tsao, K. L., DeBarbieri, B., Michel, H. & Waugh, D. S. (1996) A versatile plasmid expression vector for the production of biotinylated proteins by site-specific, enzymatic modification in Escherichia coli, *Gene.* **169**, 59-64.

14. Mindell, J. A. & Grigorieff, N. (2003) Accurate determination of local defocus and specimen tilt in electron microscopy, *Journal of structural biology.* **142**, 334-47.

15. Tang, G., Peng, L., Baldwin, P. R., Mann, D. S., Jiang, W., Rees, I. & Ludtke, S. J. (2007) EMAN2: an extensible image processing suite for electron microscopy, *Journal of structural biology.* **157**, 38-46.

16. Frank, J., Radermacher, M., Penczek, P., Zhu, J., Li, Y., Ladjadj, M. & Leith, A. (1996) SPIDER and WEB: processing and visualization of images in 3D electron microscopy and related fields, *Journal of structural biology.* **116**, 190-9.

17. Egelman, E. H. (2000) A robust algorithm for the reconstruction of helical filaments using single-particle methods, *Ultramicroscopy.* **85**, 225-34.

18. Egelman, E. H. (2010) Reconstruction of helical filaments and tubes, *Methods Enzymol.* **482**, 167-83.

19. Egelman, E. H. & DeRosier, D. J. (1982) The Fourier transform of actin and other helical systems with cumulative random angular disorder, *Acta Cryst* **A38**, 796-9.

20. Yu, X., Goforth, C., Meyer, C., Rachel, R., Wirth, R., Schroder, G. F. & Egelman, E. H. (2012) Filaments from Ignicoccus hospitalis show diversity of packing in proteins containing N-terminal type IV pilin helices, *Journal of molecular biology.* **422**, 274-81.

21. Rosenthal, P. B. & Henderson, R. (2003) Optimal determination of particle orientation, absolute hand, and contrast loss in single-particle electron cryomicroscopy, *Journal of molecular biology.* **333**, 721-45.

22. Schröder, G. F., Brunger, A. T. & Levitt, M. (2007) Combining efficient conformational sampling with a deformable elastic network model facilitates structure refinement at low resolution, *Structure.* **15**, 1630-41.

23. Emsley, P. & Cowtan, K. (2004) Coot: model-building tools for molecular graphics, *Acta crystallographica Section D, Biological crystallography.* **60**, 2126-32.

24. Falkner, B. & Schröder, G. F. (2013) Cross-validation in cryo-EM–based structural modeling, *Proceedings of the National Academy of Sciences of the United States of America.* **in press**.

25. Hess, B., Kutzner, C., van der Spoel, D. & Lindahl, E. (2008) GROMACS 4: Algorithms for Highly Efficient, Load-Balanced, and Scalable Molecular Simulation, *J Chem Theory Comput.* **4**, 435-447.

26. Lindorff-Larsen, K., Piana, S., Palmo, K., Maragakis, P., Klepeis, J. L., Dror, R. O. & Shaw, D. E. (2010) Improved side-chain torsion potentials for the Amber ff99SB protein force field, *Proteins.* **78**, 1950-8.

27. Brunger, A. T. (2007) Version 1.2 of the Crystallography and NMR system, *Nature protocols.* **2**, 2728-33.

28. Adams, P. D., Afonine, P. V., Bunkoczi, G., Chen, V. B., Davis, I. W., Echols, N., Headd, J. J., Hung, L. W., Kapral, G. J., Grosse-Kunstleve, R. W., McCoy, A. J., Moriarty, N. W., Oeffner, R., Read, R. J., Richardson, D. C., Richardson, J. S., Terwilliger, T. C. & Zwart, P. H. (2010) PHENIX: a comprehensive Python-based system for macromolecular structure solution, *Acta crystallographica Section D, Biological crystallography.* **66**, 213-21.

29. Sousa, D. & Grigorieff, N. (2007) Ab initio resolution measurement for single particle structures, *Journal of structural biology.* **157**, 201-10.

30. Griffiths, G. (1993) *Fine Structure Immunocytochemistry*, Spinger Verlag, Heidelberg, Germany.

31. Jin, T., Perry, A., Jiang, J., Smith, P., Curry, J. A., Unterholzner, L., Jiang, Z., Horvath, G., Rathinam, V. A., Johnstone, R. W., Hornung, V., Latz, E., Bowie, A. G., Fitzgerald, K. A. & Xiao, T. S. (2012) Structures of the HIN domain:DNA complexes reveal ligand binding and activation mechanisms of the AIM2 inflammasome and IFI16 receptor, *Immunity.* **36**, 561-71.

32. Hornung, V., Ablasser, A., Charrel-Dennis, M., Bauernfeind, F., Horvath, G., Caffrey, D. R., Latz, E. & Fitzgerald, K. A. (2009) AIM2 recognizes cytosolic dsDNA and forms a caspase-1-activating inflammasome with ASC, *Nature.* **458**, 514-8.

33. Burckstummer, T., Baumann, C., Bluml, S., Dixit, E., Durnberger, G., Jahn, H., Planyavsky, M., Bilban, M., Colinge, J., Bennett, K. L. & Superti-Furga, G. (2009) An orthogonal proteomic-genomic screen identifies AIM2 as a cytoplasmic DNA sensor for the inflammasome, *Nat Immunol.* **10**, 266-72.

Appendix II

Supplemental Materials for Chapter Three:

Monomeric Mutant of AIM2 PYD

Reveals Critical Interactions for Self-Association

This section contains the following 2 Supplemental Tables and Supplemental References –

Supplemental Tables

Table S1

Table S2

Supplemental References

Supplemental Tables

Table S3.1. Crystallographic statistics

Diffraction data	
Space group	$P2_12_12_1$
Cell dimensions	
a, *b*, *c* (Å)	29.94, 37.95, 76.95
Resolution (Å)	38 - 1.82
R_{sym} *	0.057 (0.679)
I / σ_I *	24.9 (7.4)
Completeness (%) *	90.6 (50.81)
Redundancy *	10.6 (9.2)
Refinement	
Resolution (Å)	38 - 1.82
No. reflections	7,497
R_{work} / R_{free}	0.18 / 0.24
No. atoms	829
Protein	738
Water	91
Average B factor (Å^2)	19.6
Protein (Å^2)	18.7
Water (Å^2)	26.8
R.M.S. Deviations	
Bond lengths (Å) / angles (°)	0.006 / 0.84
Ramachandran plot	
Favored (%)	99
Allowed (%)	1

For crystallization, the SUMO-AIM2^{PYD} F27G fusion protein was incubated overnight with Ulp1 at a molar ratio of 1/1000 of the fusion protein while dialyzing against the gel filtration buffer at 4˚C. The free His-SUMO was removed by another incubating the sample with Ni-NTA resin. The flow-through was collected and concentrated to load on a Superdex200 10/300 GL column. Fractions corresponding to the cleaved AIM2^{PYD} F27G were pooled and concentrated to 18mg/mL for crystallization. AIM2^{PYD} F27G was crystallized by hanging-drop vapor diffusion in a 48-well VDX tray (Hampton) at 16˚C by mixing equal volumes of the protein sample and a mother liquor containing 0.2 M $CaCl_2$, 0.1 M Sodium Acetate at pH 4.7, and 23 % PEG3350. During optimization, trypsin was added to a mass ratio of 1/50 of AIM2^{PYD} F27G for *in situ* proteolysis. The best diffracting crystals were shaped like rigid, single needles with a long

dimension of > 150 μm and short dimensions of < 5 μm. X-ray diffraction data were collected at the NSLS X29 beamline of Brookhaven National Laboratory and processed with the HKL2000 program suite [1]. Because of the low sequence identity of $AIM2^{PYD}$ to any known PYD structures, we generated a structural composite by superimposing PDB models of NLRP10 (2DO9), ASC (1UCP), NLRP7 (2KM6), NLRP3 (3QF2) and NLRP1 (1PN5), and selecting common secondary structural elements with high sequence similarity and low root-mean-square deviations. We trimmed the composite to a poly-Ala model and searched for the molecular replacement solution in the program MOLREP [2]. Model building and refinement at 1.87 Å was carried out using Coot [3] and PHENIX [4]

*Values in parentheses are for the highest-resolution shell.

Table S3.2. Top 20 hits from structural homology search using DALI [5]

DALI Hits	Protein domains	PDB IDs	Z-scores
1	MBP-hAIM2 PYD	3VD8	17.8
2	hASC PYD	1UCP	13.5
3	hNLRP3 PYD	3QF2	13.5
4	hASC2 PYD	2HM2	13.2
5	hASC PYD	2KN6	12.8
6	hNLRP4 PYD	4EWI	11.9
7	hMNDA PYD	2DBQ	11.8
8	hNLRP7 PYD	2KM6	11.8
9	vFLIP MC159 DED2	2F1S	11.3
10	mNLRP10 PYD	2DO9	11.2
11	hNLRP12 PYD	2L6A	10.8
12	mPEA15 DED	2LS7	10.8
13	chPEA-15 DED	4IZ7	10.6
14	vFLIP MC159 DED2	2BBZ	10.3
15	hFADD DD	3EZQ	10.1
16	mP205 PYD	2YU0	9.2
17	cCED4 CARD	3LQQ	9.0
18	cCED9 CARD	2A5V	8.9
19	hApaf-1 CARD	3YGS	8.5
20	hTNFR1 DD	1ICH	8.5

h: human; m: mouse; c: C. elegans; ch: Chinese hamster; v: viral

Supplemental References

1. Otwinowski, Z. & Minor, W. (1997) Processing of X-ray diffraction data collected in oscillation mode, *Methods Enzymol.* **276**, 307-326.

2. Vagin, A. A. & Teplyakov, A. (1997) MOLREP: an Automated Program for Molecular Replacement, *J Appl Cryst.* **30**, 1022.

3. Emsley, P. & Cowtan, K. (2004) Coot: model-building tools for molecular graphics, *Acta crystallographica Section D, Biological crystallography.* **60**, 2126-32.

4. Adams, P. D., Afonine, P. V., Bunkoczi, G., Chen, V. B., Davis, I. W., Echols, N., Headd, J. J., Hung, L. W., Kapral, G. J., Grosse-Kunstleve, R. W., McCoy, A. J., Moriarty, N. W., Oeffner, R., Read, R. J., Richardson, D. C., Richardson, J. S., Terwilliger, T. C. & Zwart, P. H. (2010) PHENIX: a comprehensive Python-based system for macromolecular structure solution, *Acta crystallographica Section D, Biological crystallography.* **66**, 213-21.

5. Holm, L. & Sander, C. (1995) Dali: a network tool for protein structure comparison, *Trends Biochem Sci.* **20**, 478-480.

Appendix III

Supplemental Materials for Chapter Four:

Plasticity in PYD Assembly Revealed by

Cryo-EM Structure of the PYD Filament of AIM2

This section contains the following 4 Supplemental Figures, a Supplemental Movie, Materials and Methods, and Supplemental References –

Supplemental Figures

Figure S4.1

Figure S4.2

Figure S4.3

Figure S4.4

Supplemental Movie

Movie S4.1

Materials and Methods

Supplemental References

Supplemental Figures

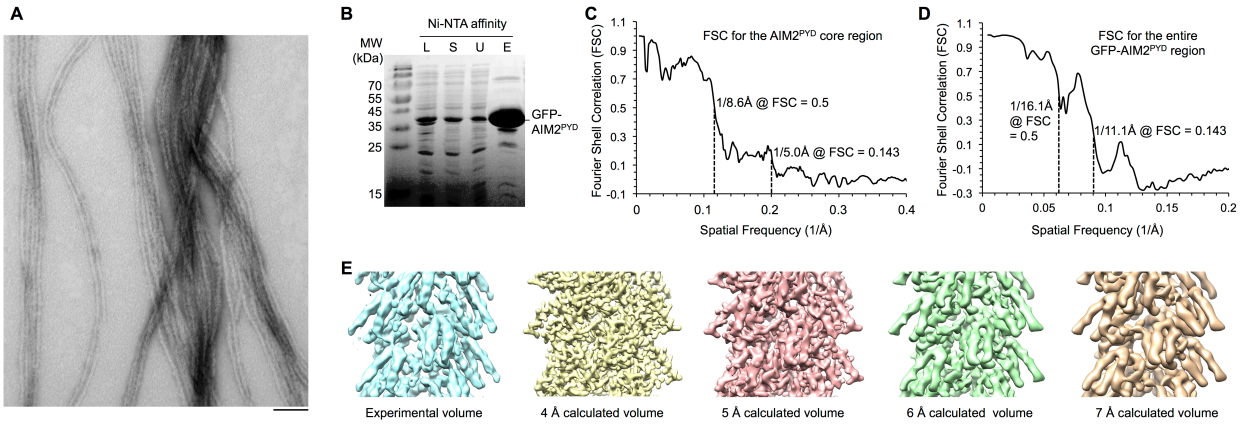

Figure S4.1. Cryo-EM structure determination of the GFP-AIM2^{PYD} filament.

A. Negative-stain electron micrograph of the bundled AIM2^{PYD} filaments after MBP tag removal. Scale bar at 100nm.

B. Ni-NTA affinity purification of the GFP-tagged AIM2^{PYD} filament. L: lysate; S: supernatant; U: unbound fraction; E: elution.

C. Fourier shell correlation (FSC) plot of the AIM2^{PYD} filament core of the reconstruction.

D. Fourier shell correlation (FSC) plot of the entire GFP-AIM2^{PYD} filament reconstruction.

E. Comparison of the experimental volume to model volumes filtered to 4, 5, 6 and 7 Å resolutions.

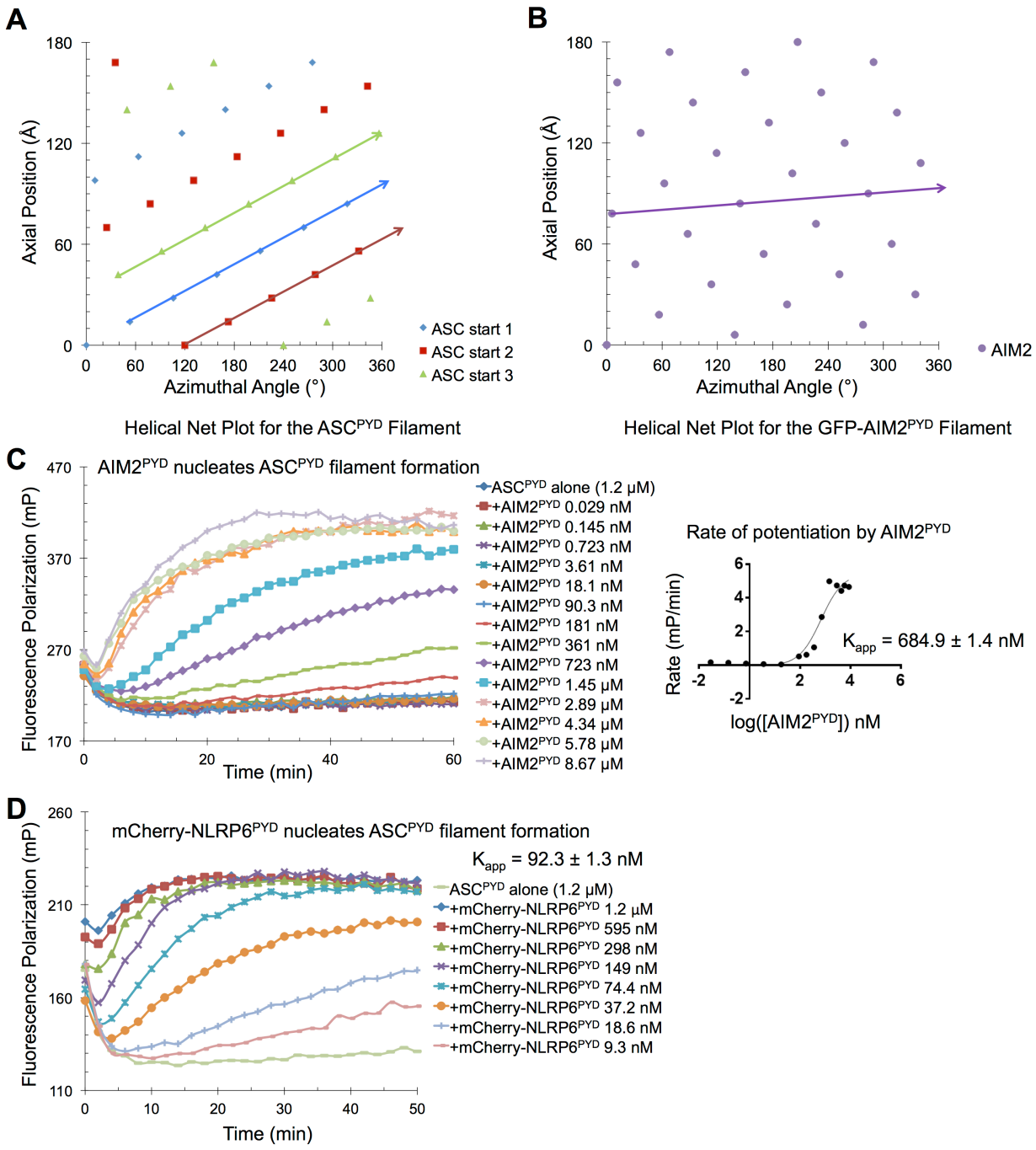

Figure S4.2. Comparison of the ASC^{PYD} filament (**A**) and the GFP-AIM2^{PYD} filament (**B**) helical net plots. Nucleation of ASC^{PYD} filament formation by AIM2^{PYD} (**C**) and mCherry-tagged NLRP6^{PYD} (**D**). The initial slopes of the nucleation experiments were extracted to estimate apparent affinity by fitting to a three-parameter agonist model.

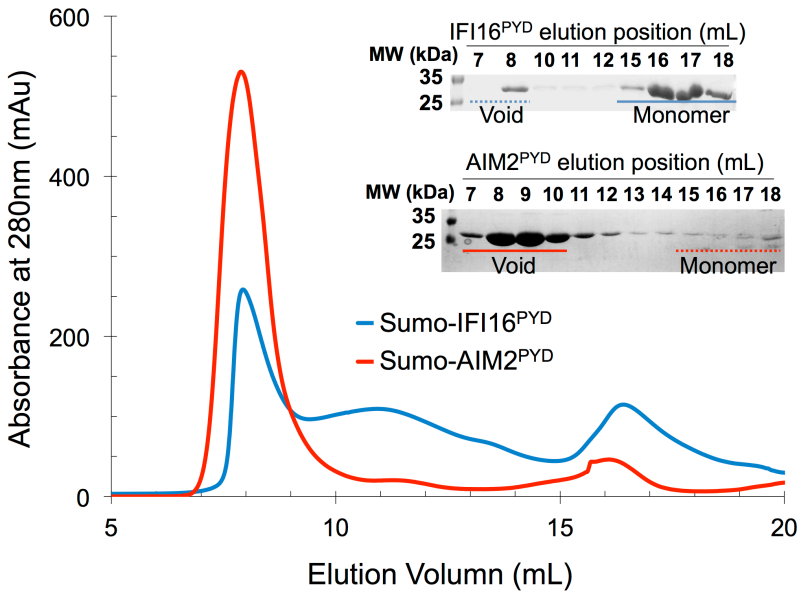

Figure S4.3. Comparison of the gel filtration profiles of Sumo-tagged IFI16^{PYD} and Sumo-tagged AIM2^{PYD}

A

AIM2^{PYD} Interface	Mutation	Effect	Assay
Type Ia	L10A/L11A	Abolishes nucleation of ASC^{PYD} filaments	FP assay (Lu *et al*, *Cell*, 2014)
		Abolishes self-aggregation	Gel filtration (Lu *et al*, *JMB*, 2014)
Type Ib	F27G	Abolishes nucleation of ASC^{PYD} filaments	FP assay (Lu *et al*, *Cell*, 2014)
		Abolishes self-aggregation	Gel filtration (Lu *et al*, *JMB*, 2014)
	F27L	Abolishes self-aggregation and AIM2^{PYD} filament formation	Gel filtration, cellular over-expression (Lu *et al*, *JMB*, 2014)
	F27Y	No effect on self-aggregation	Gel filtration, cellular over-expression (Lu *et al*, *JMB*, 2014)
	F27W	No effect on self-aggregation	Gel filtration, cellular over-expression (Lu *et al*, *JMB*, 2014)
	F27A/F28A	Abolish association with ASC^{PYD}	Yeast two-hybrid assay, MBP-fusion pulldown (Jin *et al*, *JBC, 2013)*
Type Ib	R24E	Abolishes nucleation of ASC^{PYD} filaments	FP assay (Lu *et al*, *Cell*, 2014)
	D31K	Abolishes self-aggregation	Gel filtration
Type IIb	Y74R	Abolishes nucleation of ASC^{PYD} filaments	FP assay (Lu *et al*, *Cell*, 2014)
Type IIIa	G38E	Impairs nucleation of ASC^{PYD} filaments	FP assay (Lu *et al*, *Cell*, 2014)
Type IIIa	K39E	Impairs nucleation of ASC^{PYD} filaments	FP assay (Lu *et al*, *Cell*, 2014)
Type IIIb	D15R	Abolishes nucleation of ASC^{PYD} filaments	FP assay (Lu *et al*, *Cell*, 2014)
Adjacent to type Ib	D19A/E20A/ E21A/D23A	Abolish association with ASC^{PYD}	Yeast two-hybrid assay, MBP-fusion pulldown (Jin *et al*, *JBC, 2013)*

B

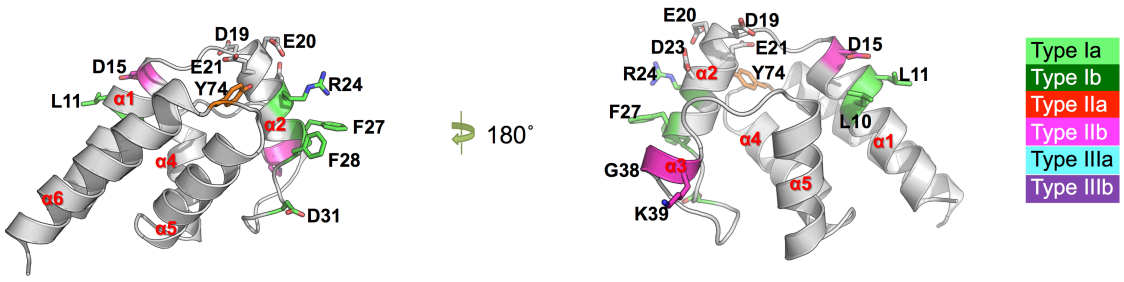

C

Figure S4.4. Mutational and sequence analysis of AIM2^{PYD}.

A. Summary of existing mutagenesis data, with the locations of these mutated residues designated by the three types.

B. Mapping of the mutated residues onto the AIM2^{PYD} structure.

C. Sequence alignment between AIM2 and IFI16 PYDs. Interfacial residues of AIM2^{PYD} in the filament are highlighted by their interaction types. Residues of IFI16^{PYD} that are conserved with those at the AIM2^{PYD} filament interface are highlighted in yellow.

Supplemental Movie

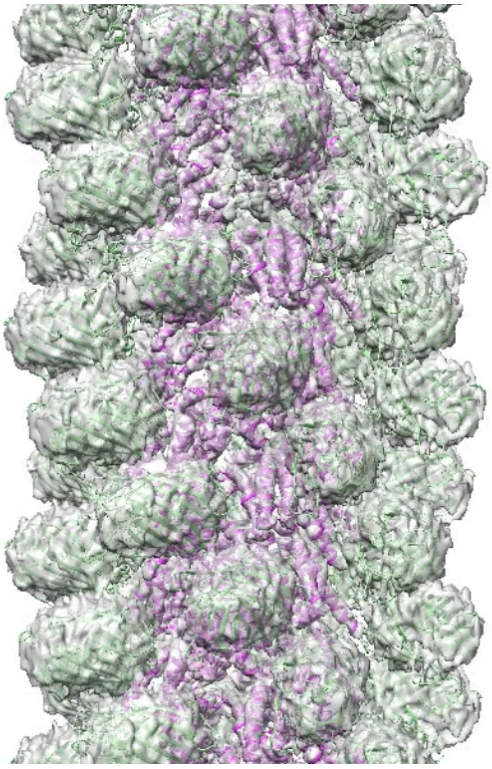

Movie S4.1. A movie showing rotations along the helical axis of the experimental cryo-EM density fitted with the crystal structure of GFP and partially refined $AIM2^{PYD}$ model.

Materials and Methods

Construct and filament sample preparation

To generate a His-GFP-tagged AIM2^{PYD}, the cDNA of monomeric GFP (M1-T230, A206K) was cloned into the pET28a backbone using the NdeI and BamHI sites. AIM2^{PYD} (M1-P100) was inserted in frame with the GFP gene using BamHI and NotI sites, which introduced a two-residue linker by the BamHI site. The construct was expressed in *E. coli* BL21(DE3) cells by overnight induction using IPTG at 18˚C. The cells were harvested and lysed in lysis buffer containing 20 mM HEPES pH 8.0, 200 mM NaCl, 5 mM imidazole, 5 mM β-mercaptoethanol (β-ME), and 10% glycerol. Following sonication, the cell debris was centrifuged at 30,000 x g for 30 min. The supernatant after centrifugation was incubated with the Ni-NTA affinity resin for 1 hour, and washed in lysis buffer containing 20 mM imidazole. His-GFP-AIM2^{PYD} filaments were eluted using lysis buffer with 300 mM imidazole. The eluate was injected onto a Superdex 200 10/300 GL column pre-equilibrated with gel filtration buffer containing 20 mM HEPES pH 8.0, 150 mM NaCl, and 2mM dithiothreitol. The filaments eluted in the void, with peak at ~8 mL. The sample was frozen in small aliquots for subsequent analysis.

Cryo-EM imaging, indexing, and reconstruction

The sample (3 μL) was applied to lacey carbon grids that were plasma cleaned (Gatan Solarus) and vitrified in a Vitrobot Mark IV (FEI, Inc.). Grids were imaged in a Titan Krios at 300 keV, and recorded with a Falcon II direct electron detector at 1.15 Å per pixel (px). A total of 207 images (each 4k x 4k) were selected that were free from drift or astigmatism. The program CTFFIND3 [1] was used for determining the Contrast Transfer Function (CTF) and the defocus range used was from 0.6 to 5.0 μm. The SPIDER software package [2] was used for most subsequent steps. The CTF was corrected by multiplying each image with the theoretical CTF, both reversing phases where they need to be reversed and improving the signal-to-noise ratio.

The program e2helixboxer within EMAN2 [3] was used for boxing long filaments from the micrographs. Overlapping boxes, 384 px long with a 10 px shift between adjacent boxes (97% overlap) were extracted from these long filaments, yielding 54,973 segments.

Starting with an averaged power spectrum, it was apparent that many different helical symmetries were possible [4]. The correct helical symmetry was determined by trial-and-error, searching for a solution using IHRSR [5] that yielded recognizable secondary structure [6]. The symmetry search was complicated by the fact that out-of-plane tilt cannot be ignored [6], and each symmetry that was tried needed to allow for such out-of-plane tilt. The symmetry that was found, a rise of 6.0 Å and a rotation of 138.9° per subunit, generated a reconstruction where the PYD was seen to be largely α-helical, and was thus taken to be correct.

AIM2 model fitting and refinement

The EM density was first transformed to CCP4 format [7]. A small region corresponding to the density of a single $AIM2^{PYD}$ molecule was cutoff with a mask, and wild type $AIM2^{PYD}$ structure (3VDB) was aligned to the density. Helices were moved slightly by fitting individually in real space and regularized in Coot to generate an $AIM2^{PYD}$ structure in the filament conformation [8]. The modified $AIM2^{PYD}$ structure was fitted individually into EM density in real space to generate an initial $AIM2^{PYD}$ filament structure with 15 molecules. The density corresponding to the 15-molecule filament was cut using a mask generated from the model and put into an arbitrary unit cell in the P1 space group. Structure factors were calculated using electron scattering factors from the resulted map, and the figure of merit (FOM) and the sigma (SIGF) were added to each reflection uniformly. Structure refinement was carried with PHENIX.refine [9], using rigid body positional refinement and a single B factor for each subunit. The refinement led to an R of 0.43, R_{free} of 0.47, rmsd in bond lengths of 0.016 Å and rmsd in bond angles of 0.48°.

Fluorescence polarization (FP) assay

Detailed protocol could be found in our previous study [10]. In short, monomeric MPB-tagged ASC^{PYD} (M1-Q105) containing an engineered Cys at the C-terminus (S106C) was expressed in *E. coli* BL21(DE3) cells and purified by Ni-NTA affinity pulldown and size-exclusion chromatography. The monomers were labeled with Maleimide-Alexa Fluor 568 (Invitrogen) by recommended protocol from the manufacturer. Excess dyes were removed by gel filtration after overnight incubation. FP measurements were taken with the SpectraMax M5e (Molecular Devices) plate reader. For the mCherry-$NLRP6^{PYD}$/ASC^{PYD} experiment, same procedure was used except Maleimide-Alexa Fluor 488 was used to label MBP-ASC^{PYD}.

Negative-stain EM analysis of $AIM2^{HIN}$/dsDNA filaments

$AIM2^{HIN}$ (residues 138-343) was cloned into pSMT3 vector using the BamHI and SalI cloning sites and expressed as a Sumo-fusion protein with an additional N-terminal 6 x His tag. The recombinant protein was expressed in *E. coli* BL21(DE3) cells by growing the culture at 37 °C to OD_{600} of 0.8 and inducing with 0.5 mM IPTG overnight at 16 °C. The *E. coli* cells were harvested and lysed by sonication in lysis buffer containing 25 mM Tris-HCl pH 8.0, 1.0 M NaCl, 5 mM imidazole, 5 mM β-ME, and 5% glycerol. The cell lysate was centrifuged at 40,000 x g for 40 minutes, and the supernatant was incubated with pre-equilibrated Ni-NTA resin. After being washed with 20 column-volume lysis buffer containing 25 mM imidazole, the protein was eluted in buffer A containing 25 mM Tris-HCl pH 8.0, 300 mM NaCl, 300 mM imidazole, 5 mM β-ME and 5% glycerol. To cleave the Sumo-tag, the recombinant protein was incubated with 1/1000 (w/w) Ulp1 protease at 4°C overnight. The cleaved protein was then loaded onto a Heparin SP column and eluted with a gradient of 0.3 - 1.5 M NaCl in buffer A. The peak corresponding to $AIM2^{HIN}$ was further purified using Superdex 200 (10/30) size exclusion chromatography (SEC) in 25 mM Tris-HCl pH 8.0, 150 mM NaCl and 2 mM DTT. Fractions containing $AIM2^{HIN}$ were collected, concentrated and flash frozen in liquid nitrogen for future use. To form

AIM2^{HIN}/dsDNA filaments, AIM2^{HIN} was diluted in SEC buffer to a final concentration of 0.05 mg/ml, and incubated with 300 bp, 1 kbp and 2 kbp dsDNA at a molar ratio of 1/60, 1/200 and 1/400 of the protein, respectively.

Full length AIM2 was cloned into pDB.His.MBP vector using the NdeI and XhoI cloning sites and expressed as a His-MBP-fusion protein in *E. coli* BL21(DE3) cells under the same condition as that used for AIM2^{HIN}. The protein was purified with Ni-NTA resin followed by Heparin SP and Superdex 200 (10/30) columns without removing the MBP-tag. The purified MBP-AIM2 protein was diluted to 0.05 mg/ml and mixed with dsDNA of different lengths at indicated concentrations, and TEV protease was added to 1/10 (w/w) ratio with the protein to cleave the MBP-tag, allowing for AIM2/dsDNA filament formation.

Modeling the AIM2^{HIN}/dsDNA filament

An 80-bp ideal B-form DNA (DNA80) is generated in WinCoot [8]. Superimposing the AIM2^{HIN}/dsDNA structure (PDB ID: 3RN5) on DNA80 generated the first HIN domain on DNA80. Sliding the first HIN domain along DNA80 every 4 base pairs (i → i+4) results in HIN domains closely packed on DNA80 without significant clashes between adjacent molecules.

Supplemental References

1. Mindell, J. A. & Grigorieff, N. (2003) Accurate determination of local defocus and specimen tilt in electron microscopy, *Journal of structural biology.* **142**, 334-47.

2. Frank, J., Radermacher, M., Penczek, P., Zhu, J., Li, Y., Ladjadj, M. & Leith, A. (1996) SPIDER and WEB: processing and visualization of images in 3D electron microscopy and related fields, *Journal of structural biology.* **116**, 190-9.

3. Tang, G., Peng, L., Baldwin, P. R., Mann, D. S., Jiang, W., Rees, I. & Ludtke, S. J. (2007) EMAN2: an extensible image processing suite for electron microscopy, *Journal of structural biology.* **157**, 38-46.

4. Egelman, E. H. (2010) Reconstruction of helical filaments and tubes, *Methods Enzymol.* **482**, 167-83.

5. Egelman, E. H. (2000) A robust algorithm for the reconstruction of helical filaments using single-particle methods, *Ultramicroscopy.* **85**, 225-34.

6. Egelman, E. H. (2014) Ambiguities in helical reconstruction, *eLife.* **3**.

7. Collaborative Computational Project, N. (1994) The CCP4 Suite: Programs for Protein Crystallography, *Acta Cryst.* **D50**, 760-763.

8. Emsley, P. & Cowtan, K. (2004) Coot: model-building tools for molecular graphics, *Acta crystallographica Section D, Biological crystallography.* **60**, 2126-32.

9. Adams, P. D., Afonine, P. V., Bunkoczi, G., Chen, V. B., Davis, I. W., Echols, N., Headd, J. J., Hung, L. W., Kapral, G. J., Grosse-Kunstleve, R. W., McCoy, A. J., Moriarty, N. W., Oeffner, R., Read, R. J., Richardson, D. C., Richardson, J. S., Terwilliger, T. C. & Zwart, P. H. (2010) PHENIX: a comprehensive Python-based system for macromolecular structure solution, *Acta crystallographica Section D, Biological crystallography.* **66**, 213-21.

10. Lu, A., Magupalli, V. G., Ruan, J., Yin, Q., Atianand, M. K., Vos, M. R., Schroder, G. F., Fitzgerald, K. A., Wu, H. & Egelman, E. H. (2014) Unified polymerization mechanism for the assembly of ASC-dependent inflammasomes, *Cell.* **156**, 1193-206.

Appendix IV

Supplemental Materials for Chapter Five:

A VHH Defines Mechanism of Inflammasome Assembly

This section contains the following 1 Supplemental Table, Materials and Methods, and Supplemental References –

Supplemental Table

Table S5.1

Materials and Methods

Supplemental References

Supplemental Table

Table S5.1. Crystallographic Statistics

Crystals	VHH_{ASC}	VHH_{ASC} + ASC^{CARD} mutant
Data collection		
Beamlines	APS 24-ID-C	APS 24-ID-C
Space group	$P4_22_12$	P2
Cell dimentions		
a, b, c (Å)	97.4, 97.4, 31.9	53.6, 31.0, 79.2
α, β, γ (˚)	90.0, 90.0, 90.0	90.0, 90.0, 90.0
Resolution (Å)	68.9 - 1.9	79.2 - 4.2
CC(1/2) (%)	99.8 (98.6)	73.6 (63.8)
I / σ_I	36.1 (13.7)	2.1 (2.0)
Multiplicity	9.4 (4.7)	6.4 (6.7)
Completeness (%)	99.2 (94.9)	99.0 (100.0)
Structure determination	Molecular replacement	Molecular replacement
Refinement		
No. reflections	12,735	2,025
R_{work} / R_{free} (%)	16.9 / 20.3	30.0 / 35.5
No. atoms	988	1,051
Protein	861	1,051
Water	127	0
Average B factor (Å^2)	28.0	85.0
Protein (Å^2)	26.8	85.0
Water (Å^2)	37.4	---
R.M.S. Deviations		
Bond lengths (Å^2) / angles (˚)	0.006 / 0.97	0.004 / 1.15
Ramachandran plot		
Favored (%)	96.4	96.0
Allowed (%)	3.6	4.0

Numbers in parentheses are for the highest resolution shell.

Materials and Methods

Primary Cells

Human monocytes were isolated from human whole blood buffy coat obtained from VWR. Cells were purified using a Ficoll-Paque Plus (GE Healthcare) cushion and monocytes adhered to cover slips in RPMI for 2 h. Cells were differentiated in RPMI supplemented with 10% FBS and 100 ng/mL recombinant human M-CSF (BioLegend) for 5 days.

Cell Lines

Human epithelial A549 cells were grown in DMEM supplemented with 10% FBS; human monocyte-like THP-1 cells were cultivated in RPMI medium supplemented with 10% FBS and 50 µM 2-mercaptoethanol. THP-1 cell lines inducibly expressing VHH_{ASC}-HA, VHH NP-1-HA, VHH_{ASC}-EGFP, VHH NP-1-EGFP, and EGFP were generated using lentiviruses produced with derivatives of pInducer20 [1] and selected in THP-1 medium with 500 µg/mL geneticin.

Virus Strains

Vaccinia virus strains Western Reserve (WR) E VHH_{ASC}-EGFP L mCherry and WR E VHH NP1-EGFP L mCherry express VHH-EGFP fusions under the control of the J2R early promoter and mCherry under the control of the F17R late promoter. The virus strains were derived from WR wt using plasmids based on pJS4 [2] to insert transgenes into the tk locus. Recombinant viruses were identified based on mCherry expression and purified through three rounds of plaque purification. Mature virions were produced in BSC-40 cells and purified from cytoplasmic extracts through a 16% sucrose cushion in 20 mM Tris pH 9.0.

Reagents

Doxycycline hyclate was purchased from Sigma Aldrich; LPS from *E. coli* K12, nigericin, and poly(dA:dT) were obtained from InvivoGen. Phorbol-12-myristate-13-acetate (PMA) was purchased from Santa Cruz Biotechnology, TAK-242 from Calbiochem, and z-YVAD-cmk from Bio-Techne. Mouse anti-HA.11 (clone 16B12) was acquired from BioLegend, mouse anti-EGFP (clone JL-8) from Clontech, mouse anti-IL-1β (clone 3A6) from Cell Signaling, rabbit anti-caspase-1 p10 (C-20) from Santa Cruz, and rabbit anti-ASC (AL177) from Adipogen (all antibodies against the human homologues). HRP-coupled sheep anti-mouse IgG was purchased from GE Healthcare, HRP-coupled goat anti-rabbit IgG from SouthernBiotech, HRP-coupled goat anti-llama IgG from Bethyl Laboratories, peroxidase-coupled rat anti-HA (clone 3F10) from Sigma Aldrich, and HRP-coupled mouse anti-GAPDH (clone 6C5) from abcam. Fluorescent secondary antibodies were acquired from Life Technologies.

VHH Library Generation

In order to raise heavy chain-only antibodies against human ASC, one alpaca was immunized five times with a mixture of proteins including MBP-ASC. A VHH plasmid library in the M13 phagemid vector pJSC was generated as described before [3, 4]. In brief, RNA from peripheral blood lymphocytes was extracted and used as a template to generate cDNA using three sets of primers (random hexamers, oligo(dT), and primers specific for the constant region of the alpaca heavy chain gene). VHH coding sequences were amplified by PCR using VHH-specific primers, cut with AscI and NotI, and ligated into pJSC linearized with the same restriction enzymes. *E. coli* TG1 (Agilent) cells were electroporated with the ligation reaction and the obtained ampicillin-resistant colonies (ca. $3.0 \cdot 10^6$) harvested, pooled, and stored as glycerol stocks.

VHH Phage Display and Panning

ASC-specific VHHs were obtained by phage display and panning with a protocol modified from [3]. *E. coli* TG1 cells containing the VHH library were infected with helper phage VCSM13 to produce phages displaying the encoded VHHs as pIII fusion proteins. Phages in the supernatant were purified and concentrated by precipitation; phages displaying MBP-specific VHHs were removed in a depletion step with MBP immobilized to the bottom of tissue culture flasks. Phages presenting ASC-specific VHHs were enriched using biotinylated MBP-ASC immobilized to MyOne Streptavidin T1 Dynabeads (Life Technologies) in the presence of excess soluble MBP and 500 mM NaCl. The obtained phages were used to infect *E. coli* ER2738 and subjected to a second round of panning. 96 *E. coli* ER2837 colonies yielded in the second panning were grown in 96-well plates and VHH expression induced with IPTG. VHHs leaked into the supernatant were tested for specificity using ELISA plates coated with MBP or MBP-ASC; bound VHHs were detected with HRP-coupled rabbit anti-E-Tag antibodies (Bethyl) and the chromogenic substrate TMB. The amino acid sequence of VHH_{ASC} is: QLQLVESGGG LVQPGGSLKL SCAASGFTFS RYAMSWYRQA PGKERESVAR ISSGGGTIYY ADSVKGRFTI SREDAKNTVY LQMNSLKPED TAVYYCYVGG FWGQGTQVTV SS.

Protein Expression and Purification

For periplasmic bacterial expression, VHH coding sequences were cloned into a derivative of pHEN6 [5] encoding a C-terminal sortase recognition site (LPETG) followed by a His_6-tag. VHH_{ASC}-LPETG-His_6 and $VHH_{Enhancer}$-LPETG-His_6 were expressed in *E. coli* WK6 cells and purified from periplasmic extracts using Ni-NTA affinity purification and size exclusion chromatography with a HiLoad 16/600 Superdex 75 pg column. To fluorescently label VHHs using sortase, proteins were incubated with sortase and GGG-Alexa Fluor 647 as described before [6], followed by removal of His-tagged sortase and size exlusion chromatography.

For cytoplasmic expression, VHH_{ASC} was cloned into pETDuet-1, expressed in *E. coli* BL21(DE3) and purified by Ni-NTA purification and size exclusion chromatography with a Superdex 200 10/300 GL column. ASC^{CARD} (N128A/E130R) was expressed using a pET28a-based vector in *E. coli* BL21(DE3) and purified as described for the cytoplasmic expression of VHH_{ASC}.

For fluorescence polarization assay, MBP-ASC^{CARD}-SUMO and MBP-ASC-caspase-1^{CARD}-SUMO constructs were expressed and purified as described in our previous study [7]. In short, ASC^{CARD} (107-195) or caspase-1 (1-95) was cloned into modified pDB-His-MBP vector containing the sequence of SUMO C-terminal to the inserted gene. For GFP-ASC^{CARD} expression, pET28a was modified to obtain an N-terminal GFP (monomeric) fusion protein, followed by insertion of ASC^{CARD} in frame to GFP. The MBP-ASC^{FL} was described previously [8]. The Y187A mutation on MBP-ASC was introduced by QuikChange site-directed mutagenesis (AgilentTechnologies). All proteins were expressed in BL21(DE3) cells and purified by Ni-NTA affinity chromatography followed by size exclusion chromatography.

For expression of *B. anthracis* PA, *E. coli* BL21(DE3) cells were transformed with pGEX-6P-1 PA. GST-PA was expressed and bound to glutathione-S agarose, followed by release of PA with PreScission protease (GE Healthcare) as described [9]. PA was further purified by anion exchange chromatography with a Mono Q column. His_6-LFn-MxiH wt and His_6-LFn-MxiH 2A (containing point mutations V58A and I78A) were expressed in *E. coli* BL21(DE3) using vectors derived from pET-15b LFN-DTA, a gift from John Collier (Addgene plasmid #11075) [10], and purified by Ni-NTA affinity purification and size exclusion chromatography with a HiLoad 16/600 Superdex 75 pg column. Endotoxins were removed from PA and LFn-MxiH preparations using two extraction with Triton X-114, followed by removal of remaining detergent with Bio-Beads SM-2 beads (Bio-Rad) [11].

X-ray Crystallography

VHH_{ASC} crystals grew in a condition containing 0.1 M citric acid at pH 3.5 and 35% PEG3350. Five microliters of sample at ~15mg/mL was mixed with five microliters of the reservoir condition in a 24 well sitting drop tray (Hampton Research). Crystals appeared during overnight incubation. Crystals were recovered and washed in reservoir condition supplemented with 25% glycerol. The dataset was collected at the APS 24-ID-C beamline at 0.979 Å.

For structure determination, molecular replacement was used for phase determination with a predicted model from SWISS-MODEL (based on a deposited VHH structure: PDB 3UX9). Manual structure refinement was done using the COOT program [12], and iterative automatic refinement was carried out in PHENIX [13]. Ramachandran plots indicate 96.4% (3.6%) in the favored (allowed) region.

ASC^{CARD} (N128A/E130R) / VHH_{ASC} complex crystals were grown in a condition containing 0.1 M citric acid at pH 3.5 and 3 M sodium chloride. Ni-NTA-purified ASC^{CARD} (N128A/E130R) was mixed and concentrated with over-stoichiometric amounts of Ni-NTA-purified VHH_{ASC}. Excess VHH was removed from the complex by size exclusion chromatography on a Superdex 75 column. The complex sample was concentrated to >30mg/mL and mixed 1µL:1µL with reservoir condition in a hanging-drop vapor diffusion experiment. Needle clusters appeared after 4 days of incubation. Crystals were separated into individual needles and frozen in reservoir condition supplemented with 25% glycerol. The dataset was collected at the APS 24-ID-C beamline at 0.979 Å. Phase determination was carried out in Phaser using nanobody crystal structure and the NMR structure of ASC^{CARD} (PDB: 2KN6 [14]) as search models. Both structures were first trimmed to poly-alanine sequence using the Chainsaw in CCP4. Subsequent refinements were carried out in PHENIX using the ASC and VHH_{ASC} structures as reference models to provide restrains. Manual model adjustment including replacement of residues at interface was done in COOT. Ramachandran plots indicate 96% (4%) in the favored (allowed) region.

Immunoprecipitation

For the immunoprecipitation of endogenous ASC, 4 mg VHH_{ASC} and $VHH_{Enhancer}$ were covalently coupled to 0.25 g CNBr-activated Sepharose 6B (Sigma Aldrich). $8 \cdot 10^7$ THP-1 EGFP cells (grown in the presence of 1 µg/mL doxycycline for 24 h to induce EGFP expression) were lysed in a high salt lysis buffer (50 mM Tris pH 7.4, 500 mM NaCl, 1% NP-40, protease inhibitor cocktail (Roche)) and lysates bound to the VHH beads in the cold. After extensive washes, bound proteins were eluted with 0.2 M glycine pH 2.0 and analyzed by SDS-PAGE. The major bands were cut out of the gel and the contained proteins identified by mass spectrometry.

LUMIER Assay

Protein interactions in transfected A549 cells were quantified using the LUMIER assay according to a protocol modified from [15]. A549 cells in 24-wells were transfected with 0.5 µg bait expression vectors (pCAGGS VHH_{ASC}-HA or pCAGGS VHH NP1-HA) and 0.5 µg prey expression vectors (empty vector, pEXPR hASC-Renilla, pEXPR $hASC^{CARD}$-Renilla, pEXPR $hASC^{PYD}$-Renilla, or pEXPR mASC-Renilla, all derived from pcDNA3-ccdB-Renilla, a kind gift of Mikko Taipale, Susan Lindquist lab, Whitehead Institute) using lipofectamine LTX (Life Technologies). 2 days post transfection, cells were lysed in 120 µL LUMIER IP buffer (50 mM Hepes pH 7.9, 150 mM NaCl, 2 mM EDTA pH 8.0, 0.5% Triton X-100, 5% glycerol, protease inhibitor cocktail (Roche)). 90 µL of the lysates were transferred to blocked LUMITRAC™ 600 plates (Greiner) coated with mouse anti-HA.11 and incubated at 4°C for 3 h. After extensive washing steps with IP buffer, incubated wells (or 10 µL lysate) were incubated with Coelenterazine-containing Renilla luciferase substrate mix (BioLux Gaussia Luciferase Assay Kit, New England BioLabs) and light emission quantified using a SpectraMax M3 microplate reader (Molecular Devices). Renilla luciferase activity in the immunoprecipitation samples was normalized by Renilla luciferase activity in the lysates.

Fluorescence Polarization Assays

The detailed protocol for fluorescence polarization assays is described in our previous study [7]. In short, MBP-ASC^{CARD}-SUMO and MBP-caspase-1^{CARD}-SUMO containing a C-terminal sortase motif were fluorescently labeled as described above [6]. Monomeric proteins were incubated with TEV to remove the MBP fusion. The rate of polymerization was enhanced by addition of the oligomeric GFP-ASC^{CARD}. To assay for inhibitory effect, VHH_{ASC} was added to the mixture prior to MBP removal.

NLRP3 Activation Assays

To assay NLRP3 inflammasome activation, THP-1 cell lines were differentiated in the presence of 50 ng/mL PMA for 16 h, followed by incubation in THP-1 medium with or without 1 µg/mL doxycycline for 24 h. Cells were then incubated with 200 ng/mL LPS in THP-1 medium for 3 h, followed by treatment with 5 µM nigericin in OptiMEM for 45 min, both in the absence of doxycycline. Supernatants were cleared by centrifugation (1000g, 4°C, 10 min) and analyzed by ELISA or immunoblot.

AIM2 Activation Assays

To assay AIM2 inflammasome activation, THP-1 cells were differentiated and gene expression induced as described above. Cells were incubated with 200 ng/mL LPS in THP-1 medium for 3 h, followed by transfection of 1 µg/mL poly (dA:dT) with 1.75 µL/mL Lipofectamine 2000 (final concentrations on transfected cells indicated). Supernatants were harvested and cleared after 4 h as described above.

NAIP/NLRC4 Activation Assays

To assay NAIP/NLRC4 inflammasome activation, THP-1 cell lines were differentiated and gene expression induced as described above. Cells were incubated with 5 µg/mL PA and

0.1 µg/mL LFn-MxiH wt or 2A in THP-1 medium supplemented with 20 µM of the TLR4 inhibitor TAK-242. After 3 h, supernatants were harvested and cleared as described above.

Vaccinia Virus Infection Assays

To infect cells with vaccinia virus, mature virions were diluted in DMEM and used to infect cells at a multiplicity of infection (MOI) of 20. 30 min post infection, the inoculum was removed and cells cultivated in full medium for 17.5 h.

IL-1β and TNF ELISAs

Concentrations of mature IL-1β and TNF in cell culture supernatants were quantified using the BD OptEIA Human IL-1β ELISA Set II or the BD Opteai Human TNF ELISA set (both BD Biosciences) according to the manufacturer's instructions. Typically, $2 \cdot 10^5$ cells were covered with 0.5 mL medium and 1:100 dilutions of the cleared supernatants were used for the ELISA. Statistical significance of differences was evaluated using the student's t test.

LDH Activity Assay

Lactate dehydrogenase activity in cell culture supernatants was quantified using the LDH Cytotoxicity Detection Kit (TaKaRa). Typically, 1:2 dilutions of cleared supernatants (see IL-1β ELISA) were used for the assay according to the manufacturer's instructions. LDH activity was corrected by the background LDH activity in the medium and normalized to the LDF activity of a well of cells lysed with 1% Triton X-100.

Immunoblots

To analyze secretion and maturation of caspase-1 and IL-1β by immunoblot, cleared supernatants from $2 \cdot 10^6$ THP-1 cells (covered with 1mL medium) were concentrated by methanol/chloroform precipitation as described by [16]. Proteins were separated by SDS-PAGE

and transferred to PVDF membranes. IL-1β was detected with mouse anti-IL-1β (clone 3A6, 1:1,000 in 5% BSA/TBS-T) and HRP-coupled sheep anti-mouse IgG; caspase-1 was detected with rabbit anti-caspase-1 p10 (1:200 in 5% milk/TBS-T) and HRP-coupled goat anti-rabbit IgG.

Immunofluorescence Microscopy

To stain proteins for immunfluorescence microscopy, cells were fixed with 4% formaldehyde and permeabilized in permeabilisation buffer (PS) (0.05% saponin, 1% BSA, 0.05% NaN_3 in PBS) for 20 min. Samples were incubated with rabbit anti-ASC (1:200 in PS) for 2 h, washed with PBS, and subsequently incubated with Alexa Fluor 594-coupled goat anti-rabbit IgG (1:1,000), Hoechst 33342 (1:5,000), and where indicated with Alexa Fluor 647-coupled VHH_{ASC} or VHH NP1 (1 µg/mL) for 1 h. Samples were washed with PBS and H_2O, and mounted with Fluoromount-G (Southern Biotech) or Duolink In Situ Mounting Medium with DAPI (Sigma-Aldrich). Images were acquired using a PerkinElmer Ultraview Spinning Disk Confocal microscope or a Nikon Eclipse Ti wide field microscope. ASC foci and nuclei in wide field microscopy images were quantified using the spot detection function of the Imaris software package (Bitplane).

Supplemental References

1. Meerbrey, K. L., Hu, G., Kessler, J. D., Roarty, K., Li, M. Z., Fang, J. E., Herschkowitz, J. I., Burrows, A. E., Ciccia, A., Sun, T., Schmitt, E. M., Bernardi, R. J., Fu, X., Bland, C. S., Cooper, T. A., Schiff, R., Rosen, J. M., Westbrook, T. F. & Elledge, S. J. (2011) The pINDUCER lentiviral toolkit for inducible RNA interference in vitro and in vivo, *Proceedings of the National Academy of Sciences of the United States of America.* **108**, 3665-70.

2. Chakrabarti, S., Sisler, J. R. & Moss, B. (1997) Compact, synthetic, vaccinia virus early/late promoter for protein expression, *Biotechniques.* **23**, 1094-1097.

3. Sosa, B. A., Demircioglu, F. E., Chen, J. Z., Ingram, J., Ploegh, H. L. & Schwartz, T. U. (2014) How lamina-associated polypeptide 1 (LAP1) activates Torsin, *eLife.* **3**, e03239.

4. Maass, D. R., Sepulveda, J., Pernthaner, A. & Shoemaker, C. B. (2007) Alpaca (Lama pacos) as a convenient source of recombinant camelid heavy chain antibodies (VHHs), *Journal of immunological methods.* **324**, 13-25.

5. Conrath, K. E., Lauwereys, M., Galleni, M., Matagne, A., Frere, J. M., Kinne, J., Wyns, L. & Muyldermans, S. (2001) Beta-lactamase inhibitors derived from single-domain antibody fragments elicited in the camelidae, *Antimicrobial agents and chemotherapy.* **45**, 2807-12.

6. Guimaraes, C. P., Witte, M. D., Theile, C. S., Bozkurt, G., Kundrat, L., Blom, A. E. & Ploegh, H. L. (2013) Site-specific C-terminal and internal loop labeling of proteins using sortase-mediated reactions, *Nature protocols.* **8**, 1787-99.

7. Lu, A., Magupalli, V. G., Ruan, J., Yin, Q., Atianand, M. K., Vos, M. R., Schroder, G. F., Fitzgerald, K. A., Wu, H. & Egelman, E. H. (2014) Unified polymerization mechanism for the assembly of ASC-dependent inflammasomes, *Cell.* **156**, 1193-206.

8. Barrios-Rodiles, M., Brown, K. R., Ozdamar, B., Bose, R., Liu, Z., Donovan, R. S., Shinjo, F., Liu, Y., Dembowy, J., Taylor, I. W., Luga, V., Przulj, N., Robinson, M., Suzuki, H., Hayashizaki, Y., Jurisica, I. & Wrana, J. L. (2005) High-throughput mapping of a dynamic signaling network in mammalian cells, *Science.* **307**, 1621-5.

9. Wu, G., Feng, C., Hong, Y., Guo, A., Cao, S., Dong, J., Lin, L. & Liu, Z. (2010) Soluble expression and purification of the anthrax protective antigen in E. coli and identification of a novel dominant-negative mutant N435C, *Applied microbiology and biotechnology.* **87**, 609-16.

10. Milne, J. C., Blanke, S. R., Hanna, P. C. & Collier, R. J. (1995) Protective antigen-binding domain of anthrax lethal factor mediates translocation of a heterologous protein fused to its amino- or carboxy-terminus, *Molecular microbiology.* **15**, 661-6.

11. Aida, Y. & Pabst, M. J. (1990) Removal of endotoxin from protein solutions by phase separation using Triton X-114, *Journal of immunological methods.* **132**, 191-5.

12. Emsley, P. & Cowtan, K. (2004) Coot: model-building tools for molecular graphics, *Acta crystallographica Section D, Biological crystallography.* **60**, 2126-32.

13. Adams, P. D., Afonine, P. V., Bunkoczi, G., Chen, V. B., Davis, I. W., Echols, N., Headd, J. J., Hung, L. W., Kapral, G. J., Grosse-Kunstleve, R. W., McCoy, A. J., Moriarty, N. W., Oeffner, R., Read, R. J., Richardson, D. C., Richardson, J. S., Terwilliger, T. C. & Zwart, P. H. (2010)

PHENIX: a comprehensive Python-based system for macromolecular structure solution, *Acta crystallographica Section D, Biological crystallography.* **66**, 213-21.

14. de Alba, E. (2009) Structure and interdomain dynamics of apoptosis-associated speck-like protein containing a CARD (ASC), *The Journal of biological chemistry.* **284**, 32932-41.

15. Taipale, M., Krykbaeva, I., Koeva, M., Kayatekin, C., Westover, K. D., Karras, G. I. & Lindquist, S. (2012) Quantitative analysis of HSP90-client interactions reveals principles of substrate recognition, *Cell.* **150**, 987-1001.

16. Jakobs, C., Bartok, E., Kubarenko, A., Bauernfeind, F. & Hornung, V. (2013) Immunoblotting for active caspase-1, *Methods in molecular biology.* **1040**, 103-15.

Appendix V

Supplemental Materials for Chapter Six:

A Novel Capping Mechanism Underlies Homotypic CARD-CARD Interaction

This section contains the following 8 Supplemental Figures, Materials and Methods, and Supplemental References –

Supplemental Figures

Materials and Methods

Supplemental References

Supplemental Figures

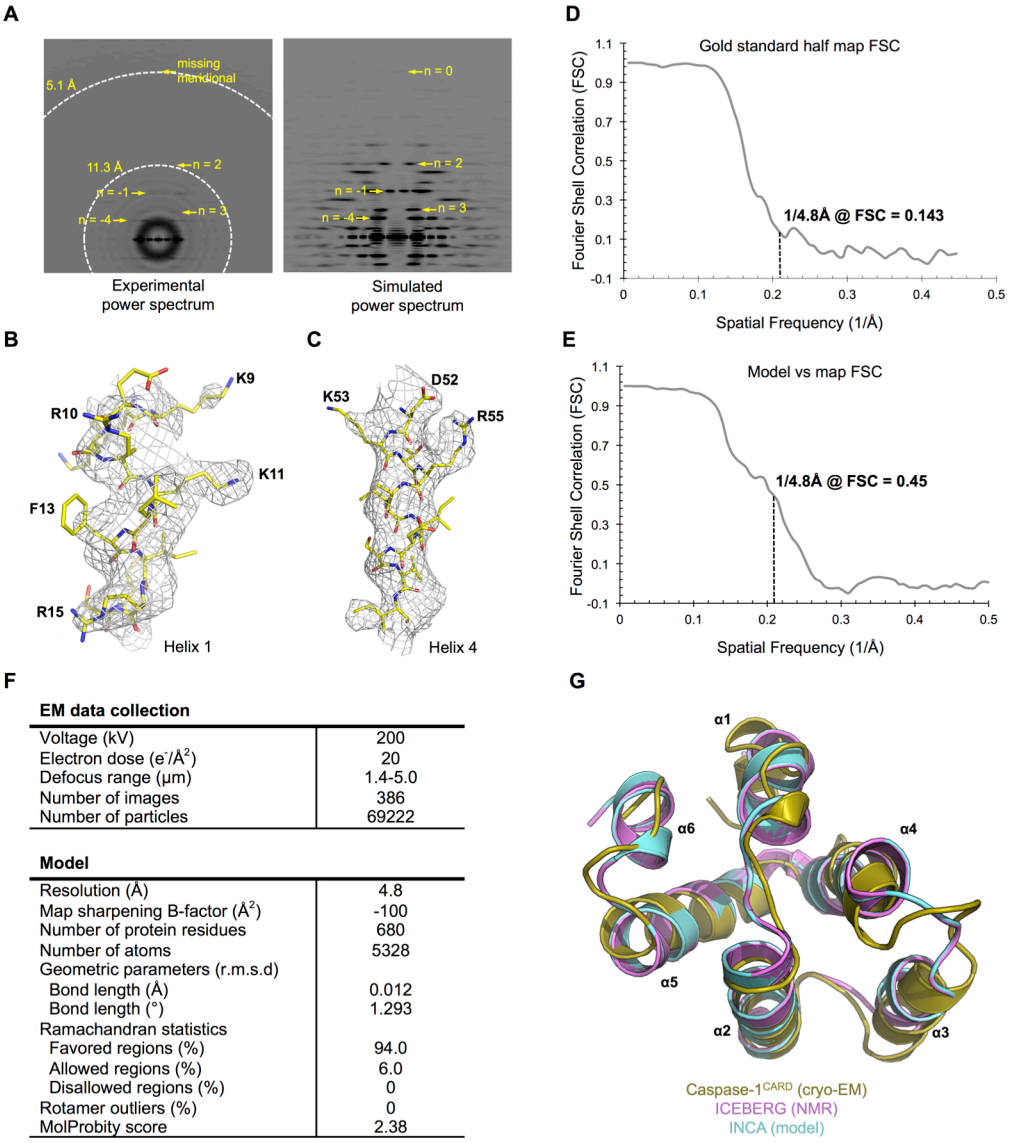

EM data collection

Voltage (kV)	200
Electron dose (e^-/Å^2)	20
Defocus range (μm)	1.4-5.0
Number of images	386
Number of particles	69222

Model

Resolution (Å)	4.8
Map sharpening B-factor (Å^2)	-100
Number of protein residues	680
Number of atoms	5328
Geometric parameters (r.m.s.d)	
Bond length (Å)	0.012
Bond length (°)	1.293
Ramachandran statistics	
Favored regions (%)	94.0
Allowed regions (%)	6.0
Disallowed regions (%)	0
Rotamer outliers (%)	0
MolProbity score	2.38

Figure S6.1. Cryo-EM structure determination of the caspase-1^{CARD} filament.

A. Enlarged experimental and simulated power spectra showing the position of the meridional layer line.

B-C. A magnified view of the cryo-EM density for helix 1 and helix 4.

D-E. Gold standard and model versus map Fourier shell correlation plots showing the estimated resolution at 4.8 Å.

F. Summary of MolProbity validation report for the caspase-1^{CARD} filament model.

G. Superposition of the caspase-1^{CARD} structure in the filament with the NMR structure of ICEBERG and a homology model of INCA based on the ICEBERG structure.

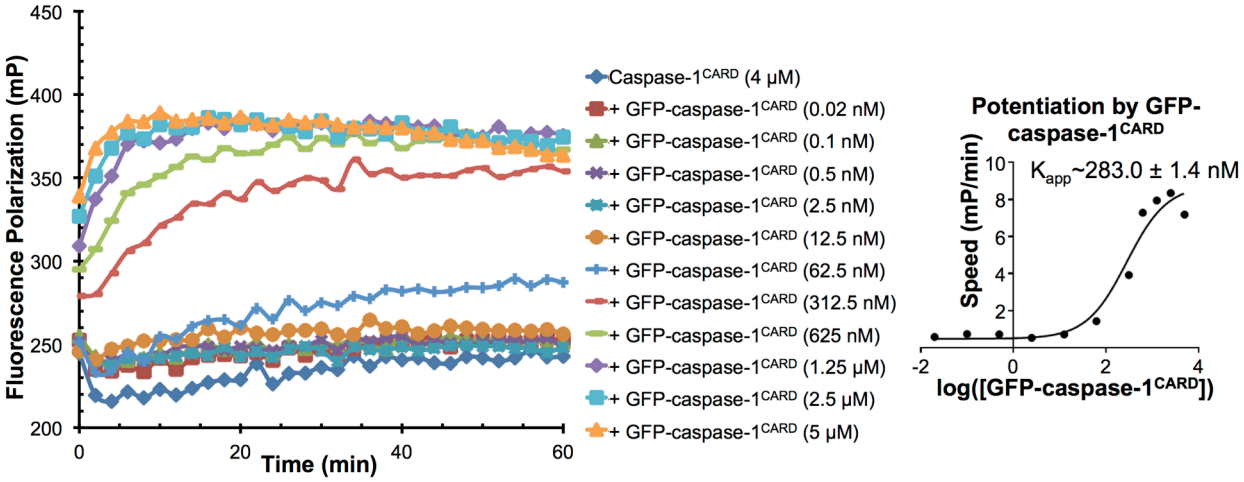

Figure S6.2. Oligomeric His-GFP-caspase-1^{CARD} nucleated caspase-1^{CARD} filament formation with an apparent dissociation constant of 283.0 nM.

Figure S6.3. Comparison with other helical DD fold structures.

A-C. Overall best alignment of the type I, II, and III dimers in caspase-1^{CARD} filament (cyan, magenta, and green) with those in MAVS^{CARD} filament (gray).

D. Structural alignment of caspase-1^{CARD} and MAVS^{CARD} as performed by the Dali server [1]. Buried interfacial residues identified by PISA [2] for each asymmetric dimer types were highlighted to show the similarity in their relative locations.

E. Comparison of relative angular differences in the caspase-1^{CARD} filament (cyan, magenta, and green) and in the MAVS^{CARD} filament, the PIDDosome complex, the Myddosome complex, and the ASC^{PYD} filament. The left subunits (Ib, IIb, and IIIb monomers) are first aligned in the respective dimers, and the rotation angles required to bring the Ia, IIa, and IIIa monomers in superposition are indicated.

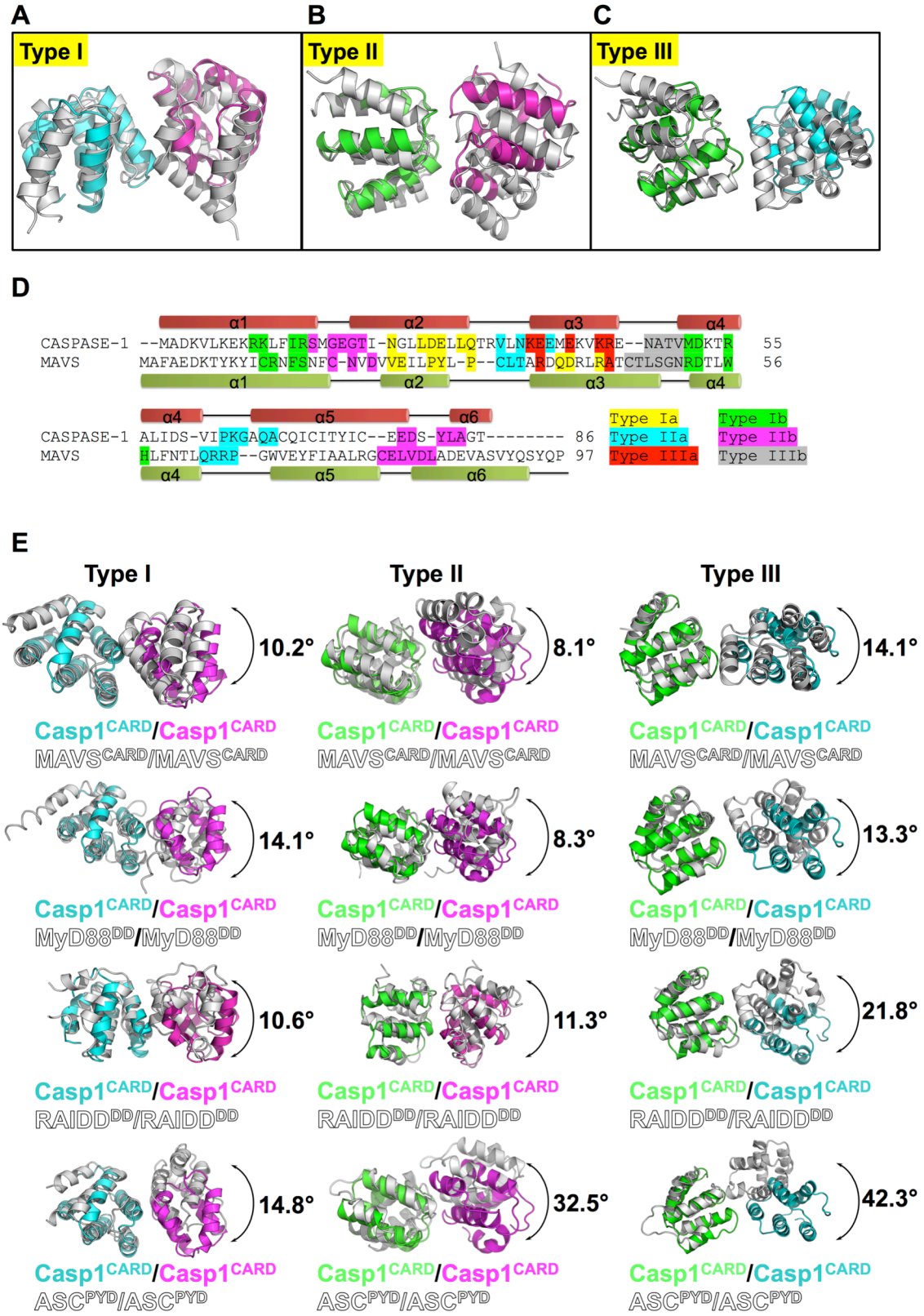

Figure S6.3 (Continued)

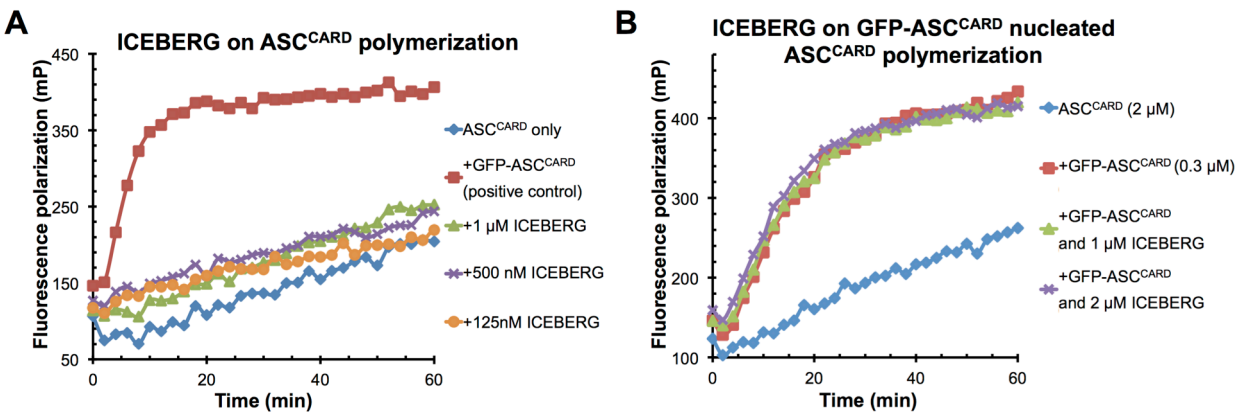

Figure S6.4. ICEBERG does not interact with ASC^{CARD}.

A. ICEBERG did not nucleate ASC^{CARD} polymerization.

B. ICEBERG did not inhibit GFP-ASC^{CARD} nucleated ASC^{CARD} polymerization.

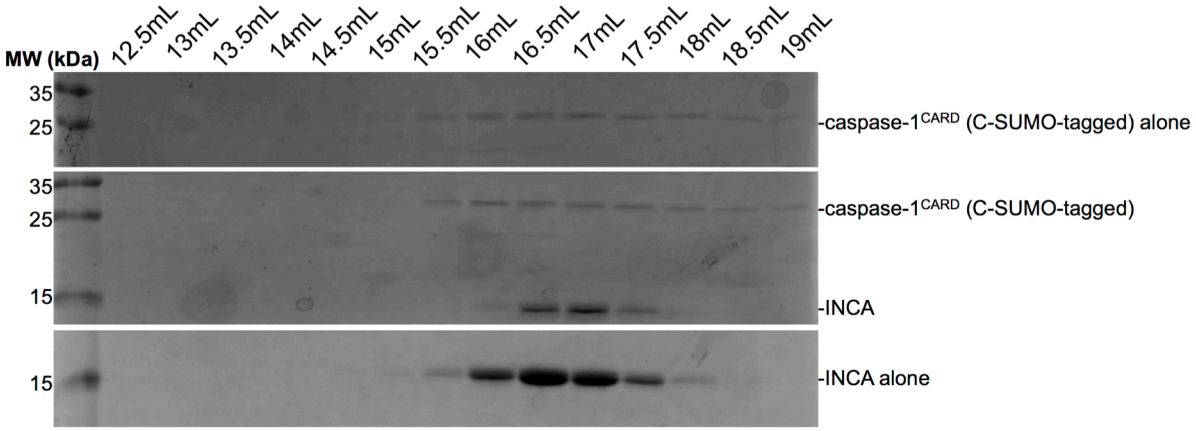

Figure S6.5. INCA does not interact with monomeric caspase-1^{CARD} as shown by gel filtration profiles of INCA alone, caspase-1^{CARD}-SUMO, and a mixture of the two proteins. Size-exclusion chromatography was done at concentrations comparable to FP assay for caspase-1^{CARD} labeled with TAMRA fluorophore and its mixture with slightly over-stoichiometric amount of INCA.

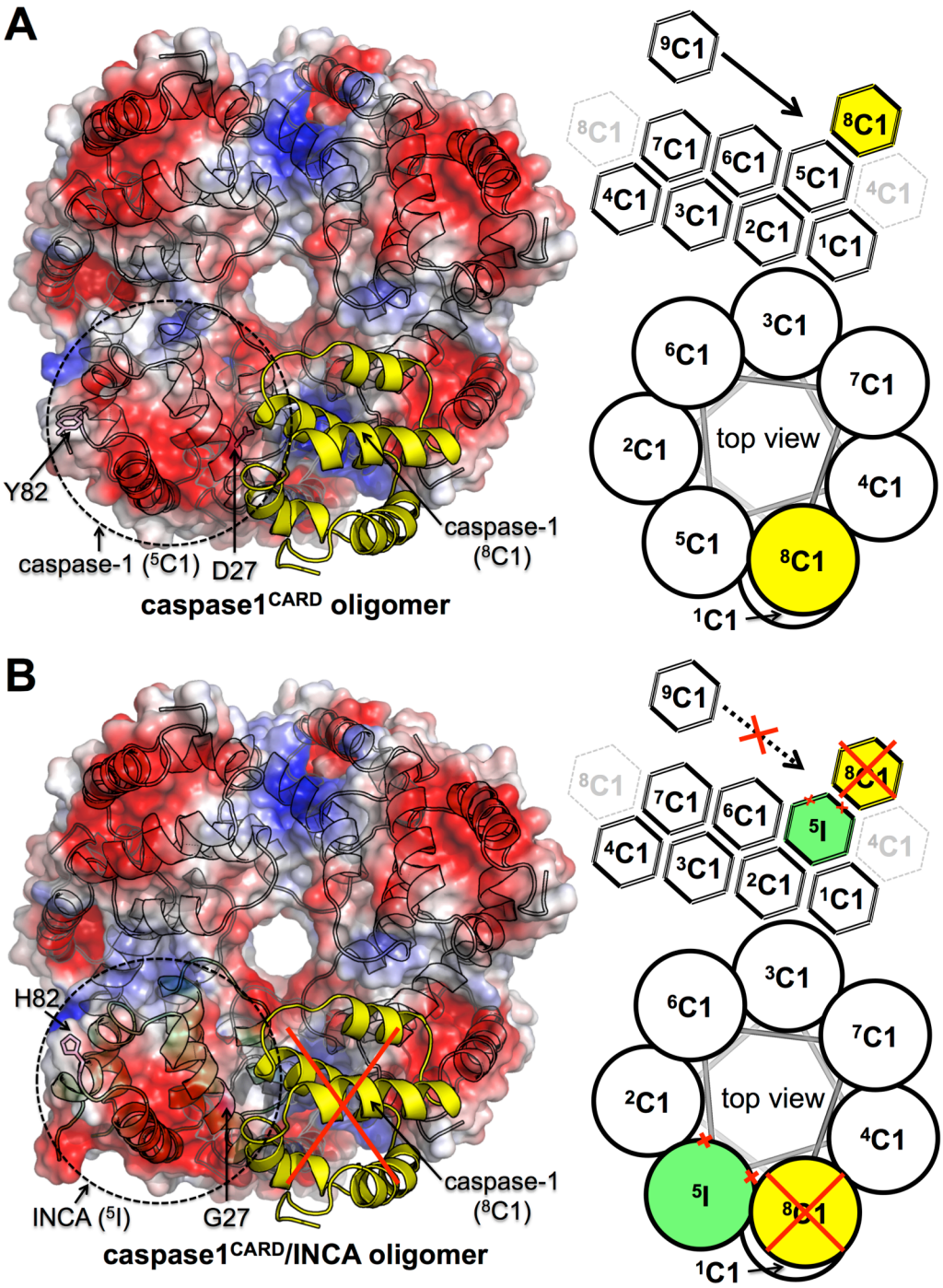

Figure S6.6. Model of how INCA caps growing caspase-1^{CARD} oligomer. Conserved type Ia, IIa, IIIa, and IIIb interfaces allow stochastic incorporation of INCA into growing caspase-1^{CARD} filament. Defective type Ib and IIb interfaces prevent caspase-1 recruitment and filament elongation. C1: caspase-1; I: INCA. The composite electrostatic surface and ribbon diagram at the right is complemented with a top view schematic and a side view helical plot at the right. (**A**) Normal activation. (**B**) Caspase-1^{CARD} capped by INCA.

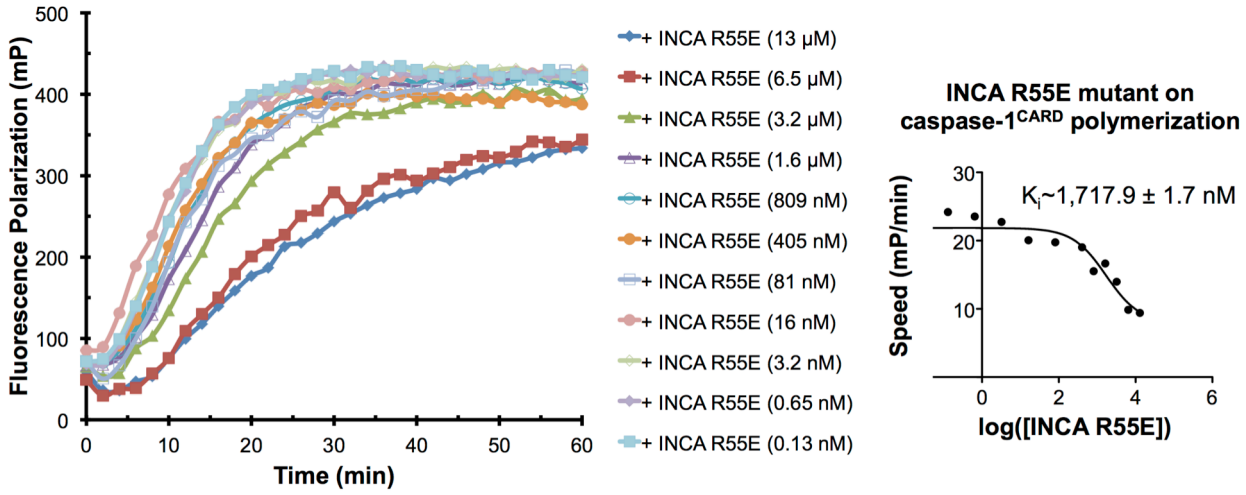

Figure S6.7. Effect of R55E mutation on the inhibition potency of INCA. This charge-reversal mutation at the type Ia interface greatly reduced INCA's inhibition potency on nucleated caspase-1^{CARD} polymerization. Notably, the K_i is increased to ~1.7 μM.

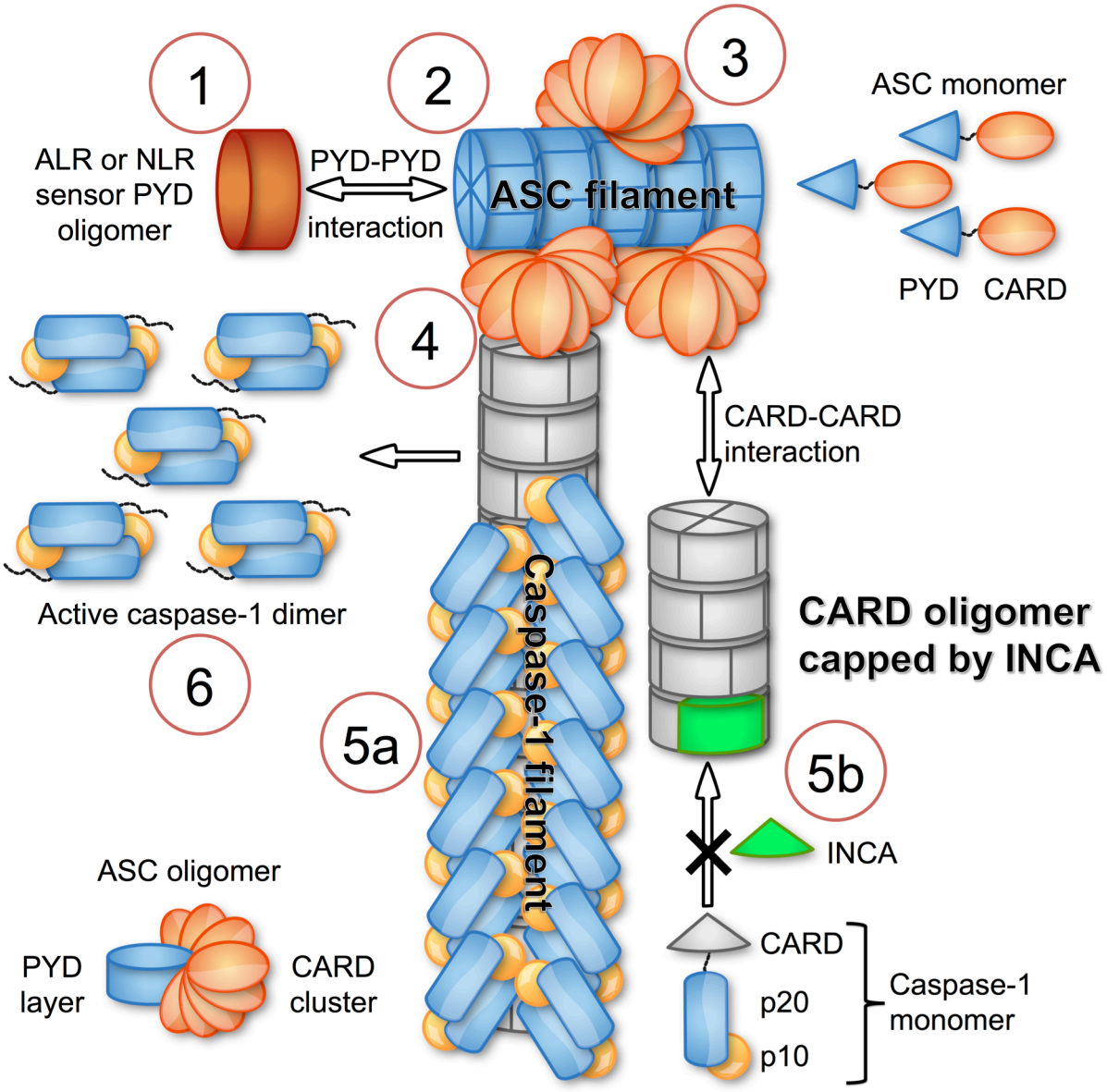

Figure S6.8. Mechanistic model for the inhibition of inflammasome activation by INCA. 1. Activation of sensor proteins such as ALRs (e.g. AIM2) and NLRs (e.g. NLRP3) forms an initial PYD layer. **2.** The sensor PYDs nucleate the formation of ASC^{PYD} filaments that further recruit ASC monomers. **3.** ASC^{CARD} clusters outside of these PYD filament core. **4.** Pro-caspase-1 monomers are recruited by CARD-CARD interaction to form CARD filaments. **5a.** During normal activation, caspase-1 filaments elongate by recruitment of pro-caspase-1 monomers. **6.** Proximity-driven dimerization and autoprocessing lead to the production of active caspase-1 dimers. **5b.** In the presence of INCA, capsase-1 filaments are capped to prevent recruitment of pro-caspase-1 thereby repressing inflammasome activation.

Materials and Methods

Protein purification

All proteins were expressed in chemically competent BL21(DE3) *Escherichia Coli* cells by overnight induction with 0.4 mM IPTG at 16 ˚C. Cells expressing hexahistidine (His)-tagged constructs were lysed by sonication in a buffer containing 20 mM Sodium HEPES at pH 8.0, 150 mM NaCl, 5 mM imidazole, 10% glycerol, and 5 mM β-mercaptoenthanol. Whole cell lysate were centrifuged at 30,000 x g for 40 minutes. The supernatant was incubated with Ni-NTA resin (Qiagen) for 1 hour. The resin was washed with lysis buffer containing 20 mM imidazole. The target proteins were eluted with lysis buffer containing 300 mM imidazole. Subsequent size exclusion purification or gel filtration analysis was done on a Superdex 200 10/300 GL column (GE Healthcare) in a buffer containing 20 mM Sodium HEPES at pH 8.0, 150 mM NaCl, and 2 mM DTT.

Cryo-EM data collection

Protein sample (3 µl) was applied to glow discharged holey carbon C-flat grids (R1.2/1.3, Photochip, CA), blotted for 3 seconds, and plunged into liquid ethane in a FEI Vitrobot Mark VI. Frame-packed micrographs were semi-automatically recorded on a FEI Tecnai Arctica Cryo-TEM operating at 200 KeV with a K2 summit direct electron detector, under super-resolution counting mode with 0.87 Å pixel size. A total of 509 video-mode micrographs were collected. The exposure time was 6 seconds and each video stack contained 30 sub-frames, with 200 ms exposure per frame. The accumulated dose in each stack was 20 electron / $Å^2$.

Cryo-EM reconstruction and structure determination

The helical reconstruction was performed using the iterative helical real space reconstruction (IHRSR) method [3]. Each sub-frame was subjected to gain correction and

motion correction with SPIDER [4], and then summed up to a single image. Defocus range determined by CTFFIND3 [5] was from 1 to 6 μm. Images with defocus higher than 5 μm or still suffering from severe astigmatism were excluded. 69,222 segments were cut out from the remaining images, with a box size of 200 x 384 pixels and an overlap of 374 pixels (97%). The experimental power spectrum was calculated from the original segments that were padded into 1024x1024 pixels, with a pixel size 0.87 Å. For the diffraction lines marked as n=2, n=-1, n=3 and n=-4, the Y coordinates were measured 78, 49, 29 and 20 pixels respectively, and the X coordinates were approximately 11, -7, 16 and -22 pixels. By indexing the power spectrum, an initial helical symmetry of 5.1 Å in rise and -100.2° in rotation per subunit was obtained. Initial reconstruction was carried on with 4 x 4 binned segments, staring from a solid cylinder to avoid any model bias. Further refinement was gradually expanded to the pixel size of the super-resolution mode. Finally out-of-plane tilt was calculated and imposed to these segments until convergence, leading to the final reconstruction. Some helical pitches and large side chains were visible in the final density. To calculate gold standard Fourier shell correlation (FSC) [6], we split sorted dataset into two independent halves. Two parallel helical reconstructions were executed starting from the solid cylinder model and with the same settings and refinement cycles. The resolution was 4.8 Å based on 0.143 cutoff of the gold standard FSC.

Model building and refinement

The nuclear magnetic resonance (NMR) structure of ICEBERG (1DGN) [7] was uploaded to Swiss-Model server [8] to generate an initial caspas-1^{CARD} homology model. The initial model was adjusted manually in COOT [9] toward the cryo-EM density. A filament model containing 8 caspase-1^{CARD} subunits was generated in UCSF Chimera [10] by applying the helical symmetry. The density corresponding to this filament model was masked in CCP4 [11] and Fourier transformed to structure factors in the MTZ format using PHENIX [12]. After rigid

body phased refinement using PHENIX.refine, the structure was further refined in real space using Rosetta [13]. The model-map cross validation FSC has a value of 0.45 at 4.8 Å resolution.

Sortase labeling and fluorescence polarization assay

Constructs for sortase labeling and polymerization assays contain a C-terminal "LPETG" polypeptide motif. Calcium-independent sortase and TAMRA conjugated tri-glycine nucleophile (GGG-TAMRA) were used [14]. In short, 30 μM of a freshly purified protein substrate with the "LPETG" motif was incubated with 5 μM sortase and 500 μM GGG-TAMRA overnight at 4˚C. The labeled substrate and the excess nucleophile were separated by size-exclusion chromatography. Labeled proteins were diluted to desired concentrations for fluorescence polarization (FP) assays on a SpectraMax M5e plate reader. Traces of polarization values were averaged for triplicate experiments and plotted in Excel.

Calculation of apparent dissociation and inhibitory constants

To estimate the apparent dissociation constants between nucleators and polymerizing monomers and the inhibitory constant of INCA, we extracted the slopes of the initial linear phase of the FP traces in the unit of mP/min and plotted them against the log of the concentrations of the added nucleators or INCA. The profiles were fitted in Prism 6.0 for Windows (Graphpad Software, La Jolla California USA, www.graphpad.com) using three-parameter agonist or antagonist function to determine the concentration of the nucleator or the inhibitor at the half maximal effect.

Nano-gold labeling and negative-stain electron microscopy

Gel filtration purified proteins and protein complexes were embedded on a Formvar carbon-coated EM grid (CFC400-Cu, Electron Microscopy Sciences) and washed 3 times. The grids were blotted to remove excess sample and incubated upside-down on a drop containing

suitable dilution of the Ni-NTA gold reagent (5 nm, Nanoprobes, Inc.) or Streptavidin-gold reagent (6 nm, Electron Microscopy Sciences). The grids were washed to remove unbound gold and stained with uranyl acetate for negative-stain EM analysis. More detailed protocols of these experiments can be found in the methods of our previous paper [15].

Generation of INCA and ICEBERG over-expressing THP-1 cell lines

THP-1 human monocyte-like cells were cultivated in RPMI with 10% FBS and 50 µM 2-mercaptoethanol. THP-1 cell lines inducibly expressing HA-tagged EGFP, ICEBERG, and INCA were generated using lentivirus produced with derivatives of pInducer20 [16] and selected in the presence of 500 µg/mL G418. Monoclonal cell lines were obtained by limited dilution in THP-1 medium with 20% FBS.

NLRP3 inflammasome activation assay

To quantify IL-1β secretion in response to NLRP3 triggers, THP-1 cell lines were seeded into 24-well plates ($2.5 \cdot 10^5$ cells per well) and cultivated in the presence of 50 nM Phorbol-12-myristate-13-acetate (PMA, Santa Cruz Biotechnology) for 16h. Cells were then grown in full medium with or without 1 µg/mL doxycycline for 24h, sensitized in the presence of 200 ng/mL LPS (from *Escherichia coli* K12, InvivoGen) for 3h, and treated with 5 µM nigericin in 0.5 mL OptiMEM per well for 45 min. Control samples were incubated with medium lacking LPS or nigericin, respectively. Supernatants were harvested, cell debris removed by a 10 min spin (1000 x g, 4°C), and samples stored at -20°C. IL-1β levels in a 1: 200 dilution of the supernatant were determined using the BD OptEIA Human IL-1β ELISA Set II (BD Biosciences) according to the manufacturer's instructions.

Homology modeling of INCA

A monomeric model of INCA was generated using the online Swiss-Model server [8] with the ICEBERG NMR structure (PDB: 1DGN [7]) as the template. The INCA model was aligned to each subunit of the caspase-1^{CARD} filament cryo-EM structure using the Dali structural alignment server to generate an oligomeric INCA model [1]. Cartoon representations and surface electrostatic potential maps were generated in PyMol [17].

References

1. Holm, L. & Sander, C. (1995) Dali: a network tool for protein structure comparison, *Trends Biochem Sci.* **20**, 478-480.

2. Krissinel, E. & Henrick, K. (2007) Inference of macromolecular assemblies from crystalline state, *Journal of molecular biology.* **372**, 774-97.

3. Egelman, E. H. (2007) The iterative helical real space reconstruction method: surmounting the problems posed by real polymers, *Journal of structural biology.* **157**, 83-94.

4. Shaikh, T. R., Gao, H., Baxter, W. T., Asturias, F. J., Boisset, N., Leith, A. & Frank, J. (2008) SPIDER image processing for single-particle reconstruction of biological macromolecules from electron micrographs, *Nature protocols.* **3**, 1941-74.

5. Mindell, J. A. & Grigorieff, N. (2003) Accurate determination of local defocus and specimen tilt in electron microscopy, *Journal of structural biology.* **142**, 334-47.

6. Scheres, S. H. & Chen, S. (2012) Prevention of overfitting in cryo-EM structure determination, *Nat Methods.* **9**, 853-4.

7. Humke, E. W., Shriver, S. K., Starovasnik, M. A., Fairbrother, W. J. & Dixit, V. M. (2000) ICEBERG: a novel inhibitor of interleukin-1beta generation, *Cell.* **103**, 99-111.

8. Biasini, M., Bienert, S., Waterhouse, A., Arnold, K., Studer, G., Schmidt, T., Kiefer, F., Cassarino, T. G., Bertoni, M., Bordoli, L. & Schwede, T. (2014) SWISS-MODEL: modelling protein tertiary and quaternary structure using evolutionary information, *Nucleic Acids Res.* **42**, W252-8.

9. Emsley, P. & Cowtan, K. (2004) Coot: model-building tools for molecular graphics, *Acta crystallographica Section D, Biological crystallography.* **60**, 2126-32.

10. Pettersen, E. F., Goddard, T. D., Huang, C. C., Couch, G. S., Greenblatt, D. M., Meng, E. C. & Ferrin, T. E. (2004) UCSF Chimera--a visualization system for exploratory research and analysis, *J Comput Chem.* **25**, 1605-12.

11. Winn, M. D., Ballard, C. C., Cowtan, K. D., Dodson, E. J., Emsley, P., Evans, P. R., Keegan, R. M., Krissinel, E. B., Leslie, A. G., McCoy, A., McNicholas, S. J., Murshudov, G. N., Pannu, N. S., Potterton, E. A., Powell, H. R., Read, R. J., Vagin, A. & Wilson, K. S. (2011) Overview of the CCP4 suite and current developments, *Acta crystallographica Section D, Biological crystallography.* **67**, 235-42.

12. Adams, P. D., Afonine, P. V., Bunkoczi, G., Chen, V. B., Davis, I. W., Echols, N., Headd, J. J., Hung, L. W., Kapral, G. J., Grosse-Kunstleve, R. W., McCoy, A. J., Moriarty, N. W., Oeffner, R., Read, R. J., Richardson, D. C., Richardson, J. S., Terwilliger, T. C. & Zwart, P. H. (2010) PHENIX: a comprehensive Python-based system for macromolecular structure solution, *Acta crystallographica Section D, Biological crystallography.* **66**, 213-21.

13. DiMaio, F., Song, Y., Li, X., Brunner, M. J., Xu, C., Conticello, V., Egelman, E., Marlovits, T. C., Cheng, Y. & Baker, D. (2015) Atomic-accuracy models from 4.5-A cryo-electron microscopy data with density-guided iterative local refinement, *Nat Methods.* **12**, 361-5.

14. Hirakawa, H., Ishikawa, S. & Nagamune, T. (2012) Design of Ca2+-independent Staphylococcus aureus sortase A mutants, *Biotechnol Bioeng.* **109**, 2955-61.

15. Lu, A., Magupalli, V. G., Ruan, J., Yin, Q., Atianand, M. K., Vos, M. R., Schroder, G. F., Fitzgerald, K. A., Wu, H. & Egelman, E. H. (2014) Unified polymerization mechanism for the assembly of ASC-dependent inflammasomes, *Cell.* **156**, 1193-206.

16. Meerbrey, K. L., Hu, G., Kessler, J. D., Roarty, K., Li, M. Z., Fang, J. E., Herschkowitz, J. I., Burrows, A. E., Ciccia, A., Sun, T., Schmitt, E. M., Bernardi, R. J., Fu, X., Bland, C. S., Cooper, T. A., Schiff, R., Rosen, J. M., Westbrook, T. F. & Elledge, S. J. (2011) The pINDUCER lentiviral toolkit for inducible RNA interference in vitro and in vivo, *Proceedings of the National Academy of Sciences of the United States of America.* **108**, 3665-70.

17. Delano, W. L. (2002) The PyMol Molecular Graphics System.